STRESS ANALYSIS AND AERODYNAMIC OPTIMIZATION OF SMALL-SCALE COMPRESSED AIR TURBINES

By

Ahmed Mahmood Abdullah Daabo

Thesis Submitted in Partial Fulfilment of Requirements for the Degree of

Doctor of Philosophy

School of Engineering
Department of Mechanical Engineering
The University of Birmingham
Edgbaston, Birmingham, UK

May - 2018

ABSTRACT

Small scale solar powered cycles offer potential for exploiting renewable energy sources with a reasonable cost, environment friendly and adaptable operation. Because of its scale, the Small Scale Solar Powered Brayton Cycle (SSSPBC) has low efficiency as a result of the low efficiency for its components separately namely compressor, expander and the solar heater. This study aims to enhance the performance of the solar heater, consisting of parabolic dish concentrator and thermal receiver, as well as the expander, Small Scale Turbines (SSTs).

Using an advance ray tracing technique, OptisWorks software, both; a small scale parabolic dish concentrator and thermal cavity receiver were developed and optically enhanced. Among three cavity receiver shapes, cylindrical, spherical and conical, the latter showed the best optical performance with 75.3% optical efficiency compared to 70.3 % and 71.5% for the spherical and cylindrical shapes respectively. With the aim of enhancing their optical performance, detailed parametric study focused on some geometrical and optical factors, such as the focal length and the reflectivity, were conducted and led to a maximum of 11% increment in their optical efficiency as well as proposing correlations relating their optical performance with their position with respect to the parabolic dish. In addition, their thermal performances were also investigated resulting with 7.38% improvement for the conical shape which shows the best overall performance among the cylindrical and the spherical shapes.

Simultaneously, small scale axial and radial turbines were developed using meanline approach and (3D CFD) modelling using ANSYS CFX software. The results for three (SSTs) (single stage and dual stage axial turbine and single stage radial turbine) showed that the power output of the Small Scale Radial Turbine (SSRT) is up to 1.7 times higher than the other two turbines with maximum efficiency of around 83%.

The stator and the rotor of the (SSRT) were parametrized using two optimization techniques of multi-objective genetic algorithm optimization. This led to increasing its efficiency to reach 88% as well as an enhanced performance during the off design conditions and at the same time around 3% enhancement in the overall cycle efficiency.

To examine the (SSRT) mechanical design reliability, finite element analysis was utilised to determine the values and the locations of each; stresses, deflection and minimum allowed cycle number (fatigue analysis) for the rotor part. Consequently, to reduce the Von Mises stresses and deflections and at the same time increase the minimum number of cycles on both the rotor shaft and blades, multidisciplinary optimization was conducted to ensure better structural performance without influencing its aerodynamic performance. This methodology led to about 17%, 9% and 25% enhancements in the three objectives mentioned above with a reduction of around 8% and 1.5% in the power output and the rotor efficiency respectively as a penalty which in turns contributed in about 3.5% overall enhancement in the (SSSPBC) efficiency.

In order to, optically and thermally, confirm the followed methodologies, a cylindrical cavity receiver was developed, manufactured and experimentally examined. Similarly, small scale radial turbine was manufactured, using 3D printing technology, with RGD 525 high temperature plastic material and tested.

Comparing numerical and experimental, results showed that the maximum deviation in predicting the compressed air outlet temperature for the thermal receiver was less than 5%. Also, the deviation in (SSRT) efficiency and power output were about 16% and 14% respectively which indicate the validity of the methodology used in this study.

AKNOWLEDGEMENTS

I would like to thank Allah (SWT) for helping me during all my life including the period of my PhD study which of course was the hardest.

Then the thanks should be to my parents for their support and prayers may Allah give them health, mercy and forgiveness.

I also thank my supervisors Dr Saad Mahmoud and Dr Raya Al-Dadah for their valuable suggestions, encouragement and support during my PhD research. Their advice, patience and immense knowledge accelerated my study.

I also thank the Higher Committee of Developing Education in Iraq HCED for funding my study and living costs.

Besides, I thank Mr Simon Rowan for his incessant evaluation, loyalty and patience during the experimental work.

My sincere thanks also go to my family for their prayers, my wife for her patience during my PhD study.

Finally, thanks to all my friends especially Abdalqader Ahmad, Tawfiq Badawi and Dr Ali Abdelhafeez for their moral support.

Ahmed Mahmood Daabo

2018

Table of Contents

List of Figures

List of Tables

NOMENCLATURE

Symbols	Description	Unit
A	Area	m^2
b	Axial Chord, Blade width	m
C	Absolute velocity	m/s
C_θ	Tangential velocity	m/s
C_w	Wall velocity	m/s
Cp	Specific heat	J/kg.K
d	Diameter	m
E	Modulus of Elasticity	Pa
F	Force	N
f	Focal length	-
f_i	I^{th} natural frequency	Cycle/ unit time
g	Gravity	m/s^2
Gr	Grashof number	-
h	Heat transfer coefficient, Height, Static enthalpy	$W/(m^2K$, m, J/kg
h_o	Total enthalpy	J/kg
k	Thermal Conductivity	W/(m/K)
m	Mass	kg
$\dot{m}$	Mass flow rate	kg/s
Ma	Mach number	-
N_f	Number of cycle	-
Nu	Nusselt Number	-
P	Static pressure	Pa
Po	Total pressure	Pa
Pr	Prandtl Number	-
Q	Heat transfer	W
R	Radius	m
R	Degree of reaction	-
Ra	Rayleigh number	-
Re	Reynolds number	-
Rr	Radius at the root	m

s	Turbine blade pitch	m
S	Entropy	J/kg.K
S_M	Momentum source	-
T	Temperature, Static temperature	K
To	Total temperature	K
U	Blade speed	m/s
$U_{Overall}$	Overall uncertainty	-
U_{random}	Random uncertainty	-
U_{Sys}	System uncertainty	-
w	Relative velocity	m/s
ΔW	Specific work	W/kg
Z	Zweifel's coefficient, Blade number, Blade thickness	-

Greek symbols	**Description**	**Unit**
α	Absolute flow angle, Boltzmann Constant, thermal expansion coefficient	Degree, -. -
β	Relative flow angle	Degree
η	Turbine efficiency	-
μ	Flow viscosity	Pa.s
ρ	Density	kg/V
ω	Rotational speed	RPM
$\emptyset$	Flow coefficient, Eigenvector	-, -
ψ	Loading coefficient	-
Ψ	Rim angle	Degree
γ	Specific heat ratio	-
ε, ε	Dissipation rate, Emissivity, Strain	m^2/s^3 -, -
ε_f	Fatigue ductility coefficient	-
θ	Tangential/circumferential direction	Degree
σ	Stress	pa
σ_f	Fatigue strength coefficient	-
$\sigma_{\bar{s}}$	Mean deviation	-
ν	Poisson’s ratio	-

τ	stress tensor	Pa
ζ_R	Rotor Loss Coefficient	-
ζ_S	Stator Loss Coefficient	-

Subscripts	**Description**
1-6	Station number
Amb	Ambient
ap	Aperture
cav	Cavity
B	Balanced
cf	Centrifugal force
Cond	Conduction
Conv	Convection
eff	Effective
f in	Inlet flow
f out	Outlet flow
H	Blade hub
T	Total
M	Blade mean, Meridional direction
T	Blade tip
ts	Total to static
tt	Total to total
th	Thermal
θ	Tangential component
R	Radial component
Rad	Radiation
rim	Rim
Sur	Surface
T	turbine
C	compressor

Acronyms	**Description**
CCD	Central Composite Designs
(CFD)	Computational Fluid Dynamic
CSP	Concentrated Solar Power
DNI	Direct Normal Irradiance
DOE	Design of Experiments
DPG	Distributed Power Generation
EPA	Environmental Protection Agency
FEA	Finite Element Analysis
GA	Genetic Algorithm
GB	Giga Byte
GDO	Goal Driven Optimization
IEO	International Energy Outlook
LFR	Linear Fresnel Reflector
LI	Laboratory Inclination
LHS	Left Hand Side
MOO	Multi Objective Optimization
ORC	Organic Rankine Cycle
PC	Personal Computer
PDC	Parabolic Dish Reflector
PR	Pressure Ratio
PTC	Parabolic Trough Collector
RANS	Reynolds Averaged Navier-Stokes
RHS	Right Hand Side
RSM	Response Surface Method
RTD	Resistance Temperature Detector
SCFM	Standard Cupic Feet Per Meter
SPT	Solar Power Tower
SSE	Summation of Square Errors
SST	Shear Stress Transport
SSDSAT	Small Scale Dual Stage Axial Turbine
SSSPBC	Small Scale Solar Powered Brayton Cycle

SSSPC	Small Scale Solar Powered Cycles
SSSSAT	Small Scale Single Stage Axial Turbine
SSRT	Small Scale Radial Turbine
SSTs	Small Scale Turbines
TEST	Thermal Energy Storage Tank
TCR	Thermal Cavity Receiver
UF	Uniformity Factor
WEC	World Energy Council

LIST OF PUBLICATIONS

Journals:

1- **Daabo, Ahmed M.**, Saad Mahmoud, and Raya K. Al-Dadah. "The optical efficiency of three different geometries of a small scale cavity receiver for concentrated solar applications." **Applied Energy** 179 (2016): 1081-1096.

2- **Daabo, Ahmed M.**, Ayad Al Jubori, Saad Mahmoud, and Raya K. Al-Dadah. "Parametric study of efficient small-scale axial and radial turbines for solar powered Brayton cycle application." **Energy Conversion and Management** 128 (2016): 343-360.

3- **Daabo, Ahmed M.**, Saad Mahmoud, and Raya K. Al-Dadah. "The effect of receiver geometry on the optical performance of a small-scale solar cavity receiver for parabolic dish applications." **Energy** 114 (2016): 513-525.

4- **Daabo, Ahmed M.**, Ayad Al Jubori, Saad Mahmoud, and Raya K. Al-Dadah. "Development of three-dimensional optimization of a small-scale radial turbine for solar powered Brayton cycle application." **Applied Thermal Engineering** 111 (2017): 718-733.

5- **Daabo, Ahmed M.**, Abdalqader Ahmad, Saad Mahmoud, and Raya K. Al-Dadah. "Parametric analysis of small scale cavity receiver with optimum shape for solar powered closed Brayton cycle applications." **Applied Thermal Engineering** 122 (2017): 626-641.

6- **Daabo, Ahmed M.**, Saad Mahmoud, Raya K. Al-Dadah, Ayad M. Al Jubori, and Ali Bhar Ennil. "Numerical analysis of small scale axial and radial turbines for solar powered Brayton cycle application." **Applied Thermal Engineering** 120 (2017): 672-693.

7- **Daabo, Ahmed M.**, Saad Mahmoud, Raya K. Al-Dadah, and Abdalqader Ahmad. "Numerical investigation of pitch value on thermal performance of solar receiver for solar powered Brayton cycle application." **Energy** 119 (2017): 523-539.

8- Pavlovic, Sasa, **Ahmed M. Daabo**, Evangelos Bellos, Velimir Stefanovic, Saad Mahmoud, and Raya K. Al-Dadah. "Experimental and numerical investigation on the optical and thermal performance of solar parabolic dish and corrugated spiral cavity receiver." **Journal of Cleaner Production** 150 (2017): 75-92.

9- Al Jubori, Ayad, **Ahmed Daabo**, Raya K. Al-Dadah, Saad Mahmoud, and Ali Bahr Ennil. "Development of micro-scale axial and radial turbines for low-temperature heat source driven organic Rankine cycle." **Energy Conversion and Management** 130 (2016): 141-155.

10- Al Jubori, Ayad M., Raya K. Al-Dadah, Saad Mahmoud, and **Ahmed Daabo**. "Modelling and parametric analysis of small-scale axial and radial-outflow turbines for Organic Rankine Cycle applications." **Applied Energy** 190 (2017): 981-996.

Conferences:

1- **Daabo, Ahmed**, Saad Mahmoud, and Al-Dadah Raya. "Effect of open cavity configuration on solar receiver thermal performance." **Extended Abstracts.** 2016.

2- **Daabo, Ahmed M.**, Saad Mahmoud, and Raya K. Al-Dadah. "Development of Small-Scale Axial Turbine for solar powered Brayton Cycle." In Students on Applied Engineering (ICSAE), International Conference for, pp. 170-175. **IEEE,** 2016.

3- **Daabo, Ahmed M.**, Saad Mahmoud, and Raya K. Al-Dadah. "Structural Analysis of Small Scale Radial Turbine for Solar Powered Brayton Cycle Application." Proceedings of the **ASME** 2018 POWER & ENERGY Conference PowerEnergy2018 June 24-28, Lake Buena Vista, FL, USA

Rewards:

A reward was received from the Iraqi minister of higher education and scientific research, personally.

CHAPTER 1: INTRODUCTION

1.1 General Background:

Despite the significant growth in power production, about 1.3 billion people are suffering from the absence or the lack of electricity and about 3 billion people are still utilizing open fires to cook [1]. Solar energy offers sustainable energy solutions, as it is available, cheap and environmentally friendly. However, solar radiation which reaches the ground's surface is still not effectively harnessed. In recent times, this form of energy received more attention from government, researchers, designers and provider companies.

As indicated by Pulsinelli et al [2], around \$51 billion and \$52 billion were invested on renewable energy systems, by China and the USA in 2011 despite the world economic crisis. By 2026, it is likely that around 26% from the total electricity consumed worldwide originates from the renewable energy whereas this ratio was only about 13% in 2012 [3]. Despite the continuous effort made by the developed countries, it is expected that the increase in the carbon dioxide emissions due to the energy production will be 3.4 billion metric tons during the period from 2012 to 2020 and about 17.6 billion metric tons by 2040 according to the International Energy Outlook 2016 IEO 2016 [4]. Most of CO_2 emissions come from the contribution of liquid fuel and coal respectively, about 43% and 39%, in 1990 and around 36% and 43% in 2012 with the aim of decreasing the level of CO_2 due to coal to 38% by 2040 as stated by IEO 2016 [4]. According to the International Energy Agency IEA 2016 the global emissions of CO_2 remains stable at 32.1 billion tonnes from 2013 to 2015 and the report suggested that the renewable energy has played a critical role in electricity generation, with about 90% of new electricity generation in 2015 [5].

Renewable energy includes many types of energy sources such as solar, wind and hydropower. They participated in about 0.45 %, 1.44% and 6.44% respectively from the global primary energy consumption by the end of 2015 according to the World Energy Council/ Resources 2016 Summary, WEC 2016 [6].

There is an exponential growth in the sector of solar electricity which reached about 227 Giga Watt Electricity (GWe) by the end of 2015 i.e. 1% of the global electricity used [5]. The two main technologies for solar electricity are the PV panels, which contributed around 222 GWe of the solar power and the Concentrated Solar Power (CSP) with around 5 GWe but it is expected to reach up to 256 GWe in 2040 according to the IEA scenarios [5].

The main advantage of the CSP over the PV panels is the high environmental risks associated with the materials utilized in solar PV such as Cadmium, Chromium, Gallium and Germanium. By contrast, the CSP technology which consists of parabolic trough collector, linear Fresnel reflector, central receiver and parabolic dish is environmentally friendly particularly if air is used as a working fluid such as the case of Brayton cycle.

In the CSP technology, solar energy is converted to thermal energy which in turn is used to drive power cycles like Brayton, Rankine and hybrid cycles which have been utilized at various scales recently. The output power of (CSP) technology can reach few Mega Watts but those with 5 – 500 kW [7] are considered to be small scale systems which utilize (SSTs).

The effect of working fluid (helium, air and tetrafluoromethane) on the closed Small Scale Brayton Cycle (SSBC) efficiency has been investigated analytically [8]. They also studied the influence of temperature ratio on the cycle thermal efficiency using a commercially available turbine and compressor. They concluded that the performance of fluids with lower specific ratios is better, as a result of requiring small amount of heat to increase its temperature. Although results showed that tetrafluoromethane is a suitable working fluid for SSBCs, they suggested that further improvement in the efficiency can be achieved using optimization.

For small scale power generation using (CSP), most of the research work focused on power output more than 500 kW [9, 10]. Only a few published papers investigated CSP for power output lower than 500 kW. In those papers the thermodynamic cycles used for power generation are either Rankine cycles [11-13] or Brayton cycles [14-16].

Using CSP to drive Brayton air cycle for power output of 5 kW was only highlighted in [8, 17, 18] who showed that an efficiency of 35 % can be achieved. Their research work was focused on enhancing the solar heater of the cycle. This thesis aims to develop an efficient SSSPBC with particular focus on the optical and the thermal analyses of the solar heater, as well as developing and optimizing an efficient small scale turbine.

Small Scale Solar Powered Cycles (SSSPC) can play a significant role in attaining sustainable, cheap and environmentally friendly energy generation. This will lead to a considerable reduction in the CO_2 emission and the global warming problem. Thus, recently, many countries put forward taking advantages of the renewable energy in their agenda [19].

The other accelerating factor for the (SSSPCs) technology is being the current situation of the production units being a long distance away from the consumer of electricity. This leads to higher energy losses during the lines transmission and higher cost of energy travelling [20] which increase the overall electrical energy price.

1.2 Research Objectives:

As mentioned in the previous section, the SSSPBC requires further development in order to improve the system's overall performance. This can be achieved through enhancing each component of the system such as the compressor, the turbine and the thermal receiver. Developing the best configuration with low optical and thermal losses of the thermal receiver and improving the (SSTs) will enhance the cycle overall performance. This research aims to develop a SSSPBC by improving two important components; solar heater and small scale radial air turbine using advance ray tracing technique, Computational Fluid Dynamic (CFD) analysis as well as design optimization through the following objectives:

- Carry out detailed study of (SSSPBC) using Engineering Equations Solver (EES) in order to assess the cycle thermodynamic performance. The main purpose of this study is to evaluate the effect of the performance of each component such as the thermal receiver and the turbine on the overall cycle efficiency.
- Develop a small scale solar heater through a detailed optical and thermal analysis of different configurations.
- Develop a SST with high efficiency that maximizes the cycle performance through (i) meanline analysis to produce initial design, (ii) detailed (CFD) and 3D design optimization simulation to produce the maximum efficiency and (iii) detailed structural analysis.
- Construct test facilities for testing the solar heater and the radial turbine with the aim of validating the developed methodology.

1.3 Thesis Outlines:

This thesis consists of seven chapters. Chapter one offers a common introduction about the study background with focus on the (SSSPCs) particularly (SSSPBC), objective and thesis outline. Chapter two gives a detail review about the studied components in the cycle such as the solar heater and the turbines. In chapter three a detailed optical and thermal analysis of small scale thermal system including the cavity receiver and the parabolic dish reflector was discussed. The development of (SSTs) based on 1D meanline modelling, 3D (CFD) simulation and 3D (CFD) optimization techniques has been presented in chapter four. Chapter five described the mechanical analysis and the integrated, structural- aerodynamic optimization. The results of both thermal receiver and the radial turbine are discussed and validated against the experimental work in chapter six and the main conclusions and recommendations of current study are included in chapter seven.

CHAPTER 2: LITERATURE REVIEW ON THE COMPONENTS OF THE STUDIED CYCLE

2.1 Introduction:

There are two methods for converting the power coming from the sunlight to electrical energy. The first one is the direct method, by using photovoltaics (PV) systems. The other, is the indirect method where solar radiation is converted to thermal energy using Concentrated Solar Power (CSP). Small Scale Solar Powered Cycles (SSSPC) have become one of the main desirable technologies for clean, sustainable and reliable electricity generation according to Environmental Protection Agency (EPA 2013) [21]. In recent years and because of the increasing concerns of global warming, the trend of this new technology has attracted more attention in order to enhance its overall performance and increase its application [21-23]. Moreover, the significant amount of electrical energy loss during transmission from centralized power plants to consumers is another reason for this technology receiving more attention in recent years for application in distributed power generation. Obviously, this can be achieved by developing each of the (SSSPC) components such as the compression, the expansion and the heating components separately and then integrate them effectively to produce maximum efficiency [24]. In this chapter a complete literature review of (SSSPC), in terms of the cycle type, applications, the solar heater and the expanders is carried out.

2.2 Small Scale Solar Powered Cycles:

Although (SSSPC) systems have been recently utilized worldwide, a specific universal definition is not available. (SSSPC) is classified depending on the amount of power produced. For instance, according to [25], (SSSPC) is from 5– 500 kW while based on [26], the range of power output is equal or less than 200 kW.

For the distributed powers cycles, their classification depends on the type of the energy source for example whether it is wind, solar or hydropower. It is suggested by some authors such as [27] that up to 5 kW, 5 MW, and 50 MW would be micro-scale, small-scale, medium-scale respectively with the term of large-scale for any number more than 50 MW. In the current study the author is focusing on range which less than 5 kW.

2.3 Small Scale Solar Powered Brayton Cycles Components:

Figure 2.1 shows a schematic diagram of the solar powered Brayton cycle system. It consists of a compressor; a solar heater, for heating the compressed air (in traditional cycles a combustion chamber); a turbine to convert the air kinetic energy to mechanical one and a recuperator to recover the exhaust energy, which would be otherwise wasted to the surroundings. This recuperator preheats the cold air before entering the solar heater. Thermal energy storage could be used in order to store the extra heat coming from the solar system for example in the zenith time, to be used in cloudy weather or during evening.

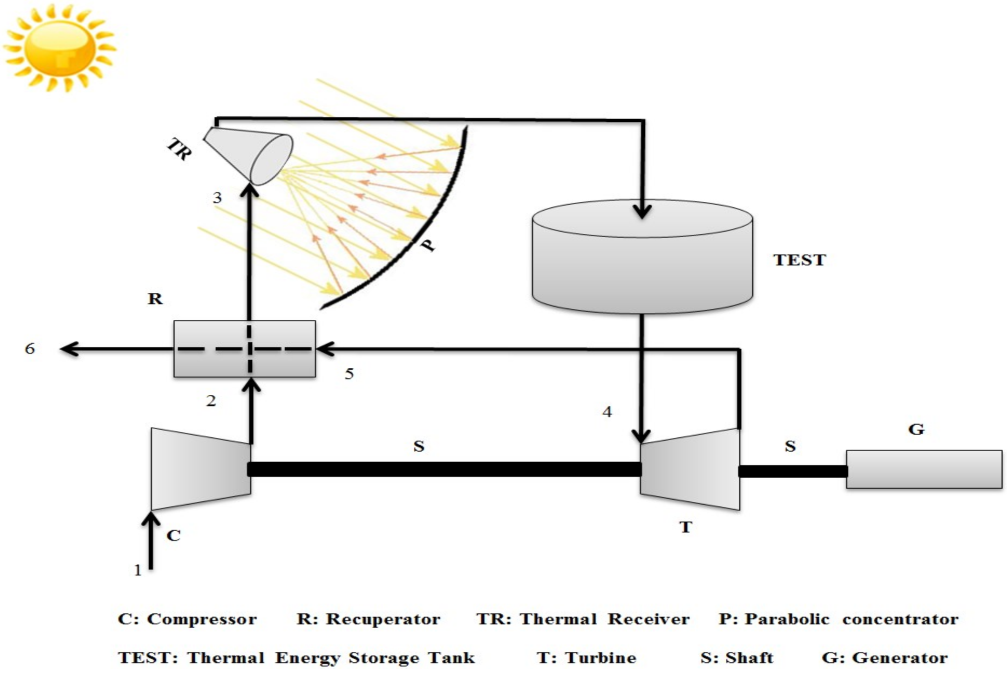

Figure 2.1: Schematic diagram of (CSPBC) system [28].

In the following sections, detailed literature review of the various components of solar powered Brayton cycle is given.

2.3.1 Compressor:

The main function of the compressor is to progressively compress the air and increase its pressure. In general, compressors consume a significant amount of power thus their performance affect the amount of net power extracted from the system as well as the overall cycle efficiency. Compressors can be classified as shown in Figure 2.2 [29, 30].

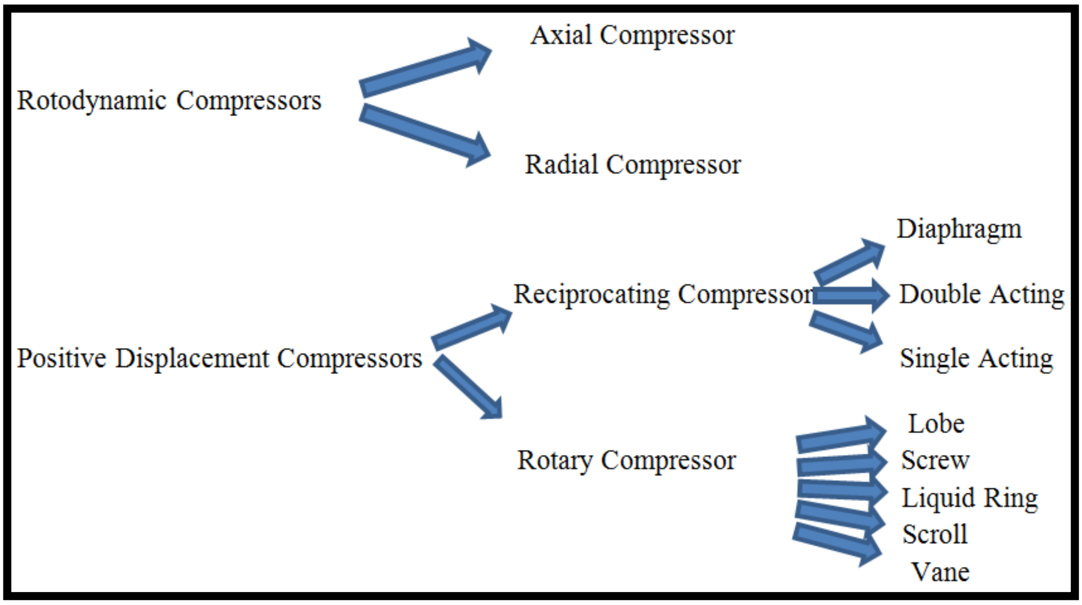

Figure 2.2: Compressors Classification.

The rotodynamic type, which depends upon the fluid's momentum, is the one of interest with regards to this study. In radial type, the rotating disk forces the gas to the rotor's rim increasing its velocity and then the gas enters a divergent duct, diffuser, which converts the gas velocity to pressure. This type of compressor is mainly used in large scale snowmaking systems, internal combustion engines and in medium size gas turbine as a final stage. It can achieve up to 69 MPa output pressure in the case of multi stage configurations cycles [29, 30].

By contrast, the axial-flow compressor uses a pair of aerofoil blade arrays, in each single stage; each array is either rotating or stationary. The rotating blades called rotor accelerates the gas while the stationary aerofoils, stator, slows down and redirects the flow to the inlet of the next stage, for multistage compressors. This type of compressor is typically used in multi stages, up to 5 stages without the need to use variable stators [31]. This type is preferred for high flow rates, compactness, tight tolerance, medium or large gas turbine engines and high efficiency applications.

2.3.2 Recuperator:

It is a heat exchanger for recovering heat from the working fluid leaving the turbine and uses the heat to increase the temperature of the air leaving the compressor before entering the solar heater. Many types and configurations for the recuperator can be found in literature which mainly depends on the application [32]. Not like the regenerators when there is no secondary medium or storage material and as a result there is no direct contact between fluids [32], the only significant heat loss in the recuperator is heat conduction through its walls which is in the same direction of working fluid flow. However, this type of heat loss can be decreased by using a low heat conductivity material such as plastics which can improve the recuperation's effectiveness to reach up to 90%. In general, regenerators are more compact and have low cost compared to recuperators [33].

2.3.3 Solar Heater:

One of the main parts for the solar powered cycles is the solar heater where solar energy is collected and transferred to the working fluid. The main function for this system is to convert the incident solar radiation energy, with as minimum optical and thermal losses as possible; into thermal energy. In general the thermal system consists of concentrator, thermal receiver and tracking system. These components will be reviewed in the following sections.

2.3.3.1 Concentrated Solar Power Collector:

There are four types of the Concentrated Solar Power (CSP) collectors which are; Linear Fresnel Reflector (LFR), Solar Power Tower (SPT), Parabolic Trough Collector (PTC) and Parabolic Dish Reflector (PDR) where the first and the last types have been used for small scale applications. The other two technologies, however, have been used in medium or large scale systems such as those located in the USA [33] and Spain [34]. Moreover, (LFR) and (PTC) are considered as a line focusing technology and the other two are known as a point focusing technique. Recently, researchers showed interest in (LFR) and (PTC) as follows:

1- Linear Fresnel Reflector:

Linear Fresnel Reflector (LFR) technology uses numerous flat mirrors in order to focus the sunlight onto a fixed receiver tube called the absorber. In the receiver tubes liquid is flowing, which will boil and change to steam in order to spin a steam turbine which is going to turn a generator to produce electricity. It is a line focus type [33] and is usually used with one axis tracking, east- to- west type with a concentration ratio ranging from 60 to 400 [34]. An example of the (LFR) type is shown in Figure 2.3 [35].

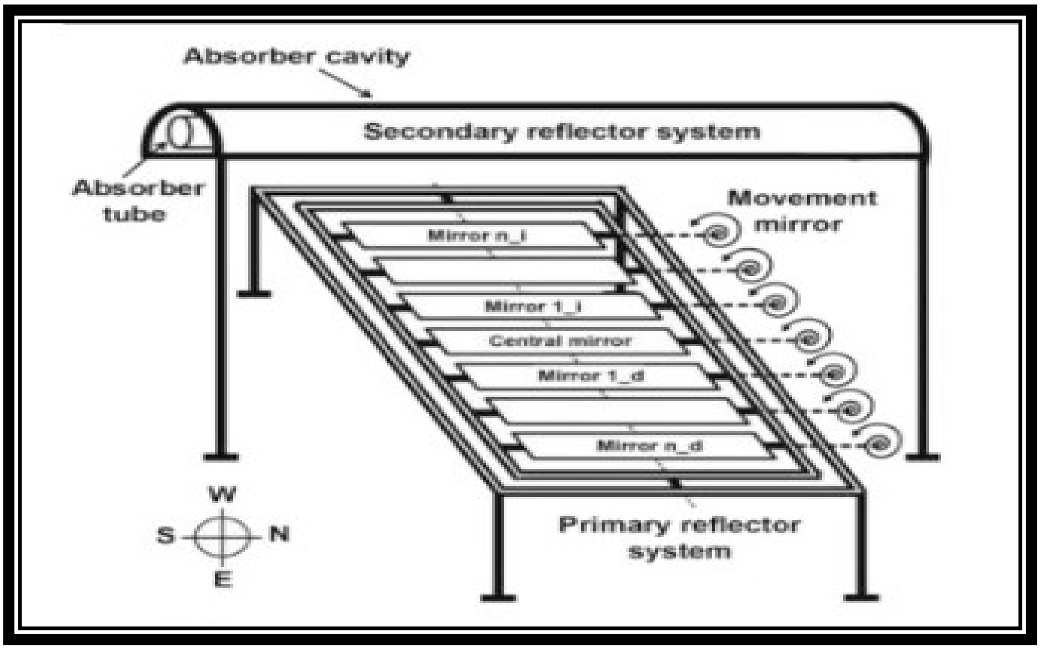

Figure 2.3: Schematic figure for small scale (LFR) technology [35].

2- Parabolic Trough Collector:

Parabolic Trough Collector (PTC) is also a line concentrator which concentrates the incoming irradiance from the sun onto a line receiver tube that has a working fluid which is often molten salts. It is the most commonly used type among the (CSP) systems and has higher efficiency and lower cost compared to the other line concentrated technology i.e. (LFR). The range of temperature achieved in this technology is from 150 °C to 380 °C which can operate a heat engine and generate electricity [36]. An example of this technology is shown in Figure 2.4 [37].

Figure 2.4: Small scale parabolic trough collector [37].

3- Solar Power Tower:

Solar Power Tower (SPT) technology is an arrangement of many thousands of sun-tracking reflecting mirrors called heliostats which are placed in a specific area or field in order to concentrate solar irradiance at one specific point located at the top of the power tower, which can reach up to 80 m. In this technology very high concentration ratio and a temperature up to 1000^{o}C can be achieved [36], depending on the Direct Normal Irradiance (DNI) and the number of used mirrors. An example of this technology is shown in Figure 2.5 [38].

Figure 2.5: Small scale solar power tower [38].

4- Parabolic Dish Concentrator:

Parabolic dish concentrator is normally manufactured using Steel or Aluminium material, with some preference to the latter because of its weight i.e. lower energy required for tracking, and typically covered by mirrors or Aluminium Foil in order to increase the reflectivity. It is also called reflector in some other references [39-41], which is a parabolic dish in shape that used to concentrate and reflect the sun’s rays onto the receiver aperture. In general Aluminium foil is the recommended material for covering its surface area, in order to enhance its reflectivity from less than 79% to 86% [39], primarily because of its worldwide accessibility and cost. Moreover, polished aluminium is also identified as a good material with around 91% specular reflectance [17]. One of the main parameters that affects the performance of the parabolic concentrator is the rim angle which is the angle that determines its focal point location [42]. However, dish manufacturing and installation errors can contribute in changing the position of the focal point [42]. Figure 2.6 shows a parabolic dish reflector consisting of 11 curvilinear trapezoidal reflective petals made using Polymethylmethacrylate known as a (PMMA) covered by special type of reflective coating. This (PDR) was studied by Sasa et al [43] where the diameter of the manufactured dish was equal to 3.8 m with a focal point located at a height of 2.26 m. The exergetic analysis showed that air is the best choice in low temperature levels and oil in higher temperatures.

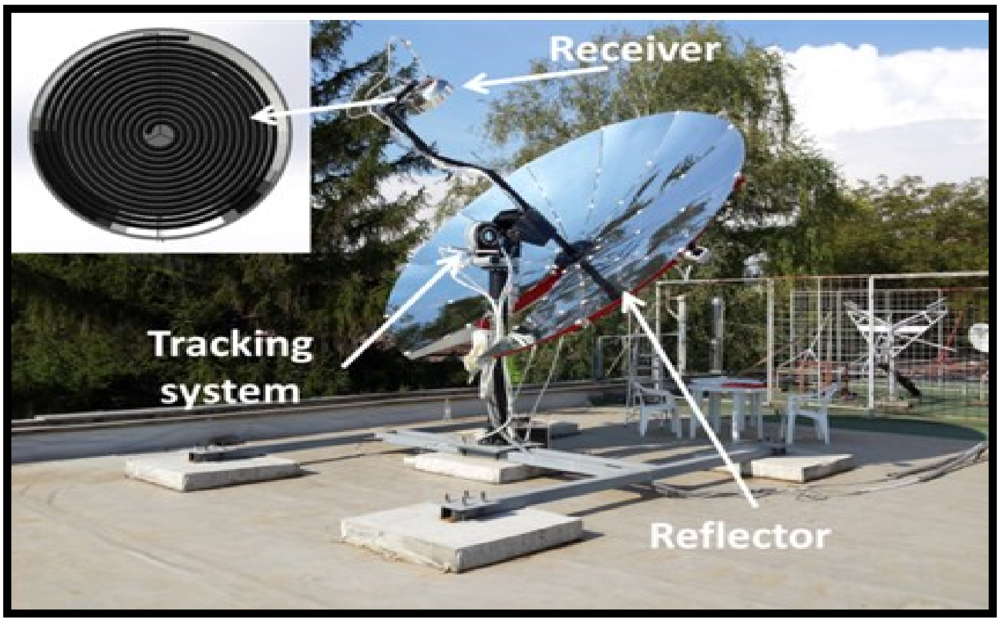

Figure 2.6: 3.8 m, (PDR) integrated with the thermal receiver [43].

2.3.3.2 Thermal Receiver:

The other important part of the thermal system is the thermal receiver, which receives the solar energy that has been reflected by concentrators and uses it to heat the working fluid that will be used to drive the expander for producing power output. Therefore, a number of researchers worked on developing thermal receiver to achieve high working fluid outlet temperature and minimum pressure drop. Thermal receivers can be found in different types, shapes and sizes depending on the application they are designed for. For example, in the trough type concentrating system the used receiver is the tube type located in the focal line of the concentrator trough as shown in Figure 2.4. However, in the solar tower type, the commonly used types of receivers are the volumetric receiver and the tubular receiver as presented in Figure 2.7 and Figure 2.8 respectively [44].

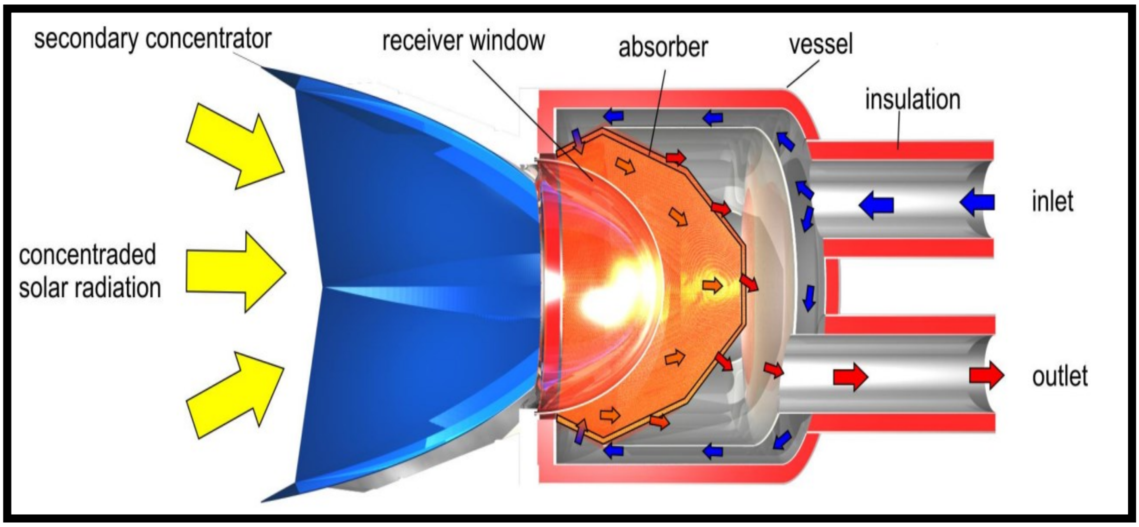

Figure 2.7: Volumetric receiver used in the tower application [44].

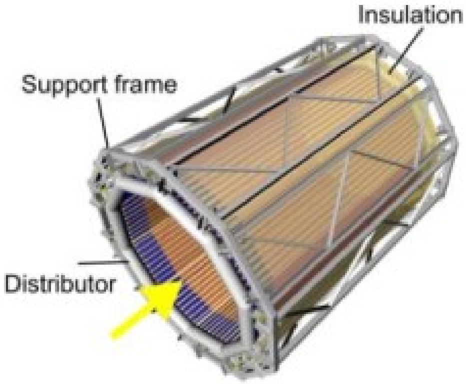

Figure 2.8: Tubular receiver used in the tower application [44].

As for the other two types of reflectors, (LFR) and (PDC), the receiver type that can be used for both of them is the cavity receiver type [45]. However, their shapes are not similar to each other; they can be classified based on their concentration ratio and application. The (LFR) type is shown in Figure 2.9.

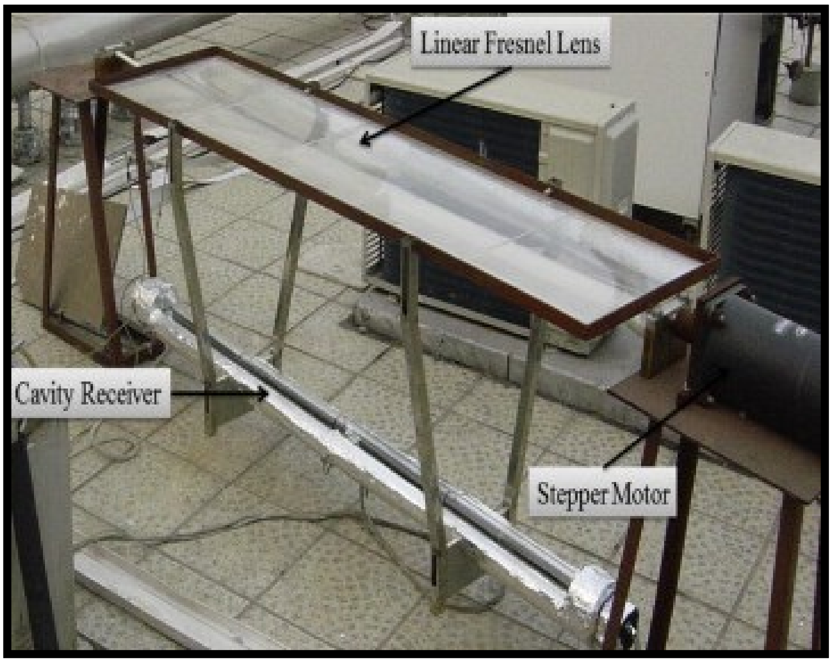

Figure 2.9: linear Fresnel lens concentrator with its thermal receiver [45].

2.3.4 Thermal Energy Storage Tank:

Thermal energy storage systems are considered in order to store energy when production exceeds demands and then make it available when needed. By doing so, the difference between the energy demand and supply will be reduced and as a result improving the overall efficiency of the system. Energy storage systems can be defined based on some factors such as capacity, power, efficiency, storage period, charge- discharge time and finally cost [46]. According to the methods used in storing the energy, thermal energy storage systems can be classified in three main types. The first one is known as sensible heat storage which is based on storing thermal energy by cooling or heating a solid or liquid storage medium such as; sand, water and molten salts [47]. The second type is called the latent heat storage where materials undergo phase change for example; solid state into a liquid state [48]. The last type of energy storage systems is the thermo-chemical storage which benefits from chemical reactions for storing and releasing the thermal energy [49].

Thermal Energy Storage Tank (TEST) is used to store the extra heat from the solar system during the zenith time, and then this stored heat will be used during dusk or in cloudy weather. In (CSP) applications, one of the methods that can be utilised in order to retain thermal energy collected by a solar collector is molten salt which is considered as a safe (nontoxic and non-flammable) thermal energy storage method especially in generating electricity when there is no solar energy. In this application specifically, this method has excellent overall efficiency according to [50-52]. As the salt melts at 131 °C and stays in its liquid phase at 288 °C when it is stored in an insulated storage tank, the liquid salt is pumped to the thermal system and it is then sent to another insulated hot storage tank. In peak electricity demand, the stored hot salt will be pumped to a steam-generator to generate superheated steam [53].

2.3.5 Turbines:

Turbines are considered as one of the most important components in all thermal cycles such as Brayton, Rankine and others. Turbines can be defined as mechanical devices which convert the working fluid’s energy to a useful dynamic energy, as a result of changing the working fluid’ pressure and momentum. In rotodynamic turbines this can be achieved through two main parts normally, the stator (fixed part) where the fluid kinetic energy will be transformed to kinetic energy and the rotor (rotating part) where the fluid kinetic energy will be transformed to rotating power to produce power output. Like compressors, turbines can also be classified into several types such as impulse and reaction turbines, inflow and outflow and axial and radial turbines, based on output power quantity, used working fluid, working fluid movement and principal of operation. As for the scale of turbines, they can be classified to micro-scale, small-scale and large-scale and their ranges in terms of power output were pointed out previously in section 2.2.

2.4 Research on the Development of (SSSPC) Components:

In this study, the focus will be on the most important two components which are the thermal system and the expanders used (SSSPC). Practically, research work on the parabolic dish concentrator [54], the thermal cavity receiver for the thermal system and both types of turbines, the Small Scale Axial Turbine (SSAT) and Small Scale Radial Turbine (SSRT) will be critically reviewed as they these components are the ones that the current study tries to enhance.

2.4.1 Research on the Development of (SSSPC) Thermal System:

As mentioned in section 2.3.3 the thermal system consists of the solar collector and the thermal receiver which combined together converts the solar energy into thermal energy that is used to drive the Brayton power cycle. The efficiency of the thermal system affects the amount of thermal energy and its temperature which in turn affect the system size and efficiency. A number of research studies were reported on the development and performance analysis of thermal systems used for (SSSPC).

The effect of working fluid on the closed solar small scale powered Brayton cycle efficiency has been analysed analytically Riazi [8] using helium, air and tetrafluoromethane. They also studied the effect of temperature ratio on the thermal efficiency of the cycle using an off the shelf turbine and compressor with high efficiencies of 95%. Their results indicated that the cycle efficiency was high for fluid with high values of specific heat ratio where Helium showed the highest efficiency of 42% at temperature ratio of 6.67 and (PR) of 5. The author recommended tetrafluoromethane, as a working fluid, for (SSBC), but highlighted that an optimization is required for the cycles to further improve their efficiencies. Also, optimum pressure ratios, for highest cycle efficiency were suggested at each temperature ratio of the various working fluids used.

In two studies, [18, 55], Roux et al studied the effect of various factors such as wind effect, receiver inclination, rim angle, recuperator geometry and concentration ratio on the performance of an open solar thermal Brayton cycle system using off the shelf turbines. The results showed that the maximum net power output was achieved at the lowest mass flow rate value (0.6 kg), concentration ratio of 500X and a concentrator dish of 4.8 m diameter. Regarding the optimum receiver tube diameter, they found that this diameter does not influence much, when only one parameter or boundary condition is changed. However, it is changed at higher mass flow rate values and also changed when wind speed increased, from 1 to 10 m/s and also when rim angle decreased from 45 to 30 Deg. They also showed that the small receiver is more useful for all the system especially at larger mass flow rates, severe wind, high concentration ratios and smaller rim angle values. They concluded that an optimum geometry for a receiver is highly dependent on a particular set of conditions which still need to be determined in order to maximize the net power output.

As for the optimum area ratio, (A_{ap}/A_{conc}), many researchers reported various values for this ratio. For example, it is reported to be 0.0004 in [56], 0.0009 in [57], 0.00024 in [58] and 0.0007 in [59]. However, it was recommended by [17] to be 0.0035 and they justified this value by the more accurate optics utilized in their studies.

Regarding the optical analysis, Kunzan et al [60] carried out numerical simulation using Monte-Carlo and experimental testing, using five lamps of Xe-arc of cavity receiver with its helical tube. They used a splitter to uniformly distribute the received flux. Their results showed that with 5 m^3/h air flow rate and an average flux of 300 kW/m^2, the working fluid exit temperature reached up to 800 ^oC. This was shown theoretically and experimentally with a maximum deviation of 8%. Moreover, an increase of around 12% in the receiver thermal efficiency can be gained when the tube diameter was reduced from 6 to 4 mm. however; there was an inevitable increment in pressure drop.

The effect of a cylindrical thermal receiver dead area on its optical efficiency, using Monte Carlo ray tracing method, was investigated by Wang et.al. [61]. They highlighted the possibility of using a cavity receiver with bottom convex surface to overcome this problem. The results showed that compared to conventional cavity receiver, the new type offers better optical performance.

As for the cavity receiver thermal performance, many studies were reported. For example, Storch et al [62] evaluated the thermal performance of three receivers; close, tubular cavity and open volumetric cavity. They concluded that both, the open volumetric one and the tubular receiver can produce high thermal performance where at least 700 ^{o} C was achieved.

Milind et al [63] used a 0.54 m diameter hemispherical cavity receiver and calculated the natural convection heat loss, experimentally, at various inclination angle from 0^{o} to 90^{o} using a 2 kW light source. The water temperature values, which varied from 50 ^{o}C to 75 ^{o}C, were used to relate their influence on the heat loss value. Their results indicated that the angle of inclination has a significant role on the heat losses at all temperature differences where the minimum convection heat loses occurred at 90^{o} receiver inclination, was measured, while the maximum values were at 0^{o} especially at high temperature difference.

A copper helical tube coil was used as a line receiver which was fixed at the focal distance of a parabolic dish for water heating applications as reported in [64]. Using an average beam of 714 W/m^2 and 1.56 m diameter with 0.55, assumed solar concentrator efficiency, they obtained 2419 W for four cycles, where water flow rate of 0.0019 kg/s can be raised to 125 ^{o}C. Also, they found that using line concentrator instead of the point concentrator increased the temperature to 190 ^{o}C and led to increasing the average temperature of the outlet water as a result of decreasing the convection losses. Eswaramoorthy et al [65], investigated experimentally the potential of using a small scale solar powered thermoelectric generator fitted in a parabolic dish with a 3.6 m diameter and 0.7 m depth coupled with 1 m diameter receiver to produce about 60 W electricity, for a small scale applications in rural places. The authors found that the receiver temperature is, as expected, completely dependent on the solar beam irradiance and derived a correlation which relates the receiver plate temperature with the beam irradiance value. Moreover, another two correlations were also obtained between the solar irradiance and both overall efficiency of the system and the power generated.

Fleming et al [66] analysed a multi-cavity receiver for high concentrated flux. They showed that attaining a 90% receiver thermal efficiency can be achieved when higher than 99.8%, absorptivity and a lower than 250 W/m^2/K, convection heat transfer coefficient is attained.

Ngo et al [67] studied a finned cavity receiver, shown in Figure 2.10, and calculated both; radiation and natural convection losses at various operating temperatures, emissivity and receiver geometry and orientation. An attempt for fins optimisation was also carried out showing that finned cavity type can contribute to a reduction of about 20%, and 5% of natural convection and the radiation losses respectively. Furthermore, they also highlighted the importance of fins' shape and position on heat losses. Overall, a marginal improvement in the receiver thermal efficiency was achieved and the authors justified this small enhancement by referring most of the heat losses to the radiation.

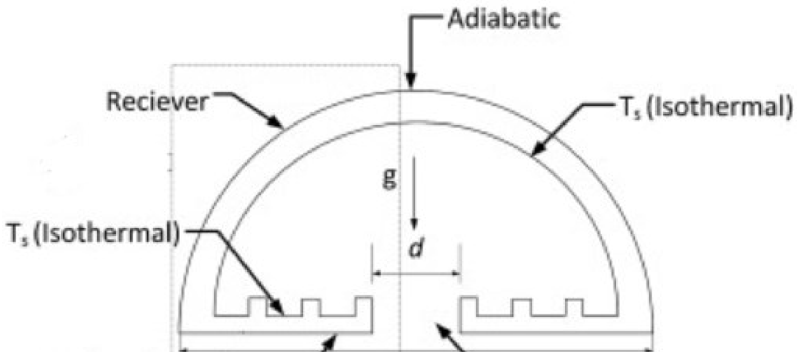

Figure 2.10: Finned thermal cavity receiver [67].

Samanes et al [68] carried out (CFD) simulation to assess five correlations for estimating the natural convection losses of solar thermal power tower plants. The results showed that four of the five investigated correlation has agreed with the simulation one. Table 2.1 summarizes studies related to the thermal receiver. The main outcome from the mentioned table is the lack of analysis for small scale study, less than 5 kW output powers, which can efficiently utilized in the domestic application especially in the remote areas. This highlights the need for further researches in this aspect to improve its performance which in turn leads to better overall efficiency for the all system.

Table 2.1: Studies covered thermal receiver.

Author	**Receiver Type**	**Receiver Dimensions (m)**	**Collector Type**	**Collector Diameter (m)**	**Tracking/ Fixed**	**Experimental/Theoretical**	**Software**	**Working Fluid**	**Mass Flow rate (kg)**	**Application**
Roux et al.[17]	Modified Cavity Receiver	-	PD	4.8	F	T	Sol Trace and MATLAB	Air	0.3 to 0.9	STBC
Roux et al.[7]	Modified Cavity Receiver	0.0374*0.06	PD	4.8	F	T	Sol Trace	Air	0.2 to 0.9	STBC
Roux et al.[18]	Modified Cavity Receiver	-	-	4.8	F	T	Sol Trace	-	-	STBC
Roux et al.[42]	Modified Cavity Receiver	0.25*0.25	PD	4.8	T	E	Sol Trace	Air	0.07	STBC
Lukas et al. [69]	Solar Receiver Air	-	PD	-		T	ANSYS FLUENT	Gas	-	Hybrid
James and Terry [56]	5 Geometries	-	PD	5.97	F	E	-	Air	-	-
Taumoefolau and Lovegrove [70]	Cylindrical	0.28*0.32	UA	UA	Laboratory Inclination	E and T	ANSYS CFD	Air	-	IRP
Paitoonsurikan and Lovegrove [71]	Cylindrical, Conical And Semi Cylindrical	-	Paraboloidal	20 and 400	Laboratory Inclination	E and T	ANSYS CFD and Fluent	Air	-	STBC
Prakash [72]	Cylindrical	2, .3 and .4	UA	UA	F	T	ANSYS CFD	Air	0.045 and 0.088	Numerical
Uhlig et al. [73]	Cylindrical	-	Heliostats	DM	T	T	ANSYS CFD/ MATLAB	Air	15.9	SHCC
Shavazi et al. [74]	Cylindrical Cavity Model	0.083*0.083 and 0.083*0.166	UA	UA	LI	E and T	-	Air	-	IRP
Lin et al. [75]	V-Shaped Cavity Receiver	0.1*0.1	Linear Fresnel	Six Pieses1*0.3 mirror	T	E and T	ANSYS CFD and Tracepro	Air	-	Absorption Process
Tu et al. [76]	Hexagonal Prism With An Inclined Top Face	1.95*1.03*1.04*.67*.67*1.04	UA	-	F	E and T	ANSYS FLUENT	Steam	50-100 kg/h	Rankin Cycle
Sendhil et al. [77]	Modified Cavity / Hemispherical)	0.2 Hemispherical	UA	-	Simulation Inclination	T	ANSYS FLUENT	Air	-	Numerical Study
Wu et al. [78]	Fully Open Cylindrical Cavity	0.229*0.278	UA	-	LI	E	-	Air	-	IRP
Reddy et al. [79]	Modified Hemispherical	-	UA	-	LI	T	GAMBIT 2.0.4, fluent and SIMPLEC	Air	-	Improve Receiver Performance

Wei et al. [80]	Cylindrical	-	UA	UA	LI	E and T	ANSYS FLUENT	Air	-	IRP
Armando et al. [81]	Cupric	CUPIC 1*2*2	Heliostats	UA	F	T	ANSYS FLUENT	Air	-	Solar System
Paitoonsurikarn et al. [82]	Different Geometries	0.23*0.29	PD	DM	LI	T	ANSYS FLUENT	Air	-	Solar System
Fang et al. [83]	Prism	8.25*3*2*2*4	Heliostats	UA	N	T	ANSYS FLUENT	Water	70 T/h	Solar System
Wu et al. [84]	Fully Open Cylindrical Cavity	d=.105, l=.191	UA	UA	LI	E	-	Air	-	Solar System
Yong et al. [85]	Spherical	-	UA	UA	F	T	ZEMAX	Air	-	Solar System
Roldán et al. [57]	Cylindrical	-	Trough	UA	T	E and T	ANSYS FLUENT and CFD	Steam	0.65 to 73	Solar System
Wang et al. [86]	Cylindrical	0.2*0.3	PD	1.68	F	T	FEMAP	Argon	0.000115	Solar System
Leia et al. [87]	Cylindrical	-	Trough	UA	F	E and T	ANSYS FEM	Air	DM	Solar System
Xiao et al. [88]	Cylinder	0.14*0.25	UA	UA	F	E	-	Air	1 to 5 m3/h	Solar System
Osama et al. [89, 90]	Cylinder	-	Trough	UA	F	T	ANSYS FEM	Air	-	Solar System
Jianfeng et al. [91]	Cylindrical Pipe	1*0.01	-	-	F	E	-	Air	-	Solar System
Fang et al. [92]	Six-Side Prism With Inclined Top And Bottom Faces	8.25*3*3*2*2*4*4	Heliostats	-	F	T	Fluent	Saturated Steam	7t/h	Solar System
Capeille`re et al. [93]	Chanel Consists Of Textured Patterns	1.2*1.2	UA	-	F	T	SOLFAST	Air	86g/s	Solar System
Liao et al. [94]	Cylindrical Pipe	Concentrated tube 0.021 and 1,2 thick	UA	UA	F	T	-	Molten Salt, Water/Steam And Steam	-	Solar System
Fend et al. [95]	Channels In Cylindrical	0.00218*0.00218 Channel	10 Xenon short-arc lamps with ellipsoid reflectors	-	F	E and T	COMSOL	Air	0.0025	Solar System
Rold et al. [96]	Cylindrical Volumetric Receiver	0.21*0.06 (Dia*length)	Heliostats and parabolic	5.6	T	E and T	CFD	Air	0.01-0.04	Furnace And Material Treatment

			mirror							
Bai et al. [97]	One Dimensional Analysis	L between .01 to 0.1	-	-	F	E	-	Air	-	Solar Furnace
Wu et al. [98]	Volumetric Receiver	0.05*0.05 Dia*Len	Heliostats and parabolic consent	-	F	E and T	CFD	Air	-	Solar Furnace
Daabo et al [99]	Cylindrical, Conical and Spherical	0.2 * 0.25 to 0.35	PD	1	F	T	CFD and OptisWorks	Air	0.01	STBS
Wu et al. [100]	Volumetric Receiver	0.05*0.05 Dia*Len	Heliostats and parabolic	-	F	E and T	CFD	Air	3.36 g/s	Solar Furnace
Xiao et al. [101]	Fully Open Cylindrical Cavity	Do -0.28 m, Lo of .32 m, and Di of .07 Li of .150	PD	-	Simulation Inclination	T	CFD	Air	-	STBC
Fang et al. [102]	Six-Side Prism With Inclined Top And Bottom Faces	8.25m h, 3mwidth.4 *4 aperture* 3*3*2*2 m, w	Heliostats and parabolic mirror	-	Simulation Inclination	T	CFD	Steam	70t/h	STBC
Melchior et al. [58]	Cylindrical	Rin =0.0254 Rout = 0.0381, width 0.01414 and length 0.15	Electrical input power	0.15 × 0.2 Rectangular	F	E and T	CFD	Air	-	Chemical Reactor
Sendhil et al. [103]	Hemispherical Surface	-	PD	-	Simulation Inclination	E and T	Fluent	Air	-	STBC
Sendhil et al. [104]	Hemispherical Modified And Secondary Reflector	-	PD	-	Simulation Inclination	T	Fluent	Water	-	STBC
Paitoonsurikan and Lovegrove [105]	Cylindrical		UA	20 and 400	LI	T	ANSYS CFD and Fluent	Air	-	STBC
Daabo et al [106]	Cylindrical, Conical and Spherical	0.2 * 0.25 to 0.35	PD	1	F	T	CFD and OptisWorks	Air	-	STBS
Xiao et al. [107]	Hemispherical	Do0.280 and 0.320 depth, Din 0.07 and 0.150 depth Different l/d an d/D	UA	-	Simulation Inclination	T	ANSYS CFD and Fluent	Air	-	-
Patil et al. [63]	Cylindrical, Conical, Cone-Cylindrical, Dome Cylindrical And	574 and 270	UA	UA	Experimental Tracking	E	-	Water	0.013	STBC

	Hetro-Conical									
Jiltea et al. [108]	Cylinder	0.5 Dia* 0.75 depth meter	PD	UA	F	T	Fluent	Air	n	STBC
Ibrahim [109]	Helical Tube Only	D 0.234 and L 0.234	PD	1.67	Experimental Tracking	E	-	Water	9KG/HOUR	Water Heating
Vinayak et al. [110]	Rectangle, Triangle, Semicircle And Arc-Shape Cross Sections	coil of 0.22 dia and 15 turns	Fresnel	UA	F	E	-	Water	995.7 kg/m3	Water Heating
Lin et al. [45]	Helical Cylinder	50 Dia* 30 open	UA	UA	F	E and T	CFD and some exp.	Oil	-	-
Prakash et al. [111]	-	0.3d * 0.5 length	-	UA	Simulation Inclination	E and T	CFD	Water	0.02	-
Daabo et al [112]	Cylindrical, Conical and Spherical	0.2 * 0.25 to 0.35	PD	1	F	T	CFD and OptisWorks	Air	0.01	STBS

2.4.2 Research on Development of (SSSPC) Turbines:

The development of an efficient turbine for small scale solar powered Brayton cycle is challenging where detailed computational fluid dynamic and optimization techniques can play major role. Both axial and radial turbines were investigated and literature review of work regarding such turbines is described in the following sections.

2.4.2.1 Axial Turbine:

When the working fluid enters the turbine, through its stator, axially and leaves it, through its rotor, axially then this type of turbines is classified as an axial turbine, see Figure 2.11. This configuration is used in applications characterized by low pressure ratio and high fluid mass flow. As a result of its relatively simple shape and the path that the flow follows, this turbine has lower aerodynamic losses and as a result higher efficiency [113].

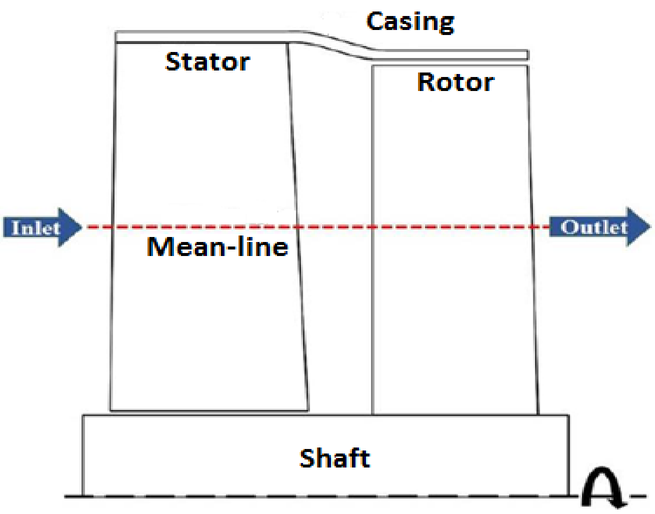

Figure 2.11: Flow through axial turbine stage [114].

As mentioned in section 2.3.5 the axial turbine can be classified as reaction type or impulse type depending on the amount of pressure and enthalpy change in the rotor compared to the whole turbine stage.

2.4.2.2 Radial Turbine:

Radial Inflow Turbines are similar to a centrifugal compressor except that the flow direction and the motion are reversed. Here, the flow enters the turbine radially and exits axially as shown in Figure 2.12. In such turbines the straight radial blades are generally preferred because the curved blades would incur additional stress and also their rotor or impeller end has an exducer [115]. A diffuser is commonly used at the end of system in order to recover some of the potential energy, which could be otherwise wasted, thus increasing the power output. In these turbines, the difference in the speed between rotor inlet and outlet contributes to increasing the work done. So, in general this type is considered a good choice for application where low mass flowrate and high pressure ratio are available [115].

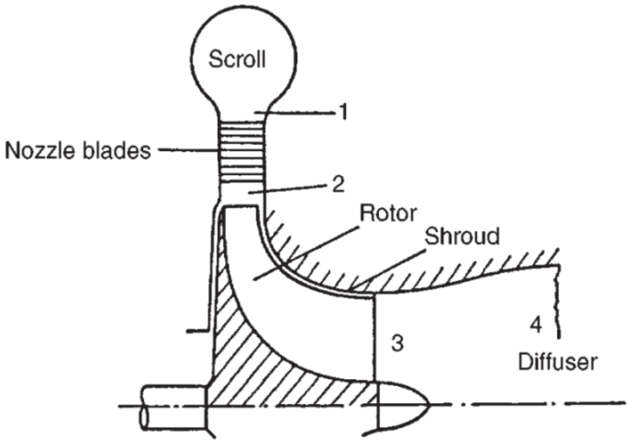

Figure 2.12: Radial flow turbine [115].

Many studies have been published in the literature on Small Scale Turbines (SSTs) analysing their aerodynamic and structural performance including studies to optimize their performance either aerodynamically or structurally or even both. Examples of such studies are:

Klonowicz et al [116] carried out a numerical study and preliminary experimental results for a single stage axial turbine with 10 to 15 kW output power. The turbine was integrated in a hermetic turbo generator operating in a low temperature, sub-critical (ORC) system with

R227ea as a working fluid. There was a very good agreement between the theoretical and measured values of the efficiency (55% and 53% respectively).

Fu et al [117] have developed an optimization approach to the structural, aerodynamic and wheel weight of a radial turbine by reselecting the main structural modelling parameters to decrease the wheel weight. The results indicated that with respect to the original design, the optimized turbine wheel had higher aerodynamic performance and relatively a satisfactory stress distribution where the maximum stress was reduced by more than 55% (from 1357 MPa to 598 MPa), with a weight less than 3.8 kg instead of 7.2 kg.

Basrawi et al [118] studied the relation between the ambient temperature and the micro gas turbine performance for a cogeneration system in cold regions. Their results showed that there is a direct relationship between the ambient temperature and the exhaust heat recovery. Similarly, with increasing the ambient temperature the exhaust heat recovery with respect to mass flow rate as well as the exhaust heat to mass flow rate escalated.

Bahr Ennil et al [119] developed a Small Scale Axial Turbine (SSAT) for energy storage application through predicting the aerodynamic losses using various approaches. Results highlighted that the Kacker & Okapuu model is the closest to the (CFD) simulation.

Kammeyer et al [120] have studied the effect of tip-gap losses on the performance of Small Scale Radial Turbine (SSRT) efficiency. They found that the tip-leakage for small scale radial turbines increases slightly with reducing the turbines' dimensions, while the total leakage losses show a severe and disproportional increase.

Klonowicz et al [121] examined several loss correlations for a mean line design approach in order to predict the turbines performance for (ORC) systems. Their results showed that while a high similarity was achieved between the efficiency values using various models for low specific speeds, the deviations were more than 15% for high specific speed values. The authors recommended that more experimental and numerical works are needed in order to gain more accurate results regarding the use of losses correlations.

Rahbar et al [122] utilized the mean-line modelling and (CFD) techniques in order to develop a (SSRT), 5 kWe, for organic Rankine cycle application in distributed power generation systems. Firstly, the mean-line was used to examine the effect of various input parameters and operating conditions, on the overall turbine performance. Then (CFD) analysis was used to evaluate the mean-line approach and also enhance the blade loading using some adjustment to the blade angles. Their results showed that for higher power output the inlet temperature, the pressure ratio and mass flow rate values must be increased. Moreover, the results showed that the value of minimum rotor blades number, which was initially suggested by mean-line modelling, was overestimated.

Jones [123] described the aerodynamic design and the test rig that were established for a single stage small scale radial turbine with 4.58 inches rotor diameter. It was a single shaft using gas turbine of 50 hp as a nominal power output with a capability to reach up to 100 hp. Their results showed that the designed small radial turbines were able to achieve high efficiency values, 86% and 88% total to static and total to total respectively, at high stage pressure ratios of 7 [28]. Furthermore, they indicated that if there was a possibility to increase the tip speed, the total to static efficiency can reach up to 87 percent at 5.7 pressure ratio. The author has also claimed that the achieved results are higher than those which can be obtained using multistage axial turbines for the same flow conditions and tip clearance values.

Chetan et al [124] designed a nozzle-less small scale, 20 kW, radial gas turbine. They used gas turbine cycle analysis to define the boundary conditions such as pressure, temperature, and mass flow rate required for developing the turbine. Then they optimized the efficiency based on the influence of different factors such as the solidity, the inlet and outlet Mach number, velocity ratio and hub to shroud ratio. They concluded that the optimized turbine can achieve higher efficiency of 80% at optimum values of absolute and relative Mach number of 0.54 and 0.41 respectively. Also, they concluded that higher values of solidity (blade length* blade number/ rotor diameter and its value varied from 4 to 12) can offer better efficiency, depending on the compactness requirement and rotational speed.

The same group studied the same effects on the same radial inflow turbine but this time with high solidity [125]. They found that there is a possibility to achieve the same level of efficiency with same solidity and higher value of relative speed ratio. This will have no significant effect on some types of losses such as windage, exit and friction losses.

Ruben et al [126] used one dimensional FORTRAN code and Visual Fortran to carry out meanline analysis for radial gas turbine of 600 kW power output. Their main conclusions were that this program offers a robust preliminary design method as well as optimization. They also concluded that the nozzle and rotor areas have an important role in prediction of choked flow. Their results showed good agreement between the one dimensional analysis and the analytical results.

2.4.2.3 Turbine Design Optimization:

Optimization can be defined as achieving the best in any design, work or application among many others. In the application of interest, small scale radial turbine optimization, it is important to determine the shape of the stator and the rotor that produce highest efficiency.

Previously, the approach of inverse shape design was followed when there was a need to enhance turbines' performance. However, recently other techniques of optimization such as multidisciplinary and multi objective has become more powerful and reliable and indeed achieved better turbines' performances [127]. In 1968 Balje and his colleague Binsley [128, 129] developed a numerical approach for optimizing the design of axial turbine using simple correlations to predict the accompanying losses at different blade profiles. The outcomes of this technique showed an improvement in the turbine's efficiency by around 5%. In 1980, Rao and Gupta [130] developed a multi-objective technique for optimizing axial flow turbine. Using this approach they were able to increase the turbine' efficiency by about 2.5% and at the same time reduces its mass by 18%. In 2001, Dennis [127] developed an analysis code based on multi-objective optimization approach to enhance both the 2-D and 3-D profile of a turbine blade. The study aimed to enhance the turbine performance through decreasing its losses and blades number by involving 18 different design parameters.

In recent years (CFD) has become one of the most effective tools in both; turbines' design and optimization because of its ability to deal with viscous 2-D and 3-D simulation. This can be performed using the (CFD) packages which successfully contributed to the aerodynamic optimization of turbines' blades profiles to reduce losses [131].

Large scale gas turbine was studied using (CFD) simulation to evaluate the potential of using adjustable nozzle vanes technique to control the amount of mass flow rate [132]. However, this technique is unachievable in the (SSTs) applications because of its complexity.

Marsan and Moreau [133] considered the effect of the stator wakes and impeller blades trailing edge on the acoustic emissions of radial turbine using (CFD) analysis. The results showed that the flow passes through the interface area, stator to rotor, causes pressure fluctuation to occur in this regime and as a result tip clearance losses occur. An iterative method based on (CFD) commercial software and an in-house code was utilised by Tsalicoglou and Phillipsen [134] to reduce the compressed air mass flow rate of a radial turbine. The methodology involved varying the geometry of the turbine blades without affecting the overall machine efficiency. However, the restriction in the number of design parameters led to large numbers of runs and only single objective optimization was established in that work. Fu et al [135] used an integrated optimization methodology to enhance a 100 kW radial turbine aerodynamically and structurally by focusing on the rotor part only. They achieved a maximum efficiency of around 82%.

Multi-objective algorithm, which involves decreasing the overall impeller moment of inertia, enhancing its efficiency and maintaining structural stresses lower than the yield limits, of a turbocharger radial turbine was reported in [136]. The maximum rotor efficiency achieved was around 80%. Similarly, a multi-objective optimization technique was established by [137] to enhance the rotor of a radial turbine. While it is claimed that the new model increased the efficiency by up to 8 %, at off design conditions, the maximum efficiency was only 77%.

An interesting work focused on the relation between the chosen range of the database, the computational time required for optimization and the correct selection of the optimization method was reported in [138]. An emphasis was highlighted by the authors on the right selection of the lower and upper limits for the chosen parameters. This chosen range should be as close as possible to the parameters which lead to the expected optimum output parameters. They also mentioned that by doing so, both better rotor geometry performance and further improvements of the convergence will be achieved.

2.4.2.4 Stress Analysis of (SSTs):

Structural analysis has been carried out by researchers to ensure mechanical reliability.

A coupled (CFD-FE) analysis for a relatively high pressure ratio radial turbine was presented by Shanechi et al [139]. In their study, the authors used the meanline approach to design a three dimensional radial inflow turbine with some emphasis on blades geometry in order to enhance both; the turbine's power output and efficiency. Then they carried out structural analysis in terms of the blades' stresses and deformation. However, the fatigue analysis, which is considered one of the main problems for rotating parts, was not included in their analysis.

The effect of sudden shut down on the transient thermal fatigue life for an edge hole crack in the casing of a gas turbine was studied experimentally and analytically recently by [140]. The results showed that despite the similarity in the stress distribution in the two different materials' used, elastic, perfectly plastic and linear elastic, the propagation of crack was different. Moreover, their analysis showed that the cooling rate of the turbine casing is the most influential parameter in the thermal fatigue crack growth.

The multi-disciplinary optimisation technique has been employed to improve the aerodynamic performance and reduce the thermal stress of a microgas radial turbine by Barsi et al [141]. By parameterization of the rotor blade camber and its half thickness some improvement in the turbine's efficiency, by about 5%, and the allowable stress has been achieved. Again no fatigue analysis was considered in their study. In [142], both; the mechanical and the thermal loads for the impeller of micro gas radial turbine and their impact on the aerodynamic and deformation performance of the impeller have been analysed. Their results indicated that the fluctuated deformation of the blade tip clearance affected negatively the structure reliability and the aerodynamic performance of the rotor. They also concluded that the blade inducer tip shroud showed the maximum deformation. Some improvement in terms by reducing deformation magnitude of impeller has been achieved by optimizing the profile of the impeller's hub section; however, the aerodynamic performance was not included.

Enhancing the strength requirements of the impeller hub by optimizing the blade shape was conducted by Feng et al [143] for 100 kW microturbine using an inverse design method. They showed that the impeller's inlet relative flow incident angle affected both the aerodynamic and the structural performance. They concluded that an angle of -32^{o} can result in high aerodynamic performance as well as good stress limit for the turbine structure.

Fu et al [135] developed a (SSRT) using an integrated optimization method. This method involves the aerodynamic, strength and weight of the achieved design. Their objective was achieved where the turbine wheel strength was increased with about 50% and at the same time a satisfactory stress distribution and good aerodynamic performance was realised.

Guo [144] has investigated the vibration taking place in the blade of a micro gas radial turbine. Experimental and analytical model using the (FE) techniques, were carried out for the coupled vibrations (torsional, longitudinal). Their results indicated that the fluctuation in the torque and the pressure have the tendency to excite the resonance of blade in a coupled manner.

2.5 Summary and Conclusions:

Regarding the literature review of the (SSSPC), the following points can be concluded:

- There is a lack of analysis for small scale solar powered system with less than 5 kW output power (less than 5 papers) which can be efficiently utilized in domestic application especially in remote areas.
- This range of power generation using (CSP) can compete with the photovoltaics and other diesel generators from cost and the maintenance point's view as mentioned. As a result, the need for an efficient system that can work at various conditions is needed to further its development.
- This technology still requires further research in order to enhance the overall efficiency of the system and this can be achieved by improving individually the efficiency of each component in the system. This includes reducing their cost and improving the system control, operation and configuration [24].
- In (CSP) the small scale parabolic dish has been chosen for this study because of its ability to achieve high concentration ratio, which reaches up to 3000 [40, 41], and also the suitability of using like this technique in the domestic applications. Furthermore, in order to efficiently capture the concentrated and reflected sun light, it is important to develop an effective cavity receiver, which are the preferred type of receivers [54], by reducing both the optical and thermal losses.

- In order to achieve the maximum system performance, both; input and output energy values need to be efficiently increased. This study aims to enhance the overall system efficiency by minimizing all the relevant losses in the system.
- There is a need to enhance each component of the (SSSPBC) to be efficiently working at on design and off design conditions. This is because of the variations in the boundary conditions such as pressure ratio, mass flow rate and turbine inlet temperature.
- In the same way, developing (SST) that can efficiently extract the energy coming from the thermal system is another important challenge that needs to be carefully considered during this study. So, both; axial and radial flow turbines were put forward in order to firstly examine their ability to work at these specific boundary conditions and secondly to develop them in order to maximize their power output and efficiency values. The reason for choosing these type of turbines is because their ability to work at low mas flowrate, higher expansion value compared to other types of volumetric expanders like screw, scroll and piston [145].
- There is a lack of analysis for the three dimensional optimization for (SSTs), so there is a need for this analysis to be carried out by minimizing their aerodynamic losses especially if no specific correlation have been developed yet for predicting the losses in such small scale turbines [146].
- Moreover, the stress analysis is another important factor which should be investigated by simultaneously integrating the aerodynamic and the structural analysis using (CFD-FE) analysis with an efficient optimization technique.
- It will be very useful if the around 30% overall cycle efficiency for like this scale can be achieved through improving each of their components' performance.

CHAPTER 3: THERMAL CAVITY RECEIVER - OPTICAL & THERMAL- ANALYSIS

3.1 Introduction:

This chapter provides a comprehensive description for the solar heater of the cycle including the development of the cavity receiver and the parabolic dish reflector. This has been achieved by employing different types of software such as SOLIDWORKS, OptisWorks, and Fluent solver of ANSYS/ Academic in order to identify suitable operating boundary conditions for the turbine.

3.2 Development of the Solar Heater:

In this section the development of both the parabolic dish reflector and the thermal cavity receiver is described [147]. They together form the solar heater which receives, concentrate and reflect the incoming solar radiation in order to provide the compressed air with the required thermal energy. Consequently, optical and thermal analyses of the concentrator and receiver have been carried out to develop efficient thermal system.

Figure 3.1 shows a schematic diagram of a parabolic dish concentrator with the cavity various geometric parameters necessary for analysis of its performance, these parameters are:

- **Aperture Area:** It is defined as the opening area through which the solar radiation enters the parabolic dish surface.
- **Receiver Area:** It is defined as the part of the parabolic area which receives the incoming solar radiation after being reflected from the parabolic surface.
- **Rim Angle:** It is defined as the angle which dimensionally connects the parabolic dish aperture and the location of the focal point.

- **Focal Point:** It is defined as the point where all the rays, reflected from the parabolic dish, are focused. Its value can be determined based on; the rim angle of the parabolic dish and its diameter.

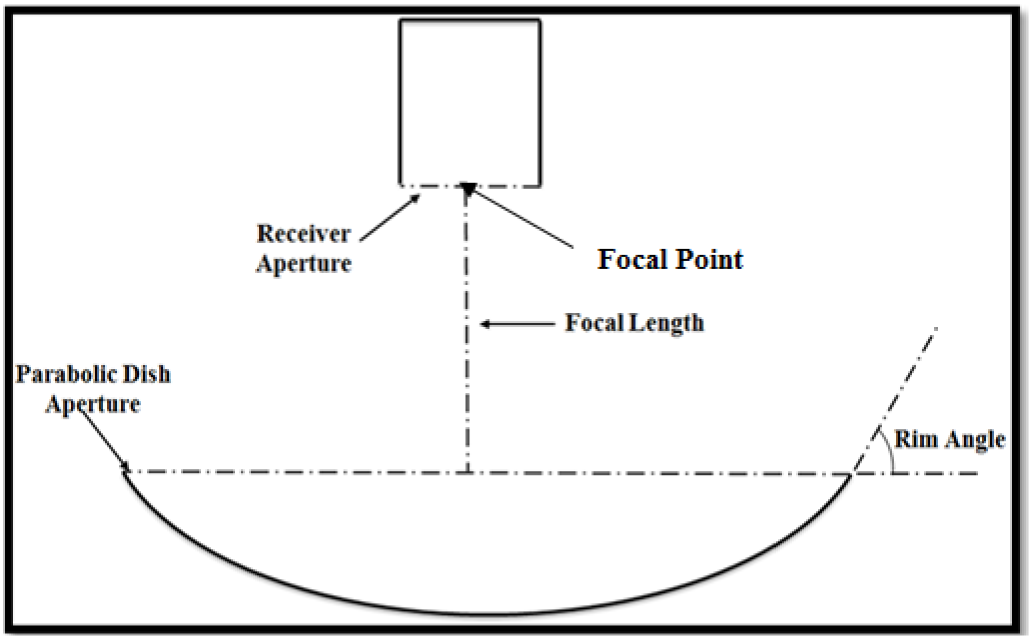

Figure 3.1: Schematic diagram for the (PDC) with the cavity receiver.

3.2.1 Parabolic Dish Concentrator:

Parabolic dish concentrators are used in solar thermal systems to concentrate solar radiation on small receivers. They have the advantages of the ability to produce high concentration ratio. Based on Kumar et al. [77], the rim angle of 45^{o} gives the highest concentration ratio. It also leads to the maximum received amount of flux, by the cavity receiver, compared to other rim angles investigated by the author [148]. Figure 3.2 illustrates the relevant geometrical dimensions equations of parabolic dish concentrator. Equations 3.1-3.3 [149] determine the concentrator focal length as a function of its diameter and rim angle.

$$h = \frac{d^2}{16f} \quad (3.1)$$

$$\frac{f}{d} = \frac{1}{4\tan\left(\frac{\Psi_{rim}}{2}\right)} \tag{3.2}$$

$$p = \frac{2f}{1 + cos\Psi_{rim}} \tag{3.3}$$

Where, Ψ_{rim}, f, h, p and d represent parabolic rim angle, the focal length, the maximum distance (depth) between the vertex and a line located across the parabola aperture, the parabolic radius and the aperture diameter respectively. The rim angle can also, be determined using equation 3.4 [148, 149].

$$\text{Tan } \Psi_{rim} = \frac{1}{\left(\mathrm{d}/_{8\mathrm{h}}\right) - \left(^{2\mathrm{h}}/_{\mathrm{d}}\right)} \tag{3.4}$$

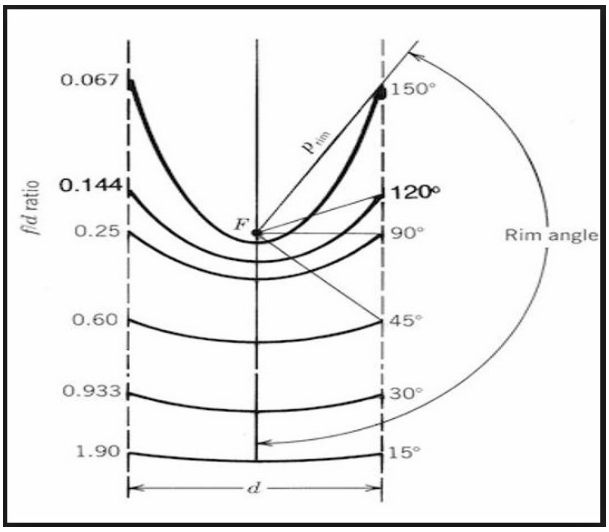

Figure 3.2: The geometrical relationship of the rim angle and the concentration ratio [148].

3.2.2 Thermal Cavity Receiver (TCR):

The cavity receiver is considered the most significant part in the (CSP) as its function is to convert the received solar radiation into thermal energy to heat up the incoming compressed air. Table 3.1 shows the dimensions of the three studied receiver shapes with parabolic dish collector of 1 m diameter and thickness of 0.01m, mentioned in Figure 3.3. The tube where the air flows has a diameter of 0.02 m and wall thickness of 0.002 m.

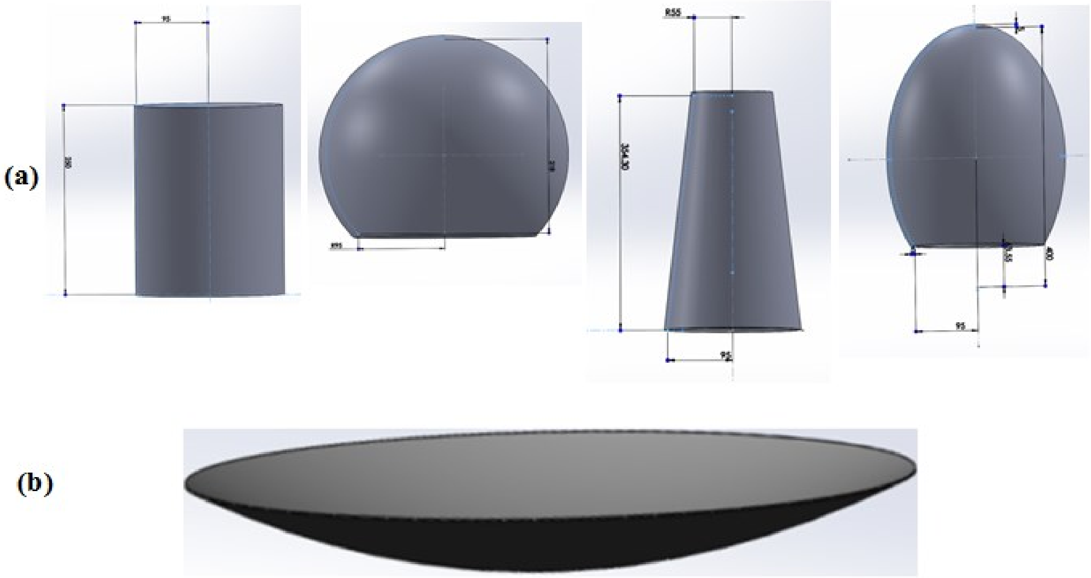

Figure 3.3: (a) The four shapes of cavity receiver (b) The concentrator, parabolic dish.

Table 3.1: The dimensions of the collector dish and the three receivers.

Parameter (m)	Parabolic Concentrator	Cylinder	Conical	Elliptical	Spherical
Diameter	**1**	**0.20**	**0.20**	**0.20**	**0.20**
Thickness	**0.01**	**0.005**	**0.005**	**0.005**	**0.005**
Height	**0.1041**	**0.2499**	**0.3542**	**0.420**	**0.218**
Focal Point	**-**	**0.6003**	**0.6003**	**0.6003**	**0.6003**

The receiver size is considered as one of the key factors as it is required to be as small as possible to decrease the amount of heat losses [149], but should be large enough to accommodate the channels for air flow.

3.3 Optical Numerical Simulation:

OptisWorks® 2016 is commercial software used to simulate the optical performance of different concentrator solar systems [148] , [150-153]. It is based on three dimensional ray tracing technique which enables detailed analysis of optical analysis. In this work four different geometries of the thermal cavity receiver as shown in Figure 3.3 are modelled to determine the effect of cavity shapes on the received and at the same time lost flux from the receiver [99]. Figure 3.4 shows flow chart for the modelling set-up used in OptisWorks® 2016. In this section, it is focused on the optical type of losses only, as they are primarily associated with each; the manufacturing issues, the imperfection during the construction and or material properties. According to the literature [154-158] the optical losses can be summarized recapped as following: * Published by the author [99].

- **Reflective Loss:** Is the difference between energy reaching the reflective area or receiver surface area and reflected energy. Based on the properties of the utilized material, this loss represent around 6–10% from the total coming energy [99, 148].
- **Spillage Loss:** It represents the radiation part which falls outside the aperture zone of receiver; it takes around 1–3% of the loss.
- **Shading Loss:** Is defined as the percentage of the reflective dish area which the receiver is shadowing. This loss can be reduced when the aperture area of the reflector is by far greater compared to the receiver area.
- **Transmission Loss:** the amount of energy which is lost in the air when it moves from the concentrator to the receiver; which can add about 2 to 4 % to the loss [99, 148].
- **Absorption Loss:** Is the amount of the absorbed energy which initially lost in either the receiver material or reflector material and causes thermal stresses.
- **Cosine Loss:** It is the difference between the projected areas, as it is seen from the sun and its real reflective area.

At this point it is worth to mention that first five types of the mentioned losses are automatically included in the analysis of this study [99], as the source is solid and perfectly round shape not like the real sun shape which is slightly flatted.

The optical efficiency of the concentrator can be expressed using equation (3.5), whereas the optical efficiency of the receiver can be determined using equation (3.6), [148]

$$\eta_C = \frac{Q_r}{Q_s} \tag{3.5}$$

Where Q_r, is the energy reached to the receiver and Q_s is the incident falls on the concentrator's aperture, [99].

$$\eta_R = \frac{Q_u}{Q_{rec}} \tag{3.6}$$

Here, Q_u, is the useful energy, that is delivered to the helical tube which contains the working fluid, and Q_{rec} is the amount of energy which is received by the receiver's aperture [99].

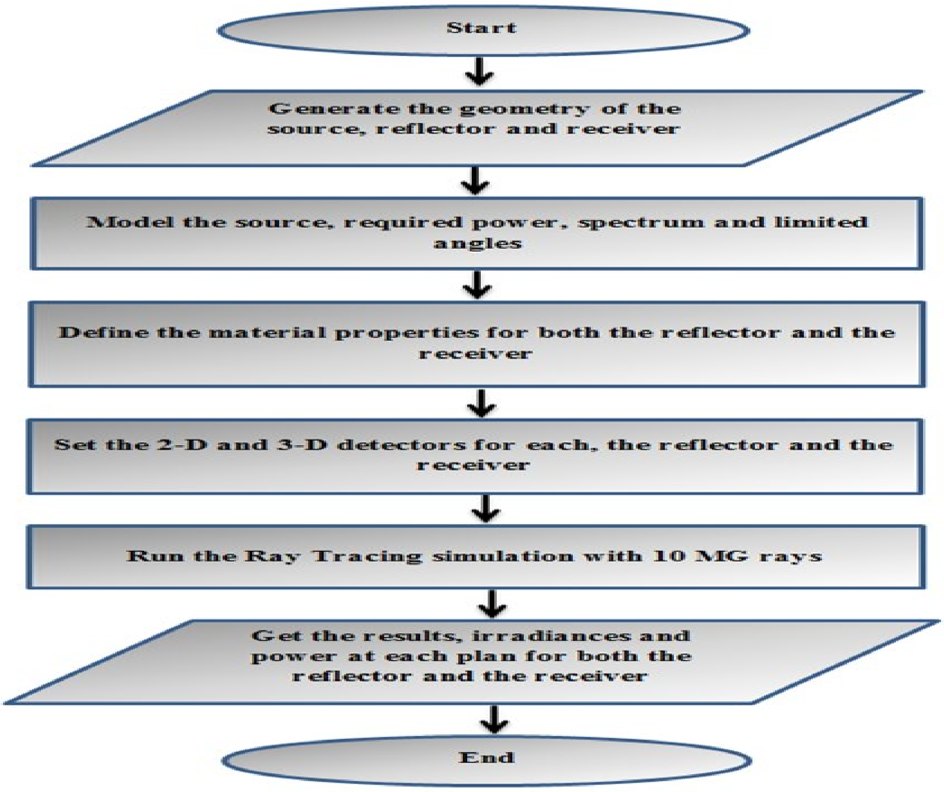

Figure 3.4: Modelling process in ray tracing technique [99].

Figure 3.5 shows the setup of the receiver optical simulation including the parabolic dish concentrator and the light source. The following summarized assumptions were considered for all cases, during the analysis [99]:

1- The source was set to generate 10 MW at radiation of 525 W/m^2 as a typical average radiation for 1 m^2 parabolic dish surface area in a typical summer day in Iraq, between latitudes 29° 5' and 37° 22' N and longitudes 38° 45' and 48° 45' N.

2- The source shape was defined as planar with a size larger than the aperture area of the parabolic collector in order to let the emitted incoming rays cover the aperture area of the three shapes [99].

3- Also, the ‘‘Lambertian” was used for intensity type and a limited half angle of 0o was set.

4- The energy was simulated and equally divided to all the incident rays [99].

5- The concentrator was set to specular and has a reflectivity of 0.95. The absorption ratio of the three receivers was set to 100%, 85% and 75% [99], to study their effects.

The detector that records the amount of incoming flux from the source as well as the reflected flux to the aperture area of the receiver is initiated and the helical tube inside each receiver takes the shape of the receiver configuration. The latter has been selected because of its compactness and ability to handle (because of the higher film coefficient) high air temperature without causing a thermal stress on the shape, as there are no joints (stress concentration)

The material property of the receiver that was located at the focal point, which depends on the rim angle and diameter of the parabolic concentrator, was defined [99].

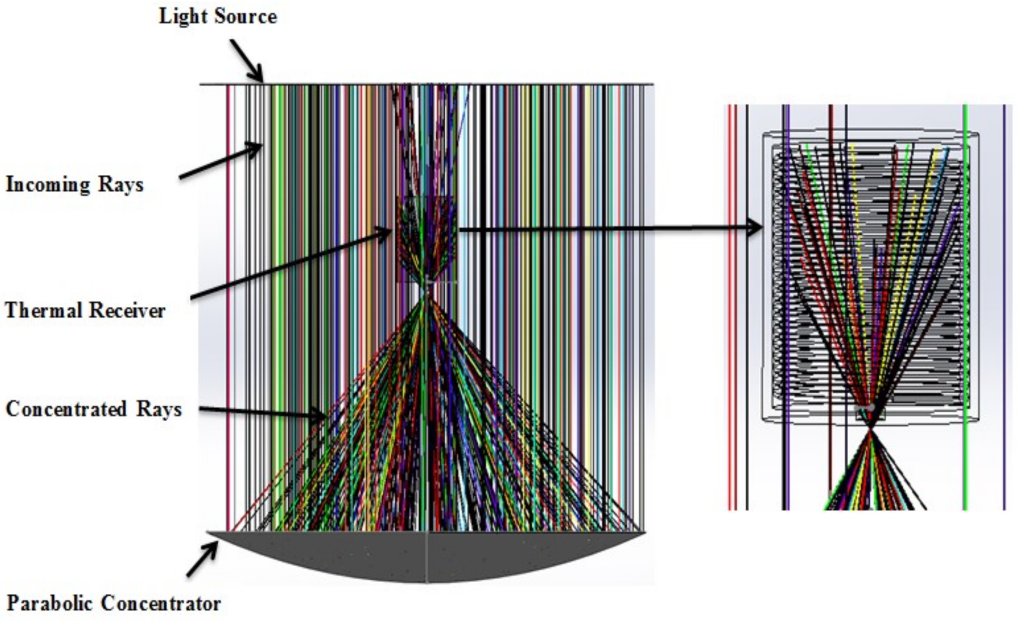

Figure 3.5: Parabolic dish with receiver under OptisWorks simulation [148].

3.3.1 Optical Analysis of the Parabolic Dish Concentrator:

In order to achieve the best system thermal performance, the parabolic dish concentrator and the thermal receiver, should be studied and analysed carefully. Firstly, the parabolic dish concentrator has been studied in the next two sections with the purpose of obtaining its best shape and dimension.

3.3.1.1 Parabolic Concentrator Dish's Rim Angle:

The parabolic dish's rim angle affects the optical performance of the parabolic concentrator in terms of the amount of radiation reflected from the concentrator surface towards the receiver. Consequently, six rim angle values, 15°, 30°, 45°, 60°, 75° and 90° were investigated using OptisWorks® 2016, where Figure 3.6 presents three cases. This Figure shows how both; the incoming flux and the received flux were influenced by the rim angle. This can be demonstrated by the relation between the receiver position and the parabolic dish's rim angle. So, with rim angle of 30°, the receiver shall approach the source, while it shall be near to the parabolic concentrator at rim angle of 90°. As a result, the amount of the incoming flux will be influenced by these configurations.

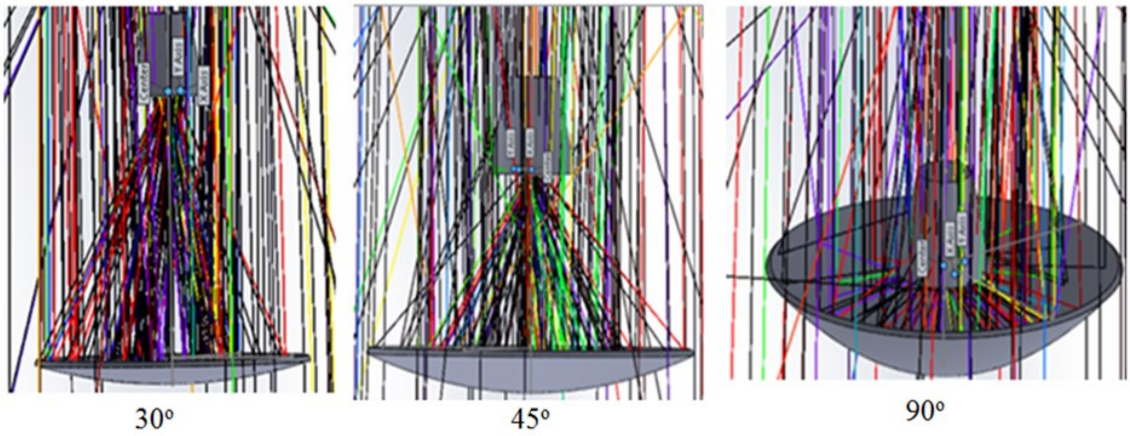

Figure 3.6: The three investigated rim angles of the parabolic dish [148].

The parabolic dish's rim angle effect on the reflected rays (incoming) from the parabolic dish concentrator and received rays (by the receiver aperture) is given in Figure 3.7 where the 45°

rim angle resulted in the highest received flux compared to the other investigated angles. Therefore the 45° rim angle parabolic dish was used in the following investigations.

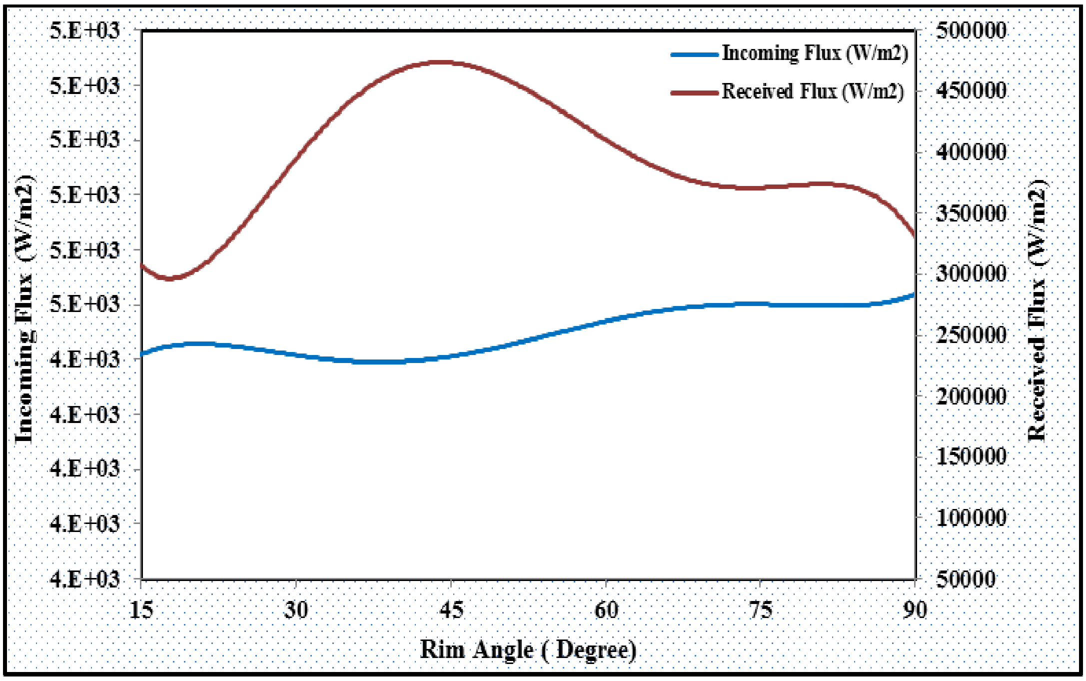

Figure 3.7: Incoming and received irradiance at various angles rim of the concentrator [148].

Accordingly, the 3D detector of the investigated parabolic dish shape as well as the received flux distribution is displayed in Figure 3.8. It also shows the effect of receiver shadow on the flux distribution for the parabolic concentrator dish.

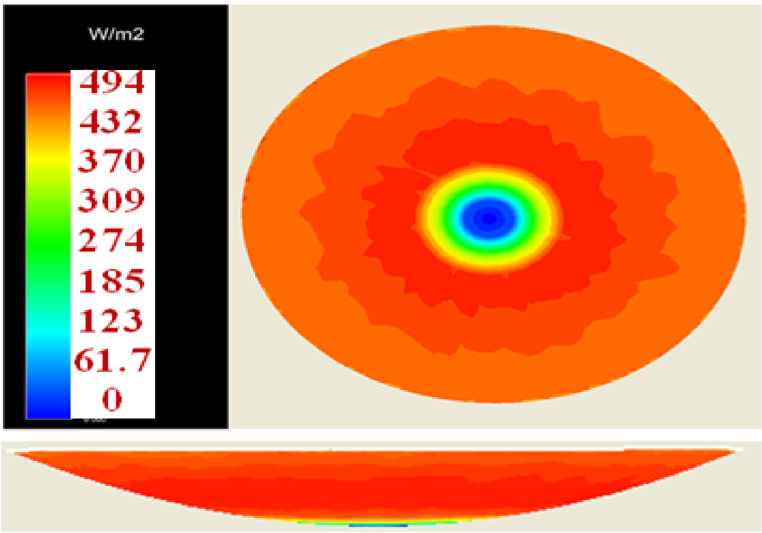

Figure 3.8: 3D Detector of the studied parabolic dish shape [148].

3.3.1.2 Parabolic Concentrator Dish's Size and Irradiance Value:

In this section OptisWorks was used to investigate the effect of the parabolic concentrator diameter on the received radiation. Also, to take into account the variation in solar irradiance throughout the day, the effect of dish diameter was investigated at different irradiance values ranging from 500 to 1000 W/m^2. Figure 3.9 shows the variation of the incoming power (which is calculated based on the parabolic dish's aperture area) with irradiance for dish diameter of 1, 2 and 3 m. It can be seen that increasing the irradiance will increase the incoming power. Figure 3.10 shows the effect of parabolic dish diameter on the optical efficiency indicating that the efficiency increases with the increase in the diameter to reach a maximum value at diameter of 3.3 m then it remains constant. Thus no further benefit can be achieved by increasing the diameter. This might be explained by the effect of shading losses caused, by the conical receiver geometry on the parabolic dish. This reduces the effective parabolic dish area as presented in Figure 3.11.

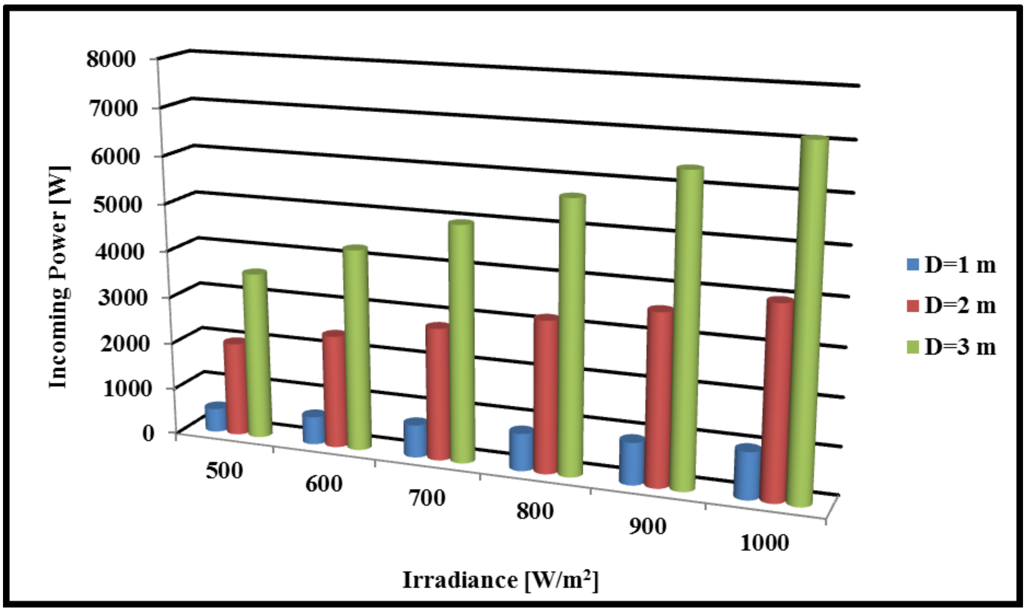

Figure 3.9: Incoming power at many irradiance and dish diameter values using conical shape receiver [147].

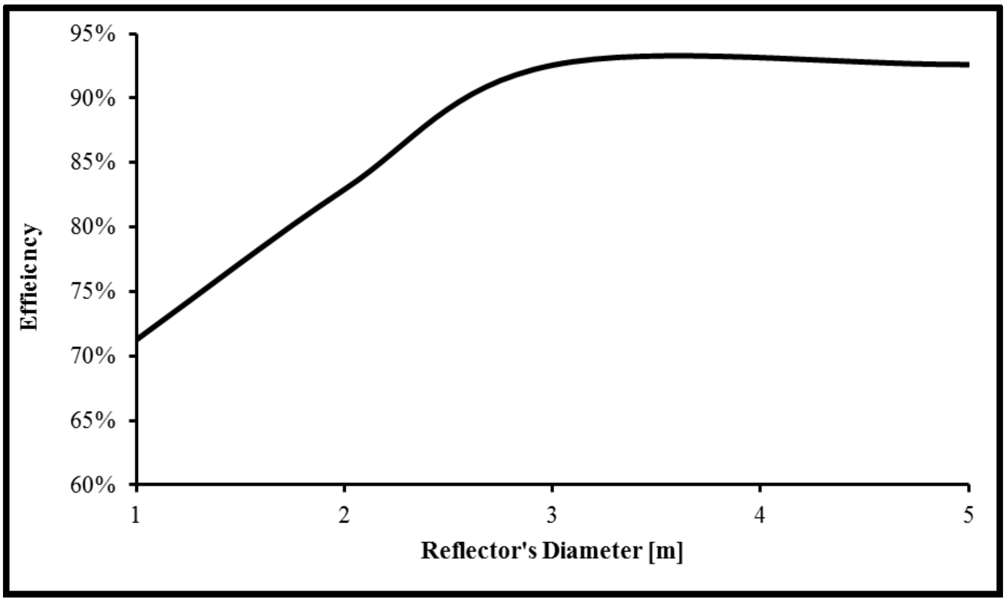

Figure 3.10: The optical efficiency of the parabolic dish with rim angle of 45° and Irradiance of 1000 W/m^2, at various diameters [147].

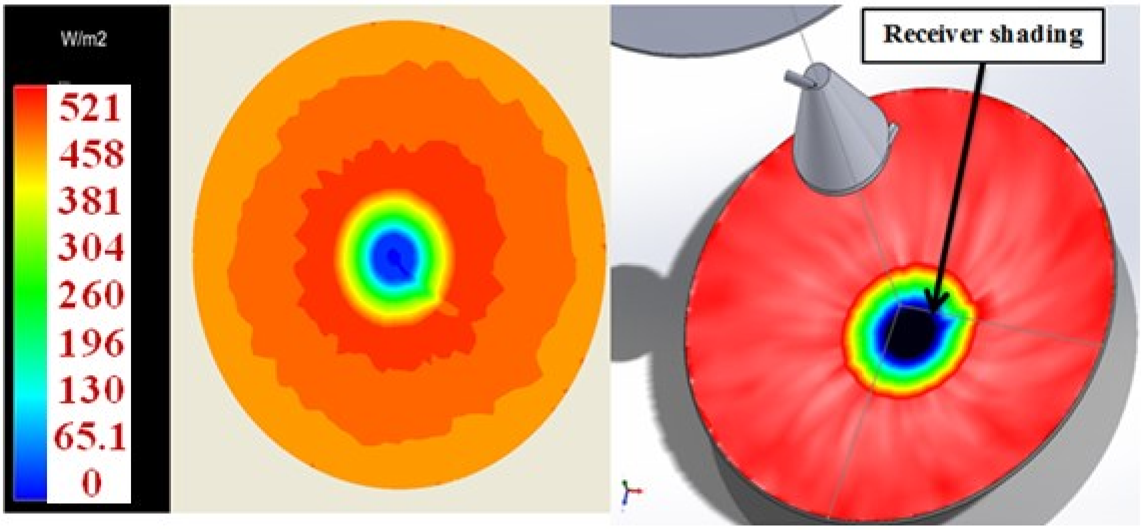

Figure 3.11: The shading effect on the received flux for 1 m diameter parabolic dish [147].

3.3.2 Optical Analysis of the Thermal Receiver:

As it has been highlighted previously, the heart of this studied cycle is the thermal cavity receiver. As a result, a detailed investigation of four different configurations of cavity receiver (shown in Figure 3.3) has been carried out. The investigations involved evaluating (i) the effect of receiver's cavity shape, (ii) the effect of receiver's position and (iii) the effect of receiver walls' absorptivity on the optical performance of the receiver. Then the best three receivers fitted with helical tube coils were simulated using ANSYS Academic/ Fluent to evaluate their thermal performance.

3.3.2.1 Effect of Receiver's Cavity Shape [148]:

Once the irradiance rays enter the cavity receiver aperture, they are either absorbed or reflected by the internal walls of the cavity or leave the cavity through the aperture without being utilized. The reflection of rays can occur in single or multi times depending on the shape of the receiver and in each reflection part of the radiation will be absorbed and the remaining radiation will be reflected again. Figure 3.12 displays the ray's distribution for four cavity receiver shapes at 500 W/m^2 and dish diameter of 1 m. The fifth is the elliptical shape integrated with a small secondary reflector inside it. This reflector has been added as a result of the rays' concentration on the internal focal point of the elliptical shape with the aim of distributing the concentrated rays uniformly on the internal walls of the cavity receiver.

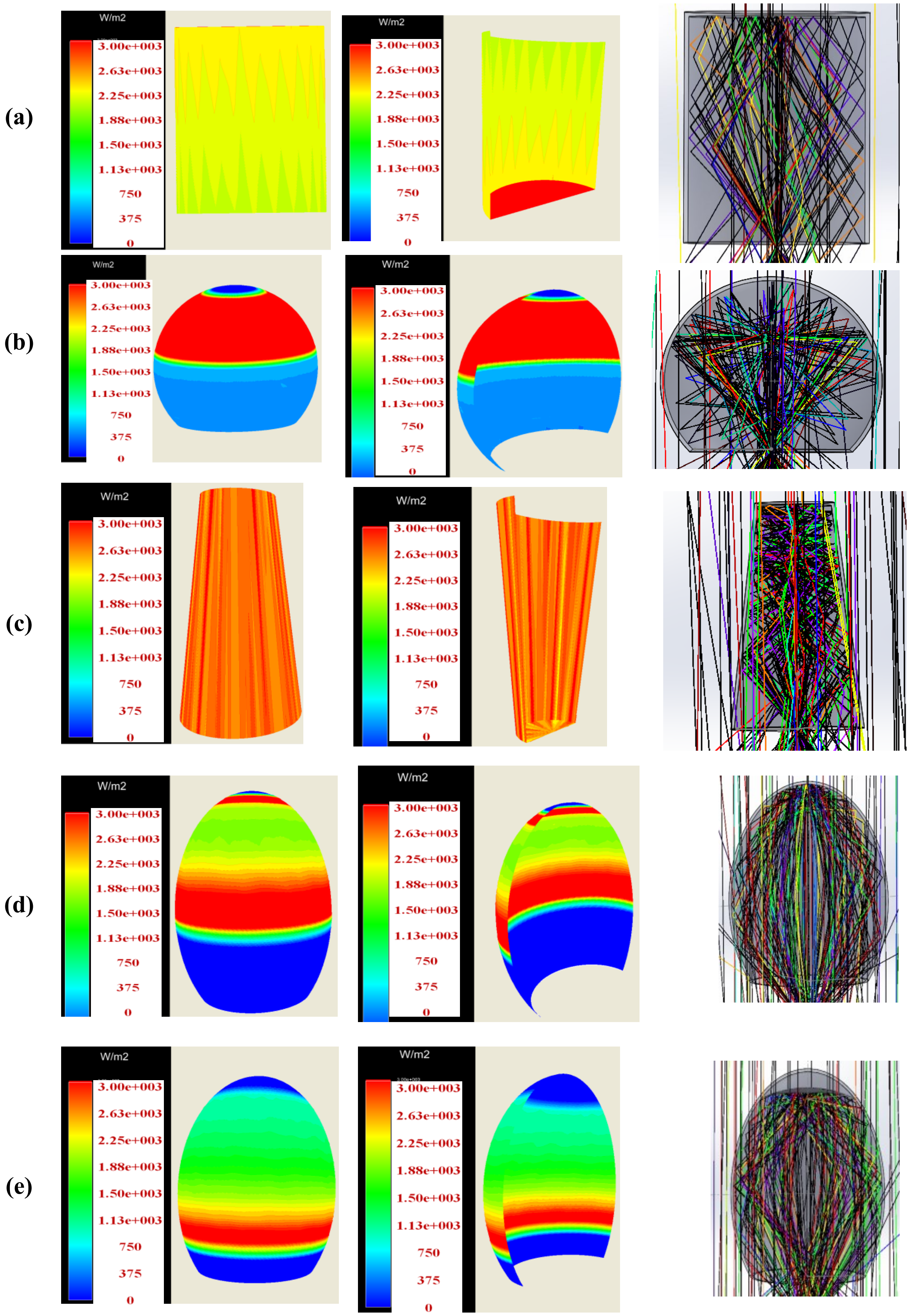

Figure 3.12: The flux distribution of (a) Cylindrical shape (b) Spherical shape, (c) Conical shape (d) Elliptical shape and (e) Elliptical shape with secondary reflector.

From this figure it is clear that both the cylindrical and conical shapes have the best distribution as a result of the small difference between the maximum and minimum received flux. In the case of the elliptical receiver, it can be observed that the rays are focused at a point at the upper surface of the receiver. Therefore a secondary reflector was added to the cavity and the simulation results are shown in Figure 3.12e, which shows that significant improvement in the distributed flux was achieved. This enhancement can also be seen in terms of the optical efficiency for the five configurations as presented in Figure 3.13.

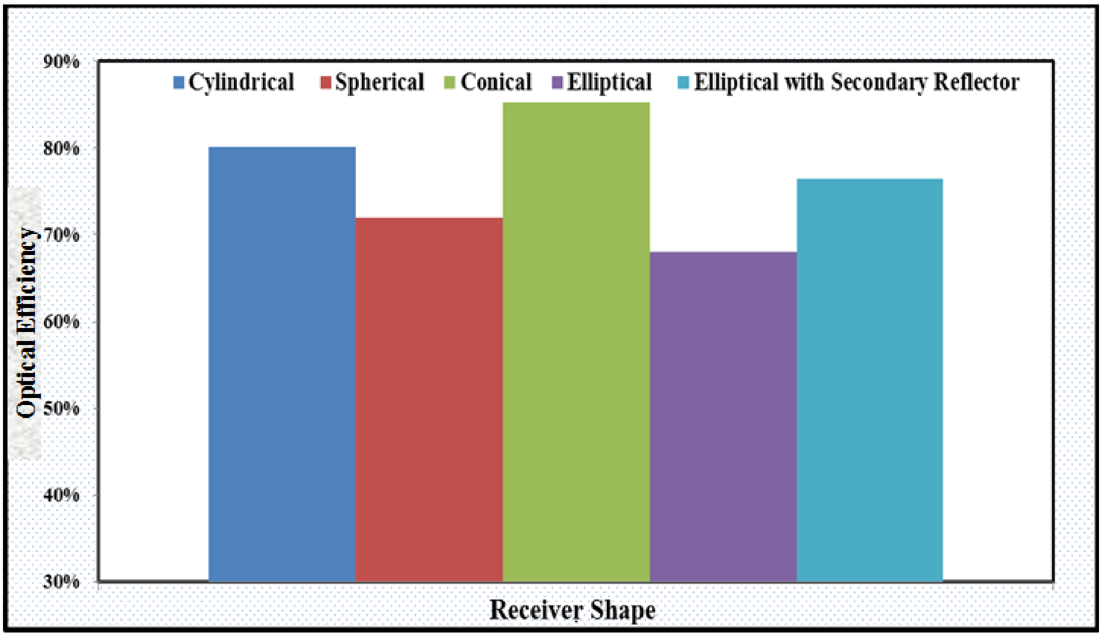

Figure 3.13: The optical efficiency of the fourth geometry shapes.

It is clear from the above analysis that the conical, cylindrical and spherical receiver shapes showed relatively better performance in terms of the optical efficiency values. Also, the elliptical shape with secondary reflector is considered a complex geometry compared to the others. Therefore, the three mentioned shapes have been investigated further in the following analysis.

- The following sections were published by the author in [99, 112, 147, 148].

3.3.2.2 Effect of Receiver's Position [99, 148]:

Figure 3.14 a, 3.14 b and 3.14 c display the radiation distribution for the spherical receiver at three various absorptivity values; 100%, 85% and 75%, at various receiver positions (around ± 10% from the focal length). The absorptivity is assumed 100% in Figure 3.14 a, where the effect of varying the receiver's position, with respect to the collector focal point can be noticed [148]. While the best rays distribution occurred when the geometry was moved away, to let the focal point be positioned outside the cavity, the worst one however was when the focal point was located in the spherical cavity geometry. Similar performance can also be seen at absorptivity ratios of 85% and 75% shown in, Figure 3.14 b & 3.14 c respectively [148]. Nevertheless, the quantity of the received rays and the areas where large ratio of irradiance was focused i.e. the tips for the last two situations are different, Figure 3.14 b and Figure 3.14 c. Likewise, Figure 3.15 a, b and c display the influence of varying the conical shape receiver position with respect to its focal point at three absorptivity values; 100%, 85% and 75%, respectively [99]. Figure 3.15 a, shows the rays distribution at absorptivity of 100% (black body), for different positions of the collector focal point with respect to the receiver. It is noticed that there was only a slight effect at the tip area when the receiver position was changed. On the other hand, the total received flux was the highest compared to the other two cases shown in Figure 3.15 b &3.15 c. The best rays distribution was noticed when the receiver was moved close to the parabolic dish i.e. the radiation focal point occurred inside the receiver geometry (at 85% absorptivity). However, at absorptivity of 75%, that was not the case, as presented in Figure 3.15 c, i.e. a better distribution was reached by shifting the receiver's position away from the parabolic dish's direction, which allows its focal point to be outside the receiver geometry [99].

In the same way, Figure 3.16 a, 3.16 b and 3.16 c, show the rays and flux distribution for the cylindrical receiver [99]. It is shown that when the absorptivity was assumed 100%, the best distribution was attained when the radiation focal point is located at the aperture plane. Again, this was not always the case when the assumed absorptivity values were assumed to be 85% and 75% as presented in Figure 3.16 b & c respectively [148]. It is clear that the best distribution was seen to be when the receiver was moved further from the parabolic dish, to make the incoming radiation focal point outside the receiver shape [99].

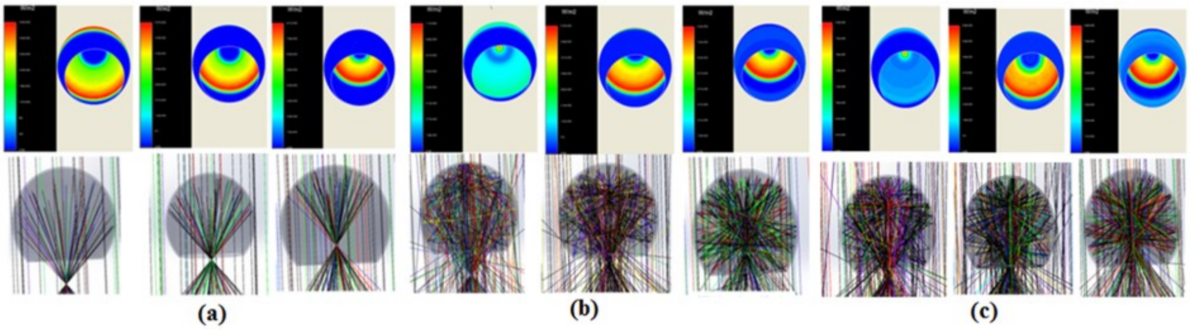

Figure 3.14: The spherical receiver position effect on the both; rays and flux distributions for an absorptivity of; (a) 100%, (b) 85% and (c) 75% [99]

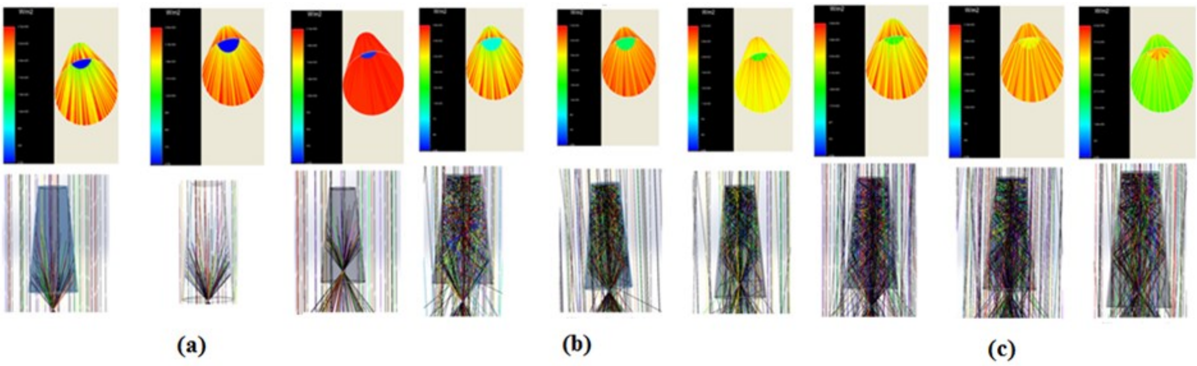

Figure 3.15: The conical receiver position effect on the both; rays and flux distributions for an absorptivity of; (a) 100%, (b) 85% and (c) 75% [99].

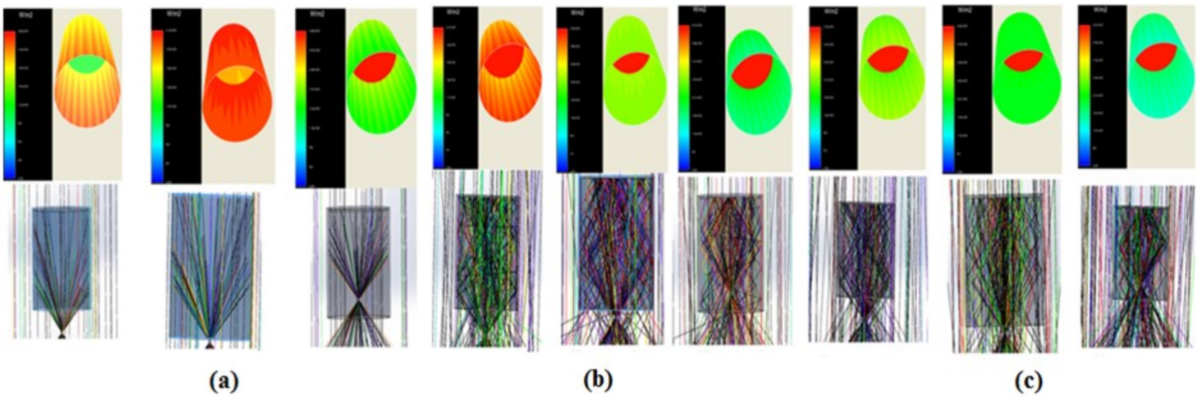

Figure 3.16: The cylindrical receiver position effect on the both; rays and flux distributions for an absorptivity of; (a) 100%, (b) 85% and (c) 75% [99].

3.3.2.3 Effect of Receiver Walls' Absorptivity [99, 148]:

The internal surfaces absorptivity effect for the receiver shapes is evaluated with respect to the received, absorbed and reflected rays. Using 3D OptisWorks® 2016detector, it became possible to observe where the highly concentrated areas and dead areas on the internal surfaces of each cavity. Both areas should be minimized in the design of any cavity receiver. Areas with high concentration lead to high local temperature (hot spot) which increase thermal losses to the surrounding and thermal stresses that lead to material failure. On the other hand, areas with low concentration (dead areas) will decrease the receiver efficiency.

The ray distribution and the flux distribution for the examined shapes at altered internal surface absorptivity values are presented in Figure 3.17 a, b and c for the spherical, conical and cylindrical shapes respectively. Here, it should be highlighted that all of the three receivers were examined at an identical focal distance and same cavity positions [99]. It can be seen that the amount of reflected rays is proportional to the absorptivity of the internal surface for all the receiver shapes investigated [148]. At this point it is important to highlight that those reflected rays are not constantly accounted as lost energy i.e. leaves the receiver aperture; instead they are highly affected by the shape of the receiver geometry and its absorptivity value [148]. For instance, at 85% absorptivity, the fraction of the rays which are reflected from the receiver and lost is by far lower in the two geometries (conical and cylindrical) compared to the spherical shape [148]. While the lower loss caused by the reflected rays happened in the conical shape. Also, the flux distribution for each receiver shape was influenced by the mentioned two factors [99]. For example, there is a large difference in terms of the lost rays between the cylindrical and the spherical shapes [99]. Also, it is noticed that while there was a uniform flux in the cylindrical receiver, that was not the case in the spherical receiver. Similar observations can be made at absorptivity of 75%, aside from the fact that there was a higher amount of reflected and lost rays.

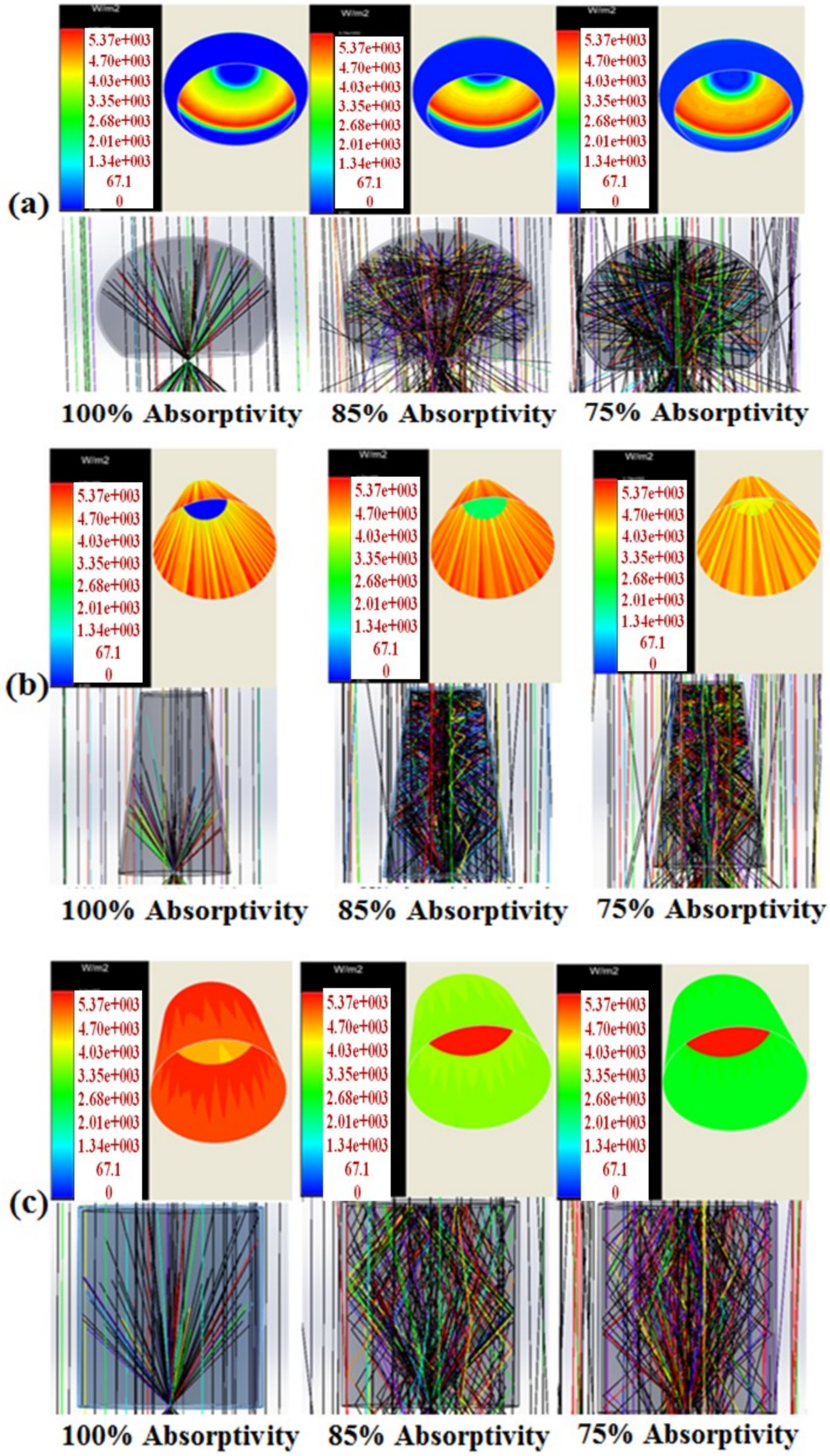

Figure 3.17: The absorptivity effect on both the, rays and flux distributions for (a) Spherical shape, (b) Conical shape and (c) Cylindrical shape with focal point at the aperture [99].

Figure 3.18, shows the absorbed energy of the various receivers at absorptivity of 85% and 75% and various receiver positions (focal lengths). It can be seen that the conical one has absorbed the highest amount of energy compared to the other two receiver shapes, most [99]. However, the maximum values of absorbed energy were altered with respect to each shape for each absorptivity value. Specifically, at 75% absorptivity, the maximum absorbed energy for the conical, cylindrical and spherical receivers were about 375, 349 and 333 W at focal distances of 560, 570 and 585 mm respectively. Yet, these values became around 378, 360 and 355 W at 555, 590 and 565 mm respectively with 85% absorptivity [148].

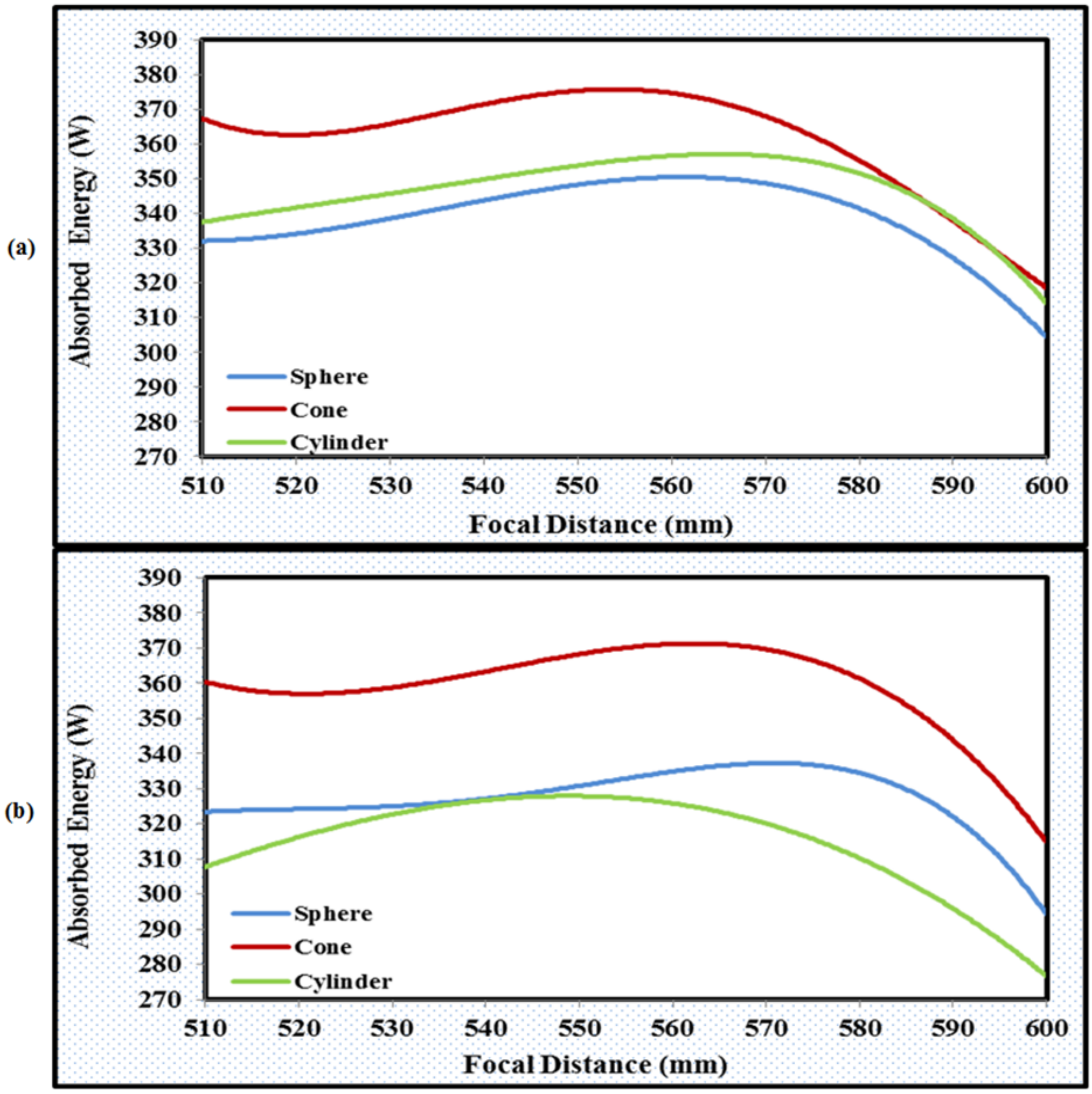

Figure 3.18: Absorbed energy by the receivers at various absorptivity and position of the cavity receiver with; (a) 85% and (b) 75% where 550 mm is the focal length [148].

The optical efficiency, at several focal distances, surface absorptivity of 75% and 85% is depicted in Figure 3.19 showing that the maximum optical efficiency reached for the conical cavity was 72.4% and 75.3% at absorptivity of 75% and 85% respectively [148]. The lowest optical efficiency is 63%, at the absorptivity of 75% for the cylindrical receiver. By contrast, at the absorptivity of 85% the spherical receiver reached the peak with around 67%.

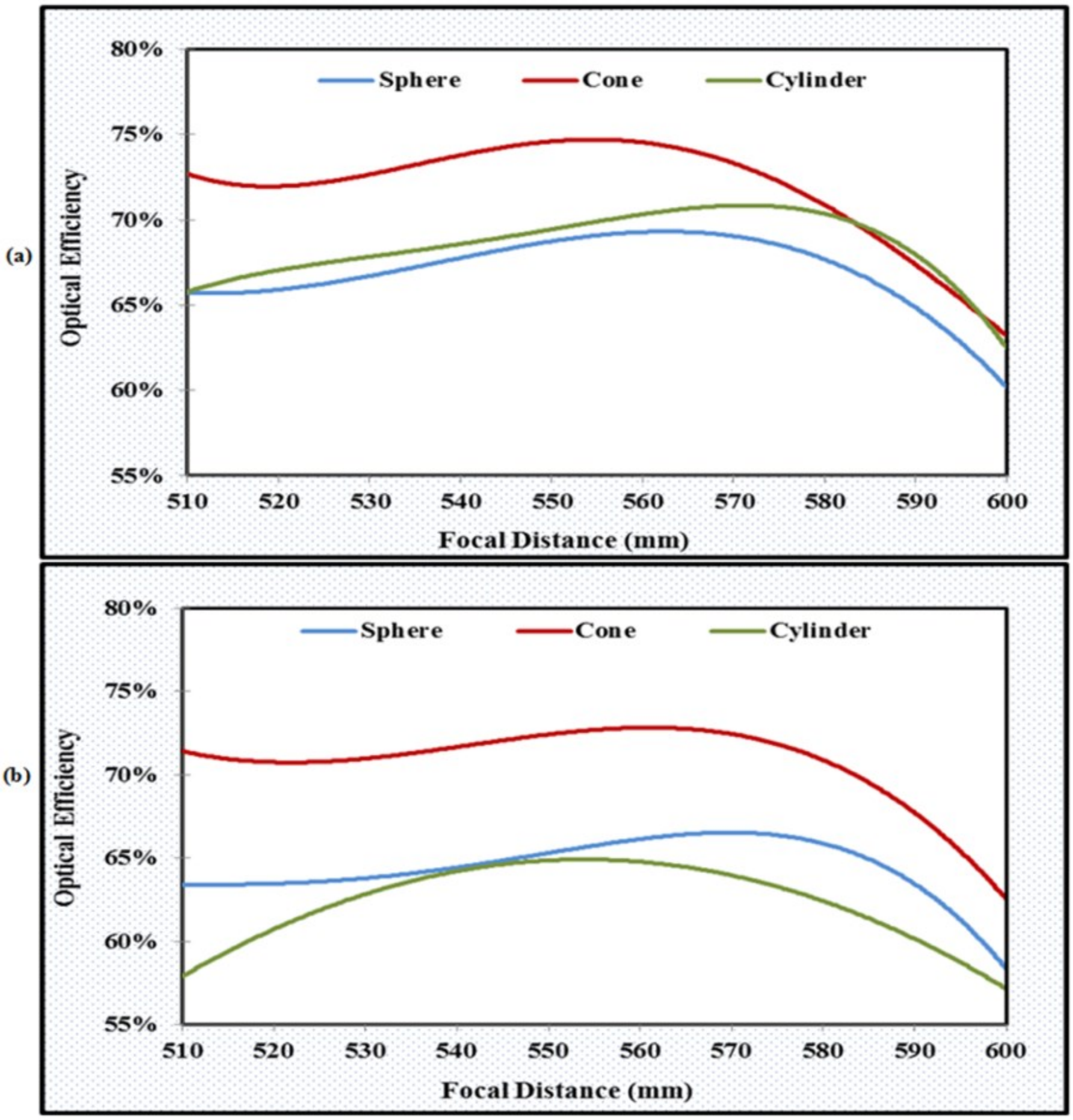

Figure 3.19: The optical efficiency of the receivers at various absorptivity and position of the cavity receiver with; (a) 85% and (b) 75% [148].

3.3.3 Uniformity Factor (UF):

Generally, the uniformity can be defined as how uniform the flux is distributed inside the cavity receiver surface. A number of methods were reported in the literature to assess the uniformity received radiation on 2D planes. These methods use equation 3.7 [159] or what is known as the standard deviation. However, as this study involves with 3D geometries, and the analysis used 3D detectors, the mentioned methods would not be efficient. The standard deviation method is too complicated and equation 3.7 would not be accurate as some parts inside the cavity may have zero minimum flux leading to UF being 100%.

$$U = \frac{Maximum\ Irradiance - Minimum\ Irradiance}{Maximum\ Irradiance + Minimum\ Irradiance} * 100\% \tag{3.7}$$

Filipa [159], used a factor called ‘ the inhomogeneity’, r as given in equation 3.8. However, if the minimum flux is equal to zero, as in this study, r will be more than unity.

$$r = \frac{Maximum\ Irradiance - Minimum\ Irradiance}{Average\ Irradiance} * 100\% \tag{3.8}$$

While there are other equations which were used in computing the uniformity as reported by [160], again they cannot be employed in the current study for the same reasons mentioned above [148]. Therefore, the author suggested the illumination uniformity of the three receiver shapes to be evaluated using a Uniformity Factor (UF), given by equation 3.9 where the average flux was calculated using the incoming energy divided by the cavity internal surface [148]. The latter can be defined as the factor that accurately described how the radiant flux, which is received from the parabolic dish, uniformly distributed inside the all receiver geometry.

$$UF = \left[1 - \left(\frac{Maximum\ Irradiance - Average\ Irradiance}{Maximum\ Irradiance}\right)\right] * 100\% \qquad (3.9)$$

Figure 3.20 displays the variation of the illumination's uniformity factor, at surface absorptivity of 85% and 75%, for the three cavity configurations with the incoming radiation. Overall, the conical shape revealed the maximum uniformity of illumination: 77% at 85% and around 84% at 75% absorptivity compared to the other shapes for all the focal distances. Moreover, by increasing the focal distance to a value in the middle of 580 and 590 mm, the uniformity for all of the shapes improved. The justification is when the geometry was positioned at high focal distances; the diffused rays will accumulate at the focal point and then split to reach nearly all the cavity internal surface areas, then the uniformity starts decreasing after a certain focal distance [148].

Furthermore, the uniformity at the absorptivity of 75% was clearly higher as a result of the number of reflected rays higher; which leads to a stronger probability of increasing the zones that can be exposed to these reflected rays [148].

Figure 3.21 shows the flux distribution of the three configurations at their maximum flux uniformities [148]. These distributions were attained at relatively high values for the focal distance which results in most of their internal surface areas maintained at the same colour. However, these locations showed relatively lower values for the optical efficiencies, which can be explained by the fact that most of the lost rays were directed outside the cavity, through their apertures. The main reason for the conical shape having the highest optical performance, in terms of both; the optical efficiency value and the flux uniformity is its length, which is the longest one compared to the other two receivers. The length as well as the convergent nature of the geometry, leads to trapping most of the rays and as a result letting them release the energy they hold inside the receiver cavity.

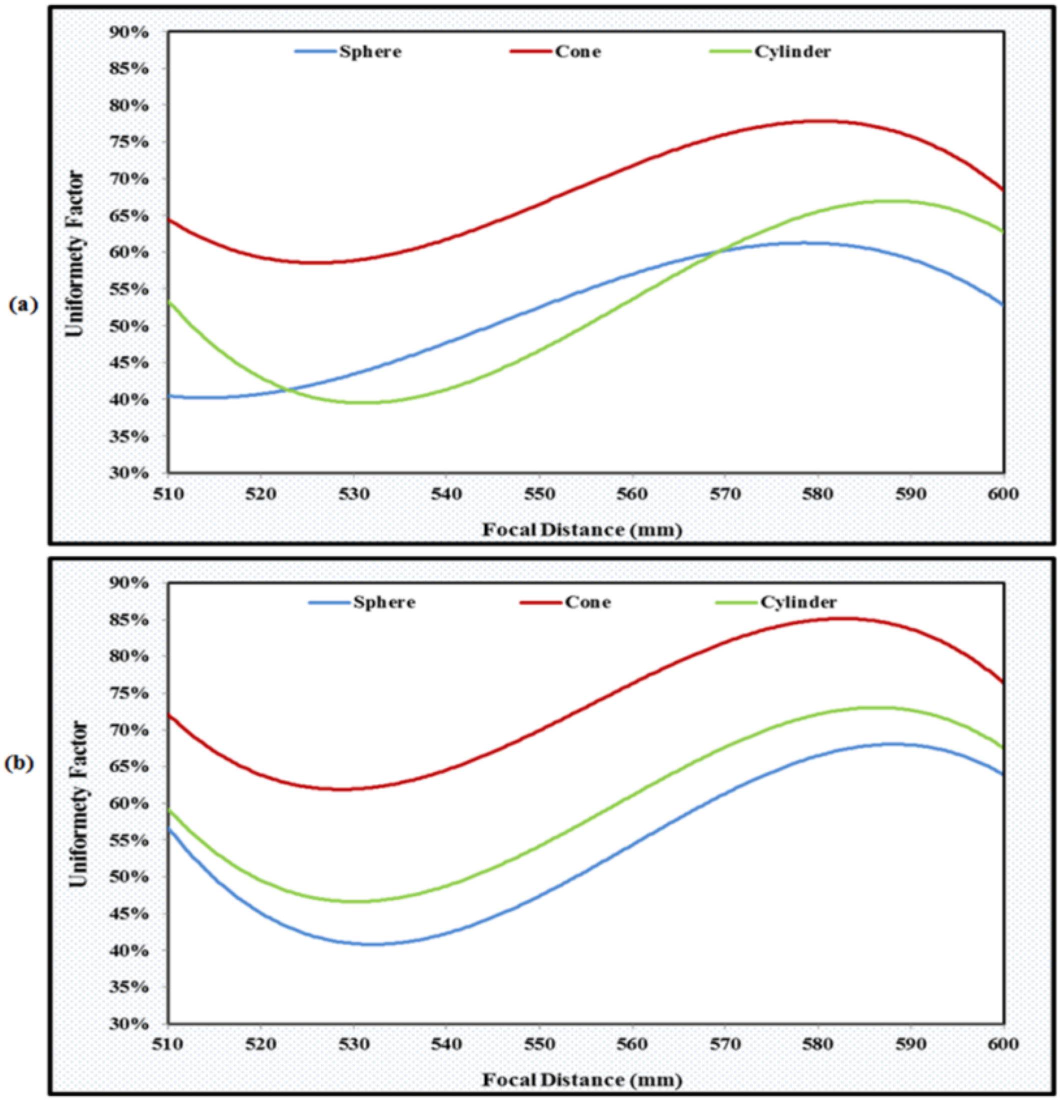

Figure 3.20: The uniformity factor of the receivers at various absorptivity and position of the cavity receiver with; (a) 85% and (b) 75% [148].

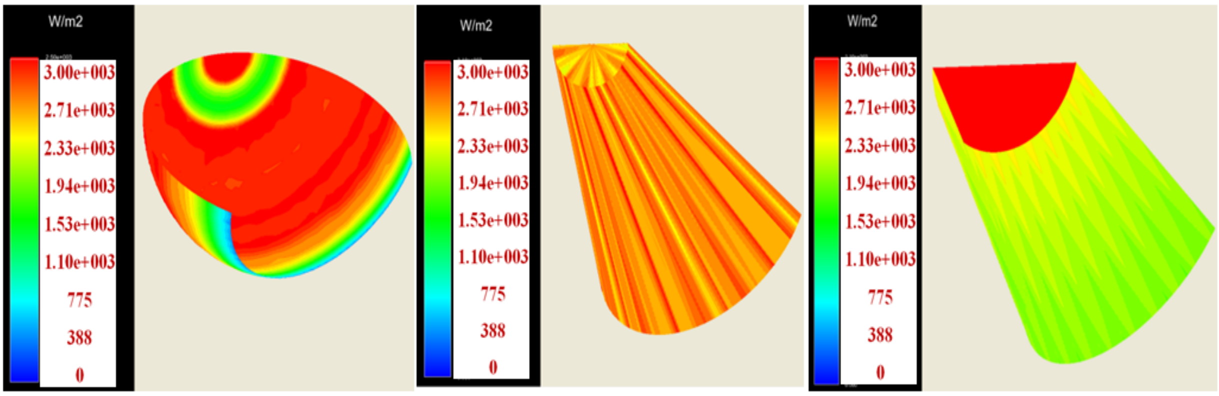

(a) **(b)** **(c)**

Figure 3.21: The best distributions achieved for; (a) Spherical shape, (b) Conical shape and (c) Cylindrical shape [148].

3.4 Thermal Simulation:

Thermal analysis has been integrated with the optical one with the aim of understanding the effect of most of the earlier mentioned factors on the receiver's behaviour and consequently the overall performance of the thermal system. In the thermal analysis, the three heat transfer modes, conduction, convection and radiation were considered as follows.

3.4.1 Heat Losses:

The energy balance and the total heat losses can be determined using equations (3.10 and 3.11) [99].

$$Q_B = mC_P\left(T_{fin} - T_{fout}\right) \tag{3.10}$$

$$Q_T = Q_{Cond} + Q_{Conv} + Q_{Rad} \tag{3.11}$$

Whereas the heat transfer by: conduction, convection and radiation, are expressed in equations (3.12-3.14) respectively [161] and [162].

$$Q_{cond} = -KA\,\Delta T = -KA(i\,\frac{\partial T}{\partial x} + j\frac{\partial T}{\partial y} + k\frac{\partial T}{\partial z}) \tag{3.12}$$

$$Q_{Conv} = hA\,(T_{surff} - T_{Amp}) \tag{3.13}$$

Where $h = kNu/L$

$$Q_{Rad} = \ \varepsilon\sigma A(T_{Sur}^4 - T_{Amb}^4) \tag{3.14}$$

Where $\varepsilon\ and\ \sigma$: are the emissivity and Boltzmann constant respectively [99].

To compute the heat transfer coefficient, in terms of the Nusselt number, there are several factors that need to be considered [99]. For example, the channel surfaces temperature, the fluid temperature, the acceleration due to gravity, the characteristic length, thermal conductivity, dynamic viscosity and specific heat capacity. Generally, Nusselt numbers for laminar and turbulent natural convections can be computed using correlations 3.15 and 3.16 respectively [99], [163] and [164].

$$Nu_{natural} = 0.508\left(\frac{Pr}{0.952 + Pr}\right)^{1/4} Ra^{1/4} \tag{3.15}$$

$$Nu_{natural} = 0.15\left(\frac{Pr^{9/16}}{0.671+Pr^{9/16}}\right)^{16/27} Ra^{1/3} \quad , where\ Pr = \frac{v}{\alpha} \tag{3.16}$$

The radiation mode of heat transfer can be determined based on view factor, the radiosity and surface emissivity. If the receiver internal surface is divided to a number of elements, the radiosity at each element can be evaluated using equation 3.17, [165-167].

$$\sigma T_{w,1}^4 = J_1 + \left(\frac{1-\varepsilon_I}{\varepsilon_I}\right) \sum_{j=1}^{N} F_{i,j}(J_i - J_j), \tag{3.17}$$

Where i and j are any two surfaces in the cavity; J and F are the radiosity and the view factor respectively [99].

So, the total radiation heat transfer is estimated using equations (3.18 and 3.19), [165-167].

$$Q_{Rad\ i} = \sum_{j=1}^{N} F_{i,j}(J_i - J_j) \tag{3.18}$$

$$Q_{Rad} = \varepsilon_{eff}\sigma A_{ap}(T_{wall}^4 - T_{amb}^4)\ , where\ \varepsilon_{eff} = \frac{1}{\left(\frac{1-\varepsilon}{\varepsilon}\right)} \frac{A_{ap}}{A_w} \tag{3.19}$$

3.4.2 Numerical Analysis and (CFD) Models:

The geometries of the three receivers were exported to the ANSYS Fluent 2015/ Academic software with the aim of evaluating the amount of useful energy that the compressed air, as a working fluid will gain. This can be achieved based on the heat losses principles; equations 3.10- 3.19 described above. The cavity shape of each receiver and its helical tube has been studied numerically via the finite volume technique to determine both; the lost and the absorbed energy amount and evaluate their performance [112].

Tetrahedral element type with smooth medium size, the mesh quality was attained, [168], as shown in the right hand side of Figure 3.22.

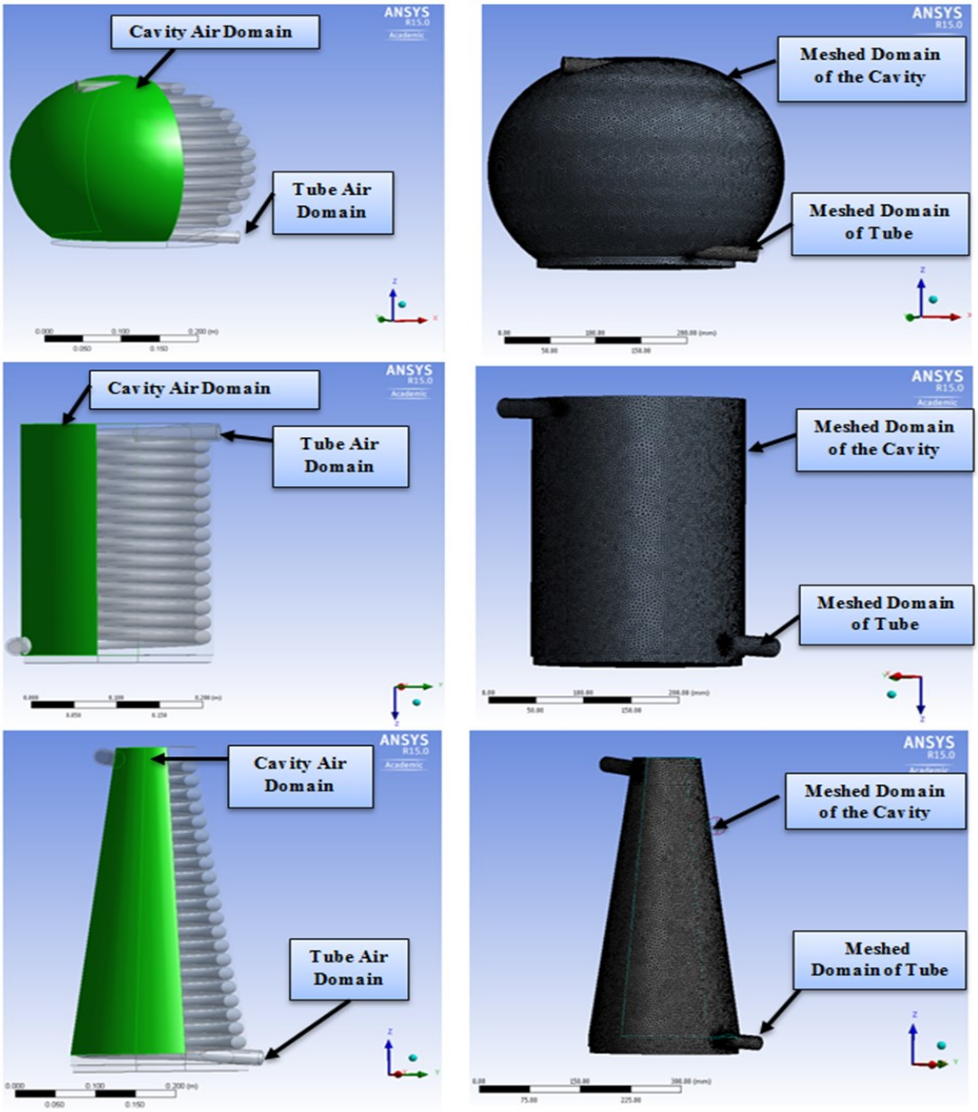

Figure 3.22: The modelled receivers with their meshed using ANSYS/ Fluent [112].

Mesh sensitivity, in terms of the exit air temperature, was carried out as shown in Figure 3.23. Moreover, a number of assumptions were used throughout the numerical analyses which are summarized as following, [99, 112, 147, 148]:

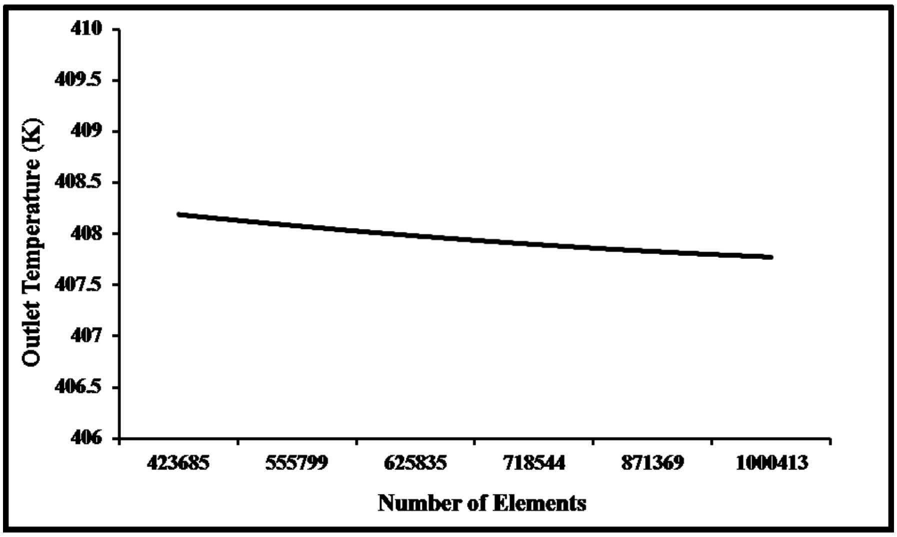

Figure 3.23: Mesh sensitivity based on the receiver outlet temperature [147].

1- The working fluid mass flow rate and its inlet temperature were set as 0.01 kg/s and 375K respectively, as provided by the compressed air supply for pressure ratio of 3.

2- High insulation material (Foam) with 0.03 m thickness was utilized as a cover for the external walls of the cavity receivers [168] to decrease the conduction heat losses.

3- The outlet boundary condition is maintained to be at atmospheric pressure. Also, there is no wind influence as natural convection heat losses only need to be assessed [112, 168].

4- All the cases were running with a 90° receiver geometry orientation as this configuration ensures the minimum convective heat losses [72, 77] i.e. no receiver inclination was considered.

The continuity, energy and Navier-Stokes momentum equations (3.20- 3.22) simultaneously govern the fluid flow in the helical tubes [112, 169].

$$\frac{\partial \rho}{\partial t}+\frac{\partial}{\partial x_i}(\rho u_i)=0 \tag{3.20}$$

$$\frac{\partial}{\partial t}(\rho C_P T)+\frac{\partial}{\partial X_i}(\rho u_i C_P T)-\frac{\partial}{\partial x_i}\left(\lambda\frac{\partial T}{\partial x_i}\right)=S_T \tag{3.21}$$

$$\frac{\partial}{\partial t}(\rho u_i)+\frac{\partial}{\partial x_i}(\rho u_i u_j)=\frac{\partial}{\partial x_j}\left[-\rho\delta_{ij}+\mu\left(\frac{\partial u_i}{\partial x_j}+\frac{\partial u_i}{\partial x_i}\right)\right]+\rho g_i \tag{3.22}$$

The solution method involved steady state analysis, surface to surface heat transfer, including radiation which requires the view-factors calculation of the zones involved with radiation [170]. The convergence conditions for the residuals of both velocity and the continuity equations were of the order of 10^{-4} [112]. However, to achieve more accurate results, the energy equation was set to 10^{-7}. The solutions were obtained once the convergence conditions were fulfilled and consequently the values of the three kinds of heat losses were described [112].

3.4.3 Thermal Simulation Results:

The following results were computed based on the value of heat absorbed (by the helical tube) for each of the three receivers as well as assuming that the helical tube always takes the cavity receiver's shape [112]. It is shown from the following analysis that there is a significant effect for the receiver shapes not only in terms the received flux distribution but also on the heat losses [112].

The walls temperature distribution for the helical tube positioned inside each of the three configurations is depicted in Figure 3.24. It is clear that the air enters the tube domain at low temperature; then it is increased with each helical tube turn as a result of the heat absorbed, until reaching its exit temperature.

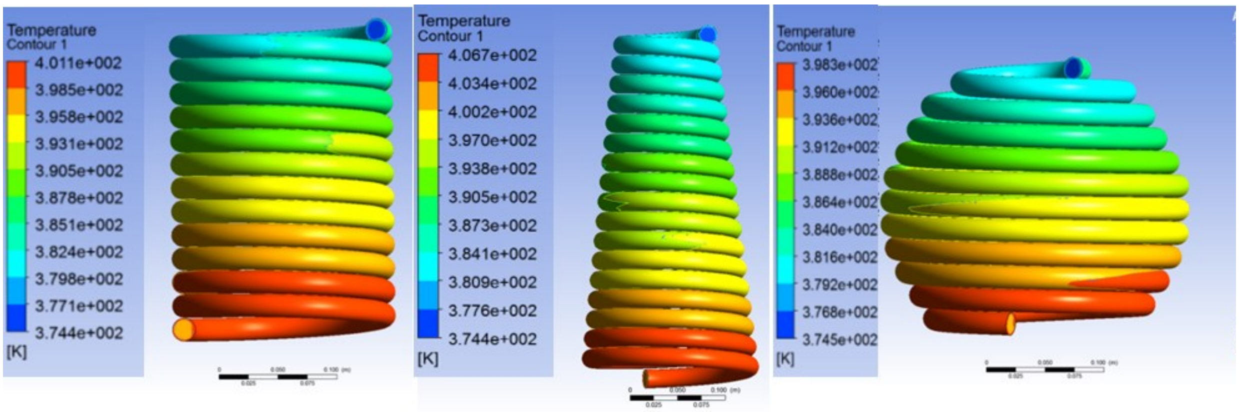

Figure 3.24: Temperature distributions for the three receivers [99].

The three heat transfer modes; conduction, convection, radiation, and the total heat loss as well as the values of the outlet temperature for the three receivers are presented in Figure 3.25. It can be noticed that the conductive heat losses are the lowest values; because of the highly insulating material (Foam) which covers the external surface of the three geometries. By contrast, the value of the convective one was higher, by reason of the relatively low temperature values of the receivers. In addition, among the three geometries, the conical cavity receiver had the smallest amount of total heat losses and accordingly delivered the highest outlet temperature of around 404 K. The values of the total heat losses were around 125, 107 and 86 W for the spherical, cylindrical and conical receivers respectively [99]. Moreover, the percentage values of heat losses because of the radiation were about 40.2%, 42.1% and 38.3% for the spherical, cylindrical and conical shapes; indicating that the spherical geometry showed the worst performance with respect to values of heat losses. Furthermore, as the employed heat source was less than 400 W, there was no large difference in the values of the outlet temperature of the three shapes.

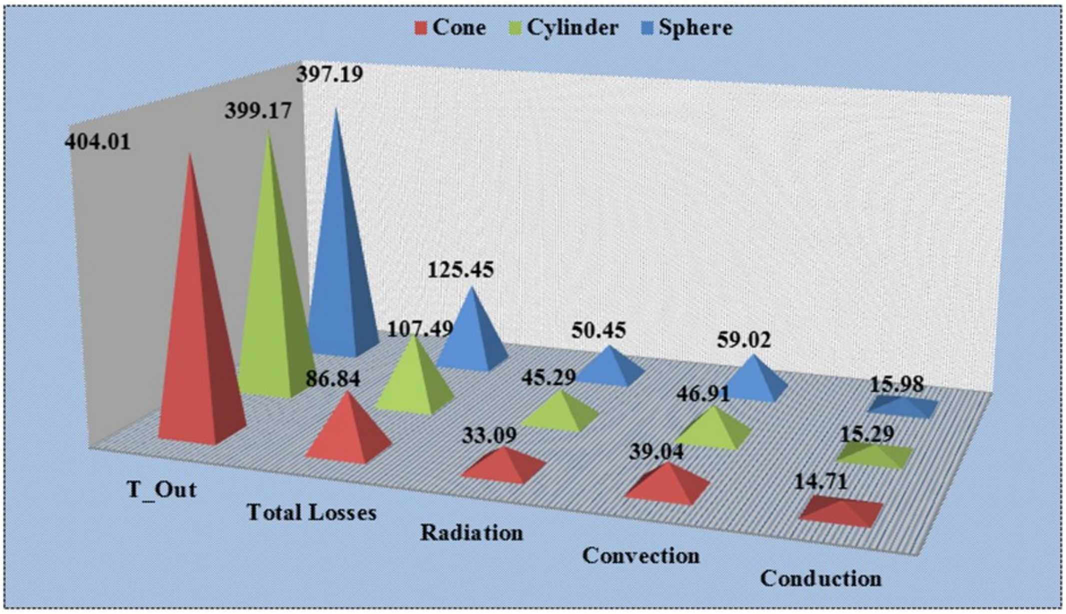

Figure 3.25: Three heat modes , total heat losses (W) and exit air temperature (K) of the three receivers [99].

3.5 Enhancing Receivers’ Thermal Performance:

In this analysis the author is trying to enhance the thermal performance of the cavity receivers using various scenarios such as using the real flux, using Glass to cover the receiver’s aperture, changing the helical tube pitch, equalizing the receivers’ surface areas and removing the dead areas. The real distribution of flux, achieved by the ray tracing software, was integrated in the thermal analysis, and established using ANSYS Academic / Fluent, by importing the actual distribution for the irradiance from the OptisWorks. Figure 3.26 presents the flux distribution on the receiver internal surface, as obtained by OptisWorks, which was imported to the ANSYS Academic fluent for thermal analysis. The results were firstly evaluated and the losses were highlighted and compared [147].

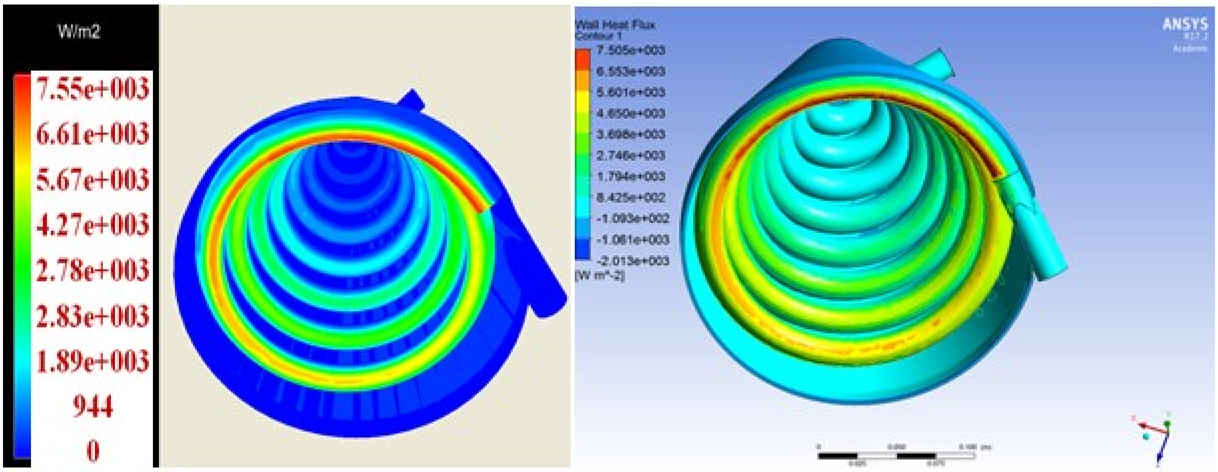

Figure 3.26: Comparison of flux distribution , at 0.5 pitch value, initiated in OptisWorks, LHS, and the imported to the ANSYS, (RHS) [147].

Next, a glass was used to cover the receiver aperture area with the aim of reducing the thermal losses. The comparison between the 0.5D pitch and zero pitch values with considering both; the optical performance and thermal one together for two models, with and without glass are given by Figure 3.27 [147]. This comparison was established based on the thermal efficiency which was defined as the absorbed energy (by the compressed air) with respect to the energy received by the receiver. It is evidence from this figure that the zero pitch was by far better than that of 0.5D value [147]. This is due to the lower amount of flux received by the tube causing a decline in the receiver optical efficiency and thus the overall receiver performance [147].

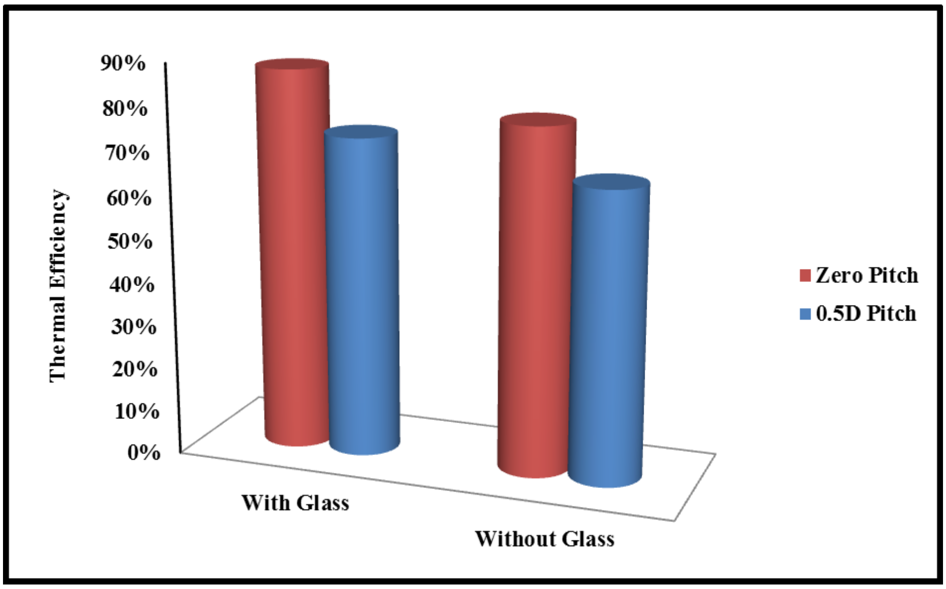

Figure 3.27: Thermal efficiency of the conical shape at different scenarios [147].

Figure 3.28 shows the total heat losses for the three studied configurations of the receiver with and without glass at zero pitch value using the equality in their surface areas assumption [147]. It is noticed from the figure that using glass the lowest values of total heat loss is achieved by the conical receiver with about 45 W while the cylindrical and the spherical shapes had about 46 and 56 W respectively. The non-glassed models, by contrast, had the values of 64, 73 and 53 W for the cylindrical, spherical and conical shapes respectively. In terms of the heat loss, the percentage enhancement, equation 3.23, for each shape was also presented in the same figure, which can be justified as a result of the change in the cavities' internal volume. In other word, by increasing the internal volume, the losses decline as a result of getting lower heat inside the cavity, which obviously reflects the enhancement, in terms of the heat loss which this function had [147]. Surprisingly, unlike the results confirmed in the previous sections, the conical shape had higher amount of losses in this analysis when the aperture was not covered by the glass. This can be justified because of the equality in their surface areas was the based assumption, not the aperture equality, used in the previous sections.

$$\text{Enhancement }\% = \frac{\text{Heat losses without glass} - \text{Heat losses with glass}}{\text{Heat losses without glass}} \tag{3.23}$$

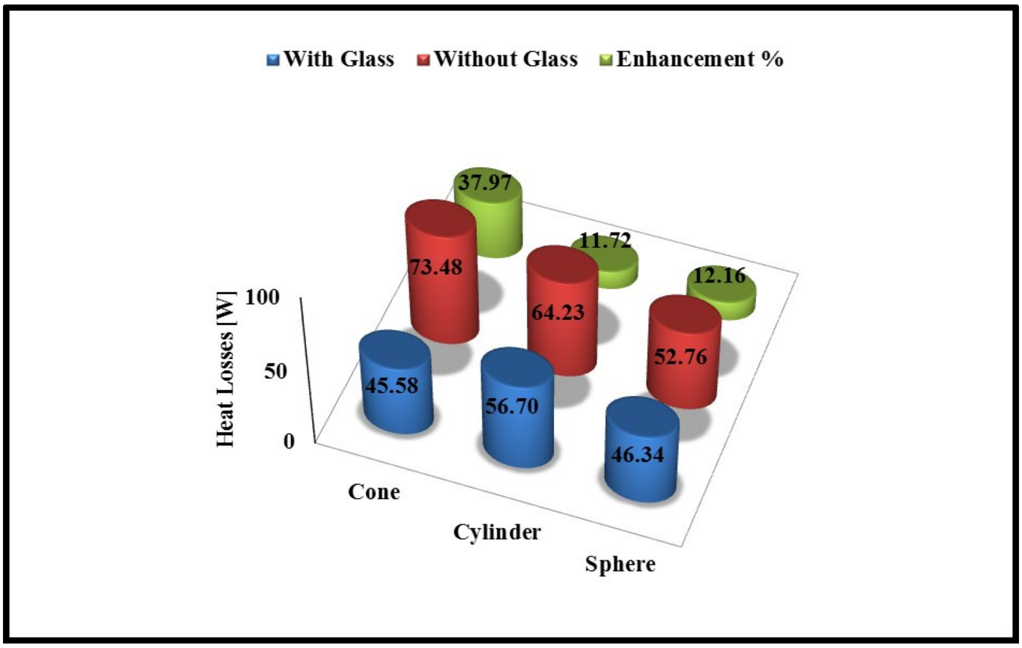

Figure 3.28: Total heat losses for the receivers at different scenarios [147].

Accordingly, Figure 3.29 shows the enhancement achieved in thermal efficiency of the three thermal receivers. From that figure it can be realised that up to 7% improvement can be achieved when the aperture area is covered with thermal glass [147]. Again, the dissimilarity in the results compared to the earlier sections is resulting from the total surface area differences for the studied receiver shapes [147]. On the other hand, this section focuses on developing a receiver shape with almost no dead area in the helical tube and basically bearing in mind having the same aperture area for the three receivers.

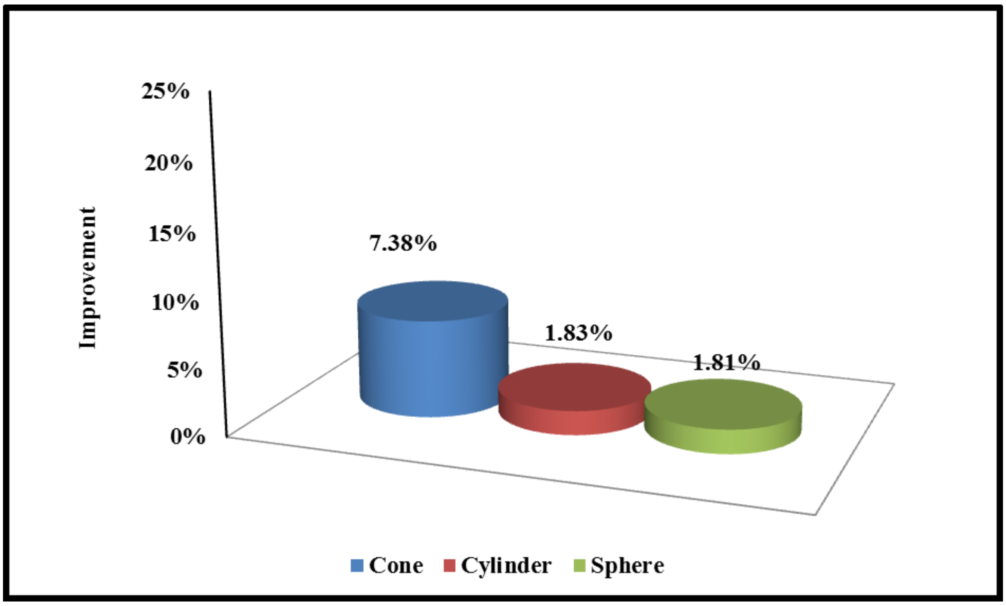

Figure 3.29: The achieved thermal enhancement in the three receivers after adding glass [147].

Figure 3.30 displays the three values of receivers' outlet temperature each at uniform flux, real flux, with covering glass and without covering glass. Interestingly, the difference in the exit temperature values was insignificant where no more than 2 K difference was noticed in the spherical receiver. This suggests that the using a uniform or constant flux on the helical surface tube is a reasonable assumption and will not lead to a significant difference in the compressed air exit temperature.

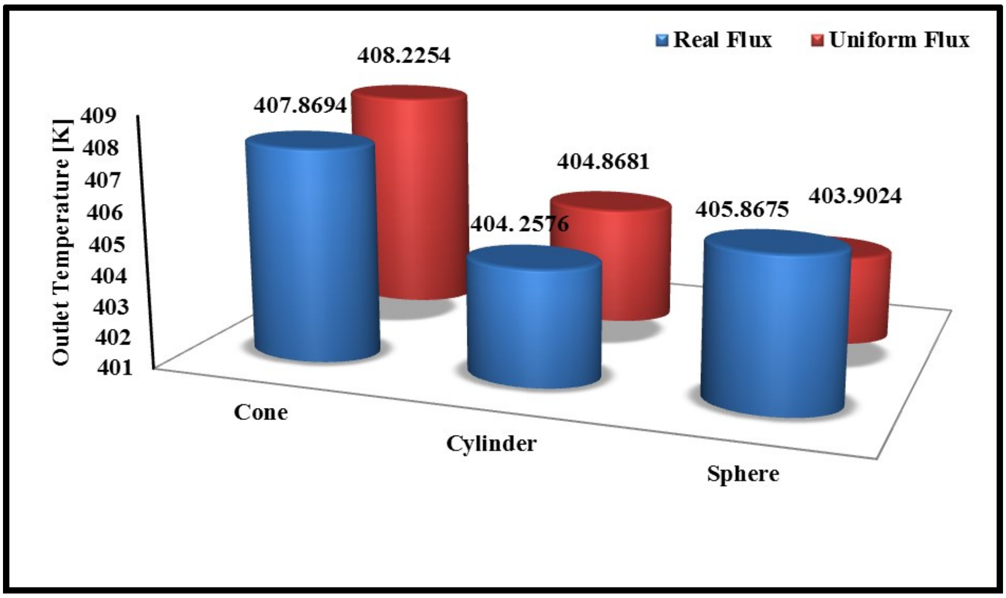

Figure 3.30: Exit air temperature using uniform flux and real flux modelling [147].

3.6 Summary and Conclusions:

In this chapter simulation work of four different cavity receiver geometries named as: elliptical, conical, spherical and cylindrical was carried out to evaluate the shapes' impact on the receiver performance both; optically using the ray tracing method and thermally using ANSYS/ Academic Fluent software. The main conclusions have been summarised as following:

- An optimum diameter for the receiver can lead to a high value of the overall system optical efficiency. This was because of the receiver shading which affects negatively the radiation falling on the parabolic dish.
- The receiver geometry has a vital role in terms of the received irradiance distribution and the amount of the heat loss [99].
- The best focal distance showed an influence to both; the receiver configuration and the absorptivity of its internal surface.
- The conical receiver was the best among the studied configurations. This is because of two reasons; the best illumination uniformity (77% to 84%) and it has the ability to hold the highest incoming energy compared to the other configurations.

Thermally,

- The conical receiver experienced the lowest amount of heat losses and therefore reached the highest thermal efficiency, about 77% compared to the 63% and 69% of the spherical and cylindrical shapes respectively. This shows that the conical receiver is more appropriate for the (SSSPC) [99].
- As for the temperature of the receiver exit air, the conical receiver showed the highest among the three investigated receivers (conical cylindrical and spherical).

- Comparing the compressed air exit temperature for the case of using uniform flux and real flux distributions on the surface of the receiver coil shows little difference. Therefore, using the uniform flux in the thermal analysis provides good method for predicting the exit air temperature values.
- Again among the modelled receivers, the conical receiver had the best response when the aperture areas of the three examined receiver configurations were enclosed using thermal glass.

CHAPTER 4: TURBINES DEVELOPMENT AND OPTIMIZATION METHODOLOGY

4.1 Introduction:

This chapter describes the development of the Small Scale Turbines (SSTs) for the Small Scale Solar Powered Brayton Cycle (SSSPBC). Firstly the cycle analysis was described in section 4.2 [171]. The development of Small Scale Axial Turbine (SSAT) and Small Scale Radial Turbines (SSRT) using meanline preliminary design approach and 3D computational fluid dynamics in described in section 4.3 [28]. This is followed by a comparison between the performance of (SSAT) and (SSRT) which is described in section 4.4 showing that (SSRT) produced higher efficiency than (SSAT). Finally, an optimization process was developed for the SSRT and described in section 4.5. A multi-objective optimization was employed in order to find the optimum turbine rotor and stator shape, aerodynamically using three Dimensional Computational Fluid Dynamic simulations. The results of the (3D CFD) were included in the cycle analysis to determine the overall improvement in the system performance.

4.2 Cycle Analysis:

The main advantage of the Brayton cycle (when the compressed air is the working fluid), is the fact that it does not have an adverse effect on the environment and is considered to be a clean cycle [172]. In the following subsections the cycle thermodynamic analysis and the effect of improving the turbine and compressor performance on the cycle efficiency are presented.

The following sections were published by the author in [28, 171-173]

4.2.1 Thermodynamic Analysis:

Figure 4.1 shows a schematic diagram of a Solar Powered Brayton Cycle (SPBC) consisting of a compressor (process 1-2), thermal receiver (process 3-4), and a turbine (process 4-5). In order to recover the energy in the hot air leaving the turbine, a recuperator, (process 2- 3) is used. A thermal Energy Storage Tank (TEST) is used to store the extra heat generated during the zenith time for use when there is not sufficient solar energy at dusk or in cloudy weather. Figure 4.2 clarifies the cycle T-S diagram.

The power required for the compressor is determined by [8]:

$$\mathrm{W_C} = \frac{Cp\, T_1(\mathrm{R}_C\mathrm{K} - 1)}{\eta_\mathrm{C}} \tag{4.1}$$

Where R_c is the compressor pressure ratio; $R_c = P_2 / P_1$, T1 is the compressed air inlet temperature, $K = \gamma\text{-}1/\gamma$ and compressor efficiency is η_C.

The heat supplied from the solar thermal receiver per unit mass flow rate is given as:

$$Q_\mathrm{Net} = \mathrm{Cp}(\mathrm{T_4} - \mathrm{T_3}) \tag{4.2}$$

The specific power extracted from the turbine can be given as:

$$\mathrm{W_T} = Cp\, \eta_\mathrm{T} T_4(1 - \mathrm{R}_T - \mathrm{K}) \tag{4.3}$$

Where $R_T = P_4 / P_5$ the turbine pressure ratio and η_T is the turbine efficiency.

If X is defined as the pressure loss coefficient in the turbine, then the previous equation can be rewritten as:

$$\mathrm{W_T} = Cp\, \eta_\mathrm{T} T_4(1 - (\mathrm{X}\mathrm{R}_c) - \mathrm{K}) \tag{4.4}$$

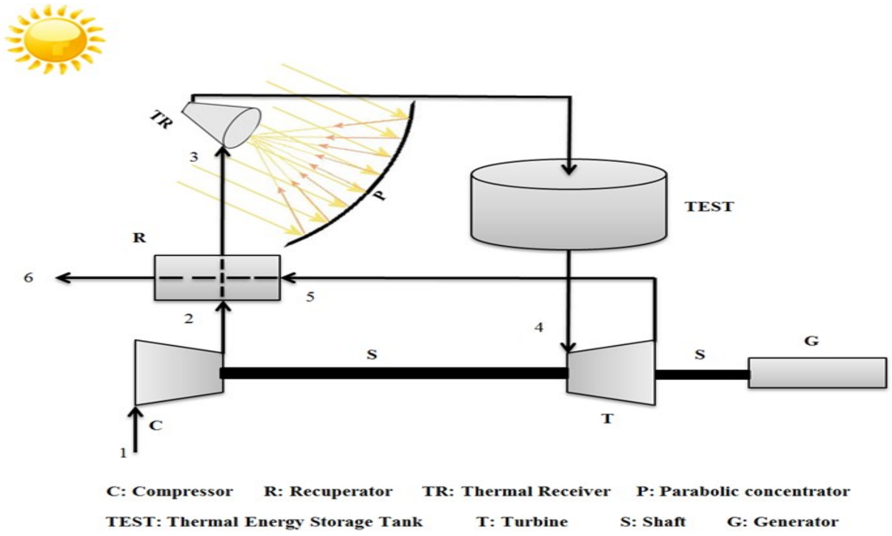

Figure 4.1: Schematic drawing for the (SSSPBC) system [28].

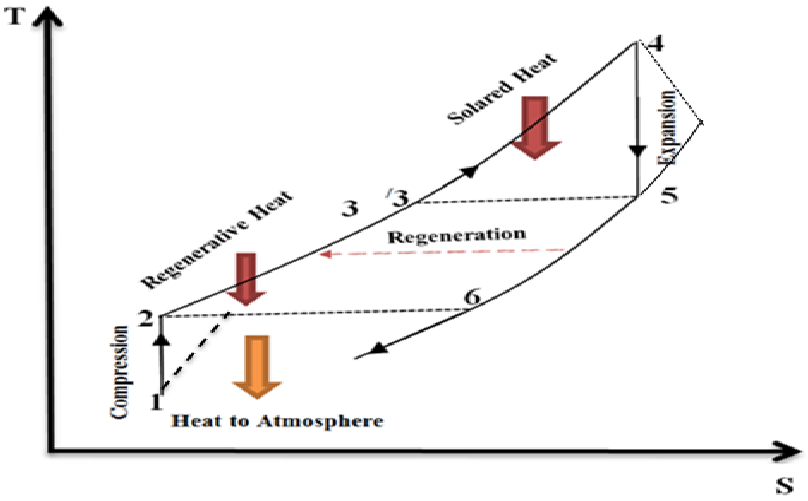

Figure 4.2: Temperature-Entropy diagram for the SSSPBC [171].

For the regenerator, the heat gained by the compressed air leaving the compressor and the heat rejected from the air leaving the turbine are specified respectively in the following two equations [171]:

$$Q_G = \dot{m}(h_2 - h_3) \tag{4.5}$$

$$Q_{cRej} = \dot{m}(h_5 - h_6) \tag{4.6}$$

The extent to which a regenerator approaches an ideal regenerator is called the effectiveness, ε, and H, is the total enthalpy, is defined as where:

$$\varepsilon = \frac{H_3 - H_2}{H_s - H_2} \tag{4.7}$$

The power gained from the system is evaluated as:

$$W_{net} = W_T - W_C \tag{4.8}$$

Using equations 4.1 and 4.4, W_{net} per unit mass flow rate can be rewritten:

$$W_{net} = Cp\left[\eta_T T_4(1 - (XR_c) - K) - \frac{T_1(R_C K - 1)}{\eta_C}\right] \tag{4.9}$$

The cycle efficiency is then calculated as:

$$\eta_{th} = \frac{W_{net}}{Q_{Net}} \tag{4.10}$$

4.2.2 Cycle Results:

It can be noticed that each of the cycle's components needs to be developed to achieve high overall efficiency of the cycle [172]. For example, developing the best turbine, with high efficiency and power output, will improve the overall performance for the system [173]. In this section, the turbine efficiency and the boundary conditions discussed earlier will be employed as input factors with the aim of determining the cycle efficiency using regenerator's efficiency of 95%, compressor pressure loss of 1.5% and turbine pressure loss 1.25% [172]. Figure 4.3 a-c shows the effect of turbine and compressor efficiency on the overall cycle efficiency at various turbine pressure ratios. It is shown that at 95% compressor efficiency, the cycle efficiency can be improved by 4.5 % and 9.5 % by raising the turbine efficiencies values from 80% to 90% at 500 K and 600 K inlet temperature respectively [172]. In contrast, the cycle performance can be deteriorated to be about 7.5% by decreasing the efficiency of the compressor by, 10%, from 95% to 85%.

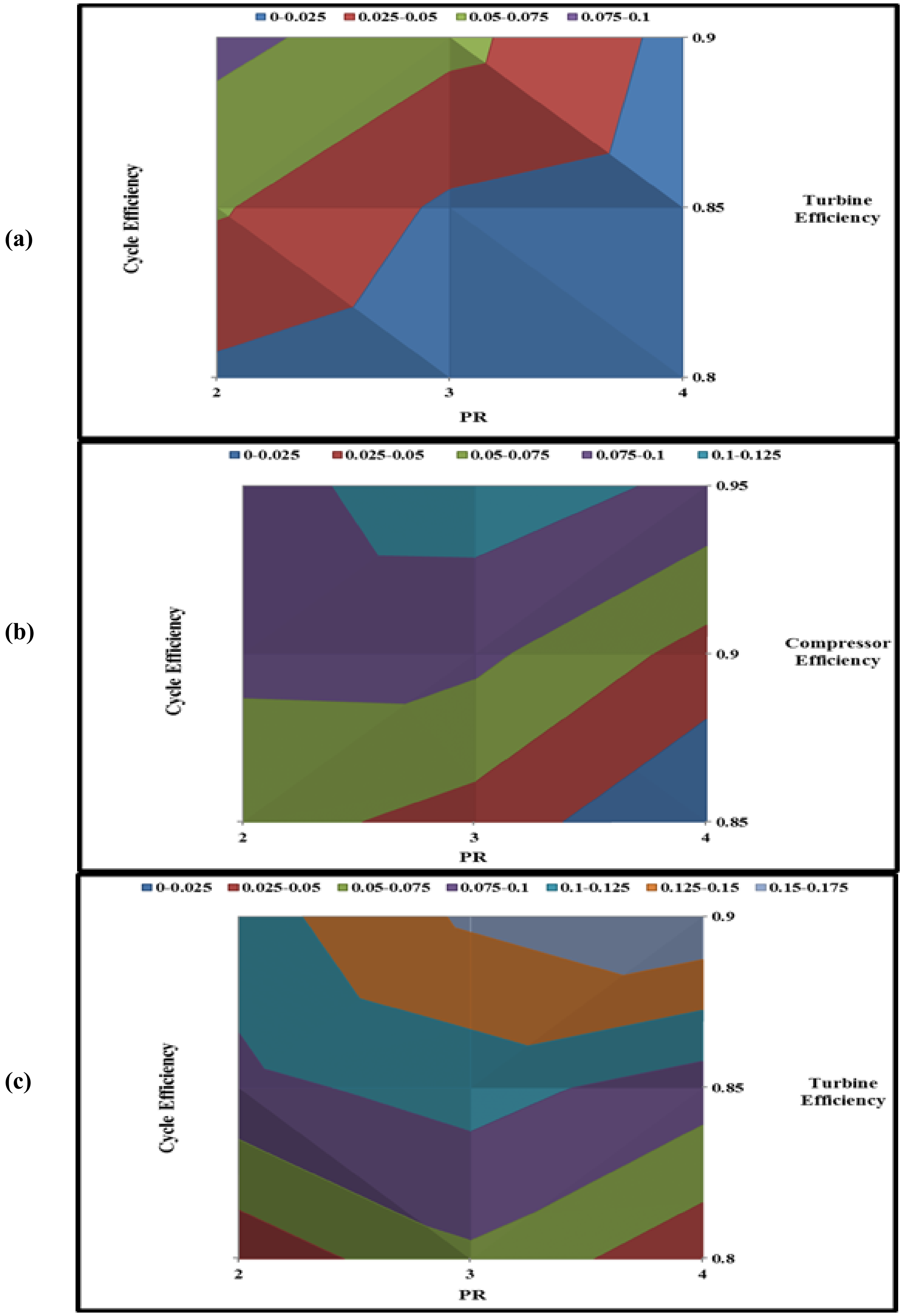

Figure 4.3: Effect of; (a) the turbine efficiency at 500 K, (b) turbine efficiency at 600 K and (c) compressor efficiency at 500 K on the cycle efficiency at various PR, numerically [172].

4.3 Turbines Development Methodology:

Turbines are central components in power generation systems based on Rankine, and Brayton cycles. There are two types of turbines which are commonly used in power generation systems namely; axial flow turbines and radial flow turbines. In the literature review chapter it was shown that there was limited published work on the development of small scale turbines of power output less than 3 kW.

4.3.1 One Dimensional Turbine Design Approach:

Mean-line approach is a one dimensional flow analysis which uses the flow characteristics at the mean radius of turbine stage to characterize the average properties of the dynamic flow in the turbine passage [174]. In other words, this approach ignores any circumferential flow variations or even radial variations and all the governing equations deal with the mean turbine radius, which is the mid distance between the hub and tip radius. The meanline design approach is a highly iterative process as it investigates a large number of possibilities. Using this approach the turbine geometric parameters such as inlet and exit rotor radii and blade heights as well as the flow properties like the inlet and exit velocity triangles can be determined. Many researchers utilised the mean line approach to develop small scale axial [175] and radial turbines [122, 176]. Figure 4.4 presents a flow chart for the meanline turbine development process. For solar powered small scale application, the use of meanline approach is summarised as follow:

- Choosing the correct non-dimensional factors such as the flow coefficient and the loading coefficient. Their intersection, for the each of the mentioned configuration, can determine the optimum turbine type as shown in Figure 4.5.
- Specifying the operating conditions such as the turbine pressure, temperature and mass flow rate. Table 4.1 shows the specifications of the studied boundary conditions

for the Small Scale Single Stage Axial Turbine (SSSSAT), Small Scale Dual Stage Axial Turbine (SSDSAT) and Small Scale Radial Turbine (SSRT) [172].

- Determining the initial rotor efficiency and its overall dimensions. If not satisfied (from the manufactural view point), then the chosen values from the two previous steps should be changed.
- Then, the overall stator and volute geometries are determined.

Using the relevant losses correlations for the stator and the rotor, the stage efficiency for the all turbine stage can be determined. If not satisfied, then the selected dimensions for the stator need to be improved.

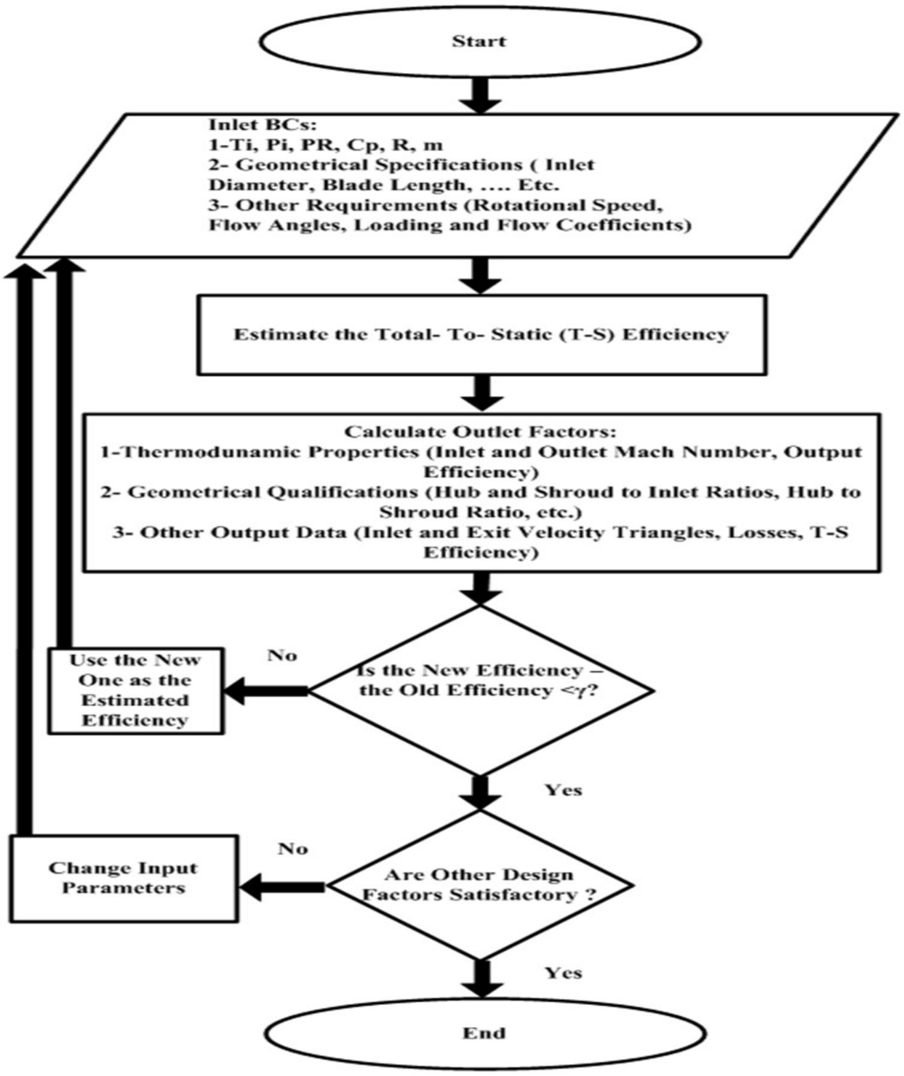

Figure 4.4: Algorithm procedure followed during the study for the development turbines [28].

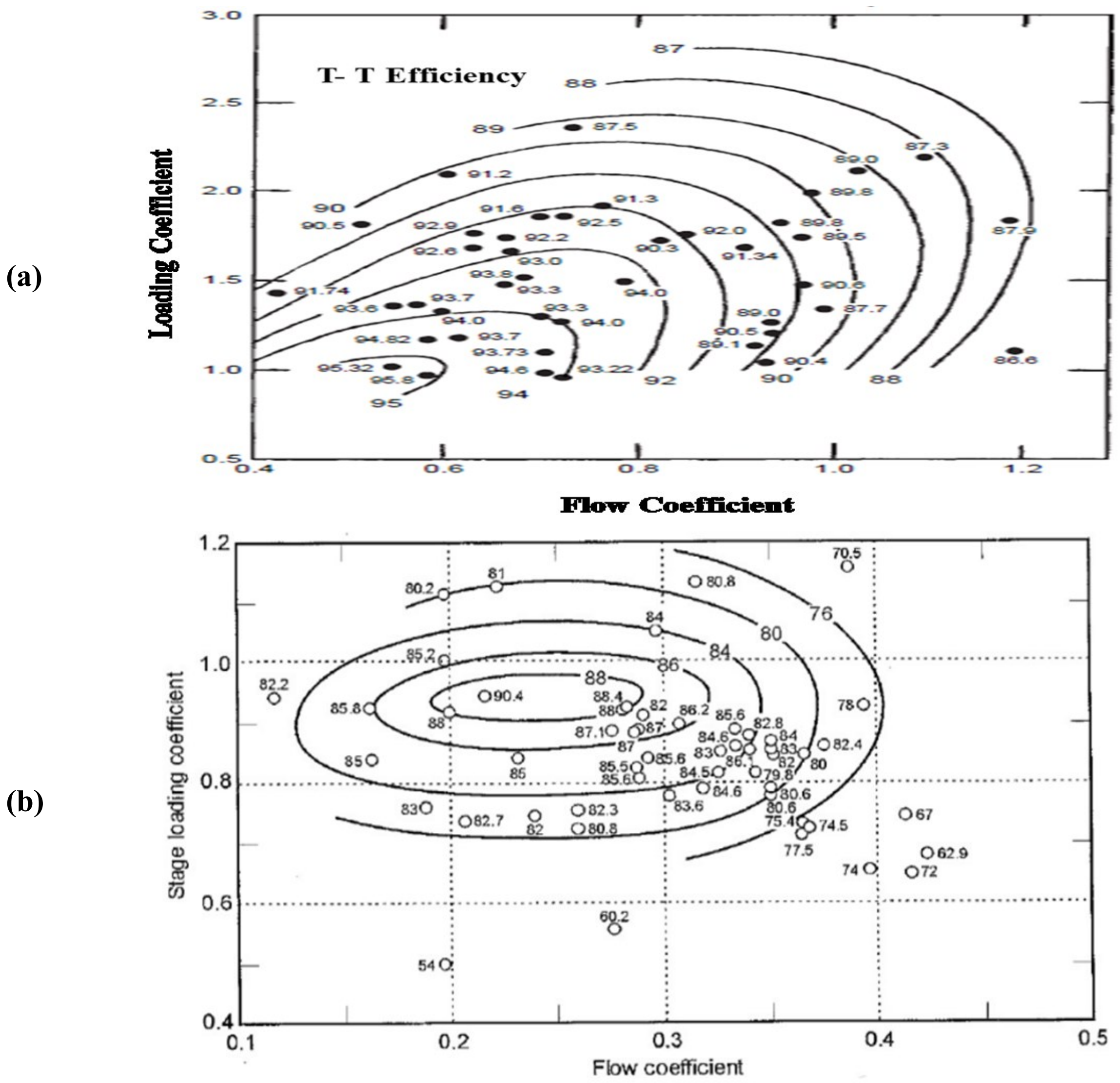

Figure 4.5: Correlations of blade loading and flow coefficient for, (a) axial turbine and (b) radial turbine [174, 177, 178].

Table 4.1: Input parameter of the axial and radial turbines for the preliminary design [28].

Parameter	**Value**			
	SSSSAT	**SSDSAT**	**Radial**	**Unit**
Output power (Target)	1- 3	1- 3	1- 3	kW
Flow coefficient (Ψ)	0.8-1.4	0.4-1, 0.6-1.3	0.6-1.2	-
Hub/tip radius ratio (r_h/r_t)	0.52	0.52	0.3	-
Total PR	2-4	2-4	2-4	Bar
Rotational speed	60-110	60-110	60-110	krpm
Total inlet temperature	400-600	400-600	400-600	K

4.3.1.1 Governing Equations of the Axial Turbine:

Figure 4.6 shows a schematic diagram of axial flow turbine and its velocity triangles. The compressed air enters the nozzle with a flow angle (α_1) and absolute velocity (C_1) and then leaves it at flow angle and absolute velocity (α_2 and C_2) [28]. The remaining angles and velocities represent the inlet relative velocity and exit relative velocity and angles (V_2, V_3, β_2 and β_3 respectively) [28].

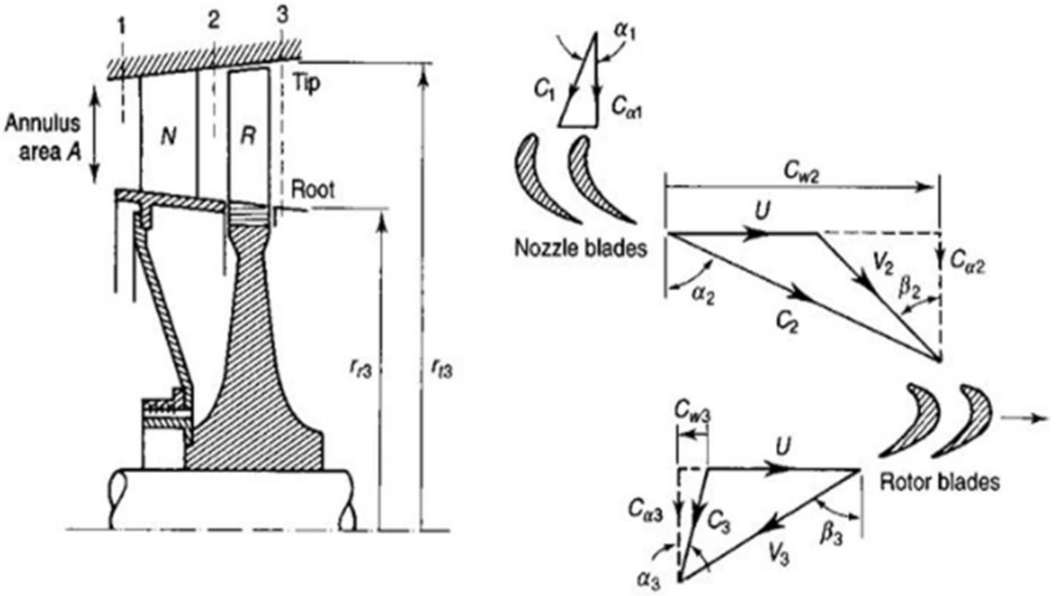

Figure 4.6: The velocity triangle of axial turbine [173, 176].

The equations are summarised below [174, 179]. The loading coefficient, which can be determined as the total enthalpy ratio drop in the stage to the blade square velocity, and flow coefficient (axial flow velocity to the blade velocity ratio), are determined by equations 4.11& 4.12 respectively

$$\Psi = \frac{\Delta h_o}{U^2} \tag{4.11}$$

$$\emptyset = \frac{C_a}{U} \tag{4.12}$$

Another important factor in this analysis is the stage reaction which can be defined as the enthalpy drop in the rotor with respect to the total enthalpy drop in all stage, equation 4.13.

$$\mathrm{R} = \frac{h_2 - h_3}{h_1 - h_3} \tag{4.13}$$

The rotor inlet and exit flow angles can then be obtained using equations 4.14 and 4.15 [173].

$$\left.\begin{aligned} \tan\beta_2 &= \frac{(\Psi - 2R)}{2\phi} \\ \tan\beta_3 &= \frac{-(\Psi + 2R)}{2\phi} \end{aligned}\right\} \tag{4.14}$$

$$\left.\begin{aligned} \tan\alpha_3 &= \frac{-\big(\Psi/2 - (1 - R)\big)}{\phi} \\ \tan\alpha_2 &= \frac{\big(\Psi/2 + (1 - R)\big)}{\phi} \end{aligned}\right\} \tag{4.15}$$

Next, both total to total, in case of more than one stage, and total to static, in case of single stage turbine efficiencies are determined using the following two equations [28, 115, 180]:

$$\eta_{tt} = \frac{1}{1 + \left[\zeta_R V_3^2/2 + \left(\zeta_S C_2^2/2\right)\right]/(h_1 - h_3)} \tag{4.16}$$

$$\eta_{ts} = \frac{1}{1 + \left[\zeta_R V_3^2/2 + \left(\zeta_S C_2^2/2\right)\left(\frac{T_3}{T_2}\right) + C_3^2/2\right]/(h_1 - h_3)} \tag{4.17}$$

Where ζ_S and ζ_R are the stator and rotor loss coefficients respectively due to flow irreversibility.

As for the turbine geometry, the blade number, Z, and height, H, can be specified using the following equations [115, 180]:

$$Z = \left(\frac{\pi}{30}\right)(110 - \alpha_1)\tan\alpha_1 \tag{4.18}$$

$$H = r_t - r_r \tag{4.19}$$

Where r_t and r_r refer to the blade tip and root blade radiuses.

Here it is worth mentioning that all the equations which govern the flow and Euler turbomachinery are resolved at mean radius r_m of the turbine.

This radius can be specified via the next equation:

$$r_m = \frac{r_r + r_t}{2} \tag{4.20}$$

4.3.1.2 Governing Equations of the Radial Turbine:

Figure 4.7 shows a schematic diagram of radial flow turbine and its velocity triangles. The loading and flow coefficients for the radial turbine are determined using equations 4.21& 4.22, [181]:

$$\Psi = \frac{\Delta h_{actual}}{{U_4}^2} \tag{4.21}$$

$$\emptyset = \frac{C_{m5}}{U_4} \tag{4.22}$$

The hub diameter r_h, tip diameter r_t and the number of rotor vanes Z_{rotor} are given as below:

$$r_{5_t} = \sqrt{\frac{A_5}{\pi} + r_{5hub}^2} \tag{4.23}$$

$$Z_{rotor} = \frac{\pi}{30}\,(110 - \alpha_2)\tan(\alpha_2) \tag{4.24}$$

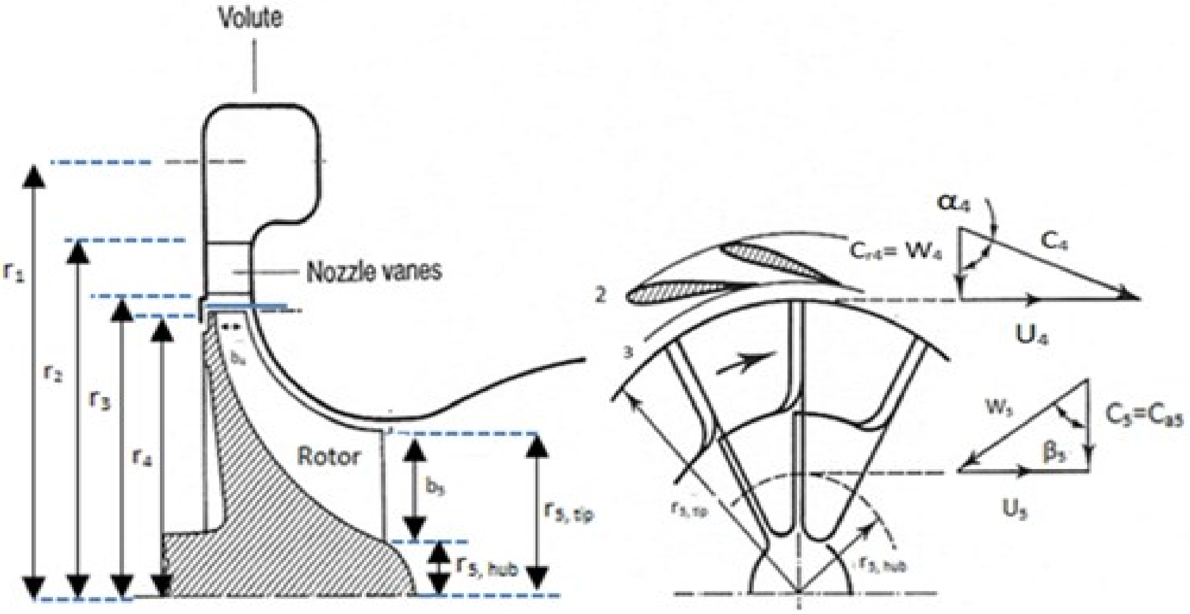

Figure 4.7: Schematic figure and velocity triangle of radial flow turbine [173, 176].

Once the mass flow rate of the working fluid specified, based on its absolute velocity and density, the maximum and the volute radii values can be evaluated using equations 4.25- 4.27, [182] and [181].

$$A_1 = \frac{\dot{m}_{working\,fluid}}{\rho_1 C_1} \tag{4.25}$$

$$r_{volute} = \sqrt{\frac{A_1}{(0.75\pi + 1)}} \tag{4.26}$$

$$r_{max} = (\, r_1 + r_{volute}) \tag{4.27}$$

The volute losses, subsequently the enthalpy total losses and the total to total efficiency can be determined using the following equations:

$$\Delta h_{loss,total} = \Delta h_{loss,volute} + \Delta h_{friction,nozzle} + \Delta h_{tip,clearance}$$

$$+\Delta h_{secondary} + \Delta h_{friction} + \Delta h_{exit} \tag{4.28}$$

$$\left(\eta_{turbine,stage,ts}\right)_{new} = \frac{\Delta h_{actual}}{\Delta h_{actual} + \Delta h_{loss,total}} \tag{4.29}$$

$$Turbine\ Efficicency = \frac{1-\frac{T_5}{T_{t,4}}}{1-\left(\frac{P_5}{P_{t,4}}\right)^{\frac{\gamma-1}{\gamma}}} \tag{4.30}$$

The meanline approach was used to develop Small Scale Single Stage Axial Turbine (SSSSAT), Small Scale Dual Stage Axial Turbine (SSDSAT) and the Small Scale Radial Turbine (SSRT) [172]. The output geometry dimensions for; are given in Table 4.2.

Table 4.2: Turbines dimensions from the preliminary design [28].

Parameter	Value			Unit
	SSAT	DSAT	SSRT	
Hub diameter (D_h)	20	20	20	mm
Tip diameter (D_t)	38	38	-	mm
Rotor number of blade	9	8,9	11-19	-
Stator number of blade	8	11,8	22-30	-
Rotor Stagger angle	45	45, 45	39	Degree
Stator Stagger angle	45	35,45	41	Degree
Tip clearance	0.45	0.45, 45	0.45	mm
Tip Width	-	-	1.95	mm
Blade height (H)	15	15, 12	-	mm
Relative Inlet flow angle (β_2)	21	63, 66	10	Degree
Relative outlet flow angle (β_3)	-45	-63, -56	-79	Degree
Absolute inlet flow angle (α_1)	66	63, 66	0.0	Degree
Absolute outlet flow angle (α_2)	-43	3, -43	71	Degree

4.3.2 3D CFD Turbine Analysis:

Although the one dimensional meanline approach can be used to determine the shape, size, turbine efficiency and power output, it cannot provide detailed information on the complex flow characteristics inside the turbines. Computational Fluid Dynamic (CFD) can be described as numerical methodology for determining fluid flow characteristics using partial differential equations known as the Navier-Stokes (N-S) equations and utilizing computer simulation based on finite volume and finite difference approaches [183]. Computational Fluid Dynamics (CFD) simulation is a powerful tool that provides detailed three dimensional fluid flows in complex geometries and taking into account working fluid characteristics and behaviour. Therefore, (CFD) fluid flow simulation which takes into account the fluid viscosity was used in the current study to predict fluid behaviour in the three turbines developed using the meanline approach as described in the previous section. The (CFD) procedure for the simulation steps is shown in Figure 4.8.

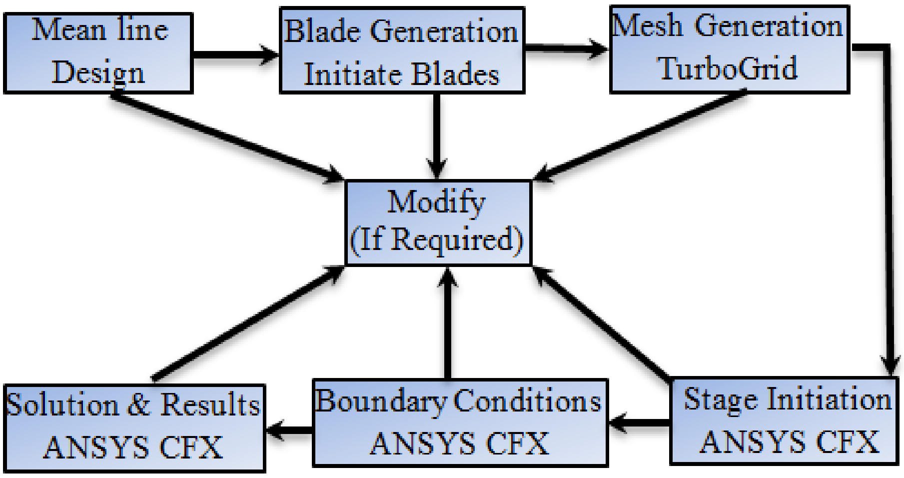

Figure 4.8: Procedure followed in designed turbines using (CFD) modelling [172].

4.3.2.1 3D Blade Generation:

Using the preliminary design, Blade-Gen, of ANSYS Workbench was used to produce 3D geometry of the blades for the stator part and rotor part for the (SSSSAT), (SSDSAT) and (SSRT) [172]. Figure 4.9 a, b and c shows the 3D model of the complete stage geometry of each turbine [172].

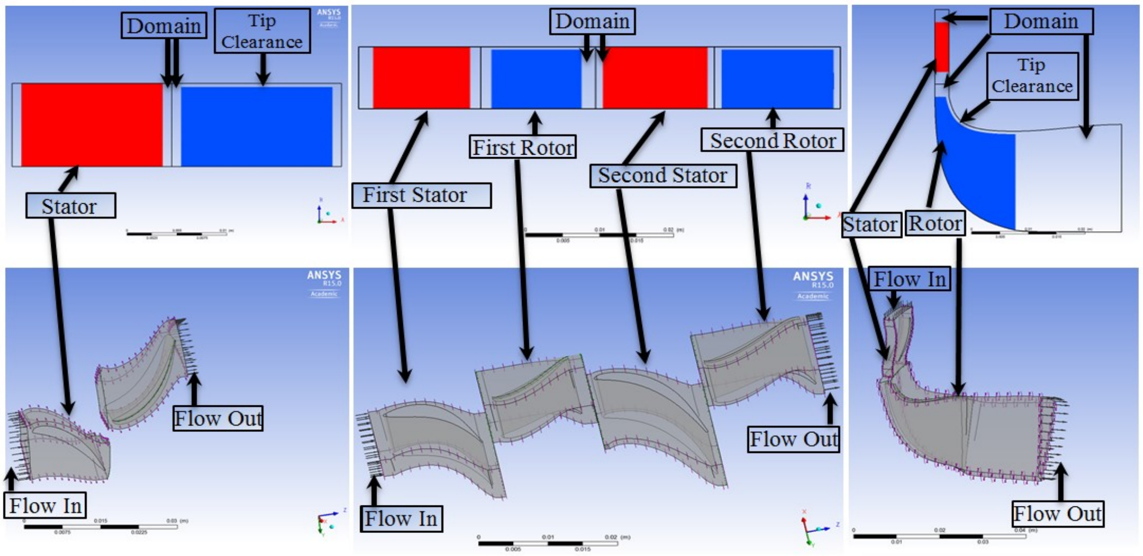

(a) **(b)** **(c)**

Figure 4.9: 2D and 3D view for the stator and rotor blade domains of the (a): (SSSSAT), (b): (SSDSAT) and (c): (SSRT) [172] using CFX/ ANSYS.

4.3.2.2 3D Mesh Generation:

The blade geometry developed using Blade-Gen was meshed using the Turbo-Grid module available in ANSYS Academic / Workbench. Figure 4.10 a, b and c show the 3 dimensional meshes for the (SSSSAT), (SSDSAT) and (SSRT) respectively [172]. It is worth noting that in the zone near to the blade surface, the grid was refined to simulate accurately the fluid behaviour including viscous effects.

The grid's sensitivity analysis was carried out based on (SSSSAT) total to static efficiency as shown in Figure 4.11 where no change in the predicted efficiency with the increase in number of elements above 75000.

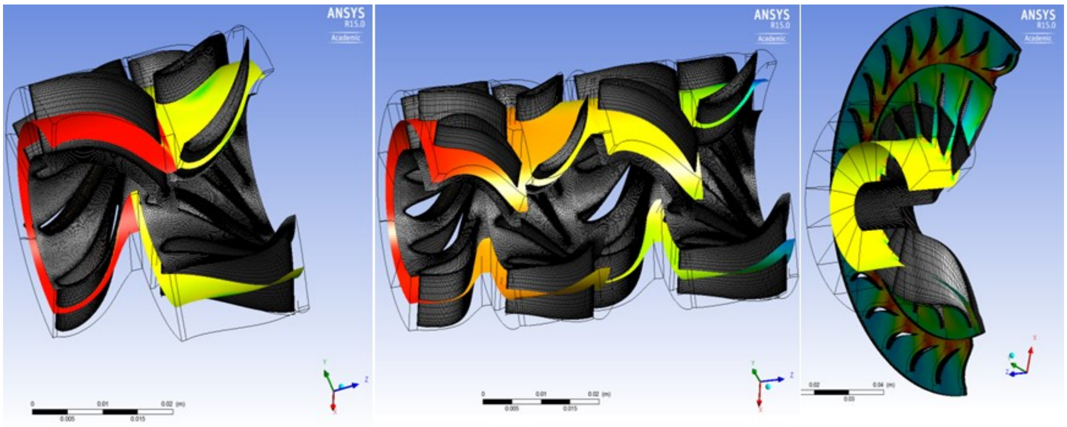

(a) **(b)** **(c)**

Figure 4.10: 3D views showing only the hub, the blades with their mesh lines of both the stator and rotor for the (a): (SSSSAT), (b): (SSDSAT) and (c): (SSRT) [172].

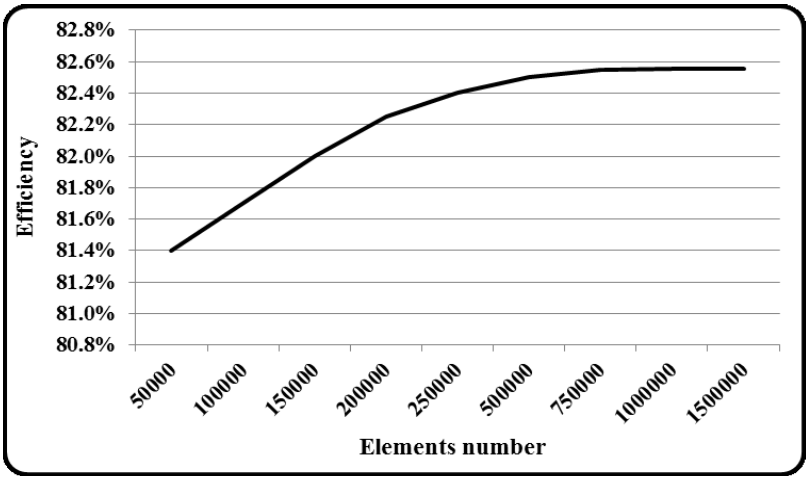

Figure 4.11: Mesh sensitivity with respect to the turbine efficiency [172].

4.3.2.3 CFD Turbine Model Setting:

The fluid flow modelling setup for the various turbines was carried out based on the assumptions suggested by [184, 185], which can be summarized as [28, 172]:

1- The first step in the solver, setting was to decide whether; the model is for axial or radial then specify the axis of rotation followed by choosing whether the model is transient or steady state [185].

2- Each part of the selected turbine, stator or rotor is defined and the passages aligned to form one complete stage.

3- Next, the flow directions for the working fluid, the rotational speed for the rotating part were defined and then specifying if there is a tip clearance at the shroud or not is specified i.e. stator or rotor [172].

4- After that, the viscosity and the compressibility of the fluid were appropriately selected. Likewise, ideal gas was chosen for the working fluid, as it is compressed air, while the first order upwind advection scheme was selected as it is numerically steady [171, 185].

5- To connect one complete stage or even two stages together, in the case of multistage turbine, Generalized Grid Interface GGI feature of CFX was used [172].

6- To ensure accuracy of the simulation, the average y^+ value was kept about unity as suggested by the theory guide of CFX-Solver [185, 186].

7- Finally, with the physics scheme, the required boundary conditions for the total inlet pressure and temperature values as well as the total or the static outlet pressure were specified [185, 186]. The transport equations of k-ω are as below:

$$\frac{\partial}{\partial t}(\rho k) + \frac{\partial}{\partial x_i}(\rho k u_i) = \frac{\partial}{\partial x_j}\left(\Gamma_k \frac{\partial k}{\partial x_j}\right) + G_k - Y_k + S_K \qquad (4.31)$$

$$\frac{\partial}{\partial t}(\rho \omega) + \frac{\partial}{\partial x_i}(\rho \omega u_i) = \frac{\partial}{\partial x_j}\left(\Gamma_k \frac{\partial \omega}{\partial x_j}\right) + G_\omega - Y_\omega + S_\omega \qquad (4.32)$$

Here, Gk and Gω, characterise turbulence kinetic energy (because of mean velocity gradients) and ω generations respectively and Γk and Γω indicate the effective diffusivity of k and ω respectively. Because of the turbulence flow that needs to be dissipated, the dissipation of k and ω are represented by Yk and Yω respectively.

The model of k-ω, which is based on the SST model, has been considered and that is because this model has the ability to account the turbulent transport of the shear stress and at the same time provides a very precise expectation of the quantity of flow separation which is expected to happen under adverse pressure gradients.

4.3.2.4 Solution Convergence:

In the current analysis and for the sake of accurate results, the residuals were set to be 10^{-6}, 10^{-5} and 10^{-5} for the equations of the energy, continuity and momentum respectively.

The velocity distributions across the model stage for the three turbines, (SSSSAT), (SSDSAT) and SSRT, are given in Figure 4.12 a, b and c respectively. Also, the Blade-to-Blade views for the pressure distribution through the complete turbine, of the three turbines are depicted in Figure 4.13 a, b and c respectively. It is clear from these two figures the variation of flow speed and the pressure through the stator and the rotor for each stage.

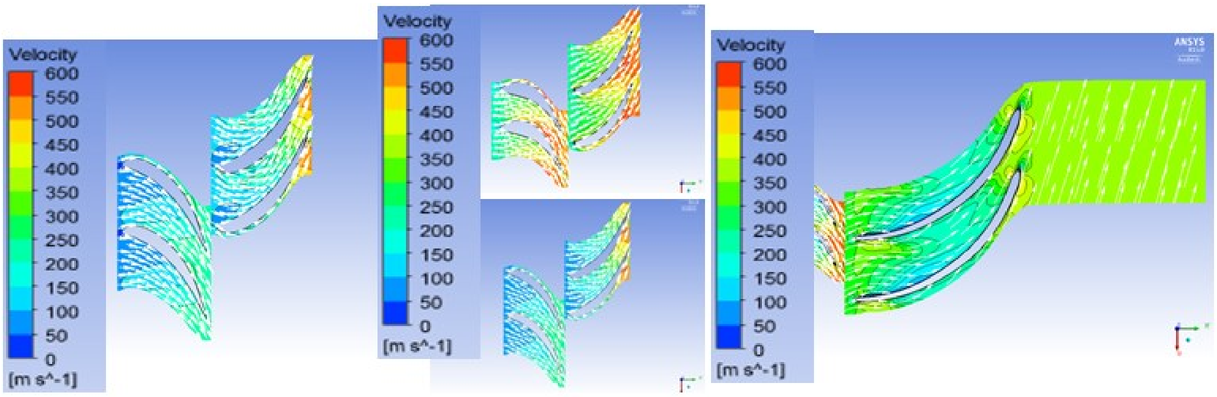

(a) **(b)** **(c)**

Figure 4.12: Velocity distributions (a): (SSSSAT), (b): (SSDSAT), 1st up and (c): (SSRT), [172].

Figure 4.14 shows the temperature distribution for the Blade-to-Blade view of the complete stages of the modelled turbines, where the highest temperature values are located at the stage inlet and the minimum was found at the exit of each turbine stage.

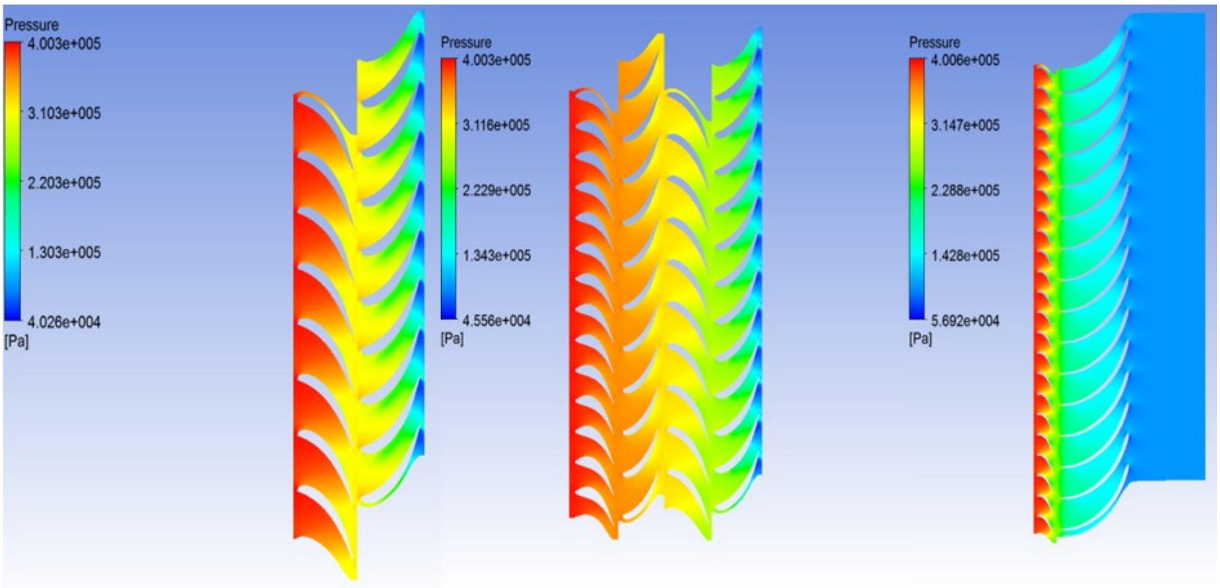

(a) **(b)** **(c)**

Figure 4.13: Stage pressure distributions (a): (SSSSAT), (b): (SSDSAT) and (c): (SSRT), [172].

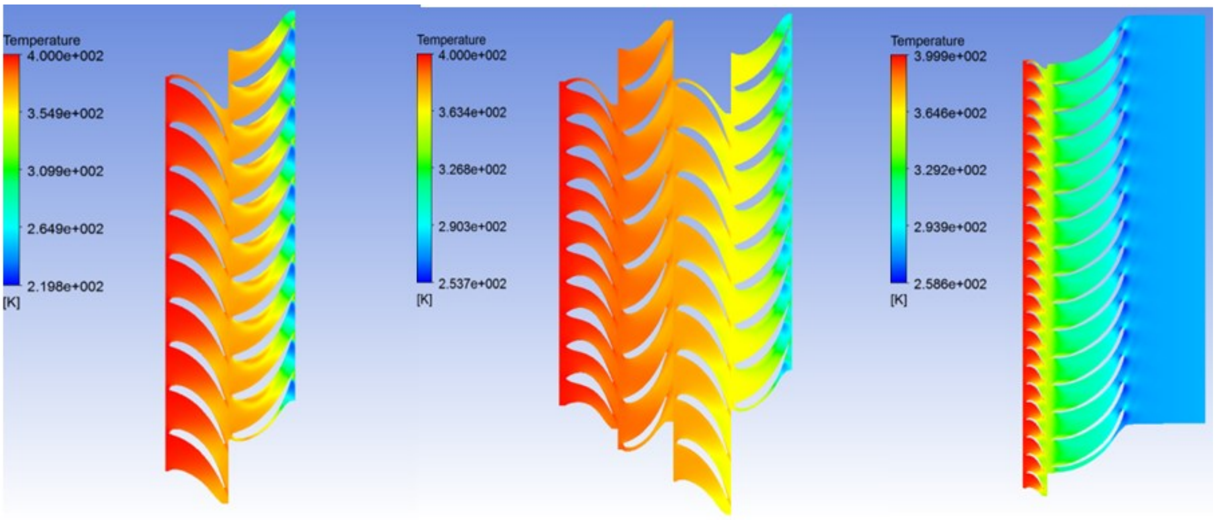

(a) **(b)** **(c)**

Figure 4.14: Stage temperature distributions; (a): (SSSSAT), (b): (SSDSAT) and (c): (SSRT), [172].

4.4 Results and Discussion:

In order to examine the performance of the axial and radial turbines, some geometrical factors (like rotor blades number and stator trailing edge angle) were selected to be examined using (CFD) analysis in the this section. The main aim is to have a good map that shows their influence and then select the most influence ones among them as parameters for the optimization study established in the this chapter.

- The following sections were published in [28, 172].

4.4.1 Geometrical Factors

The influence of four various geometric factors (two in each stator and two in each rotor) on the two turbines' performance are presented in this section [171]. Figure 4.15 a shows the effect of the rotor blades number on the SSRT efficiency and power output. It is clear that the power decreased slowly with increasing the rotor blades number; as a result of the decrease in the mass flow rate. On the other hand, the efficiency reached a maximum (within the studied range) of 82.9%, at blade number equals to 13. Figure 4.15 b shows the effect of varying the trailing edge angle for the stator blade on the output power and efficiency of the (SSRT). It is clear from this figure that the output power increased with decreasing the trailing angle to reach a maximum value of 1.8 kW at angle of 61^{o}. Also, it can be noticed, that the efficiency reached a maximum value at angle of 67^{o} and then decreased with further increase in the angle as a result of cumulative loss generation because of the dissimilarity concerning the angle value with respect to the rotor leading edge angle. Figure 4.16 a demonstrates the variation of output power with the increase in the number of the axial turbine rotor blades. It is clear that the output power decreased from its maximum value of around 3 kW at rotor blade number of 6 to around 1 kW at rotor blade number of 16 as a result of the reduction in the throat area which led to lower mass flow rate value.

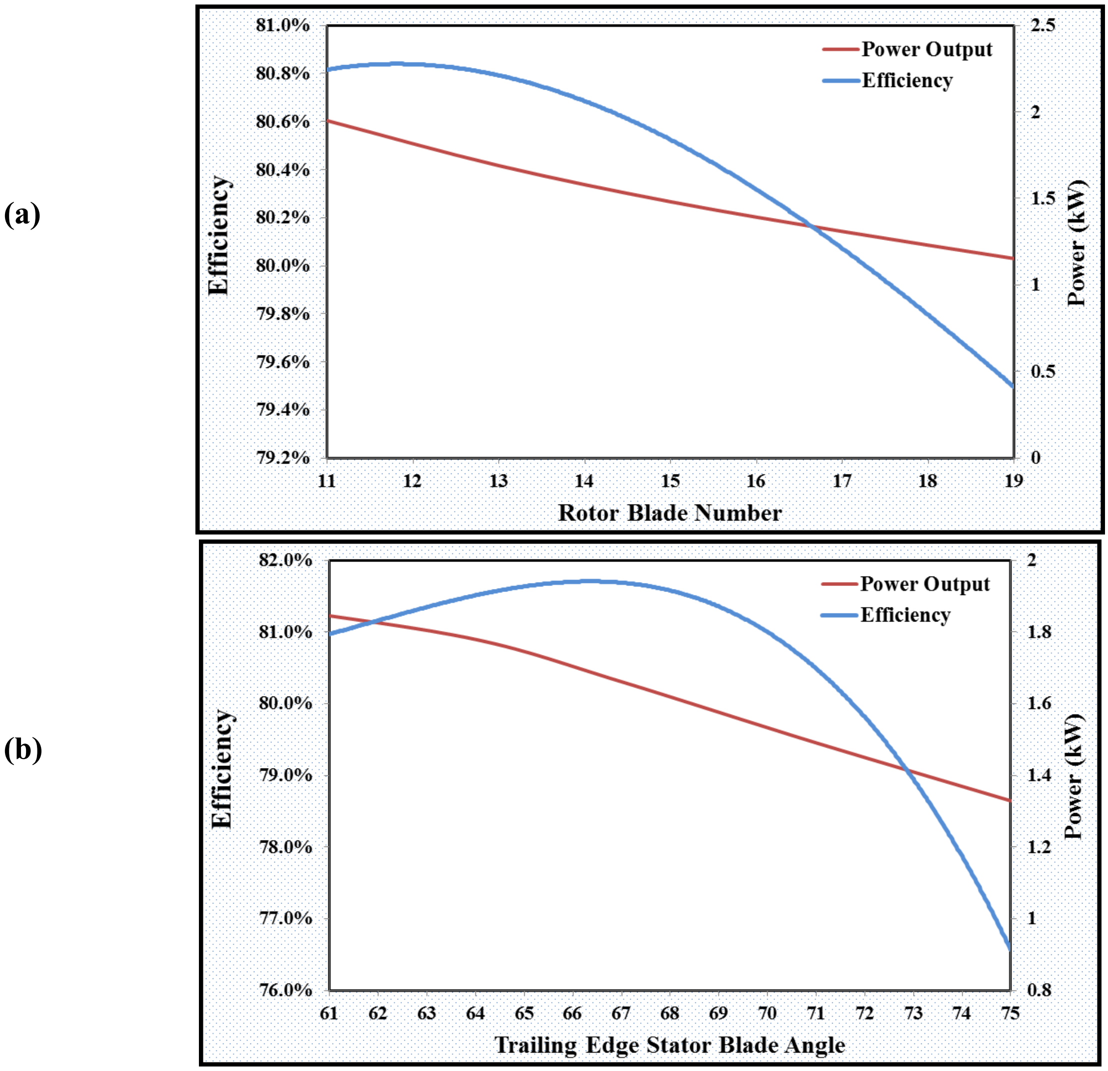

Figure 4.15: The SSRT power output and efficiency at; (a): various rotor blades number and (b): various trailing edge angle values for the stator.

The effect of stator trailing edge angle on the output power and efficiency of the (SSSSAT) is shown in Figure 4.16 b. It is clear from this figure that turbine efficiency reached a maximum of 82.1%, at the angle value of 60^{o} and then it decreased with increasing the angle. This is because of the edge separation between the stator trailing edge and rotor leading edge along the stage which leads to corresponding entropy generation. The results indicate that incidence has a significance influence on the rotor passage flow.

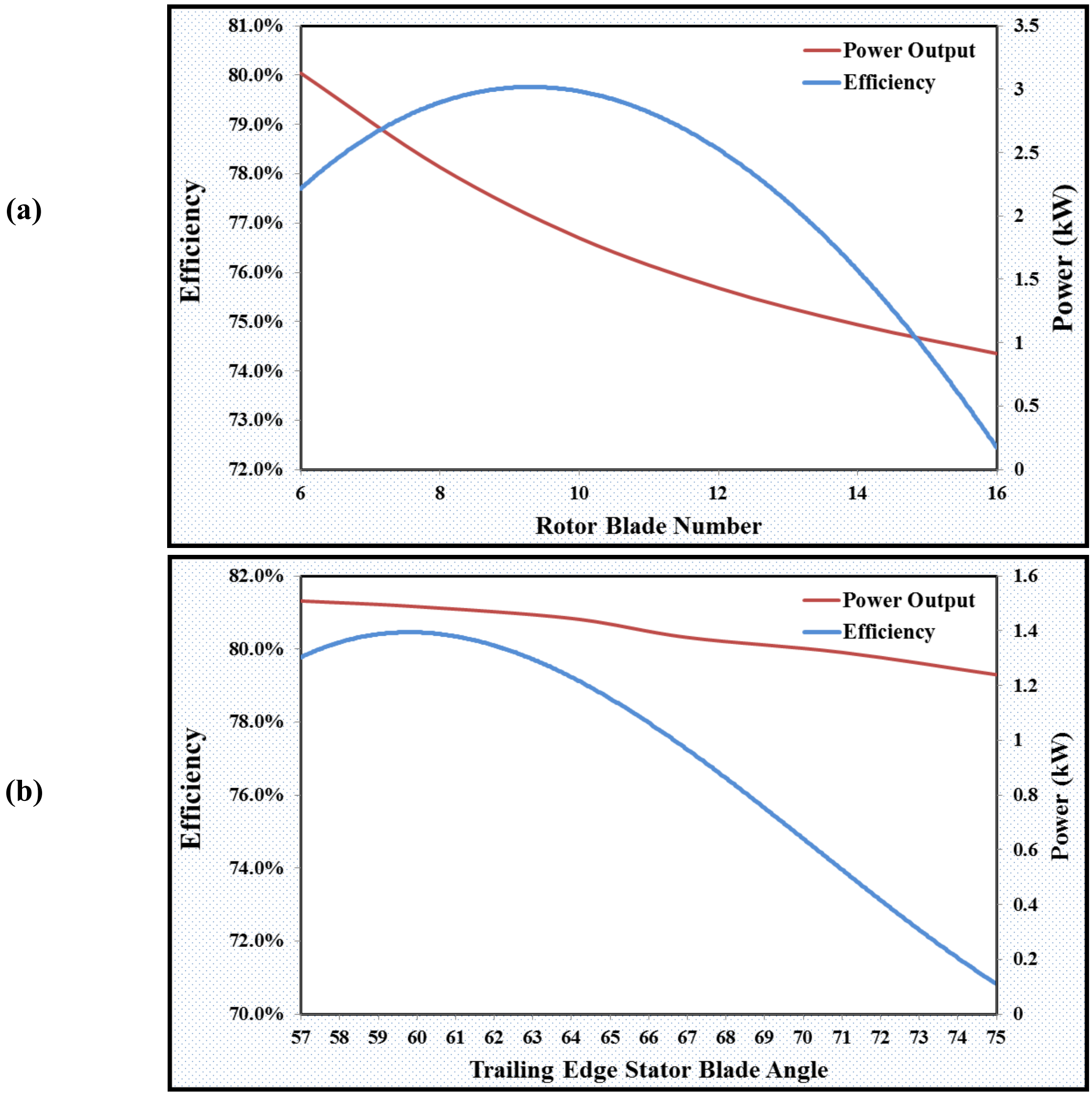

Figure 4.16: The (SSSSAT) power output and efficiency at; (a): various rotor blades number and (b): various trailing edge angle values for the stator.

4.4.2 Boundary Conditions:

In most applications, the developed turbine is not expected to work at its design conditions. Therefore, a detailed assessment of the power generated by each turbine at various pressure ratios and inlet temperatures was conducted. Pressure ratio ranging from 2 to 4 and air inlet temperature ranging from 400 K to 600 K, were used [172].

Generally, the pressure ratio shows almost similar impact on the all studied turbines. Because of the slight difference in the mass flow rate value for each turbine and for the sake of accuracy, specific work was considered [172]. The effect of the rotational speed on the turbine power and efficiency for the three turbines at inlet air temperature of 400 K and a pressure ratio ranging from 2 to 4 is depicted in Figure 4.17 [172].

For all the rotational speeds the (SSSSAT) and the (SSDSAT) showed higher efficiency values than the (SSRT) at all examined inlet temperature values while there were fluctuations in those values for the other two single stage turbines, the axial and the radial. However, the alteration between their efficiency values developed because of the increase in the Mach number at the blade trailing edge which guides to a reduction in the efficiency at high value of pressure ratio. Moreover, it can be seen that there was detraction for the (SSAT) efficiency at higher speed which might be because of the high peripheral speed which makes the exit flow experiencing supersonic flow which might not be the case for the (SSRT). With increasing the value of the rotational speed, the difference between the efficiency trend lines of the other two turbines reduced, until around 105 krpm were they were closely matched. The reason might return to the reduction in both the leakage and secondary losses which occurs at higher rotational speed of (SSRT). The maximum efficiency for (SSSSAT), 84.5%, was at 95 krpm as this rotational speed was within the operational range, whilst for (SSRT) the highest value was noticed to be at 70 krpm, and pressure ratio of 2 with around 81%. However, for the (SSSSAT) and (SSDSAT) the maximum point noticed at 100 krpm with a maximum deviation of around 17 % 9% and 3% for the (SSRT), (SSSSAT) and (SSDSAT) respectively.

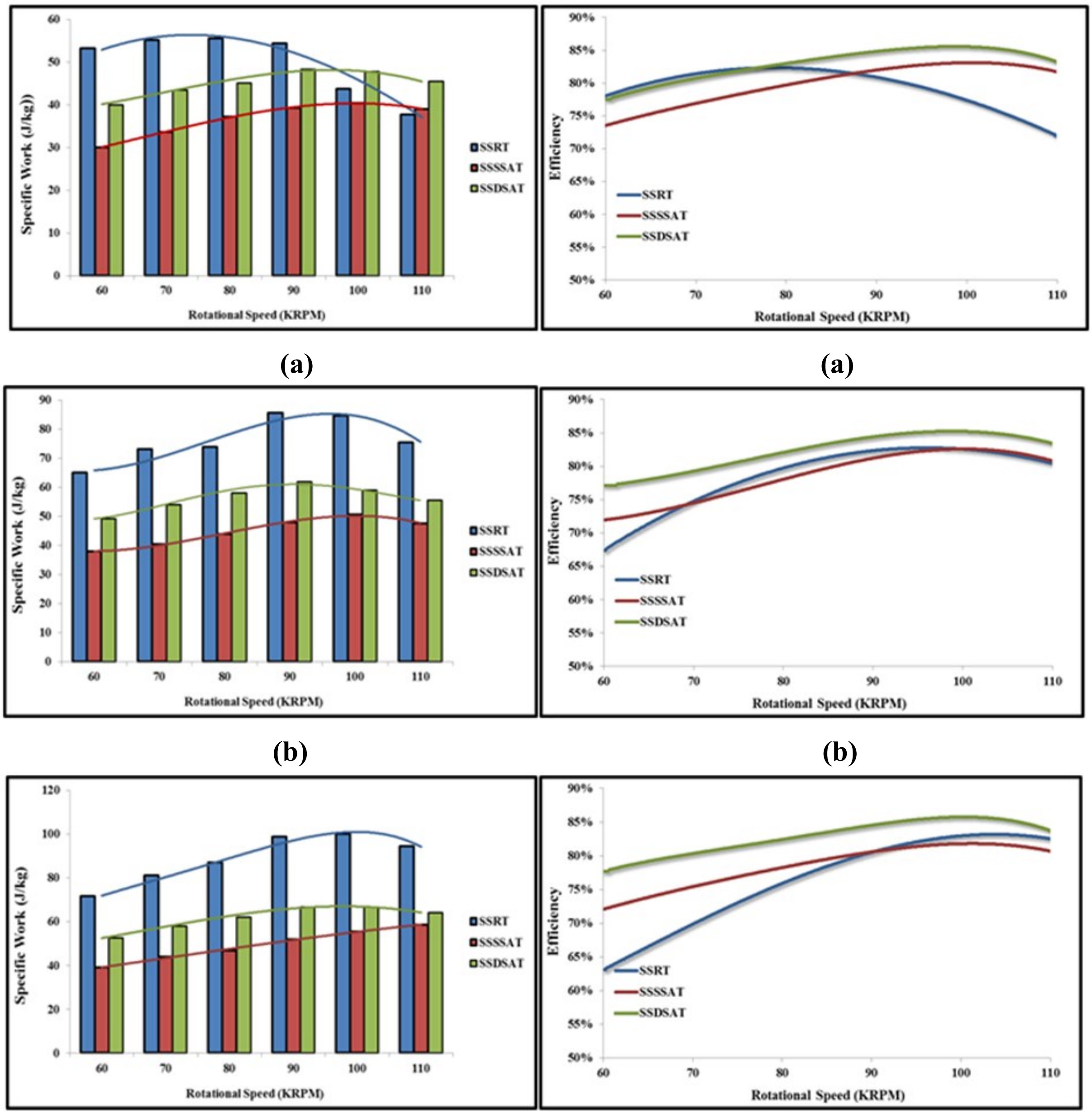

(a) **(a)**

(b) **(b)**

(c) **(c)**

Figure 4.17: Specific work and efficiency for the (SSTs) at 400 K inlet temperature of, various rotational speed and pressure ratio of; (a): 2, (b): 3 and (c): 4 [172].

As for the specific work, it can be seen that the maximum difference in their values was remarked found at lowest rotational speed value, 60 krpm, for the three studied values of pressure ratio [172]. Similar to the efficiency, by increasing the rotor rotational speed the difference between their values tends to reduce, while they were almost matched at and after 107 krpm, as a result of the rapid drop of the SSRT power [172]. In terms of specific work values, at 2 pressure ratio the maximum specific work were about 40 J/kg, 49 J/kg and 55

J/kg at 110 krpm, 90 krpm and 75 krpm for the (SSSSAT), (SSDSAT) and (SSRT) respectively [172]. The corresponding values at 3 and 4 pressure ratios for the three turbines, (SSSSAT), (SSDSAT) and (SSRT), were about 50 J/kg and 58 J/kg, 61 J/kg and 66 J/kg, 85 J/kg and 100 J/kg respectively [172].

Figure 4.18 shows the effect of the rotor rotational speed on both; the power output and the efficiency for each (SSSSAT), (SSSDAT) and (SSRT) at 500 K inlet temperature and pressure ratio ranging between 2 to 4. It is noticed that the efficiency of both the (SSSSAT) and (SSDSAT) had almost similar trend despite the difference in values; while they respectively reached around 79% and 84.5% at a rotational speed of 90 krpm.

The (SSRT) efficiency trend, in contrast, was relatively different where it starts at low efficiency of 67% and then increases to about 81% throughout the examined range of rotational speed and at pressure ratio equals to 2, see Figure 4.18 A. However, this efficiency reached maximum at pressure ratio of 3with about 84.5%. Overall, the (SSDSAT) produced a better performance than the (SSSSAT) and (SSRT) for the wide range of operating design conditions. It can also be seen that after 95 krpm rotational speeds, the efficiency of the (SSRT) was increased as a result of the low leakage and secondary losses at higher values of the rotor rotational speed.

The specific work values at PR of 2 were about 45 J/kg, 57 J/kg and 71 J/kg for the (SSSSAT), (SSSDAT) and (SSRT) respectively. The trends of specific work values for the three turbines were characterized in Figure 4.18 which displays maximum differences of about 15%, 13% and 23% compared to their off design conditions. While, the maximum values of the specific work were approximately 56 J/kg, 76 J/kg and 99 J/kg at 90 krpm, signifying that the SSTs worked at the on design operation.

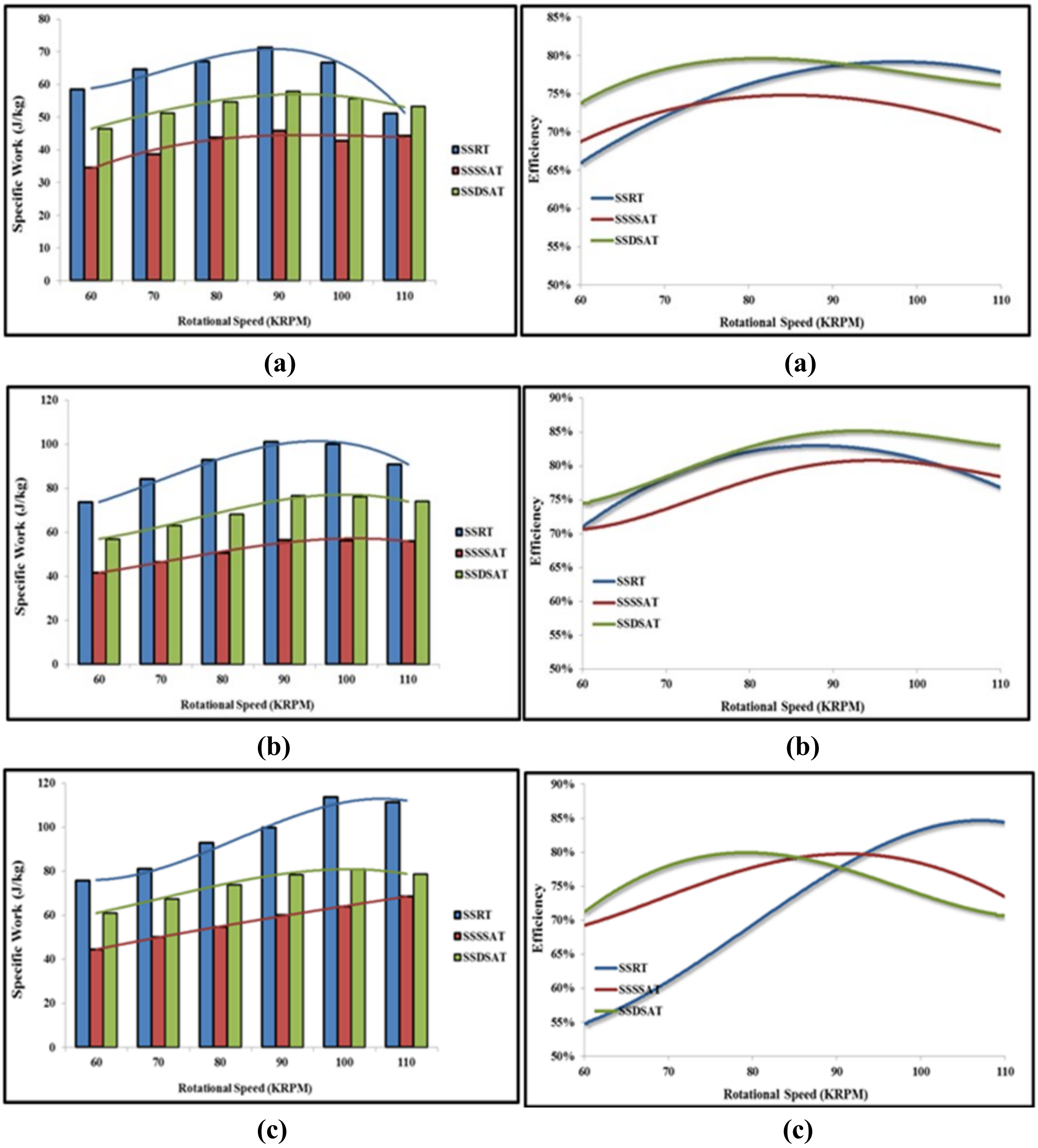

Figure 4.18: Specific work and efficiency for the (SSTs) at 500 K inlet temperature of, various rotational speed and pressure ratio of; (a): 2, (b): 3 and (c): 4, [172].

Figure 4.19 shows the specific work output and efficiency for the three turbines at compressed air with 600 K inlet temperature [172].

In general, the efficiency of the (SSRT) became higher than the other two turbines at this temperature especially at high rotational speed values exceeding 95 krpm. While at PR of 3 and 4 the (SSDSAT) showed comparatively higher values of efficiency between 70 krpm and

90 krpm, the (SSSSAT) showed high efficiency values at 4. At pressure ratio of 2 and 95 krpm the (SSRT) efficiency was around 84.5%; this is because the designed range of the rotational speed, within on design conditions, whereas the maximum of 81%, was noticed at 80 krpm for the (SSDSAT).

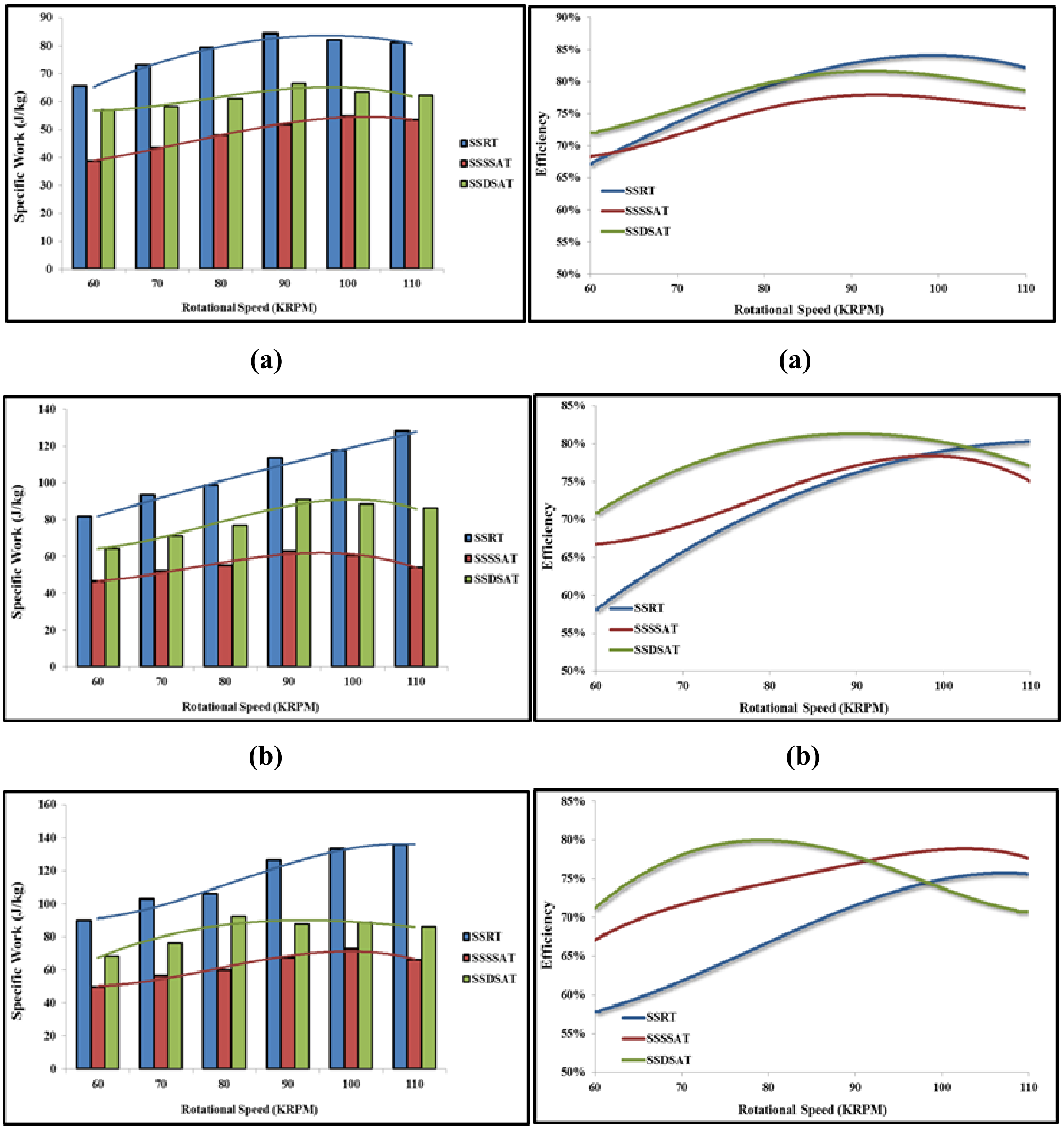

(a) **(a)**

(b) **(b)**

(c) **(c)**

Figure 4.19: Specific work and efficiency for the (SSTs) at 600 K inlet temperature of, various rotational speed and pressure ratio of; (a): 2, (b): 3 and (c): 4, [172].

Similarly, the highest efficiency was at 100 krpm and the maximum deviation from the optimum value was around 11%, 9% and 6% for the (SSRT), (SSSSAT) and (SSDSAT) correspondingly. While the (SSATs) showed better efficiency values but, their specific work values were lower than these of (SSRT) during all the speeds particularly at higher speeds, higher than 95 krpm, as radial turbine can produced higher output power at same mass flowrate especially at high temperatures. The achieved specific work for the (SSRT) was almost double and about 1.7X of that achieved by the (SSSSAT) and (SSDSAT) respectively.

4.4.3 Aerodynamic losses:

Losses in any real system are inevitable [172]. In gas turbines losses are associated with either the turbine structure like the skin friction losses or the flow behaviour of the turbine working fluid like the endwall flows which is one of the forms of the secondary flows which are the main sources of recirculating flow and generating what is known as passage vortex [172]. Also, one of the main limitations in manufacturing and using small scale turbines is the clearances that lead leakage such as the tip leakage losses which affects the amount of pressure losses and as a result the turbines efficiencies. Figure 4.20 shows the difference between the two flow behaviours and the entropy generation which is considered as an indicator of losses and leads to decrease the turbine efficiency. Like this flow behaviour occurs mainly in the radial flow turbines as a result of their blades’ complexity compared to the axial flow turbines [172]. To tackle these problems, both; the blade geometry and the rotor rotational speed need to be carefully studied [172]. In this section, a brief study on some types of losses such as the trailing edge and the tip clearance as well as evaluating the overall losses in terms of the loss coefficient have also been carried out [172].

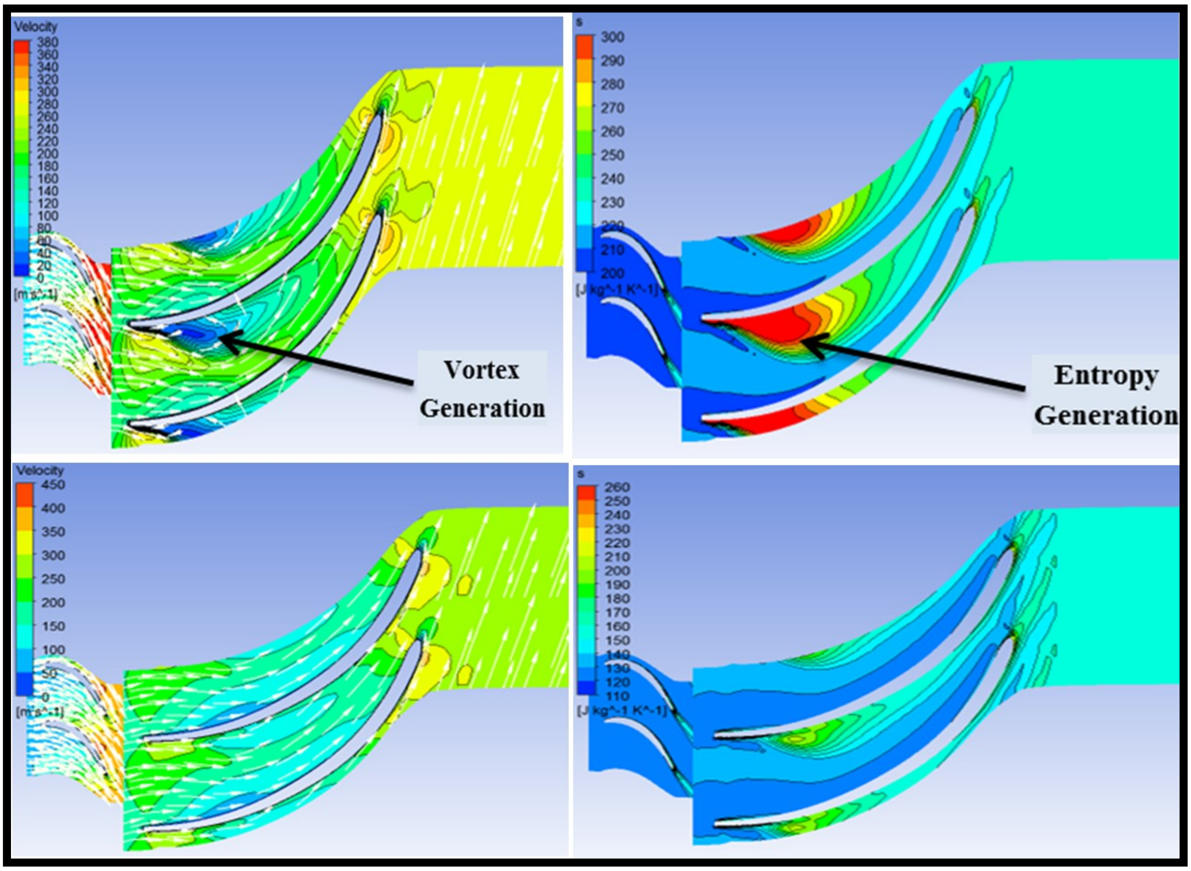

Figure 4.20: Velocity distribution (LHS) and entropy generation (RHS) for two different flow speeds [172].

4.4.3.1 Tip Clearance and Trailing Edge Losses:

In this section, the effects of the stator trailing edge and the rotor shroud tip clearance on the amount of losses for the (SSDSAT) and (SSRT) are carried out. These factors were selected in order to investigate because of the connection between the two stages of the (SSDSAT) [172]. For the sake of comparison, the SSRT was also included. It is worth to mention that this analysis has been done at only one boundary condition i.e. the nominal design condition for the sake of abbreviation [172]. It is clear from Figure 4.21 that the efficiency and the power output of each stage alone was higher with low tip clearance and lower values of stator trailing edge, while the dual stage turbine showed higher influence to the stators' trailing edge than those of the rotors' tip clearance [172].

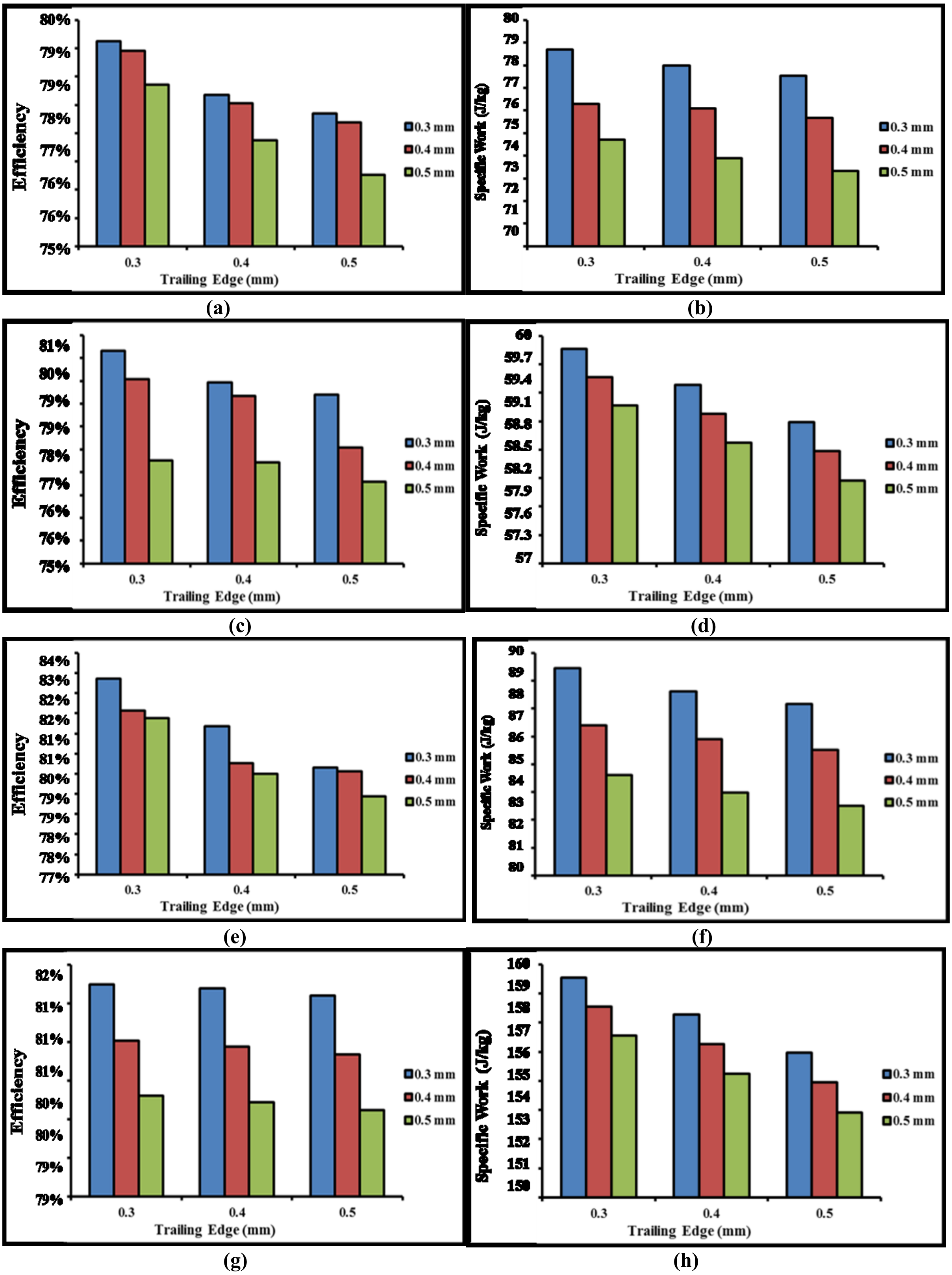

Figure 4.21: The effect of stators' trailing edge values and tip clearance values on the efficiency and power of the first stage of the (DSAT) (a& b), the second stage (c& d), the all (DSAT) (e& f) and the (SSRT) (g& h), at 90 krpm, temperature of 500 K and (PR) of 3 [172].

Therefore it is important to match the stator trailing edge of the first stage with the rotor leading edge of the second stage resulting in secondary losses which arise during the flow turning inside the passage [172]. The other outcome from this investigation is that while the efficiency of each stage separately was relatively higher influenced than the dual stage. On the other hand, the rotor's tip clearance was by far the most influential parameter on the performance of the (SSRT) [172] as there is only single stage radial turbine analysed in this study.

In terms of efficiency values, it can be seen that while the maximum difference in the efficiency values in each stage separately was around 1.4 % when tip clearance increased from 0.3 to 0.4 mm Figure 4.21 a and c, this difference was less than 1% in the dual stage Figure 4.21e [172]. Similarly the efficiency of each stage separately was around 1.25 % when trailing edge thickness became 0.5 mm while this factor produced larger effect on the dual stage efficiency when the relevant difference in the efficiency was about 2.4 % [172]. This however, indicates the importance of matching the trailing edge of the first stage rotor, which was fixed at 0.3 mm during this study, with the leading edge values of the second stage stator. The corresponding figures of the power output of each stage separately as well as the dual stage have also been included in Figure 4.21. Similarly, the maximum loss in the efficiency value in the SSRT was less than 0.25 % by increasing the stator trailing edge but this value became around 1.6 % with increasing the rotor tip clearance Figure 4.21g. The increment of trailing edge and tip clearance to 0.5 mm each resulted in decreasing the power output by 7 and 5 J/kg respectively Figure 4.21h.

4.4.3.2 Losses Coefficient:

Finally the overall loss coefficients of each of the three configurations at different boundary conditions have been briefly discussed in this section [172]. In turbines, losses can be divided to those which take place in the stator and those that happen in the rotor, more details can be found in [114, 175, 187-190]. In this analysis the loss coefficients in terms of pressure losses for each of the three turbines and at different boundary conditions is evaluated and discussed [172]. Figure 4.22 shows the pressure loss coefficients for both the stator and rotor of each of the three investigated turbines for the various investigated boundary conditions It can be seen from this figure that by increasing each the fluid inlet pressure and temperature, the value of pressure coefficient increases [172].

4.4.3.3 Selecting the Turbine:

As it shown from the previous analysis, the radial turbine has shown superiority in terms of the amount of the developed out power at low mass flow rate compared to the other two turbines. Moreover, the radial turbine shows higher efficiency at high rotational speeds where the opposite was the case for the other two configurations of the axial turbine at relatively low rotational speeds [28]. Furthermore, the (SSRT) experienced showed the lowest values for the rotor total loss coefficients at certain rotational speed values.

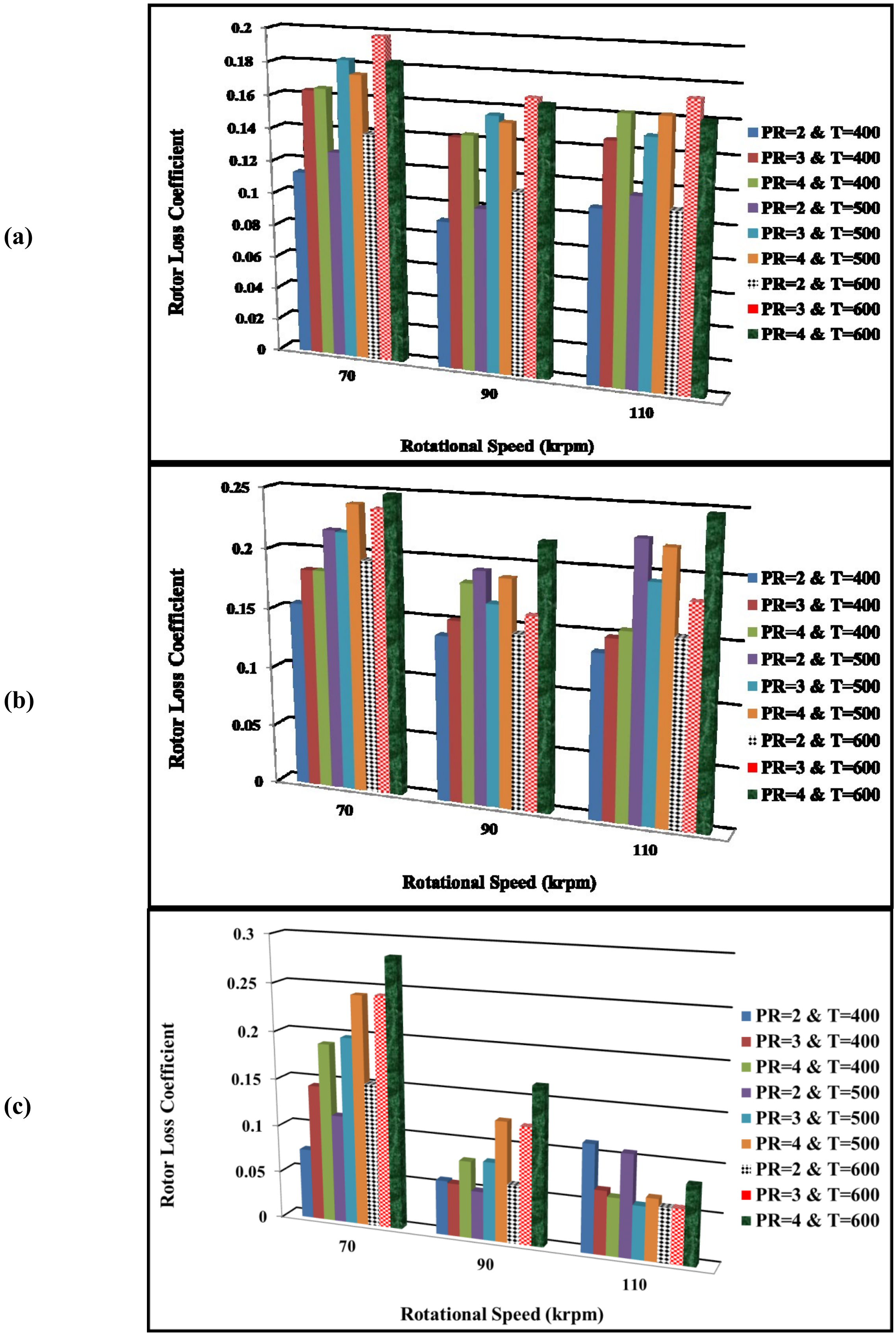

Figure 4.22: Rotor total loss coefficient during the all studied boundary conditions for the (SSSSAT), (SSDSAT) and (SSRT) (a), (b) and (c) respectively, [172].

4.5 Turbine Optimization:

Engineers still need to search for the best design among the available possible designs. Yet, the term ‘best’ can come with many meanings and what is excellent in some terms or applications may not be the best in other applications; thereby this term does not have an absolute meaning [171]. Therefore, understanding the optimization procedure in depth will certainly lay the groundwork for optimization of the turbines; especially the Small Scale Turbines SSTs whose sizes might add to the challenge of their optimization [171].

4.5.1 Optimization Background:

The word “optimum”, which is a Latin word, means “the ultimate ideal;” likewise the word, “optimus” means “the best” [191]. The idea of optimization was firstly established in 1940 by George Danjxign who developed a linear program for military applications. This was achieved through translating the idea of optimization to firstly a mathematical model then identifying through decision making tool in which activities can be controlled and which activities have influence on the results. Such activities, which are associated with variables, are in fact achieved before identifying other constants quantities. Then vectorisation of the problem using the variable values to determine whether maximization or minimization is required, depending on what is known as the objective function. Importantly, the level of the required activity should not be arbitrarily chosen as such problem needs to be associated with other relevant requirements’ availability such as time, computational cost, labs etc. [191].

In general, optimization problems can be classified to four types, linear when the variables and constraints are linear; nonlinear in case they are nonlinear; discrete problems and continuous problems [192]. Optimization methods can also be classified depending on whether there are optimal solutions or not as exact optimization methods or heuristic optimization [192].

4.5.2 General Optimization Approaches:

In order to achieve the required “optimum” solution, a suitable approach is essential to be followed. There are four different approaches in optimization, these can be summarised as analytical methods, graphical methods, experimental methods and numerical methods. Each one of these methods has its advantages and disadvantages and as a result can only be applied for specific applications [193].

4.5.2.1 Analytical Method:

This method uses the classical procedures of differential calculus where the optimum value can be determined by calculating the parameters’ values i.e. $x_1, x_2, . . . , x_n$ that cause the derivatives of the function ($fx_1, fx_2, . . . , fx_n$) with respect to $x_1, x_2, . . . , x_n$ to assume zero values. There is no need, in using these methods, for using digital computers as it can be described in mathematical terms before applying the rules of calculus. The main disadvantages for these methods are the fact that they are unsuitable for the highly nonlinear problems or in case of using more than three independent parameters [194, 195].

4.5.2.2 Graphical Method:

This method is based on plotting the function to be minimized or maximized thus it is limited to variables’ number of two. If the function depends on one or two variables, for example, x_1, a plot of $f(x_1)$ versus x_1 will directly make the minima and/or maxima of the function known otherwise, a set of contours can be built when there are two variables [194, 195].

4.5.2.3 Experimental Method:

The procedure followed in the experimental methods is that, when setting up the system, each variable has to be adjusted with monitoring the system performance in order to determine the optimum or near the optimum values. As some systems have two or more variables affecting each other and those values have to be adjusted simultaneously (to get the optimum performance), these method can lead to unreliable results which is considered the main drawback of such method [194, 195].

4.5.2.4 Numerical Methods:

This approach is the most important one as an iterative procedure is utilized to produce the required improved solutions, starting from the initial estimated solutions, for the problem that needs to be optimized. With recent advances in computers, this optimization method is becoming highly used for various applications particularly when complex, multi variable optimization problem is considered [194, 195].

4.5.3 Optimization Categories:

There are different types of procedures followed when designers want to optimize a specific model. In turbomachinery particularly, each one of those types has its power and it can be useful at a specific application which depends on the designers' requirements. In the next sub sections an explanation on the main types of optimization has been given.

4.5.3.1 Single Objective Optimization:

This type of optimization uses only one objective as being the main required output parameter. So, the values of many input parameters can be changed with the aim of enhancing or finding the best value of one output parameter, the objective. As an example the turbine's efficiency can be considered the designers main concern regardless of other outputs like the power generated or size.

4.5.3.2 Multi Objective Optimization:

In contrast to single objective optimization, multi objective optimization is based on using more than one objective function to be optimised. This type of optimization can be defined as the problem of discovering a vector of chosen variables that fulfils constraints and at the same time optimize a vector function whose elements characterise the objective functions [196]. Normally, this type of optimization is preferable for real-life engineering problems because it offers a better performance enhancement [197].

4.5.4 Turbine Optimization Methodology:

In the previous sections ANSYS Academic 15 VISTA, was used to develop an initial design of the SSRT. Then (3D CFD) modelling was used to enhance the (SSRT) using ANSYS15 CFX tool, through investigating the effect of various geometrical parameters like the stator trailing edge, the blade number and the operating conditions on the turbine efficiency and power output [172].

The following sections of this chapter are focusing on the SSRT optimization. Firstly, one dimensional optimization, using the mean line design results, has been conducted for the rotor only. Once the best shape for each; the stator part and rotor part was attained, a number of high impact parameters were recognized and selected to optimize the complete shape of the (SSRT) blades using the 3D Design Exploration feature of ANSYS15 which utilised a genetic algorithm for the multi objective optimization [171]. Two optimization techniques were used namely the direct method and the Response Surface Optimization RSO. While both of them are multi objective optimization methods, the main difference between them are the parameters number which can be used during the optimization. The latter allows for only 20 parameters and was utilised to confirm the achieved results whereas the direct optimization is able to include more than 20 parameters during the optimization process. Additionally, the results were directly inputted to the cycle analysis code using Engineering Equation Solver EES code [198], similar to the analysis achieved in 4.2.

4.6 1D Optimization Approach in ANSYS:

4.6.1 Procedure

Figure 4.23 shows the velocity triangles and a meridional shape for the rotor developed using the Vista RTD in ANSYS Academic Workbench, where this shape is largely affected by factors like mass flow rate, pressure ratio, flow coefficient and the rotational speed. Vista RTD Radial Turbine Design tool is 1D design analysis for the radial turbine which enables a quick evaluation of the initial model performance and also understanding the effect of some geometrical parameters on the model behaviour. Using this approach enables the researcher from choosing the most influential factors and nominating them as parameters in order to develop the model output in a relatively quick and trustful way. In next subsections, a detailed explanation for the procedure followed in this analysis is given.

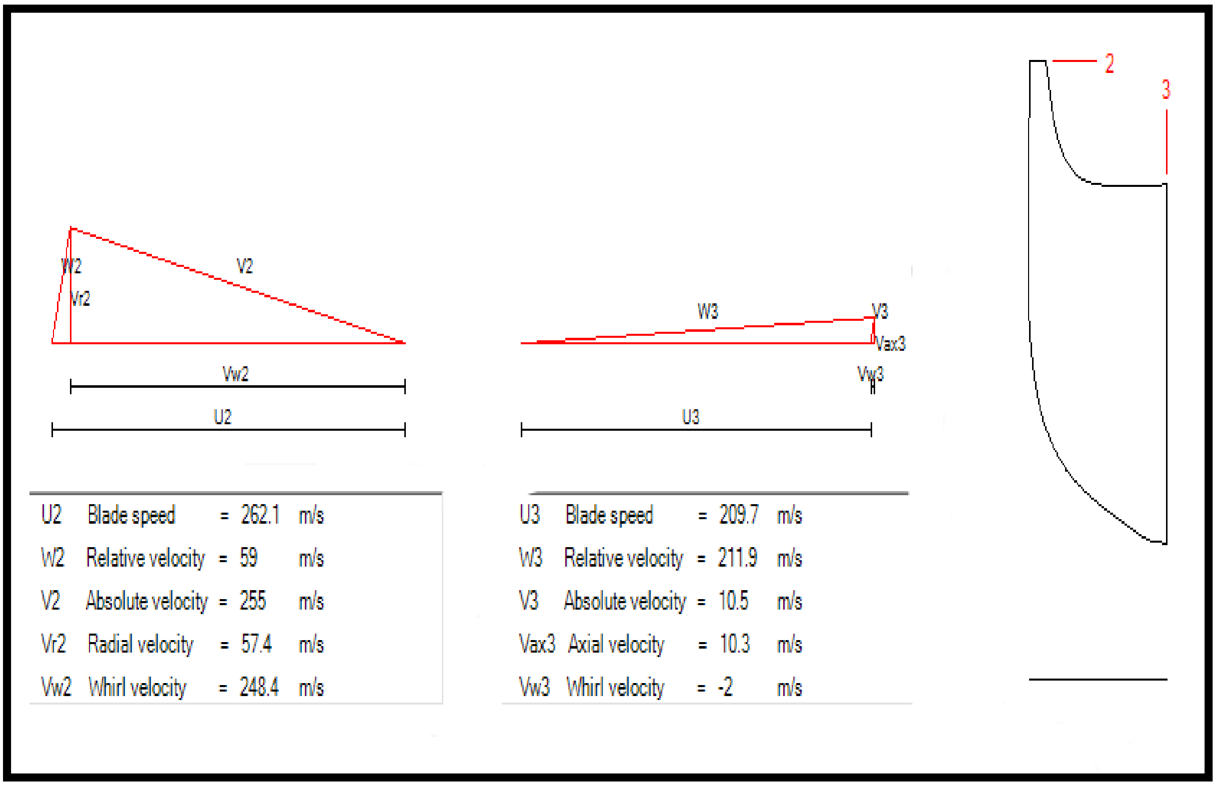

U2 Blade speed = 262.1 m/s
W2 Relative velocity = 59 m/s
V2 Absolute velocity = 255 m/s
Vr2 Radial velocity = 57.4 m/s
Vw2 Whirl velocity = 248.4 m/s

U3 Blade speed = 209.7 m/s
W3 Relative velocity = 211.9 m/s
V3 Absolute velocity = 10.5 m/s
Vax3 Axial velocity = 10.3 m/s
Vw3 Whirl velocity = -2 m/s

Figure 4.23: Velocity triangles and a meridional figure for the rotor using the Vista RTD in ANSYS15 Workbench.

4.6.1.1 1D Design Variables:

The first step is to identify the factors or the variables which will be included in the study in order to generate different design models during the optimization process. The criterion of choosing the variables number and their types (geometrical or operating conditions) depends on the researchers' requirements as this can directly affect the model performance and the computational cost. In this study the variables used are listed in Table 4.3.

Table 4.3: Design variables used in Vista RTD 1D optimization.

Design Variable Number (Unit)	Design Variable Name	Optimization Classification	Optimization Limits	Type
1 (kg/s)	Mass flow rate	Continuous	0.020-.033	Input
2 (Deg.)	Absolut Inlet Flow Angle	Continuous	65-79	Input
3 (Deg.)	Absolut Outlet Flow Angle	Continuous	-25-0	Input
4 (-)	Rotor Blade Number	Discrete	11, 13, 15, 17	Input
5 (-)	Shroud Exit/Inlet Radius Ratio	Continuous	0.7-0.83	Input
6 (-)	Hub Exit/Inlet Radius Ratio	Continuous	0.2-0.24	Input
7 (W)	Power Output	-	-	Output
8 (-)	Rotor Efficiency	-	-	Output
9 (-)	Stage Efficiency	-	-	Output
10 (mm)	Rotor Tip Width	-	-	Output
11 (-)	Nozzle Choke Ratio	-	-	Output

4.6.1.2 1D Design Constraints:

The second step is to decide whether there are constraints or not. In this optimization the constraints were chosen to make the rotor manufacturable. Other constraints might be the working fluid mass flowrate value, the turbine power output or the rotor blade number. Here, it is important to mention that it is possible to use the tip width (defined previously) and nozzle choke ratio, mentioned in the table above, as constraints.

4.6.1.3 1D Variable Limits:

Figure 4.24 shows a screen shot of the design variables and their arbitrary distribution. The design variables range for each parameter is bounded by upper and lower limits of variables. Otherwise, the optimization process will be continuing without reaching the final values. On the other hand if the chosen limit was low, this might give the optimum values which were found within the small specified limit, however, better than the selected (optimum values) might be outside the chosen limits. In contrast, working with large limits, will be computationally cost and time consuming. So, choosing the appropriate limit which shows the highest impact on the required objective function and at the same time within the range is extremely important.

4.6.1.4 1D Objective Function:

The main goal of optimization can be specified using objective function. This objective might be more than one where maximizing the rotor output power and efficiency were both specified as the objective function as in this study. Here it is worth mentioning that it is also possible for one output parameter to be more objective than others (priority).

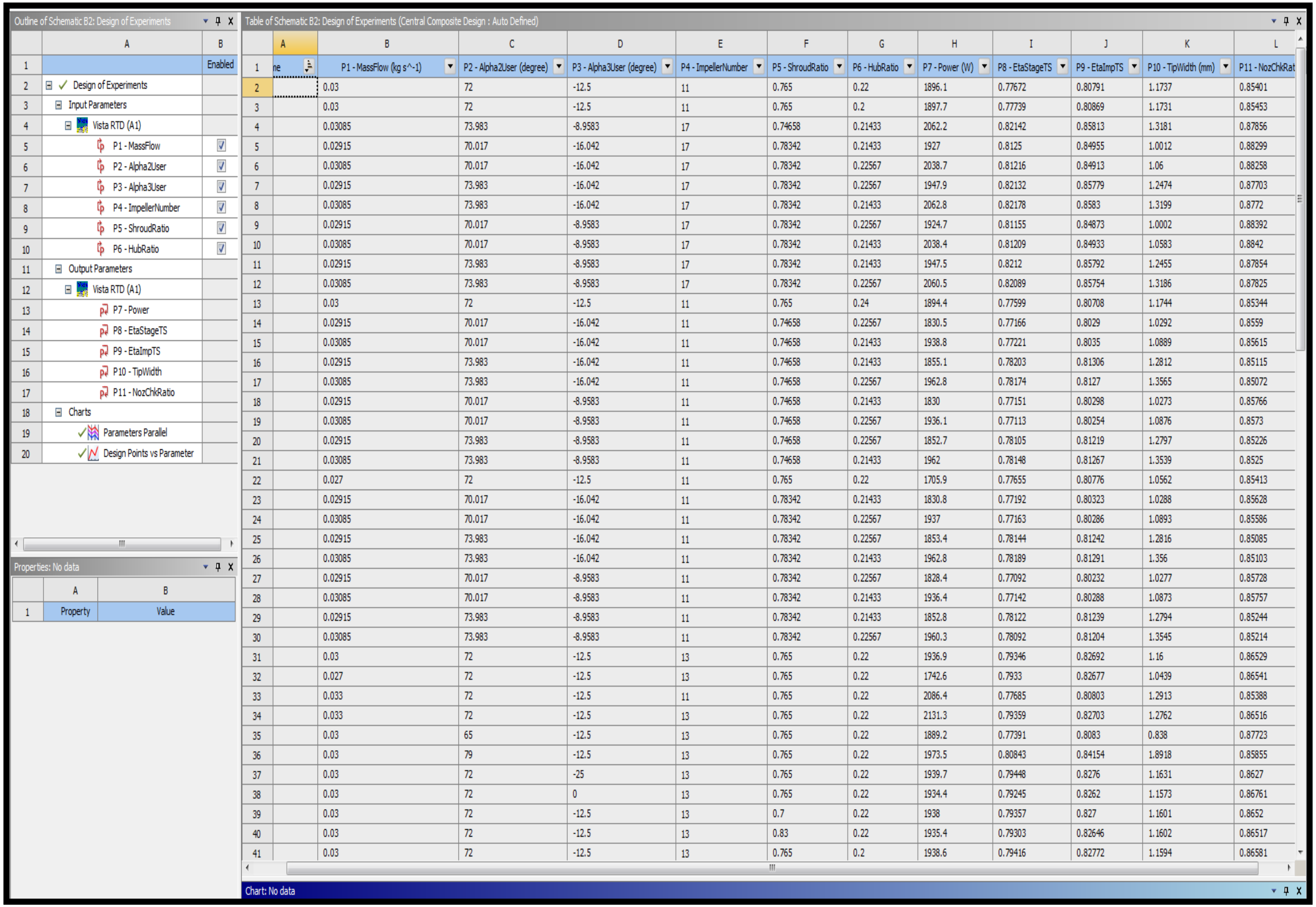

Outline of Schematic B2: Design of Experiments

	A	B
1		Enabled
2	⊟ ✓ Design of Experiments	
3	⊟ Input Parameters	
4	⊟ Vista RTD (A1)	
5	P1 - MassFlow	☑
6	P2 - Alpha2User	☑
7	P3 - Alpha3User	☑
8	P4 - ImpellerNumber	☑
9	P5 - ShroudRatio	☑
10	P6 - HubRatio	☑
11	⊟ Output Parameters	
12	⊟ Vista RTD (A1)	
13	P7 - Power	
14	P8 - EtaStageTS	
15	P9 - EtaImpTS	
16	P10 - TipWidth	
17	P11 - NozChkRatio	
18	⊟ Charts	
19	✓ Parameters Parallel	
20	✓ Design Points vs Parameter	

Properties: No data

	A	B
1	Property	Value

Table of Schematic B2: Design of Experiments (Central Composite Design : Auto Defined)

	A	B	C	D	E	F	G	H	I	J	K	L
1	ne	P1 - MassFlow (kg s^-1)	P2 - Alpha2User (degree)	P3 - Alpha3User (degree)	P4 - ImpellerNumber	P5 - ShroudRatio	P6 - HubRatio	P7 - Power (W)	P8 - EtaStageTS	P9 - EtaImpTS	P10 - TipWidth (mm)	P11 - NozChkRat
2		0.03	72	-12.5	11	0.765	0.22	1896.1	0.77672	0.80791	1.1737	0.85401
3		0.03	72	-12.5	11	0.765	0.2	1897.7	0.77739	0.80869	1.1731	0.85453
4		0.03085	73.983	-8.9583	17	0.74658	0.21433	2062.2	0.82142	0.85813	1.3181	0.87856
5		0.02915	70.017	-16.042	17	0.78342	0.21433	1927	0.8125	0.84955	1.0012	0.88299
6		0.03085	70.017	-16.042	17	0.78342	0.22567	2038.7	0.81216	0.84913	1.06	0.88258
7		0.02915	73.983	-16.042	17	0.78342	0.22567	1947.9	0.82132	0.85779	1.2474	0.87703
8		0.03085	73.983	-16.042	17	0.78342	0.21433	2062.8	0.82178	0.8583	1.3199	0.8772
9		0.02915	70.017	-8.9583	17	0.78342	0.22567	1924.7	0.81155	0.84873	1.0002	0.88392
10		0.03085	70.017	-8.9583	17	0.78342	0.21433	2038.4	0.81209	0.84933	1.0583	0.8842
11		0.02915	73.983	-8.9583	17	0.78342	0.21433	1947.5	0.8212	0.85792	1.2455	0.87854
12		0.03085	73.983	-8.9583	17	0.78342	0.22567	2060.5	0.82089	0.85754	1.3186	0.87825
13		0.03	72	-12.5	11	0.765	0.24	1894.4	0.77599	0.80708	1.1744	0.85344
14		0.02915	70.017	-16.042	11	0.74658	0.22567	1830.5	0.77166	0.8029	1.0292	0.8559
15		0.03085	70.017	-16.042	11	0.74658	0.21433	1938.8	0.77221	0.8035	1.0889	0.85615
16		0.02915	73.983	-16.042	11	0.74658	0.21433	1855.1	0.78203	0.81306	1.2812	0.85115
17		0.03085	73.983	-16.042	11	0.74658	0.22567	1962.8	0.78174	0.8127	1.3565	0.85072
18		0.02915	70.017	-8.9583	11	0.74658	0.21433	1830	0.77151	0.80298	1.0273	0.85766
19		0.03085	70.017	-8.9583	11	0.74658	0.22567	1936.1	0.77113	0.80254	1.0876	0.8573
20		0.02915	73.983	-8.9583	11	0.74658	0.22567	1852.7	0.78105	0.81219	1.2797	0.85226
21		0.03085	73.983	-8.9583	11	0.74658	0.21433	1962	0.78148	0.81267	1.3539	0.8525
22		0.027	72	-12.5	11	0.765	0.22	1705.9	0.77655	0.80776	1.0562	0.85413
23		0.02915	70.017	-16.042	11	0.78342	0.21433	1830.8	0.77192	0.80323	1.0288	0.85628
24		0.03085	70.017	-16.042	11	0.78342	0.22567	1937	0.77163	0.80286	1.0893	0.85586
25		0.02915	73.983	-16.042	11	0.78342	0.22567	1853.4	0.78144	0.81242	1.2816	0.85085
26		0.03085	73.983	-16.042	11	0.78342	0.21433	1962.8	0.78189	0.81291	1.356	0.85103
27		0.02915	70.017	-8.9583	11	0.78342	0.22567	1828.4	0.77092	0.80232	1.0277	0.85728
28		0.03085	70.017	-8.9583	11	0.78342	0.21433	1936.4	0.77142	0.80288	1.0873	0.85757
29		0.02915	73.983	-8.9583	11	0.78342	0.21433	1852.8	0.78122	0.81239	1.2794	0.85244
30		0.03085	73.983	-8.9583	11	0.78342	0.22567	1960.3	0.78092	0.81204	1.3545	0.85214
31		0.03	72	-12.5	13	0.765	0.22	1936.9	0.79346	0.82692	1.16	0.86529
32		0.027	72	-12.5	13	0.765	0.22	1742.6	0.7933	0.82677	1.0439	0.86541
33		0.033	72	-12.5	11	0.765	0.22	2086.4	0.77685	0.80803	1.2913	0.85388
34		0.033	72	-12.5	13	0.765	0.22	2131.3	0.79359	0.82703	1.2762	0.86516
35		0.03	65	-12.5	13	0.765	0.22	1889.2	0.77391	0.8083	0.838	0.87723
36		0.03	79	-12.5	13	0.765	0.22	1973.5	0.80843	0.84154	1.8918	0.85855
37		0.03	72	-25	13	0.765	0.22	1939.7	0.79448	0.8276	1.1631	0.8627
38		0.03	72	0	13	0.765	0.22	1934.4	0.79245	0.8262	1.1573	0.86761
39		0.03	72	-12.5	13	0.7	0.22	1938	0.79357	0.827	1.1601	0.8652
40		0.03	72	-12.5	13	0.83	0.22	1935.4	0.79303	0.82646	1.1602	0.86517
41		0.03	72	-12.5	13	0.765	0.2	1938.6	0.79416	0.82772	1.1594	0.86581

Chart: No data

Figure 4.24: Screen shot of the design variables and their arbitrary distribution.

4.6.1.5 Solution of 1D Optimization:

For the current results, it can be seen from Figure 4.24 and Figure 4.25 that more than 100 design points have been initiated in order to cover the range of each specified input design parameter.

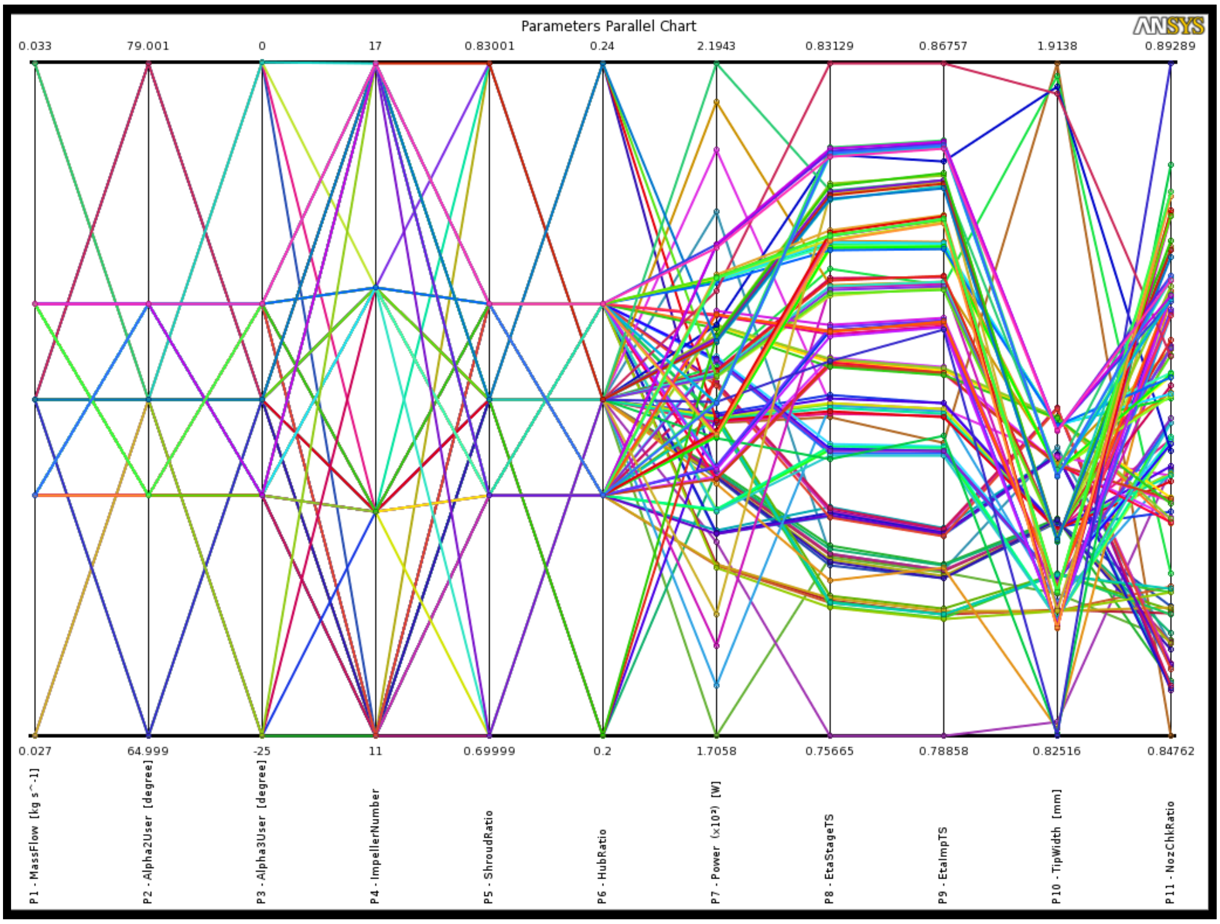

Figure 4.25: Parameters parallel chart for the 1D optimization.

4.6.1.6 Response of 1D Optimization:

Figure 4.26 explains how each of the output parameter was influenced by the input parameters separately, with other input parameters were fixed. For example, it is clear that the mass flow rate was the most effective input parameter on the power output and tip width values with around 81% and 19% respectively, while it showed lower effect on the nozzle choke ratio. In contrast, the inlet flow angle affects all output parameters including the nozzle choke ratio, the tip width, the rotor efficiency, the overall stage efficiency and the power output showing a sensitivity of 75%, 81%, 90%, 90% and 18% respectively. As a result only the most sensitive parameters will be discussed.

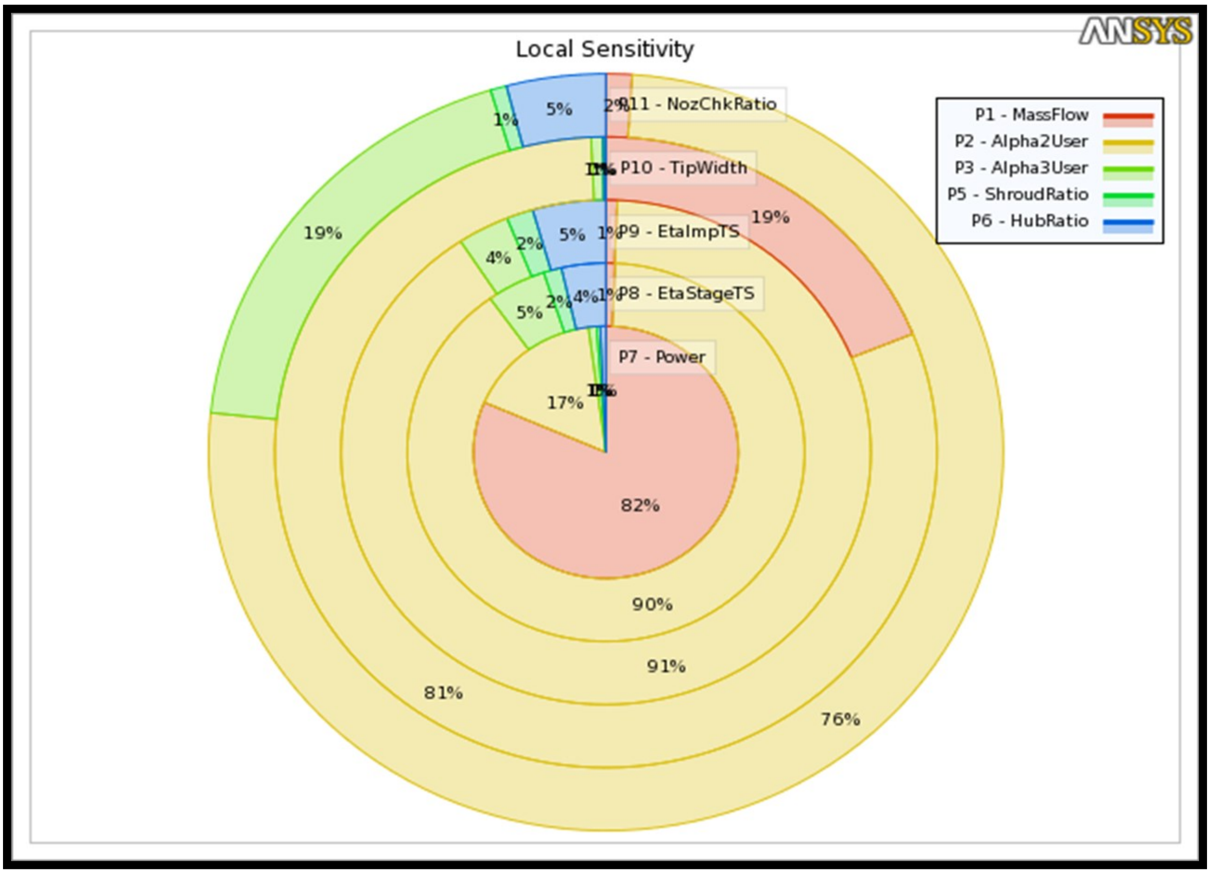

Figure 4.26: The local sensitivity of the outlet parameters with respect to the inlet parameters.

In Figure 4.27 the effect of the rotor inlet flow angle and mass flow rate values on the rotor efficiency is presented. From this figure it is evidence that up to 87% rotor efficiency can be achieved at inlet flow angle of 77^{o} at rotor blade number of 13 and it reaches 90.6% when increasing it to 17.

Figure 4.28 presents the effect of the two mentioned input parameters on the amount of power output at rotor blade number of 17 where the maximum value of about 1.93 kW was achieved at inlet and outlet flow angles of 79^{o} and -25^{o} respectively.

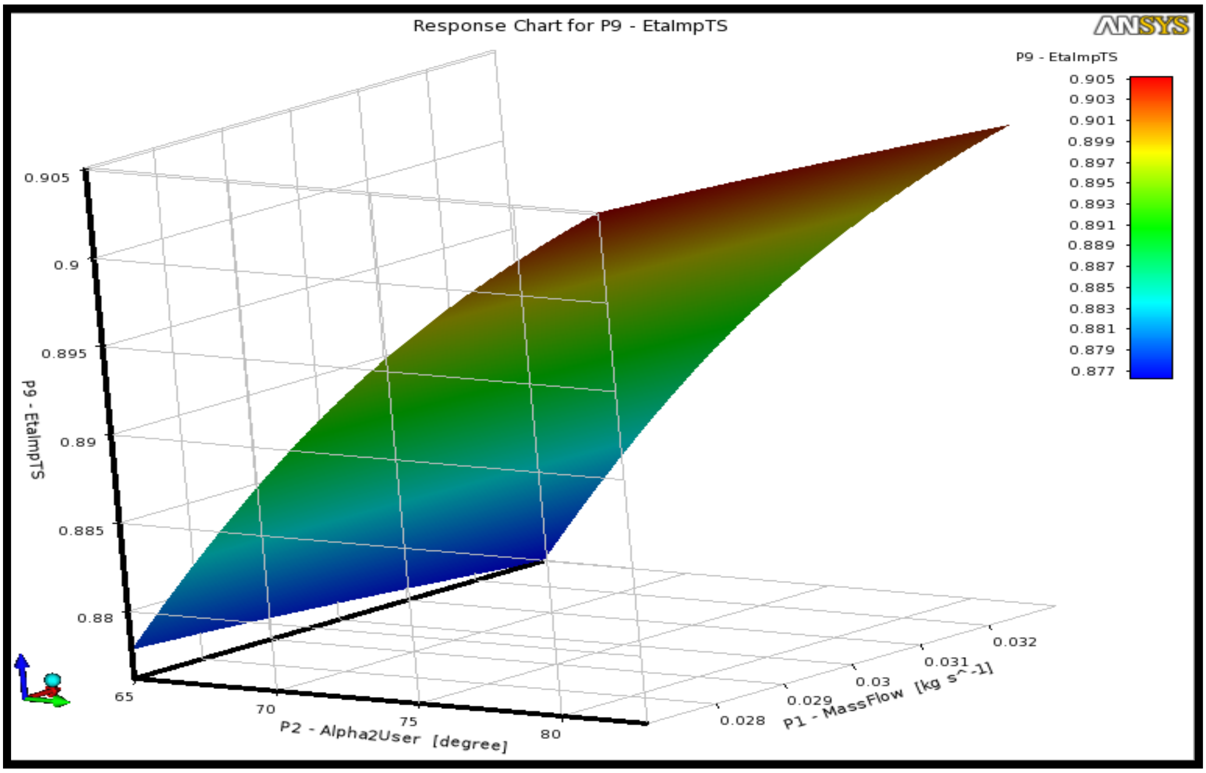

Figure 4.27: Samples of the effect of the most influence input parameters on the rotor efficiency at rotor number of 17 and stator number 13.

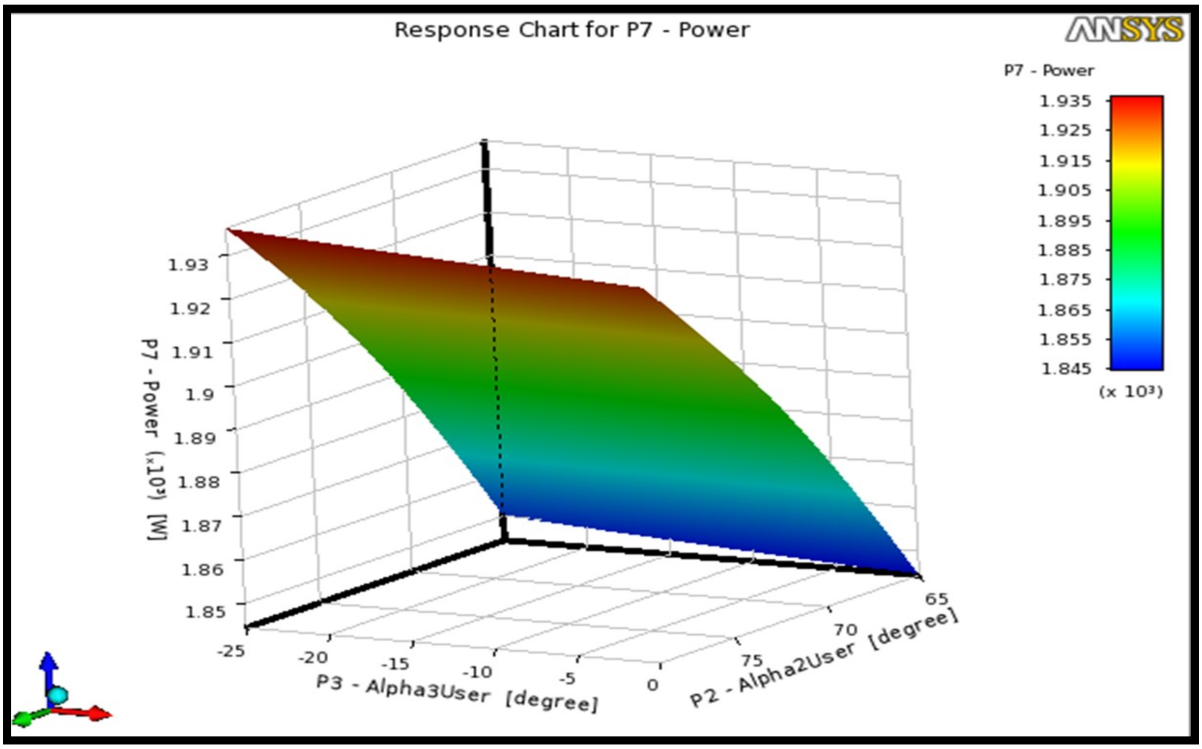

Figure 4.28: Samples of the effect of each inlet and outlet flow angles together on the amount of extracted power at rotor number of 17.

4.6.2 Results of 1D Optimization:

In order to achieve that point, a compromise based on the objective priority, needs to be applied during this step. Figure 4.29 shows the setup of 1D optimization highlighted the objectives and constraints and Figure 4.30 shows the 1D optimization feature of Vista RTD ANSYS/ Workbench. Figure 4.31 shows the trade-off between the rotor tip width, efficiency and power output. In this figure it can be seen that while there are many design points, there are only few of points, feasible points, which satisfy the required objectives and constraints simultaneously. Table 4.4 shows the range which was considered for each of the selected parameters as well as the achieved optimum value for the output objective.

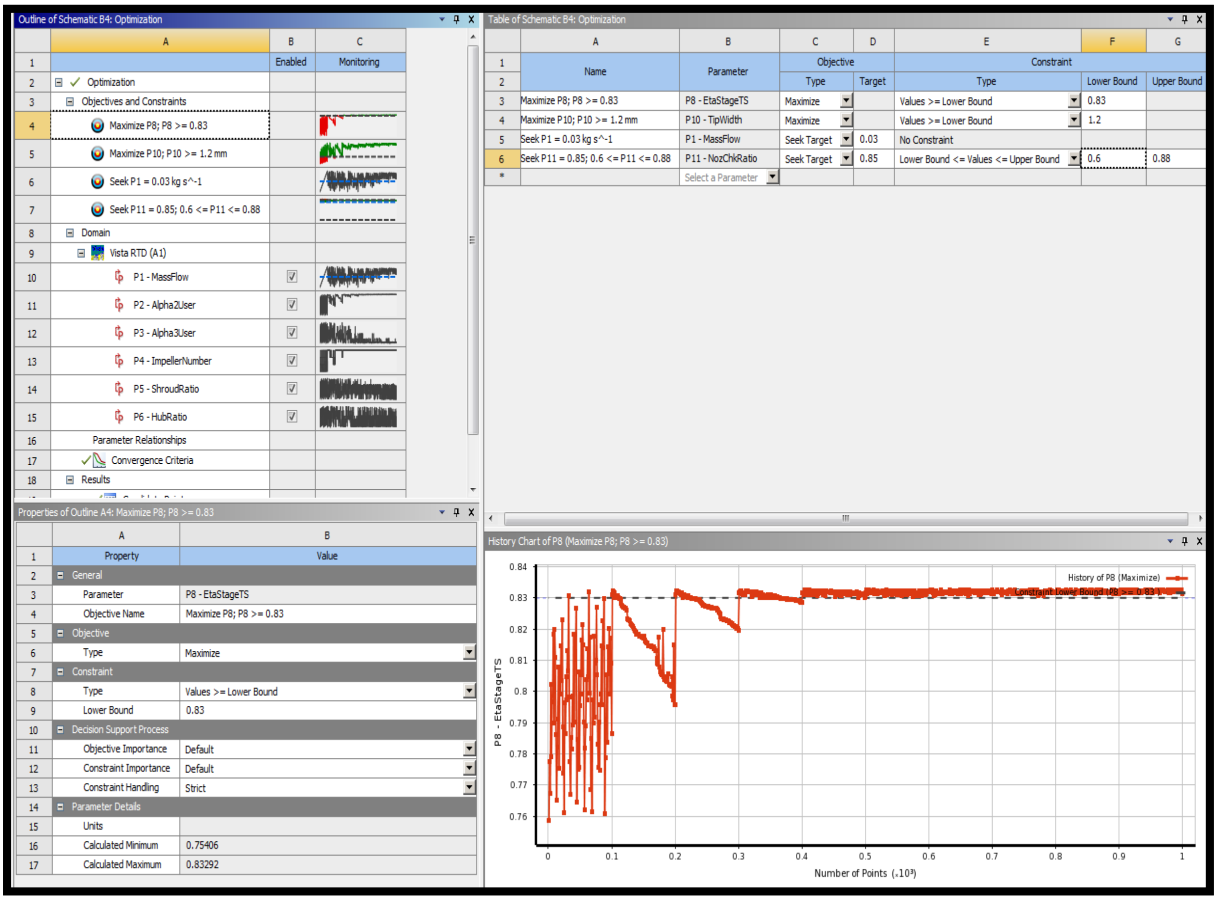

Outline of Schematic B4: Optimization

	A	B	C
1		Enabled	Monitoring
2	⊟ ✓ Optimization		
3	⊟ Objectives and Constraints		
4	Maximize P8; P8 >= 0.83		
5	Maximize P10; P10 >= 1.2 mm		
6	Seek P1 = 0.03 kg s^-1		
7	Seek P11 = 0.85; 0.6 <= P11 <= 0.88		
8	⊟ Domain		
9	⊟ Vista RTD (A1)		
10	P1 - MassFlow	☑	
11	P2 - Alpha2User	☑	
12	P3 - Alpha3User	☑	
13	P4 - ImpellerNumber	☑	
14	P5 - ShroudRatio	☑	
15	P6 - HubRatio	☑	
16	Parameter Relationships		
17	✓ Convergence Criteria		
18	⊟ Results		

Table of Schematic B4: Optimization

	A	B	C	D	E	F	G
1	Name	Parameter	Objective		Constraint		
2			Type	Target	Type	Lower Bound	Upper Bound
3	Maximize P8; P8 >= 0.83	P8 - EtaStageTS	Maximize		Values >= Lower Bound	0.83	
4	Maximize P10; P10 >= 1.2 mm	P10 - TipWidth	Maximize		Values >= Lower Bound	1.2	
5	Seek P1 = 0.03 kg s^-1	P1 - MassFlow	Seek Target	0.03	No Constraint		
6	Seek P11 = 0.85; 0.6 <= P11 <= 0.88	P11 - NozChkRatio	Seek Target	0.85	Lower Bound <= Values <= Upper Bound	0.6	0.88
*		Select a Parameter					

Properties of Outline A4: Maximize P8; P8 >= 0.83

	A	B
1	Property	Value
2	⊟ General	
3	Parameter	P8 - EtaStageTS
4	Objective Name	Maximize P8; P8 >= 0.83
5	⊟ Objective	
6	Type	Maximize
7	⊟ Constraint	
8	Type	Values >= Lower Bound
9	Lower Bound	0.83
10	⊟ Decision Support Process	
11	Objective Importance	Default
12	Constraint Importance	Default
13	Constraint Handling	Strict
14	⊟ Parameter Details	
15	Units	
16	Calculated Minimum	0.75406
17	Calculated Maximum	0.83292

History Chart of P8 (Maximize P8; P8 >= 0.83)

Figure 4.29: The outline schematic optimizations showing the objectives and constraints.

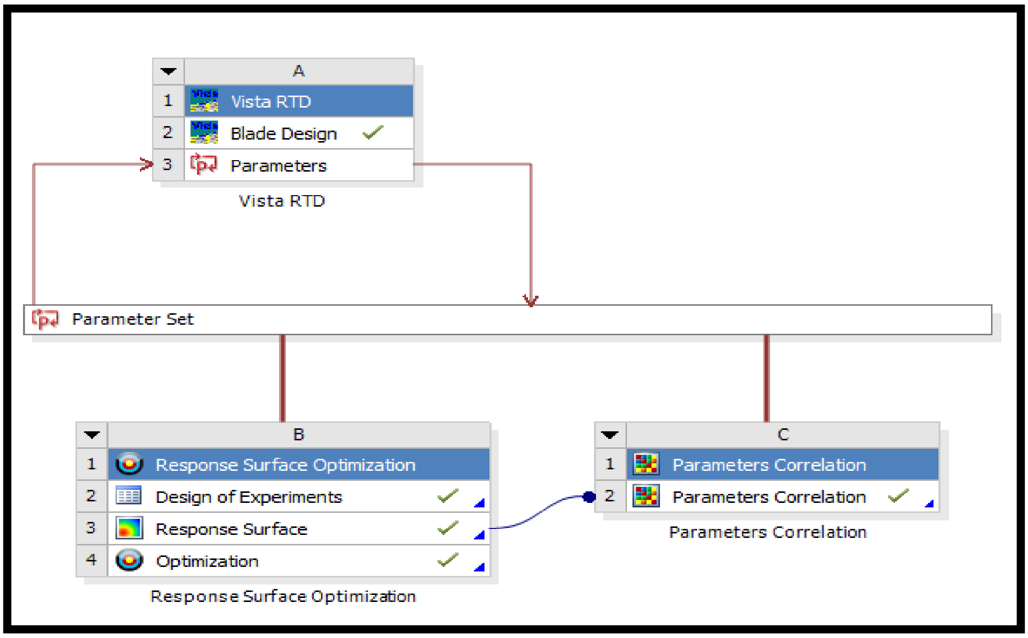

Figure 4.30: The1D optimization feature using Vista RTD in ANSYS Workbench.

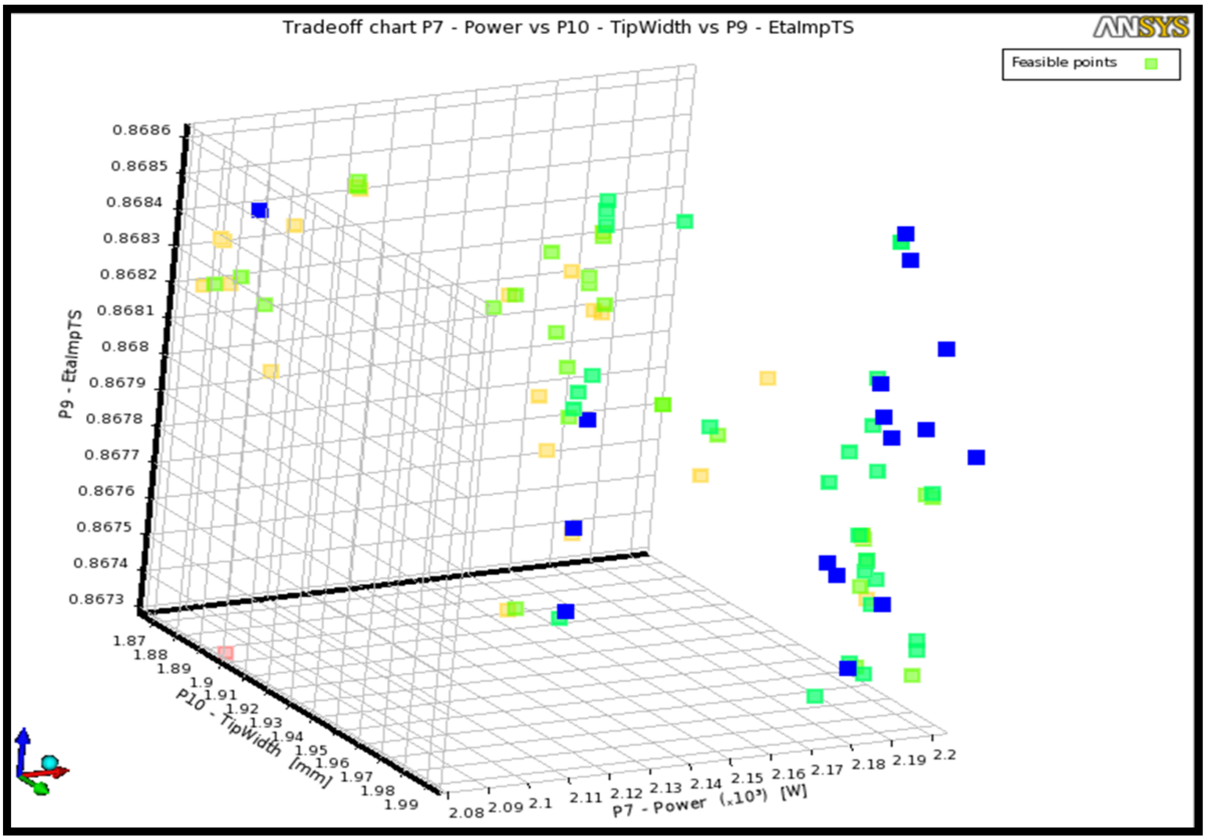

Figure 4.31: Samples of the tradeoff chart between the rotor tip width, output power and efficiency.

Table 4.4: The variables ranges' values and their optimum values from 1D optimization.

Design Variables	Optimization Limits	Optimum Value
Rotor No. of Blade (-)	11-17	17
Rotor Outlet Flow Angle (deg.)	62-79.7	77.3
Rotor Inlet Flow Angle (deg.)	-29-0	-15.8
Shroud Ratio	0.67-0.85	0.81
Hub Ratio	0.18-0.26	0.23
Tip Width of Rotor (mm)	-	1.25
Rotor Tip Clearance (mm)	-	0.45
Power Output (kW)	-	2.3
Rotor Efficiency (-)	-	90.7

Three correlations represent the relation between the rotor power output and efficiency with respect to the inlet parameters have been proposed with high value of the R^2, which represent the accuracy of the proposed equation.

The relation between the inlet flow angle and the rotor efficiency in terms of two correlations, linear and quadratic trend lines with the value of R^2 for each of them was proposed. Figure 4.32 shows the relation between the inlet flow angle and the rotor efficiency in terms of two correlations, linear and quadratic trend lines with the value of R^2 for each of them.

The linear correlation is given as $Y = 0.0024733X + 0.62898$; with $R^2 = 98.894\%$ and the quadratic one is imported as $Y = -0.000054234X^2 + 0.010272X + 0.34954$; with $R^2 = 99.563\%$, where the Y and X are the rotor efficiency and the inlet flow angle respectively. Similarly, the two proposed correlations for the rotor output power is given in Figure 4.33 where the mass flowrate was the inlet parameter which has been considered. The linear correlation is given as $Y = 64210X -31.812$; with $R^2 = 95.03\%$ and the quadratic one is imported as $Y = -1578400X^2 + 158870X - 1446.4$; with $R^2 = 95.175\%$, when the Y and X are the rotor output power and the inlet mass flow rate respectively.

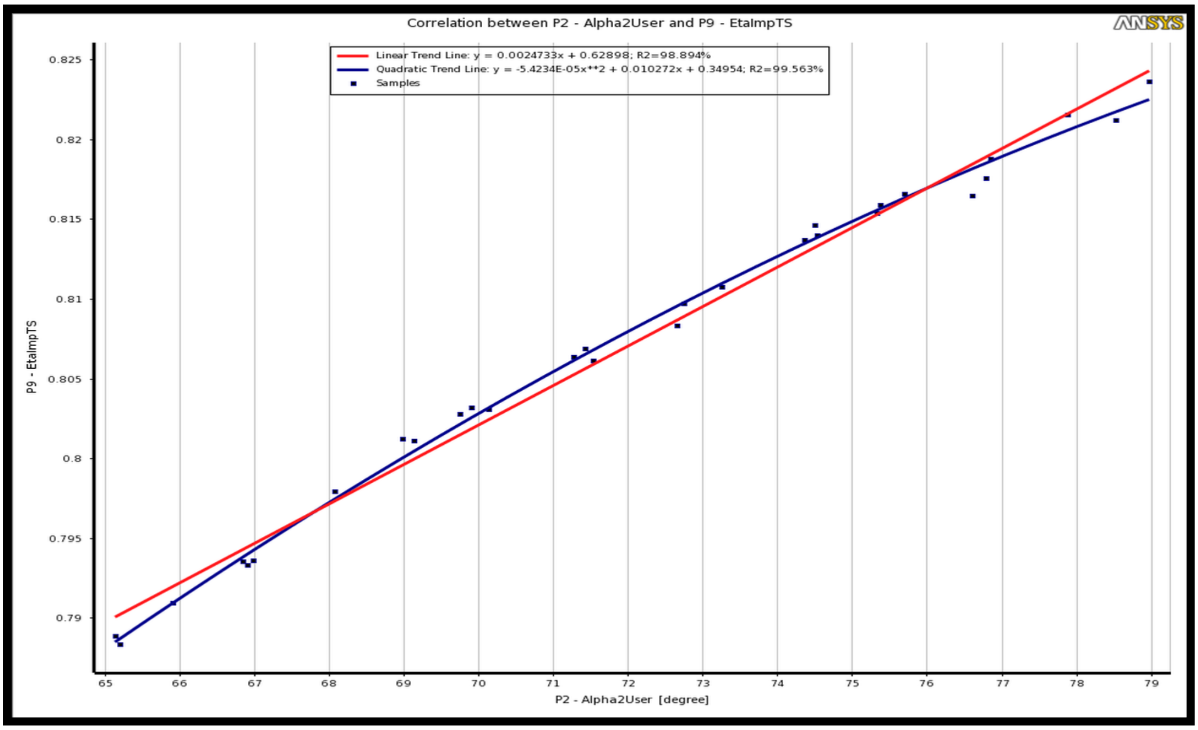

Figure 4.32: Sample for the correlation between the rotor efficiency and the inlet flow angle.

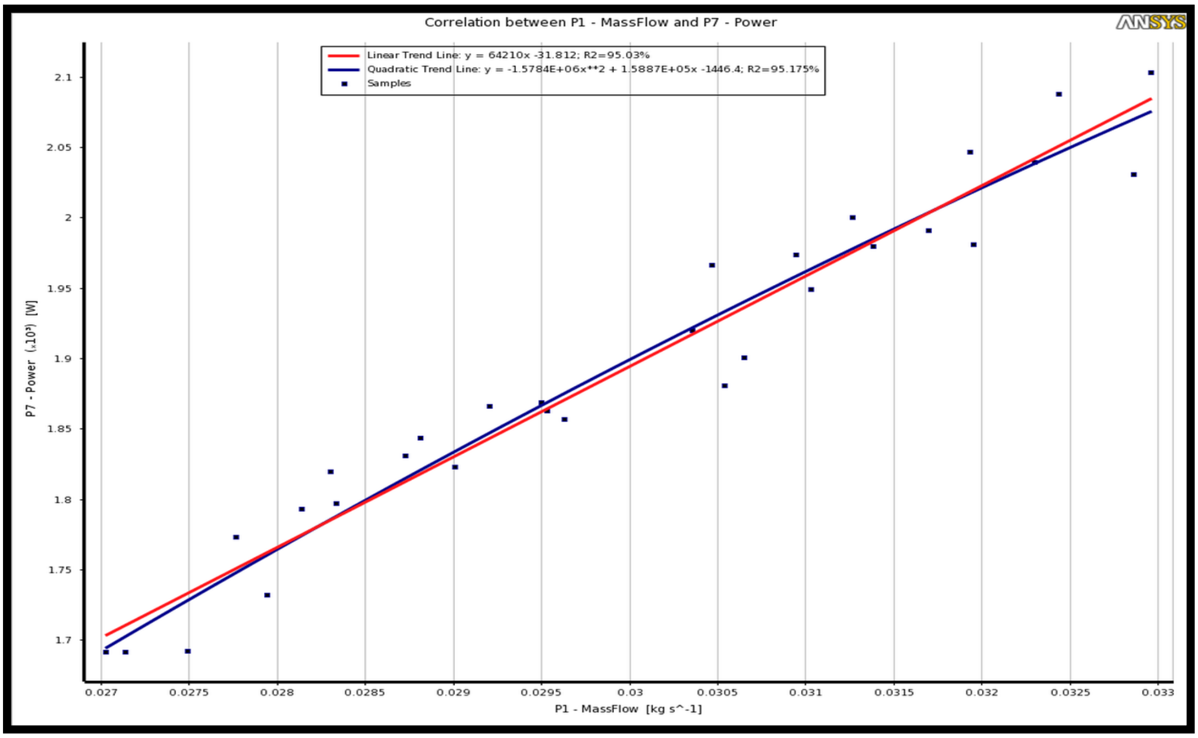

Figure 4.33: Sample for the correlation between the rotor output power and mass flowrate.

4.7 3D Optimization Approach in ANSYS:

It is useful at this point to define some of the terms which are frequently utilized in the optimization process and in the ANSYS Academic software technique. In order to design any model, the first step is normally generating a simulation model which can utilize different boundary conditions for any design dimensions and shape. Through this step, defining the input parameters, which need to be investigated, (this can include boundary conditions). This can be parameterised using the ANSYS Design Modeller application. In contrast, the output parameters such as model performance i.e. efficiency and power output or even manufacturing constraints will be selected after the results of simulation are achieved. These parameters can be defined using the parameter set bar in the project scheme.

4.7.1 Design Exploration:

Design exploration utilizes deterministic approach based on Design of Experiments (DOE) for achieving the required goal of optimization. The key point of design exploration is to categorise the relationship between the model performance and the design variables. Depending on these results, the designer will be capable of varying the design in order to meet the model's requirements and understand how its performance can be influenced. Furthermore, Design Exploration includes Response Surface Methods (RSM), which can be used to carry out parametric studies with a number of parameters reaching up to 15 input parameters.

4.7.2 Identify Design Candidates:

After creating the initial model and defining the required parameters, a response surface will be created. Then, the design space for each of the input variables is defined, by providing the minimum and maximum values. Depending on this information, the DOE section of the Response Surface scheme will generate the sampling for the design space and updates the model output parameters. The accuracy of this response depends on whether the chosen output parameters were complex or not and also on the number of selected design points. There are five types of standard response surfaces which are: full 2nd order polynomials, Kriging, non-parametric regression, neural network and sparse grid. The first two types are the most commonly used ones and the main difference between them is that the first one can be used when the variations of the output parameters is mild and the second one is favourable in case of stronger variations. Once the response surfaces are generated, the model will be ready for analysis using numerical and graphical tools and then the suggested design points (solutions) are verified. This analysis can be carried out using the sensitivity graphs which can give an initial indication about how much the input parameters really have an effect on the output parameters around each given response point. Using both the response surfaces and sensitivity charts the designer will be able to have an answer about "What-if" questions. Finally, the main step of optimization is finding the candidate points using the correct type of Goal Driven Optimization (GDO) systems. Two types of (GDO) optimization are available in ANSYS Academic namely the direct optimization and the response surface optimization. Once the required type of optimization is selected, laying down the objectives and constraints and then identifying the domain need to be completed and the problem will be ready to be solved.

At this point it is important to emphasise that the final candidates need to be verified in order to check their validity to achieve accurate results.

4.7.2.1 Genetic Algorithms:

Figure 4.34, shows the genetic algorithm structure which begins with a random strings population representing the design factors. Subsequently, the fitness value for each separate string is determined. Then a new population of points are created using reproduction, cross over and mutation. In order to terminate the mentioned process, the latest population is assessed using a criterion [171]. If the termination criterion was not met, the population, by using the three mentioned operators, will iteratively run and then evaluated again [171]. Then the process will continue repeatedly until the termination criterion will be attained.

The major differences between the (GA) techniques and other traditional optimization approaches such as Newton-Raphson [171] are:

1- It works with the coding of the parameter set, not the parameters themselves [171].

2- It searches for a population of points, not a single point [171].

3- It uses the objective function information and not the derivative or second derivative [171].

4- It uses stochastic transition rules, not deterministic rules [171].

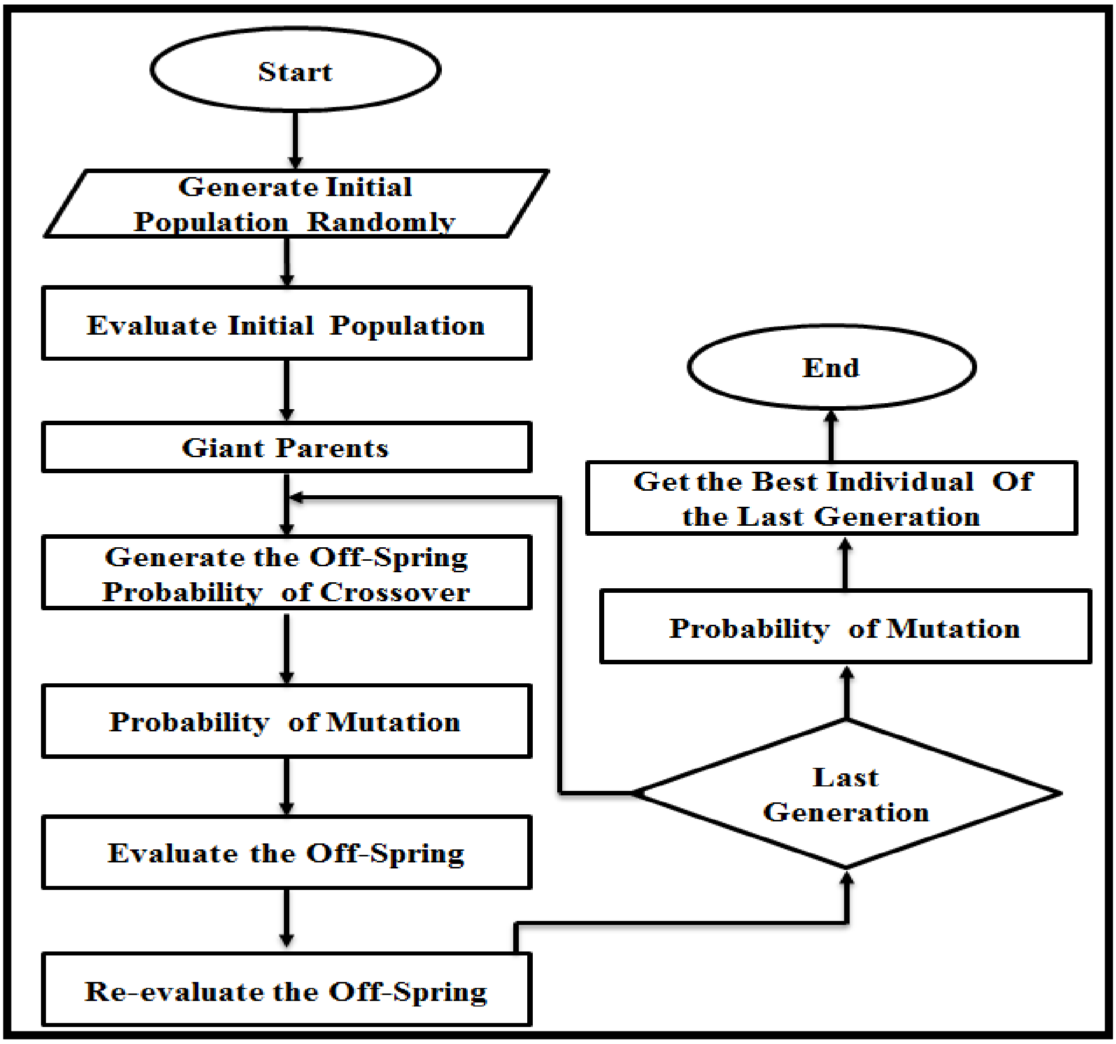

Figure 4.34: Flow chart for the Genetic Algorithm [171].

4.7.2.2 Multi-Objective Genetic Algorithms:

The Multi-Objective Genetic Algorithm (MOGA) is a hybrid variant method which works based on controlled elitism ideas. The main important feature of this type is its ability to support various input parameters and also it ensures that the feasible solutions are ranked higher than the unfeasible ones. Compared to single objective optimization, the multi-objective optimization is capable of maximizing or minimizing many functions based on their constraints. The modern (CFD) packages which integrated with these techniques can be used efficiently to achieve an efficient design model. Recent (CFD) packages are integrated with several advanced optimisation techniques which can be utilised to perform an effective design process [199] and [131]. This can also affect the design constrains which their changes will influence the optimization results as the amount of information will be changed [200]. Figure 4.35 illustrates the steps used in multi-objective optimization process which are summarised as following:

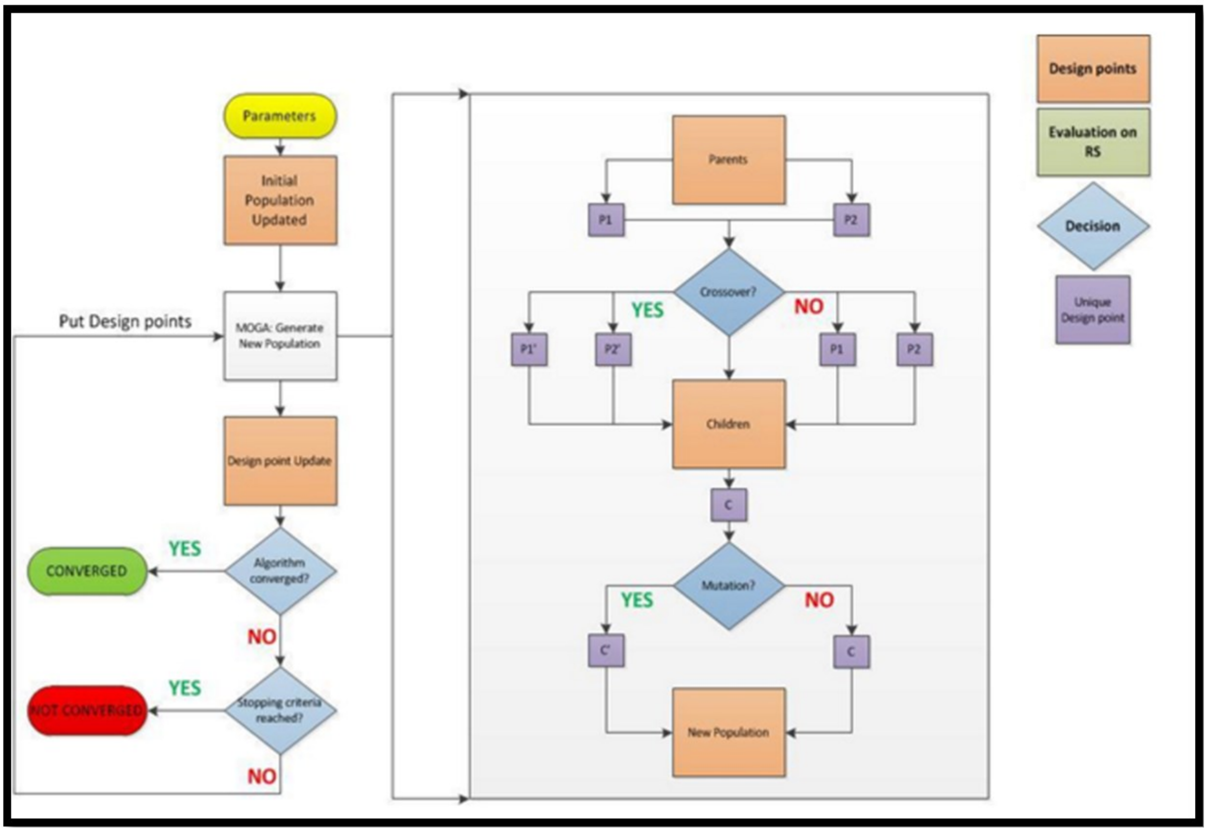

Figure 4.35: The procedure of the (MOGA) method [201].

1- Initiating the first population and use it in the (MOGA).

2- Generate the new generation by crossover and mutation of the previous generation using the (MOGA). Once completing the first iteration, each population will run till it reaches the required samples' number, which was already specified using number of samples per iteration.

3- Design point update, where all design points for the new population will be updated.

4- Convergence Validation. The convergence of the optimization process is examined, so if the answer is yes, that means the optimization is achieved however, if not the opposite is correct. The first is achieved when the Maximum Allowable Pareto Percentage or the Convergence Stability Percentage is met while the second choice, the not, means that the optimization process will continue to the next step, 5.

5- Stopping criteria validation. This step is to check the other possibility which causes solution stopping. Here if the maximum number of iteration, which was already specified by the designer, has been reached, this means that the solution is converged, otherwise, it will return to step 2.

6- Conclusion which enables steps from 2 to 5 to be repeated in the same sequence until the solution reaches the convergence by reaching either the criteria mentioned in step 4 or that mentioned in the previous step.

4.7.2.3 3D Design Variables of (SSRT):

Figure 4.36 clarifies the process established in the (3D CFD) optimization for optimizing the (SSRT) using the direct optimization method [171]. This method is provided with a polynomial model and has the best compromise between the accuracy and the computational cost time [184]. It involves using the design of exploration module in ANSYS for the blade parameterization, design points generation and objective functions [171].

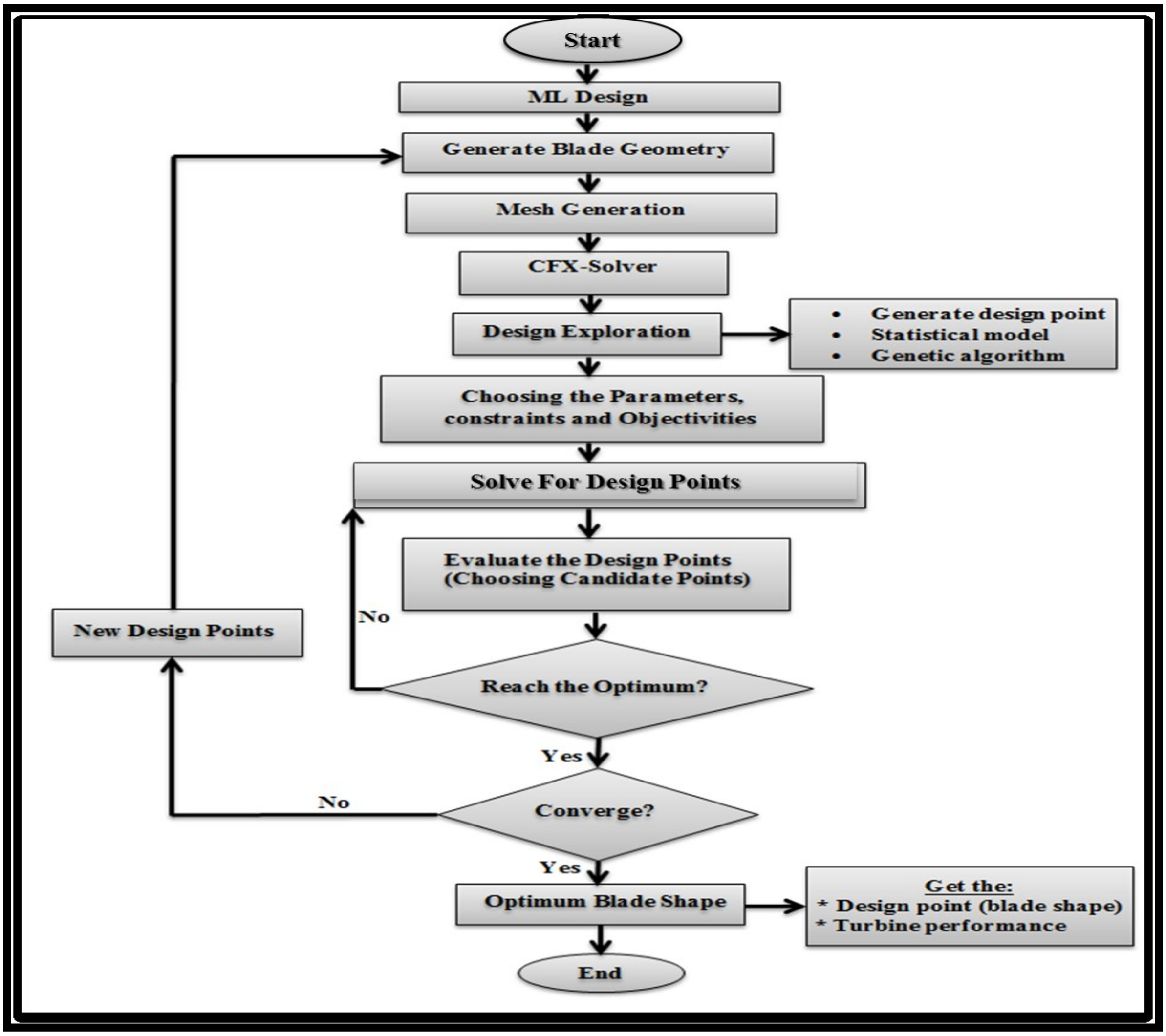

Figure 4.36: The procedure followed by the (3D CFD) optimization [171].

Then, a statistical function known as response surface approximation [202] is employed. The purpose of this function is to connect the input parameters (blade profile) with the output ones, using the Direct Method. Once the numerical solution for each single design point is completed, the discrete response for each of them takes place [171]. The second order polynomial response can be formulated [203] and [204], [171] as:

$$f(x) = \beta_0 + \sum_{j=1}^{N} \beta_j x_j + \sum_{j=1}^{N} \beta_{jj} x_j^2 + \sum \sum_{i \neq j}^{N} \beta_{ij} x_i x_j \qquad (4.33)$$

Here, f(x) is the function to be optimized; β characterizes regression coefficients; and x is a set of design parameters [171].

However, in a constrained minimization problem, the objective function is replaced by the penalized function given as follows [171]:

$$P(x) = f(x) + \sum_{j=1}^{N} u_j \langle g(x_j) \rangle^2 + v_k \sum_{k=1}^{K} [h_K(x)]^2 \tag{4.34}$$

Where u_j and v_k known as penalty coefficients, whose values are typically constant through the GA modelling. Also, g(x) and h(x) are the inequality constraints and equality constraints respectively, and the fitness function can be determined based on the penalized function as shown below:

$$F(x) = \frac{1}{(1+P(x))} \tag{4.35}$$

If the RSA function has an intensive variation with respect to the design parameters, then the space sample between the design points will be redesigned and the objective function will be restructured [171, 194]. The principal aim of this 3D optimization is to improve the geometry of blade to reduce the losses and enhance the SSRT efficiency, in addition to minimize the working fluid flow rate.

In this work the stator and the rotor blade geometries were included in the (3D CFD) optimization [171]. Both; parameterization of the blade geometry and choosing the correct range of the parameters are considered very important and critical steps in a successful optimization procedure [171]. Therefore, they need to be carefully selected in order to achieve the goal of optimization. Unlike the axial rotor blade (the airfoil), the radial rotor blade geometry is presented via a camber line and layered surface because of its high curvature and the difficulty in representing the exact blade shape using two or three points [171]. Therefore, in addition to the rotor blade number, twelve other parameters, (some of them in terms of the X and Y coordinates), which together represent the rotor blade shape and required throat width, have been selected as input parameters [171]. Thus, the full definition of the rotor blade will be established. Regarding the stator geometry, the parameters which have been selected are the leading edge angle, trailing edge angle, stager angle, and blade number. These have a direct impact on the stator shape and control the flow rate delivery to the rotor during the optimization process [171].

In order to successfully achieve the optimum design for the (SSRT), the optimization process was implemented for the range of design boundary conditions shown in Table 4.5. Maximizing the output power and the turbine efficiency were selected as objective functions [171]. Also, some constraints like the stator throat area (to supply the required air flow rate to the rotor), the tip clearance and blade thickness (for manufacturing purposes), were also supplied [171].

Table 4.5: Input operating conditions of integrated (SSRT) and the Brayton cycle model [171].

Parameter	**Range/value**
Loading Coefficient (-)	0.8-1.4
Flow Coefficient (-)	0.1-0.5
Shroud $_{\text{Exit}}$/Shroud $_{\text{Inlet}}$ (-)	0.8
Hub $_{\text{Exit}}$/Hub $_{\text{Inlet}}$ (-)	0.22
Rotational Speed (rpm)	50000-90000
Inlet Total Pressure (bar)	2 - 5
Inlet Total Temperature (K)	350 -550
Mass Flow Rate (kg/s)	0.02 – 0.05
Working Fluids (-)	air
Cp (J/kg K)	1005
Inlet Blade Velocity (m/s)	253.1
Exit Blade Velocity (at shroud) (m/s)	202
Inlet Relative Velocity(m/s)	65.8
Exit Relative Velocity(m/s)	206.3
Inlet Absolute Velocity(m/s)	250.5
Exit Absolute Velocity(m/s)	14.7
Rotor Inlet Density(kg/m^3)	1.153
Rotor Inlet Mach (abs) (-)	0.7

Figure 4.37 and Figure 4.38 show the parametrization screen shot of the rotor and the stator respectively.

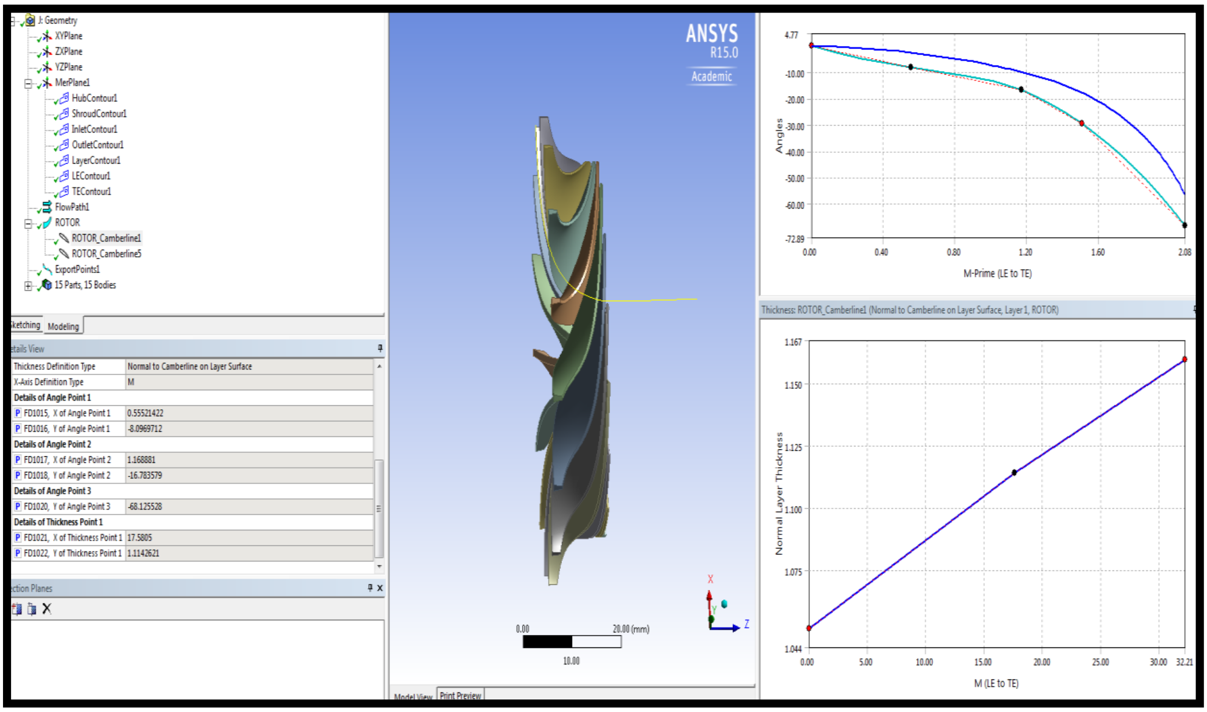

Thickness Definition Type	Normal to Camberline on Layer Surface
X-Axis Definition Type	M
Details of Angle Point 1	
P FD1015, X of Angle Point 1	0.55521422
P FD1016, Y of Angle Point 1	-8.0969712
Details of Angle Point 2	
P FD1017, X of Angle Point 2	1.168881
P FD1018, Y of Angle Point 2	-16.783579
Details of Angle Point 3	
P FD1020, Y of Angle Point 3	-68.125528
Details of Thickness Point 1	
P FD1021, X of Thickness Point 1	17.5805
P FD1022, Y of Thickness Point 1	1.1142621

Figure 4.37: The layout of the rotor- camber line parametrization.

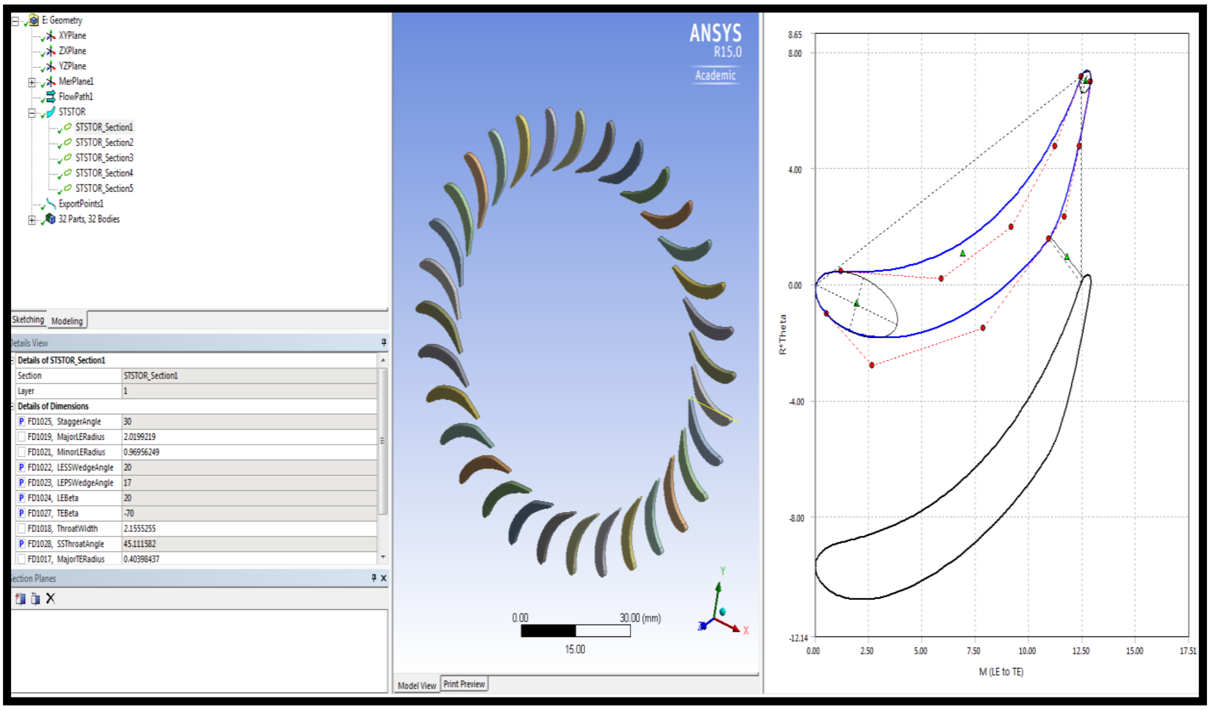

Details of STSTOR_Section1	
Section	STSTOR_Section1
Layer	1
Details of Dimensions	
P FD1025, StaggerAngle	30
☐ FD1019, MajorLERadius	2.0199219
☐ FD1021, MinorLERadius	0.96956249
P FD1022, LESSWedgeAngle	20
P FD1023, LEPSWedgeAngle	17
P FD1024, LEBeta	20
P FD1027, TEBeta	-70
☐ FD1018, ThroatWidth	2.1555255
P FD1028, SSThroatAngle	45.111582
☐ FD1017, MajorTERadius	0.40398437

Figure 4.38: The layout of the stator aerofoil parametrization.

4.7.2.4 Solution of 3D (SSRT) Optimization:

For the 3D (SSRT) optimization, two methods were used namely the direct method shown in Figure 4.39 and the response surface optimization method shown in Figure 4.40, which was used in order to confirm the achieved results.

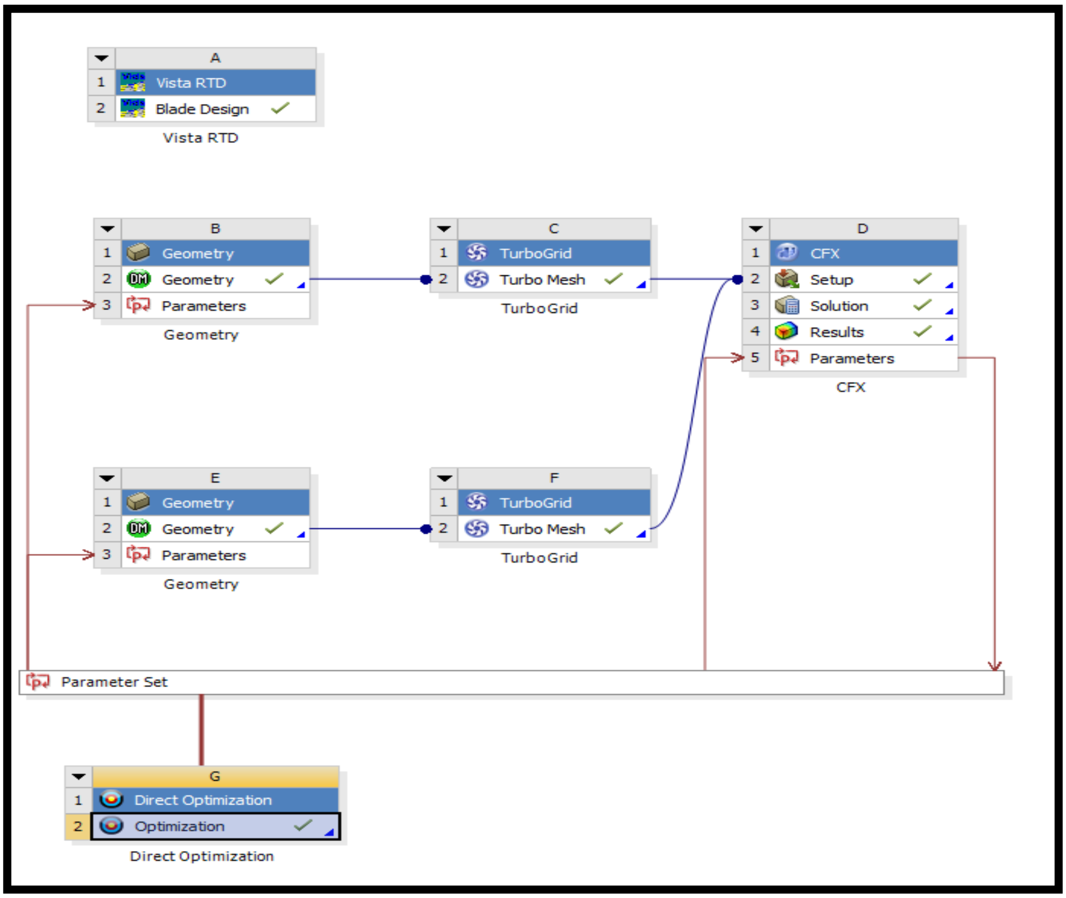

Figure 4.39: 3D optimization feature for the (SSRT) using the direct method.

Figure 4.41, shows the effect of the blade angle and its thickness along the blade layer on the rotor efficiency. From this figure it is clear that up to 85% rotor efficiency can be achieved using when the angle, at that layer, reached 10 Degree.

Figure 4.42 shows how the efficiency decreased by changing the rotor blade number at the same blade configuration where in both cases the maximum efficiency achieved was only around 82%.

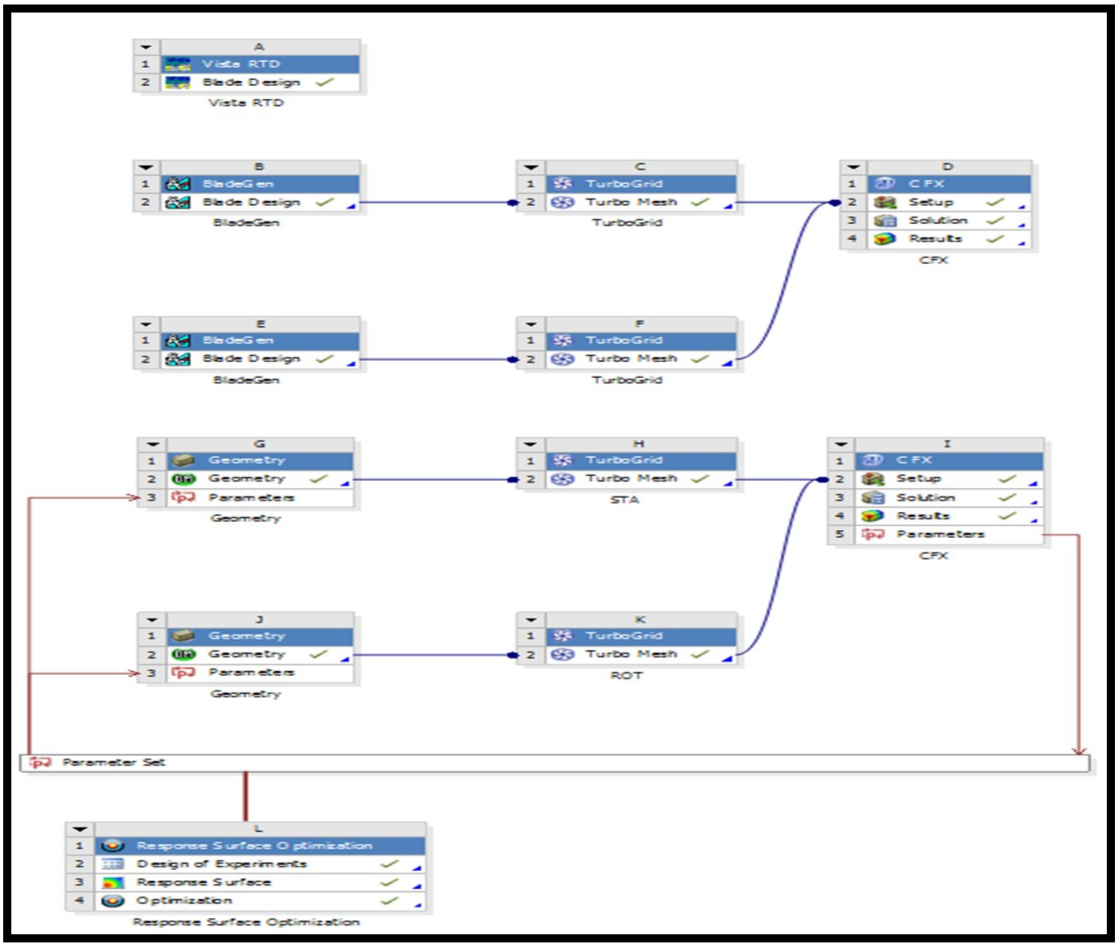

Figure 4.40: The optimization achieved using the Response Surface optimization method.

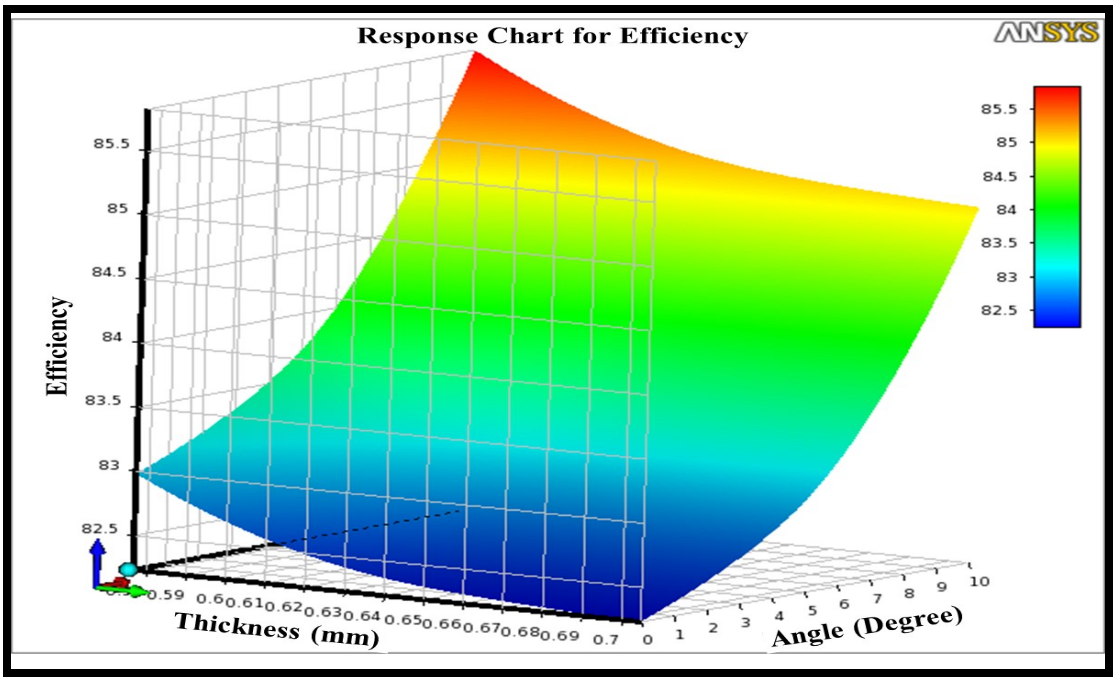

Figure 4.41: The rotor shape effect on the turbine efficiency at 15 and 36 rotor and stator blades number using Response Surface Optimization.

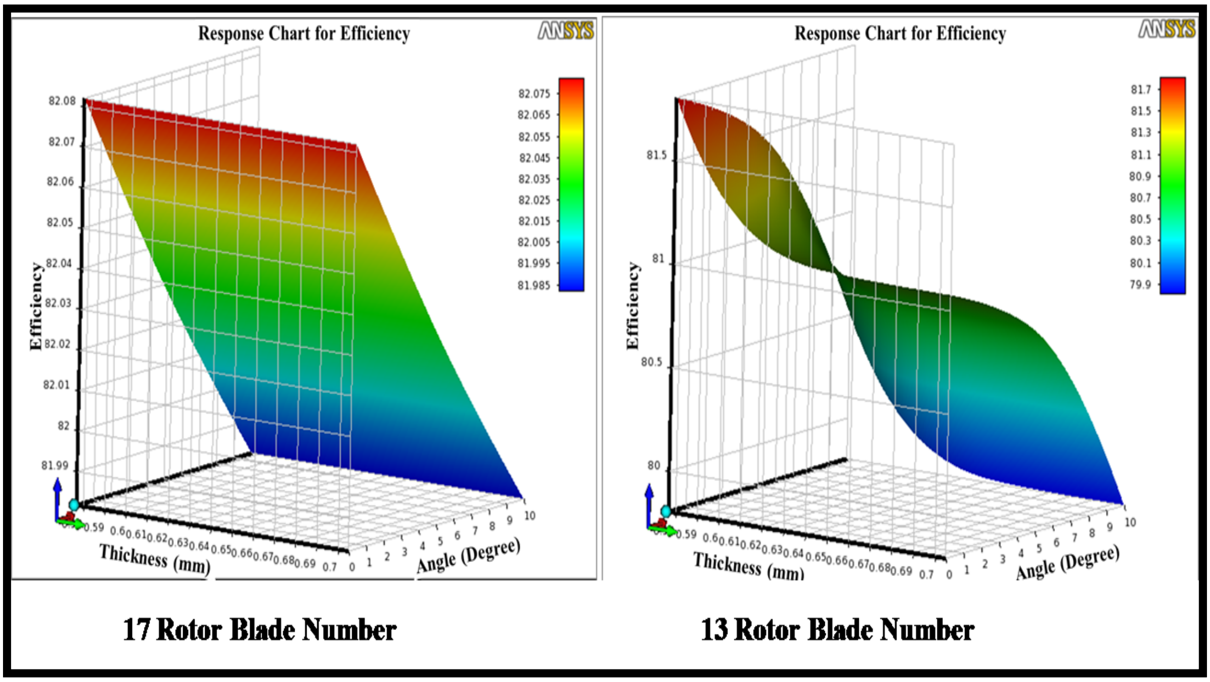

17 Rotor Blade Number

13 Rotor Blade Number

Figure 4.42: The effect of rotor blade on the turbine efficiency at the stator blades number of 29 using Response Surface Optimization.

Figure 4.43 shows the influence of changing the stator number of blade on the turbine efficiency at the same rotor blade configuration where in both cases the maximum efficiency achieved was around 83.5% while changing the blade angle affects significantly through the air flow rate which in turns alters the efficiency.

The precision and quality of the chosen model has been assessed based on what is known as the goodness of fit for the whole turbine stage i.e. the stator and the rotor as shown in Figure 4.44. It is clear from this figure that the nominated Meta-model showed excellent accuracy with the coefficient of determination equals to unity and maximum relative residual close to zero. As a result the chosen model, which is the Meta-model based on Standard Response Surface-Full 2nd –order Polynomial algorithm, is able to drive the (GA) optimizer and find the global optimum shape for the turbine stage in a precise manner.

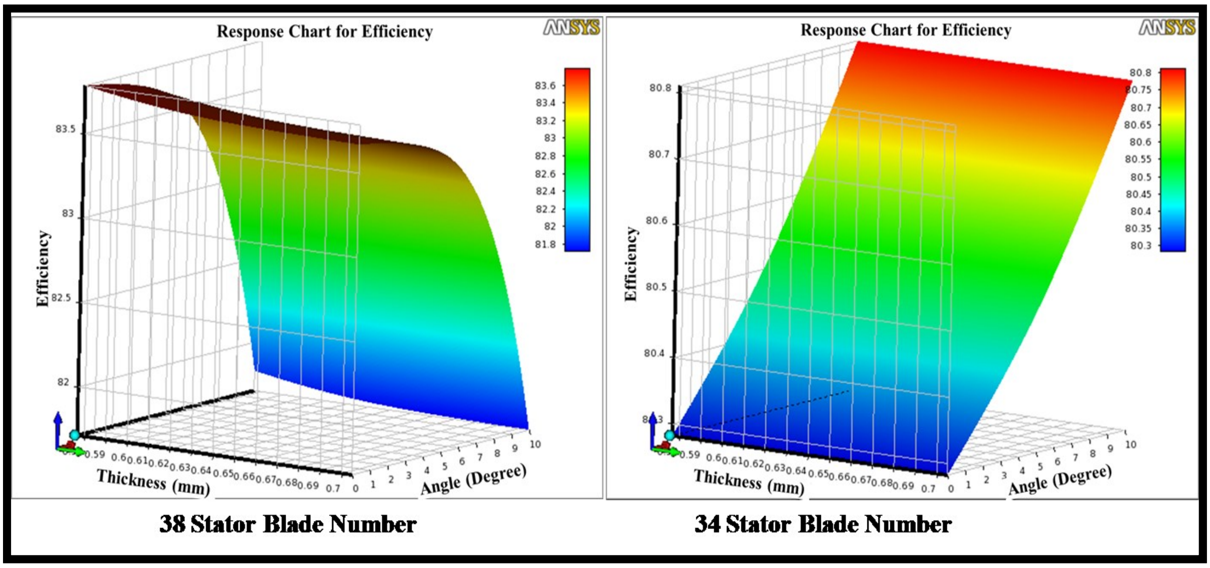

38 Stator Blade Number **34 Stator Blade Number**

Figure 4.43: The effect of stator blade number on the turbine efficiency at the optimum rotor shape and number using Response Surface Optimization.

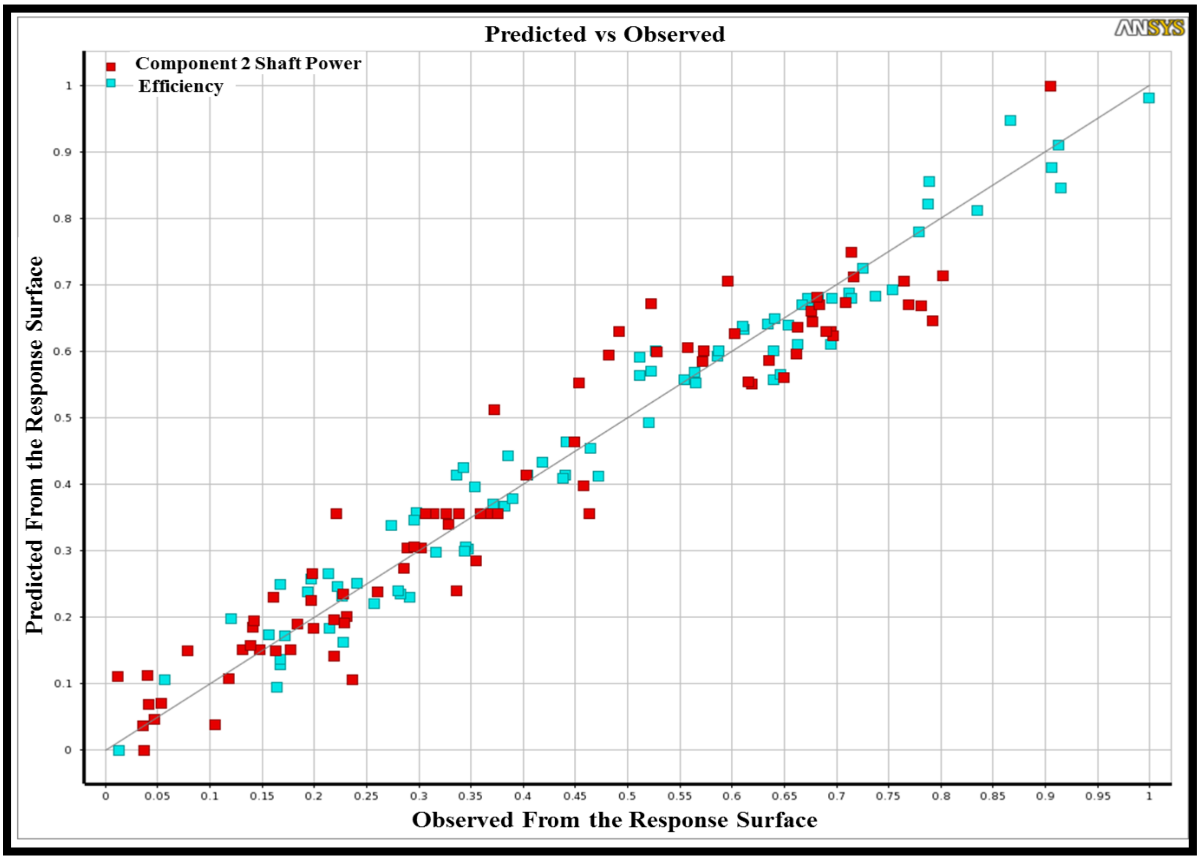

Figure 4.44: The predicted and observed efficiency and power output for the (SSRT) in terms of goodness of fitness shape.

4.7.3 Results of 3D Optimization:

Once the input parameters, the constraints and the objective functions were specified, over 1200 various design points suggested solutions were originated based on random distributed data. The solution consumed more than 515 continuous hours on a computer with Core I7 3.7 GHz processor and 48 GB RAM [171].

Figure 4.45 displays a case of some suggested solutions as candidate design points. Due to their large number, the design points were split into two figures, each has around 250 potential solutions (which together represent only around 63% of all the design points) with respect to the turbine efficiency and the output power [171]. From these figures it can be seen that some candidate points gave efficiency value of 90% which is higher than the selected optimum point, 87.5%. Yet, they didn’t fulfil the required mass flow rate, thus they were omitted [171].

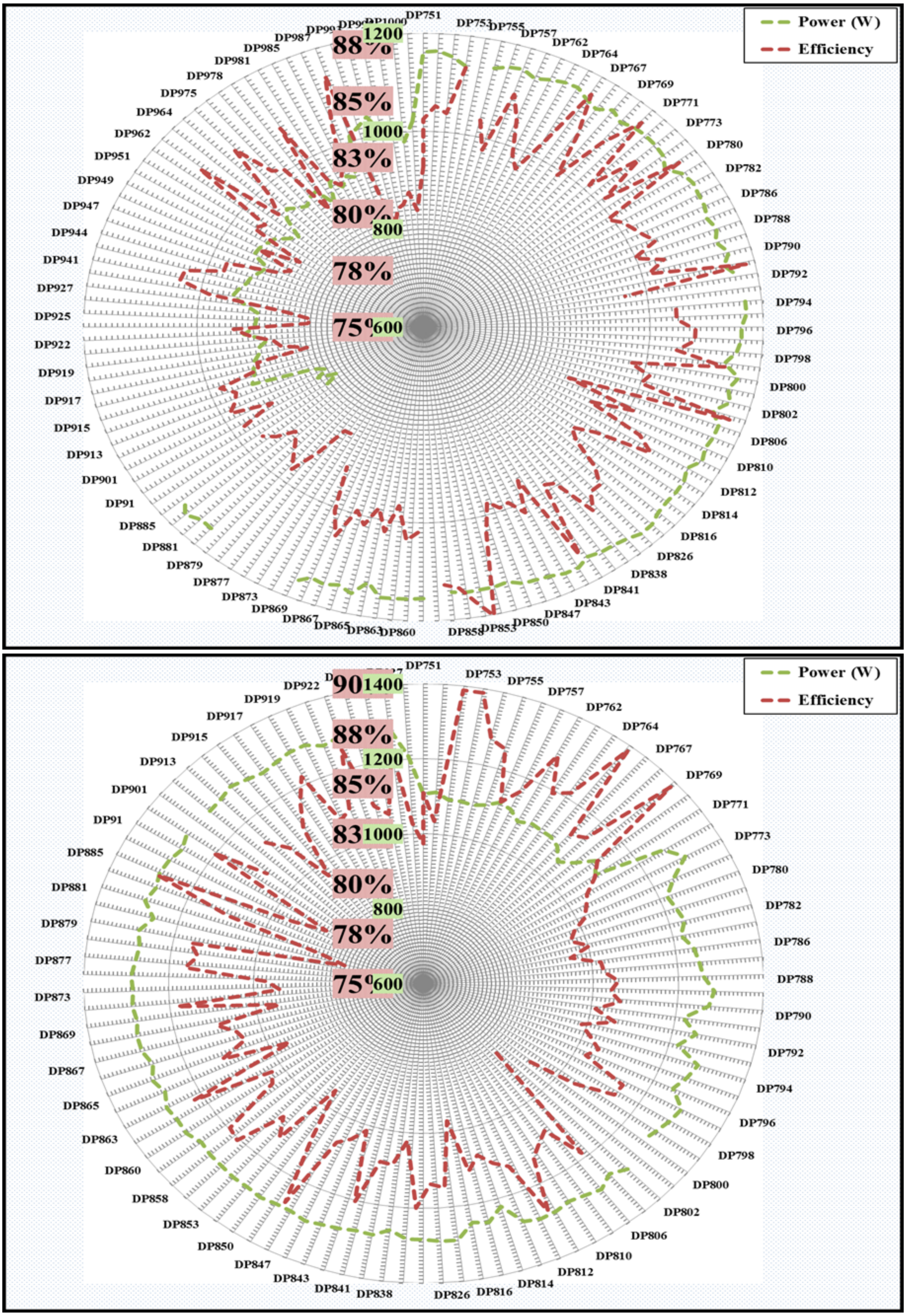

Figure 4.45: Modulation of the (SSRT) efficiency and power output values with some of the investigated design points [171].

Table 4.6 shows the base-line (before the optimization) and the optimum values for the design variables of (SSRT), while Figure 4.46 shows the two profiles of the rotor blade; for the base-line and the optimum design.

Table 4.6: The base-line and optimum design variable from (CFD-MOGA) optimization [171].

Design Variables	**Baseline**	**Optimum**
Stator No. of Blade (-)	32	36
Stator Stagger Angle (deg.)	33	37.739
Stator TE Beta Angle (deg.)	69	73.70
Rotor No. of Blade (-)	13	15
Rotor LE Beta Angle (deg.)	16.2	-46.3109
Rotor Inlet Flow Angle (deg.)	-58.3	74.03
Rotor Stagger Angle at Span 0.0 (deg.)	14.4	-16.8
Rotor Stagger Angle at Span 0.5(deg.)	-44.7	-37.1
Rotor Stagger Angle at Span 1(deg.)	-64.5	-59.3
Rotator TE Beta Angle (deg.)	-18.5	-9.9457
Rotor Outlet Flow Angle (deg.)	78.9	83.36
Tip Width of Rotor (mm)	1.35	2.1
Rotor Tip Clearance (mm)	0.45	0.33

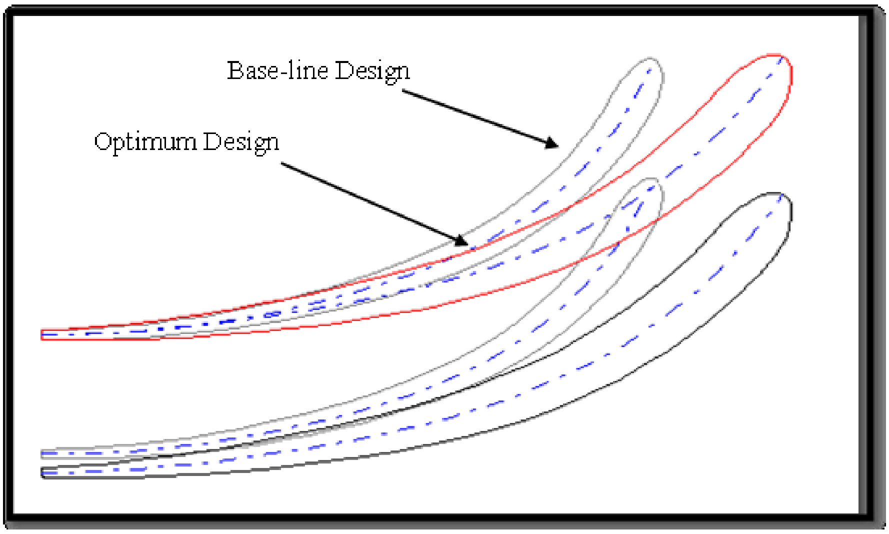

Figure 4.46: Comparison between blade geometry at the base-line and optimum design [171].

Figure 4.47 compares the performance of the baseline design (CFD- Base) and the Optimum Point (OP) at the on design and off design conditions. The efficiency and power output values were plotted at various: rotational speed, pressure ratio and inlet temperature. Figure 4.47 a displays the efficiency and power output values at turbine inlet temperature ranging from 350 K to 550 K, (PR) of 3 and rotational speed of 70 krpm. It is clear that the power output rises with the increase in the temperature while the turbine efficiency increases to reach a maximum value at 450 K then decreases with further increase in the temperature. Figure 4.47 b and Figure 4.47 c characterize the (SSRT) efficiency and power output at various rotational speed and pressure ratio values respectively at temperature of 450 K. It can be seen from the given figures that both, the power output and the efficiency values rose to reach a maximum increment of around 7.5% in the turbine efficiency and about 37% in its output power at (PR) of 3 and rotational speed equals 70 krpm. The justification for that improvement is the reduction in the secondary losses, profile losses and incidence losses due to reaching the optimum shape of blade geometry. Moreover, it is evidence from Figure 4.47 that the off-design, the overall performance of the optimized (SSRT) is better than the baseline design in terms of the amount of output power and turbine efficiency [171].

$$\text{Enhancement}\ \% = \frac{\text{OP Efficiency} - \text{BL Efficiency}}{\text{OP Efficiency}} \tag{4.36}$$

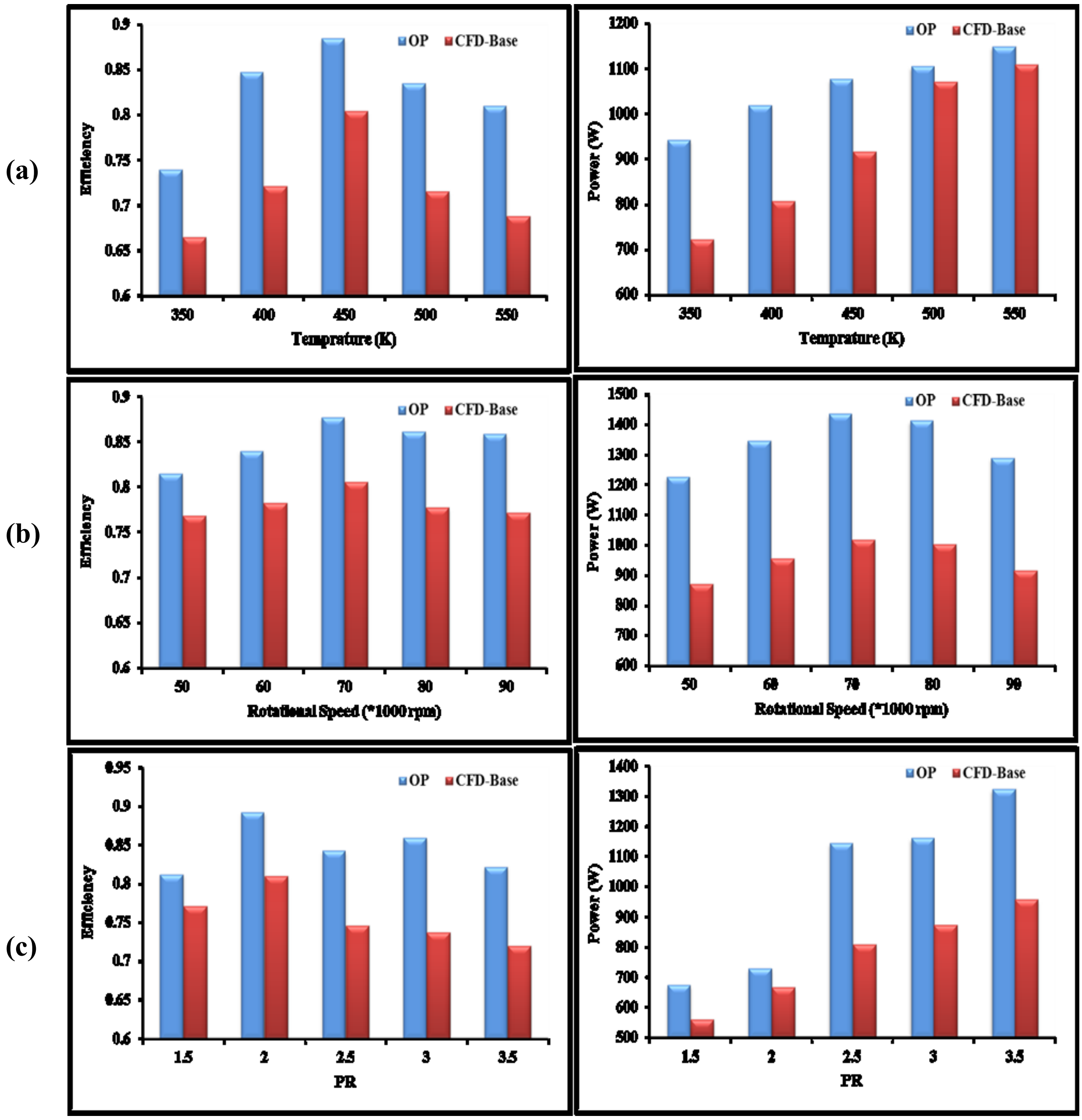

Figure 4.47: Comparison between (CFD) and (OP) results; efficiency and power output at different: (a) Inlet temperature, (b) Rotational speed and (c) Pressure ratio[171].

Figure 4.48 a displays the load distribution through the rotor passage where the maximum flow velocity occurred just after the throat area and that led to minimize the pressure on the suction surface. Conversely, the opposite was the case for the velocity distribution on the pressure side starting from the leading to the trailing edges [171]. Figure 4.48 b shows the pressure contours through the turbine stage where the pressure was spread uniformly starting from the highest value in the stator to the lowest at the diffuser [171].

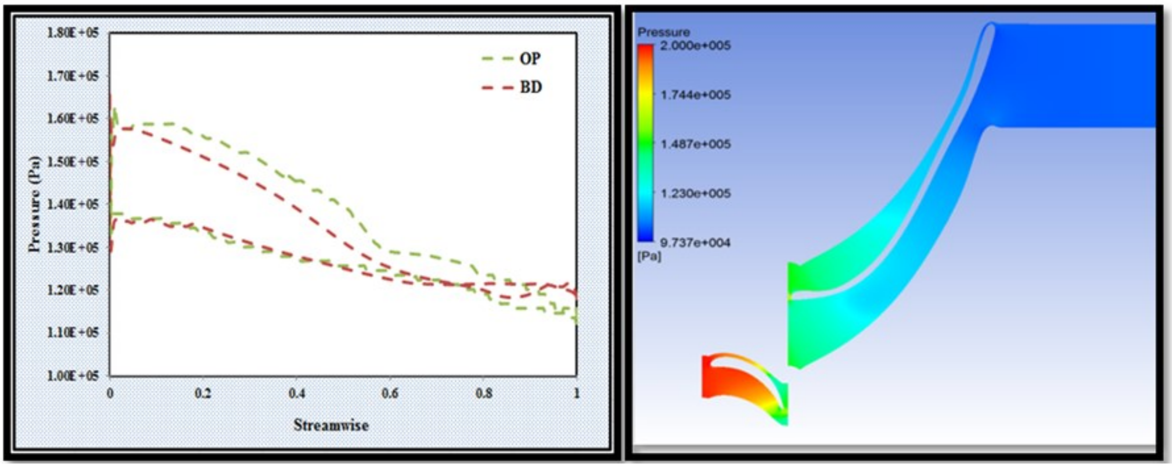

(a) **(b)**

Figure 4.48: (a): Pressure distribution of the (BL) and (OP) for the rotor blade and (b): Contours of pressure distribution of the (OP) in the stator, rotor and diffuser at 50% span [171].

Figure 4.49 shows the entropy generation in the baseline and optimum design of the turbine showing lower entropy generation values in the case of optimum design. This lower entropy values indicates lower aerodynamic losses.

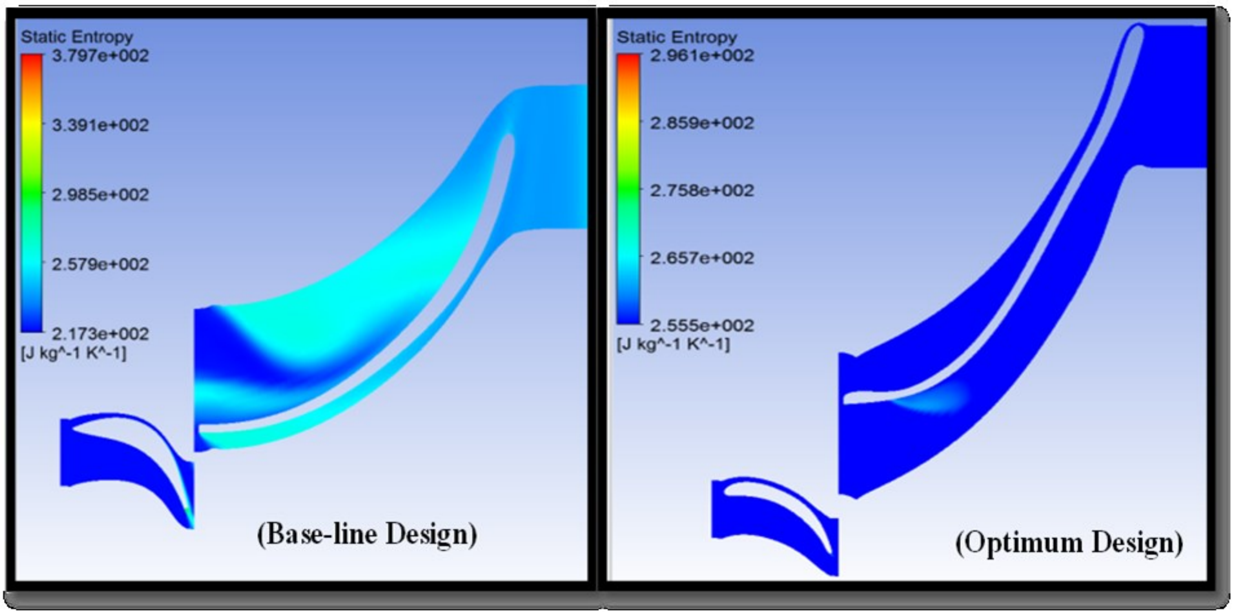

Figure 4.49: Entropy generation at base-line and optimum designs [171].

4.8 Results of Brayton Cycle Analysis:

Figure 4.50 shows the cycle efficiency using the optimum turbine design developed through the (CFD) and optimization methods in the previous sections compared to those of the baseline turbine design. The predicted turbine efficiency was inputted in the cycle analysis described in section 4.2 at various pressure ratios and inlet temperature ranging from 450 K to 550 K. It can be seen that the maximum cycle efficiency is obtained at nominal operating conditions with pressure ratio of 3 when the operating temperature was 450 K and increased with increasing the temperature. At the moment it is imortant to highlight that for the nominal conditions, the optimum pressure value which provides maximum cycle efficiency is 3 [171]. However, with increasing the turbine inlet temperature that value becomes 3.5 and 4 at 500 K and 550 K respectively since the relationship between the turbine pressure ratio and its inlet temperture [171]. Additionally, at the nominal conditions, improving the (SSRT) efficiency to 87.5%, led to around about 4.1% increment. Finally, using this methodolgy led to achieving a maximum cycle efficiency of 9%, 14.5% and 20% at the optimum pressure ratio values and inlet tempertures of 450 K, 500 K and 550 K respectively.

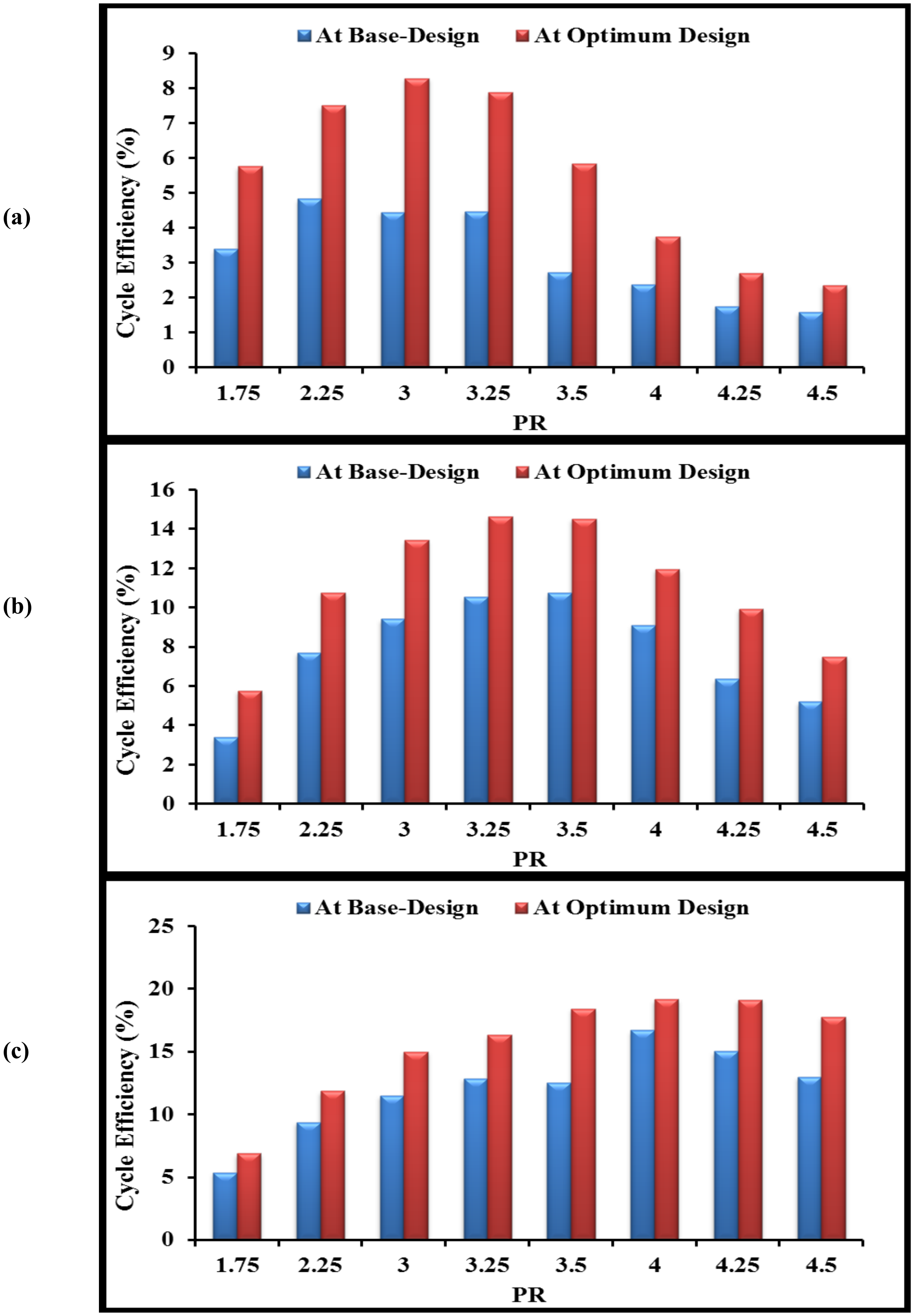

Figure 4.50: The effect of pressure ratio values before and after turbine optimization at inlet temperature of: (a) 450 K, (b) 500 K and (c) 550 K on the cycle efficiency [171].

4.9 Summary and Conclusions:

In this chapter, compressed air (SSTs) including (SSSSAT), (SSDSAT) and (SSRT) were developed and their performance was analysed using various geometrical factors and operating conditions with the purpose of selecting the most suitable turbine for the current application.

Furthermore, a numerical simulation to optimize the (SSRT) was carried out. Starting from the one-dimensional meanline approach and then using (3D CFD) simulations, the best turbine type was firstly achieved. Then, 3D optimization for the whole turbine has been carried out and consequently, the highest reachable efficiency for the (SSSPBC) was achieved. The main conclusions from this work can be briefly summarised as [171]:

- The (SSRT) is much influenced by the tip clearance instead of trailing edge thickness. Together the trailing edge and tip clearance losses contributed about 4 % and the trailing edge loss can be decreased in the (SSDSAT) by matching the first stage rotor trailing edge and the second stage stator leading edge [172].
- The radial turbine is superior when the principal concern is to offer high power output at a relatively low pressure ratio and mass flow rate values. It achieves around 1.7 times the power produced by the axial at high pressure ratio. Moreover, it is more efficient at high rotational speeds where the opposite was the case at relatively low rotational speeds [28].
- At low rotational speed the axial configurations behave better than the radial at the off design conditions, which can attain quite stable cycle efficiency; however, the radial has the advantage at high rotational speed.
- For the investigated scale, the highest efficiency was achieved with 10 and 13 rotor blades and at a stator blade trailing edge angle of 67^o and at 60^o for the (SSSSAT) and (SSRT) respectively [28].

- As for the cycle analysis, it is shown that up to 10 % enhancement in the cycle efficiency is achievable, when the compressor efficiency is 95% and depending on other operating conditions, if the turbine efficiency reaches 90%. Likewise, up to 7.5% decline in the cycle efficiency was noticed when the compressor efficiency reduced from 95% and 85%.

The main points concluded for the aerodynamic radial turbine optimization can be summarised as below:

- A high increase in the (SSRT) efficiency, from 82.3% to 87.5% at the same output power ranges was achieved as a result of optimizing the shape and the number of both the stator and the rotor blades of the radial turbine using the direct method of optimization which allows for more than 20 input parameters to be used together [173].
- In order to confirm the accuracy of the direct optimization method, which achieved high turbine efficiency, the response surface optimization method was also used and the results showed relatively lower efficiency 86.7%. However, it is still high value for this scale of turbines.
- Moreover, the load on the rotor blade as well as the losses, in terms of the entropy value showed a significant enhancement with respect to the standard design.
- The methodology of integrating the cycle modelling with the meanline (3D CFD) simulation and (MOGA) optimization are considerably beneficial in improving the turbine’s performance and the overall performance of a small scale solar powered Brayton system. Consequently, the thermal cycle efficiency has been increased by about 5% as a result of increasing the turbine’s efficiency [173].

CHAPTER 5: STRUCTURAL ANALYSIS OF SMALL SCALE RADIAL TURBINE

5.1 Introduction:

Developing small scale turbines poses challenges in terms of increased stresses due to high rotational speed leading to increase in component thicknesses and turbine overall weight. Also failure of such turbines leads to economic losses as well as loss in human life. Therefore this chapter assesses both; the structural and aerodynamic performance of a Small Scale Radial Turbine (SSRT) by integrating finite-element methods (FEM) and Computational Fluid Dynamics (CFD). Starting from the research work carried out in chapter 4, a 1-3 kW output power was firstly developed to have a very high efficiency of 87.5%. Then both; the turbine's shaft and its blades were structurally analysed under various loading conditions in order to visualise the effect of various rotational speed values and blade shapes on the stress distribution and displacement over the blades. Fatigue analysis was also included in this chapter to evaluate the rotor part of the (SSRT). After evaluating the structural stresses, decreasing these stresses was carried out to achieve the best performance of the proposed turbine through the multidisciplinary optimization.

5.2 Methodology:

Following to the work done in chapter 4, the optimized (SSRT) has been further analysed by considering the structural analysis in order to have a reliable turbine with a good performance for the application under investigation. SSRT has been selected for two reasons; the first is because of the excellent efficiency that was achieved and the achieved range of its output power. Using the integrated (CFD-FE) Workbench in ANSYS Academic 18, (the latest version of ANSYS) optimum design of the (SSRT) was used to carry out stress analysis and the fatigue analysis. Then, a multidisciplinary optimization was carried out in order to enhance the overall structural turbine's performance.

Figure 5.1 demonstrates the procedure which was followed during the current chapter. This chapter will focus on the FE structural analysis by integrating the (CFD) and FE analysis to develop efficient and mechanically reliable SSRT.

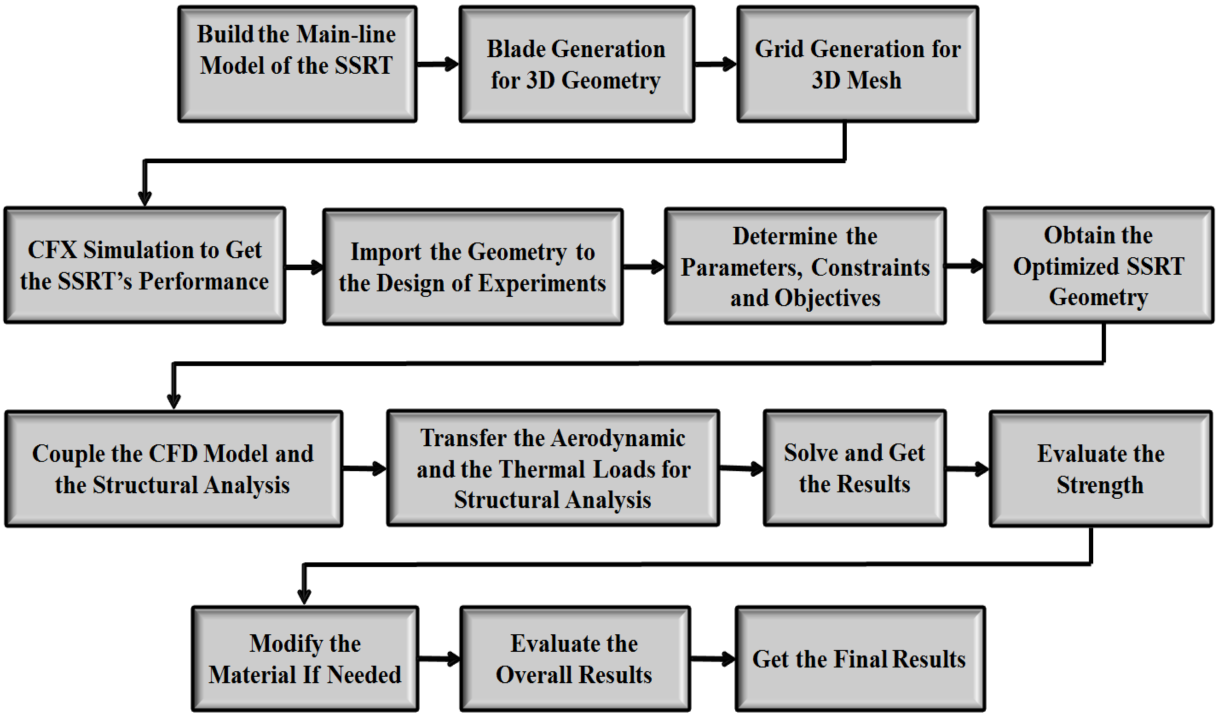

Figure 5.1. Overview process of the analyses' procedure.

5.3 Mathematical Model:

The turbine blades are operated in aggressive environments; therefore they are required to withstand high centrifugal forces and sometimes high elevated temperatures. The stress fields are the combined effect of the thermal gradient, the steady stress and vibratory stress. The thermal stress can be calculated as:

$$\sigma = D.\varepsilon \qquad (5.1)$$

Where σ is stress, D is the elasticity matrix, and ε is the strain. At this point it is important to highlight that the RGD 525 plastic material was chosen as the turbine material for the current study because of its good properties compared to others, more details in chapter 6.

The studied material, RGD 525, is assumed to be isotropic, see Table 5.1 and within the regime of elastic deformation, the stress–strain relations can be written in Cartesian coordinates as:

$$\varepsilon_x = \frac{1}{E}\left[\sigma_x - V_p\left(\sigma_y + \sigma_z\right)\right] + \alpha\Delta\mathrm{T}(x, y, z) \tag{5.2}$$

$$\varepsilon_y = \frac{1}{E}\left[\sigma_y - V_p(\sigma_x + \sigma_z)\right] + \alpha\Delta\mathrm{T}(x, y, z) \tag{5.3}$$

$$\varepsilon_z = \frac{1}{E}\left[\sigma_z - V_p\left(\sigma_x + \sigma_y\right)\right] + \alpha\Delta\mathrm{T}(x, y, z) \tag{5.4}$$

Where E, V_p and α are the modulus of elasticity, Poisson's ratio and the thermal expansion coefficient respectively. In the above equations, $\Delta\mathrm{T}(x, y, z)$ represents the temperature gradient at a point(x, y, z). The temperature fields were directly predicted by the (CFD) results.

Table 5.1: RGD525 Material > Isotropic Elasticity.

Young's Modulus (MPa)	Poisson's Ratio	Flexural Modulus MPa	Tensile Strength (MPa)
2.e+003	0.3	3300	75

On the other hand, the steady stresses result from both; the fluid force on the blades and the centrifugal force which greatly depends on the rotor rotational speed.

The alternating or the vibratory stresses, however, which happened as a result of the disturbance during the fluid flow and the resonance phenomena, [205], is out of the scope of this study. While there are some other loads acting on the turbine body which initially are caused by [206] centrifugal force, which greatly depends on the rotor rotational speed, is acting specifically on the shaft blade connection [207] and can be calculated in terms of the following equations:

$$F_{cf} = mr\omega^2 \tag{5.5}$$

Where F_{cf} is the centrifugal force; and m, r and ω is the blade mass, radius of rotation and the rotor rotational speed respectively. However, calculating the exact value of the centrifugal force was achieved by considering a small element of the blade section and then integrating it to include the all blade body, as shown below.

$$df_{cf} = dm.\omega^2(R_r + z) \tag{5.6}$$

Where;

$$dm = \rho.A(z)dz \tag{5. 7}$$

$$df_{cf} = \rho\omega^2.A(z).(R_r + z)dz \tag{5.8}$$

$$F_{cf}(x) = \int_x^{lb} \rho.\omega^2.A(z).(R_r + Z)dz \tag{5.9}$$

Where, ρ is the blade material density, A is the blade area, z is the blade thickness and R_r is the radius at the root. By considering the blade as a cantilever with variable cross sectional area [208], written as:

$$\left(\frac{A_{(z)}}{A_r}\right)^{lb} = \left(\frac{A_t}{A_r}\right)^{z} \tag{5.10}$$

$$A_{(z)} = A_r.\left(\frac{A_t}{A_r}\right)^{z/lb} \tag{5.11}$$

Finally, the centrifugal force at any point on the blade can be determined using the following equation:

$$F_{cf(x)} = \rho\omega^2 \left[\frac{A_r.(\frac{A_t}{A_r})^{\frac{z}{lb}}.R_r.lb}{\ln\left(\frac{A_t}{A_r}\right)} + \frac{A_r.(\frac{A_t}{A_r})^{\frac{z}{lb}}.z.lb}{\ln\left(\frac{A_t}{A_r}\right)} - \frac{A_r.(\frac{A_t}{A_r})^{\frac{z}{lb}}.lb^2}{\left[\ln\left(\frac{A_t}{A_r}\right)\right]^2}\right]_x^{lb} \tag{5.12}$$

Where A_t and A_r are the cross sectional area at the tip and the root respectively and lb is the blade length.

5.4 Structural Simulation of the (SSRT):

The rotor was modelled using the Mechanical Workbench of ANSYS Academic 18. Firstly, the (CFD) model and the static-structural model were coupled with the purpose of determining the turbine's deformation. Then, aerodynamic forces, which were calculated in the (CFD) model, were exported through system coupling to the structural model. An adequate element concentration, using 3D solid element, for each; the rotor blades and the hub was conducted. This mesh was based on a 20 node solid element type which has well-matched displacement shape suitable for modelling curved boundaries. The thermal properties of the defined RGD 525 material are given in Table 5.2. Another important issue is whether it is required generating a full mesh for all the rigid body or for surface contact mesh only. This can be controlled via the rigid body behaviour. In this study the choice of dimensionally reduced for the surface contact elements has been set to reduce the computing time. The other significant factor in the mesh analysis is the transition ratio which can be defined as the controller that decides the rate at which adjacent elements grow and the values of transition ratio are between 0 and unity. In the current study it is chosen to be 0.272 as it is recommended by [170].

After, the relevant side of the hub and blade surfaces were selected to be prevented from translation as the support for the structure and then choosing the pressure side of the rotor blade for applying centrifugal forces, in terms of angular velocity which initially was imported from the rotational speed of the aerodynamic analysis. Centrifugal forces were simulated by applying an angular velocity to all elements in the model [209]. At this point it is important to emphasise that the compressed air temperature, was also imported to the structural model. Fixed time stepping was utilised and the procedure of system coupling was enabled in order to activate the technique of 2-way coupling analysis. This type of analysis evaluates the (CFD) model by extracting the aerodynamic loads using the fluid-solid interfaces and delivering it to the blades. For example the load distribution, which results from the aerodynamic load, at three different values of pressure ratio (2, 3 and 4) is presented in Figure 5.2. It shows the pressure profiles on both; the suction side and pressure side along the non-dimensional meridional coordinate. The calculations of the displacements, stresses, strains and fatigue will start once the required properties of the selected material are chosen. By transferring the required aerodynamic force from the (CFD) model to the mechanical, structural, model and setting the required time step and the convergence's accuracy, the solution will converge.

Table 5.2: RGD525 Material > Constants.

Density	7.85e-006 kg mm^-3
Coefficient of Thermal Expansion	1.2e-005 C^-1
Specific Heat	4.34e+005 mJ kg^-1 C^-1
Thermal Conductivity	6.05e-002 W mm^-1 C^-1
Resistivity	1.7e-004 ohm mm

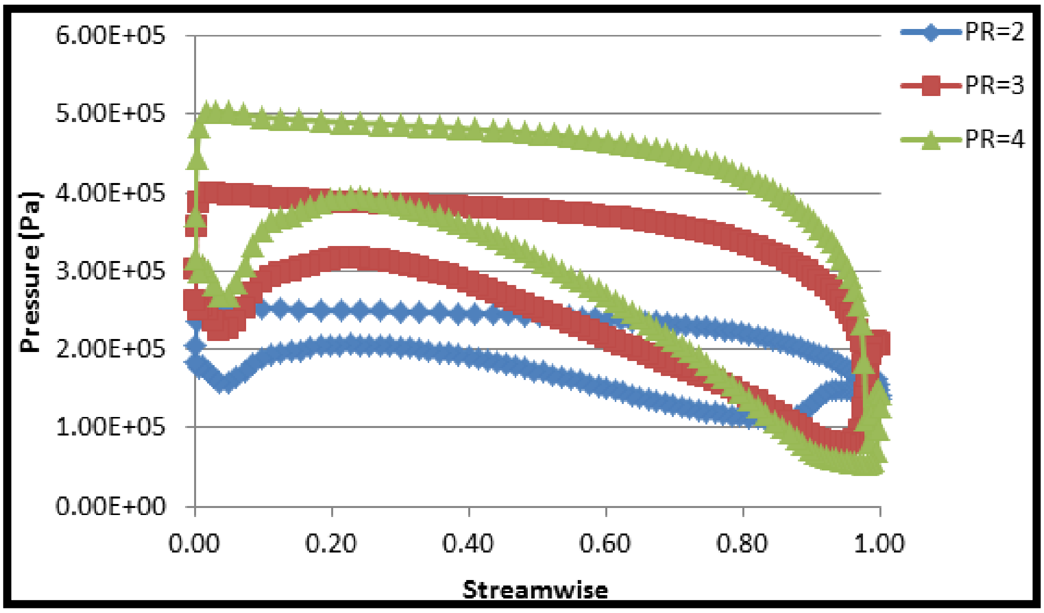

Figure 5.2: Load distribution of the (SSRT) [28].

The mesh independence for the rotor is shown in Table 5.3. Table 5.4 has some properties for one of the chosen structural mesh.

Table 5.3: Mesh independence.

Number of Element	Total Stress (MPa)
11054	225.8
13962	238.7
17051	243.8
19351	259.5
22439	260.4
26692	260.5

Table 5.4: Model > Mesh.

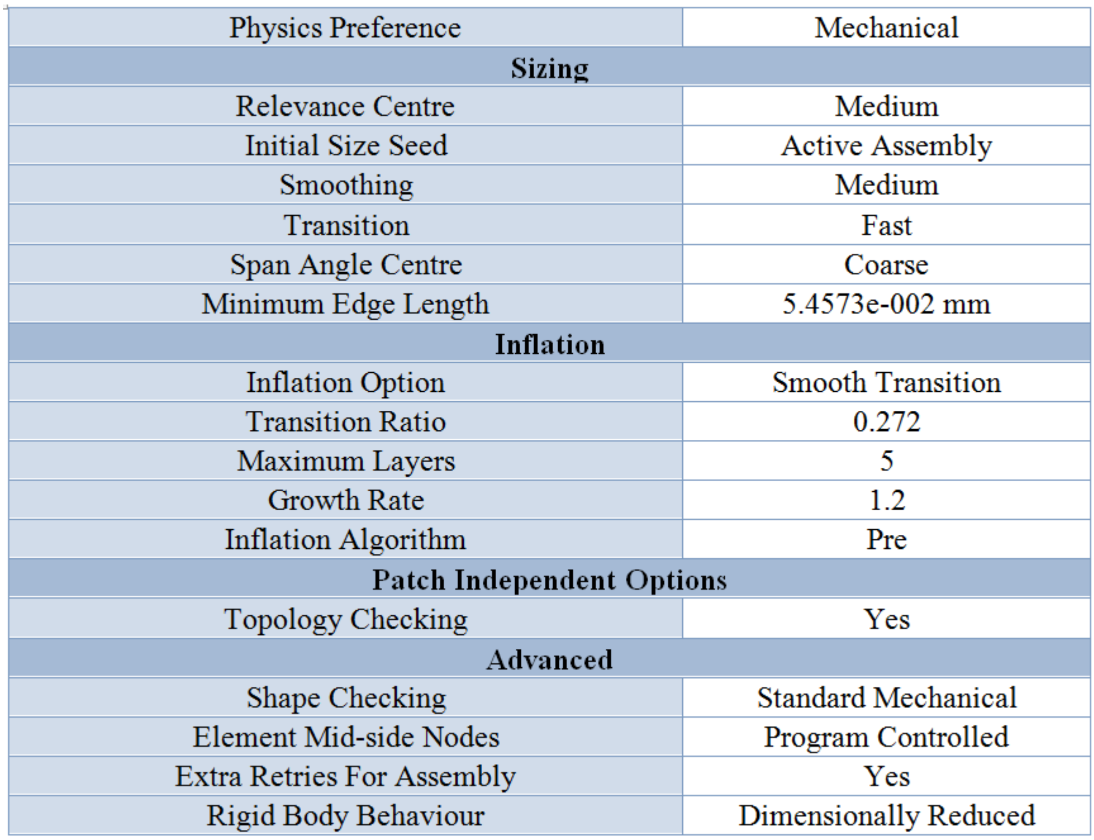

Physics Preference	Mechanical
Sizing	
Relevance Centre	Medium
Initial Size Seed	Active Assembly
Smoothing	Medium
Transition	Fast
Span Angle Centre	Coarse
Minimum Edge Length	5.4573e-002 mm
Inflation	
Inflation Option	Smooth Transition
Transition Ratio	0.272
Maximum Layers	5
Growth Rate	1.2
Inflation Algorithm	Pre
Patch Independent Options	
Topology Checking	Yes
Advanced	
Shape Checking	Standard Mechanical
Element Mid-side Nodes	Program Controlled
Extra Retries For Assembly	Yes
Rigid Body Behaviour	Dimensionally Reduced

Figure 5.3 and Figure 5.4 show the structural geometry and the mesh for the (SSRT) model, while the imported load and temperature are demonstrated in Figure 5.5 a and Figure 5.5 b respectively. From Figure 5.5 a it can be seen that the pressure side of the blade is where the incoming air flow is located, as an aerodynamic load, in order to produce the required amount

of torque. On the other hand Figure 5.5 b demonstrates the temperature distribution on the blades of the (SSRT). The maximum value is located at the tip width of the inlet rotor blades as the incoming air flow rate is at its highest value of temperature and then gradually decreased when the compressed air distributed on the other blade's area especially at the leading edge side of the blades.

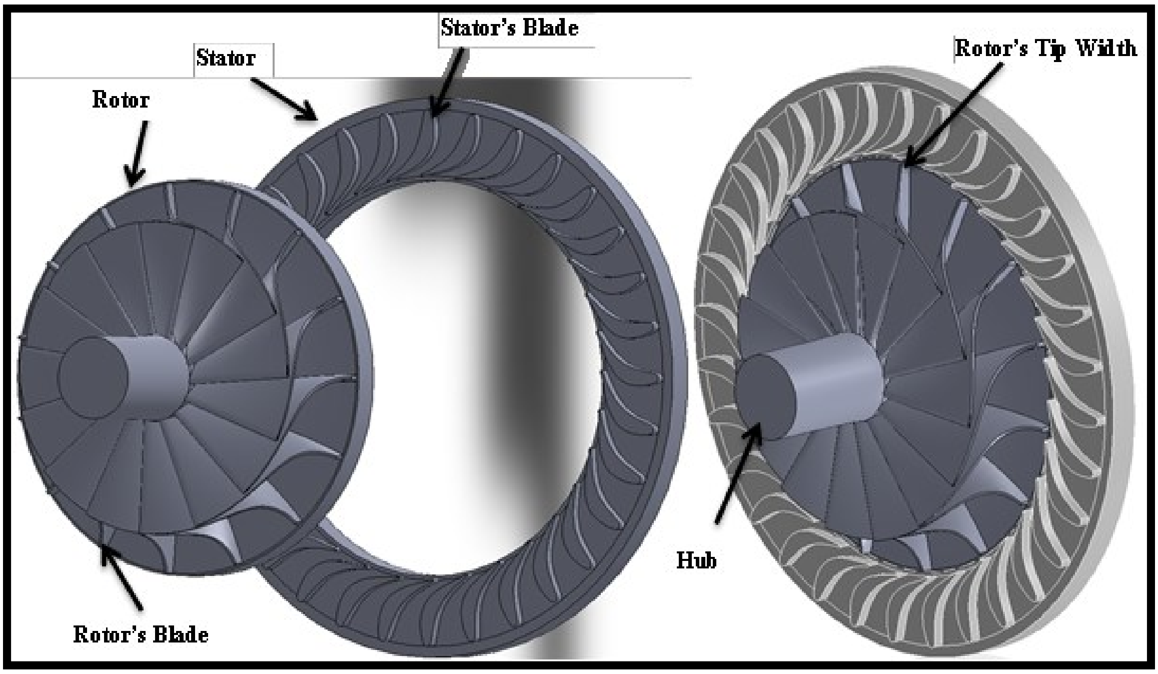

Figure 5.3: Structural geometry of the designed (SSRT) model.

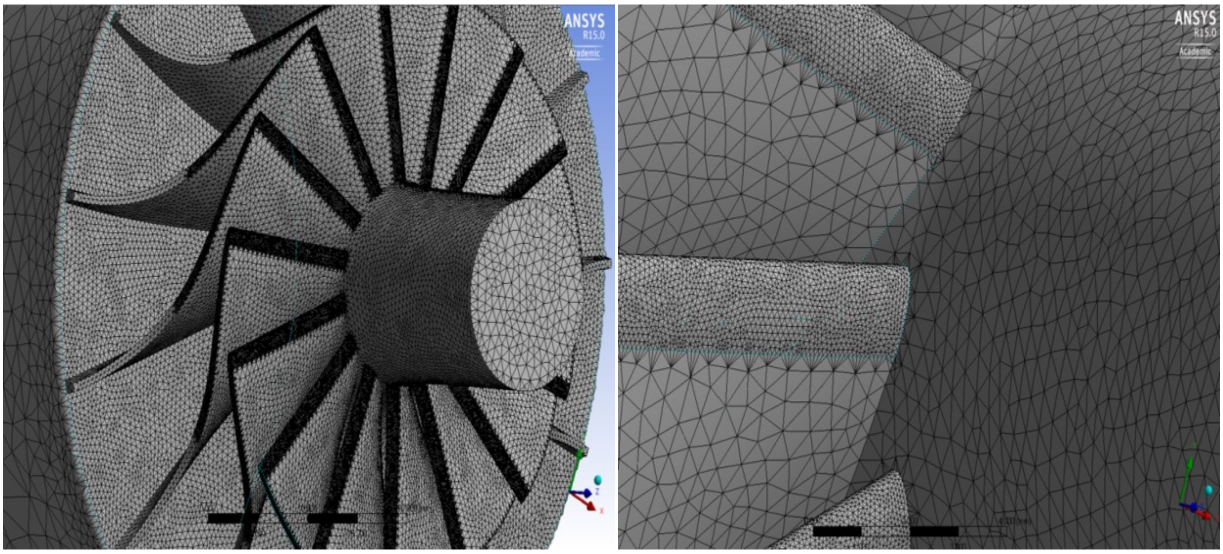

(a) **(b)**

Figure 5.4: (a) Structural mesh for (SSRT) model and (b): Closer look to the refined mesh.

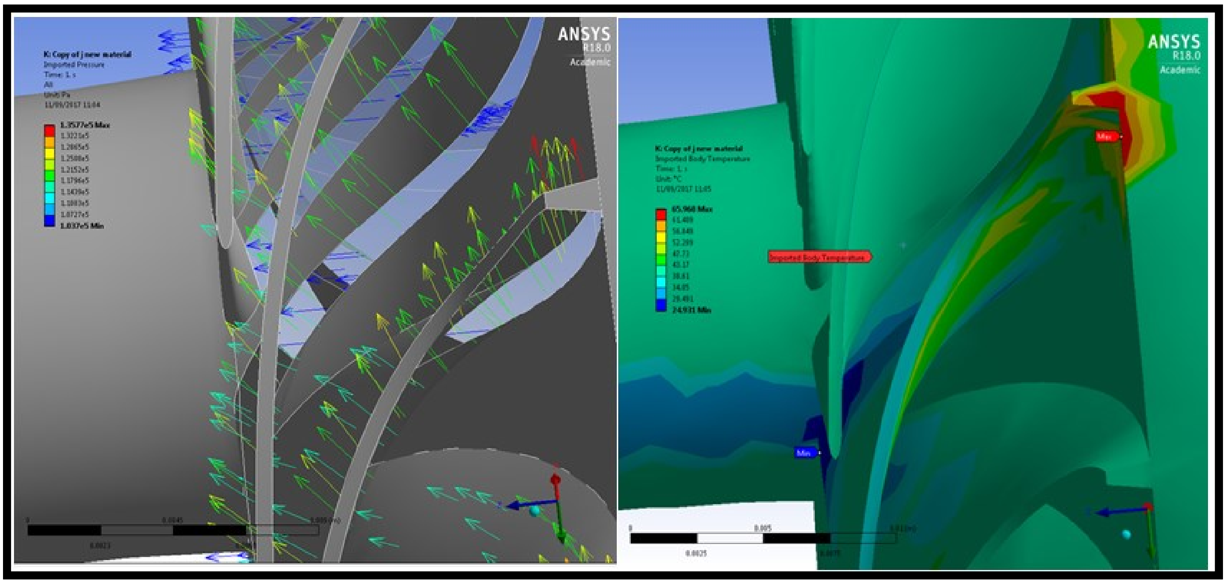

(a) **(b)**

Figure 5.5: (a): Imported loads on (FEA) model and (b): Imported temperature on (FEA) model.

5.5 Results and Discussion:

5.5.1 The Thermal Effect:

The thermal analysis plays an important role in terms of the amount of endurance of structural stresses because the blade material (RGD 525) is highly affected by the temperature of the working fluid. In this analysis the investigated range of temperature was only between 25 ^{o}C to 65 ^{o}C, as it is shown in the next few figures. This temperature range represents the temperature of the inlet air which enters the turbine. Also, it needs to be highlighted that only the rotor has been structurally analysed because it is subjected to higher stresses and deflections.

Figure 5.6 shows the distribution of stresses and the produced deformation. From these figures it can be noticed that the air inlet temperature has an important effect on each; the stress, the deformation and their distribution on the rotor as well as the safety factor. For instance, the maximum value of the equivalent stress at 25 ^{o}C air temperature was only about

39.7 MPa but the value became about 51.6 MPa when the inlet air temperature was increased to be 65 ^{o}C. This confirms the direct relationship between the thermal and the structural stresses. Moreover, in both cases, the most affected regions in the turbine with high stress concentration were those blade- hub connections as a result of being the only connecting region which can be considered as simply support beam. Also, the maximum principle stress which reached only 35.19 MPa at 25 ^{o}C air inlet temperature and became around 42.47 MPa at 65 ^{o}C air inlet temperature (see Figure 5.6 B) for the same reason mentioned above. The maximum deformation, which is located on the shroud region the blade free side, at 25 ^{o}C was only about 0. 43 mm and the corresponding value at 65 ^{o}C is around 1.01 mm. It is true that the difference between these two values is small but this value is much appreciated when the tip width of the blade is only about 1.69 mm. Similarly, the higher temperature of the inlet working fluid to the rotor led to the lower overall value of the safety factor, which was calculated based on the Max Shear Stress theory, and vice versa. The safety factor ranged between 2 to 3 while the minimum was less than one and it is located where the higher concentration stresses positioned.

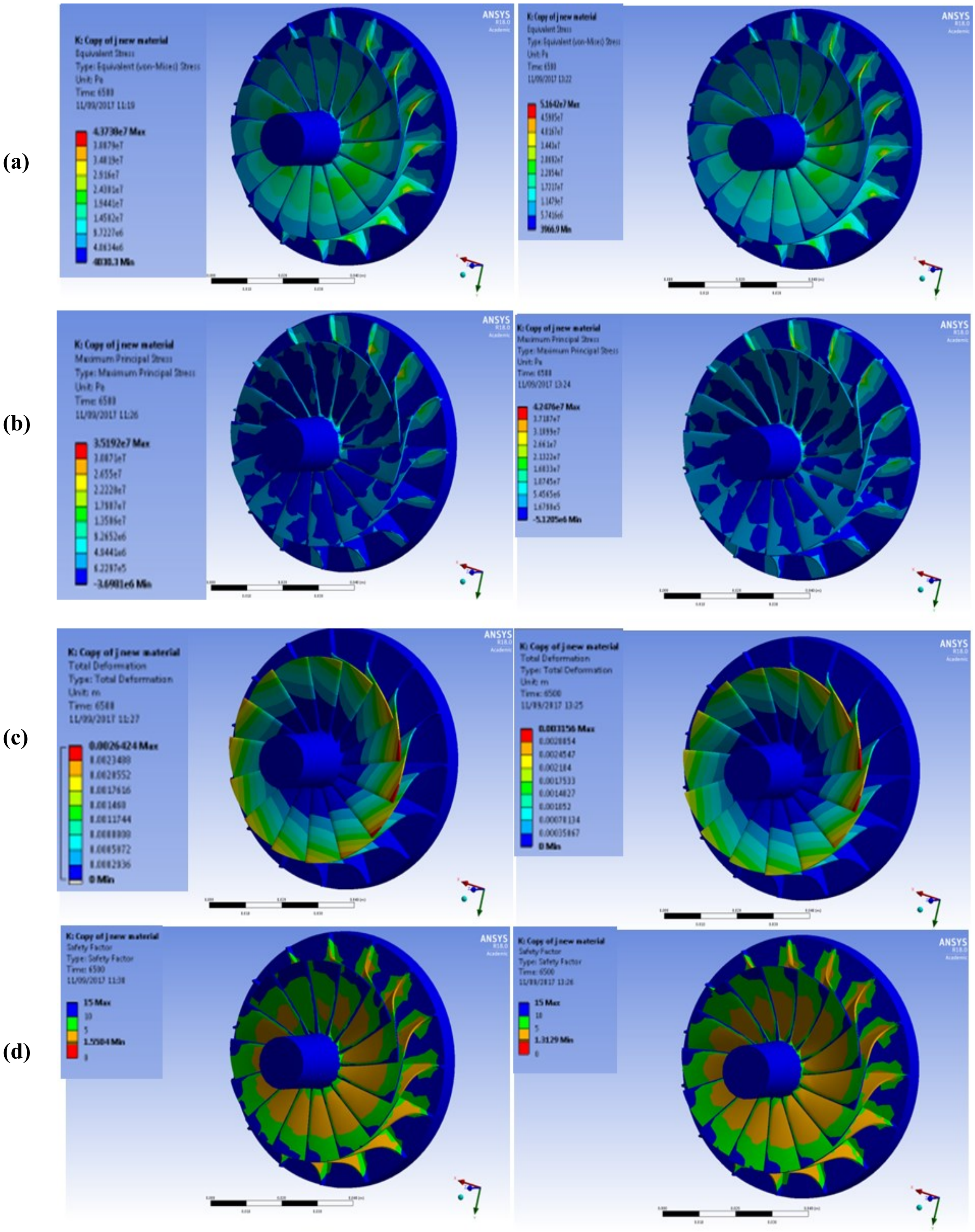

Figure 5.6: The stress tool (Equivalent stress (a), Maximum Principle stress (b), Total Deformation (c) and Safety Factor (d)), respectively, in the rotor at two different values of inlet air temperature; 25 ^{o}C (LHS) and (RHS): 65 ^{o}C.

5.5.2 The Fatigue Effect:

Fatigue is one of the main important phenomena which need to be carefully examined in any rotating part, Figure 5.7, shows a constant fully reversed type of load where material failure occurs due to applying repeated load even though that load was lower than the material strength. In this section a complete evaluation for the fatigue analysis, based on Goodman correlation 5.15, for the (SSRT) is investigated using Finite Element Analysis in ANSYS Academic 18 software.

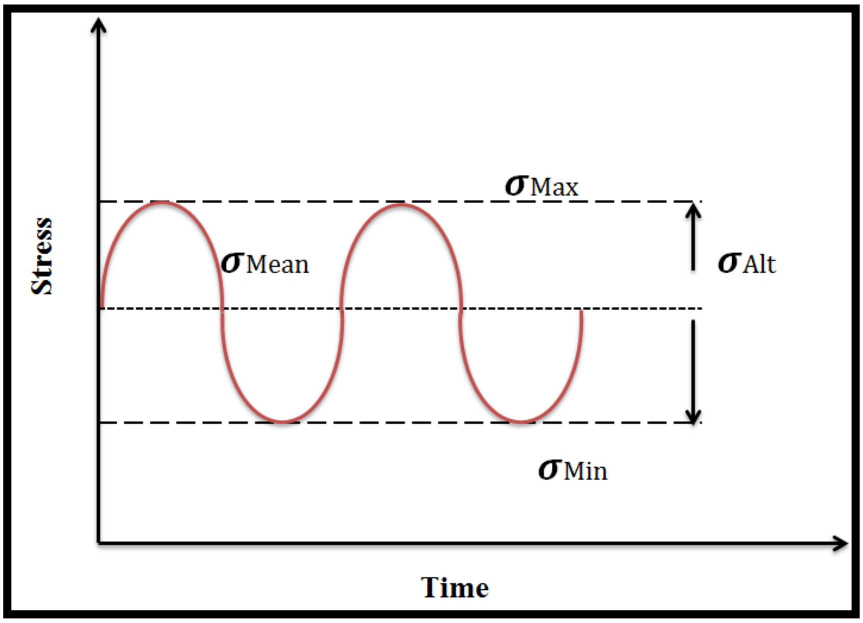

Figure 5.7: Simultaneous mean and cyclic loading.

$$\frac{\sigma_{Alternating}}{S_{Endurance\ limit}} + \frac{\sigma_{Mean}}{S_{Ultimate\ strength}} = 1 \qquad (5.13)$$

This cyclic loading can be expressed using a number of ways, the most common one being to maintain the alternating stress value σ_{alt} and the stress ratio, $\sigma_{min}/\sigma_{max}$.

After completing the required setting such as the definition of the new material, RGD525, and characterizing the S-N curve, based on the experimental fatigue test carried out (more details in the next chapter), that was established based on the following relations:

$$\frac{\sigma_{Max}\Delta\varepsilon_t}{2} = \sigma_f\varepsilon_f\left(2\varepsilon_f\right)^{b+c} + \frac{(\sigma_f)}{E}\left(2\varepsilon_f\right)^{2b} \tag{5.14}$$

Whereas the fracture time at specific stress can be determined using Larson-Miller equation:

$$\log(t) = b_0 + \frac{b_1}{T} + \frac{b_2\log(\sigma)}{T} + \frac{b_3(\log(\sigma))^2}{T} + \frac{b_4(log(\sigma))^3}{T} \tag{5.15}$$

On the other hand, the fatigue damage can be calculated based on the following equation:

$$D_f = \sum_{i=1}^{n}\frac{n_i}{N_{fi}} \tag{5.16}$$

Where N_f is the number of cycles accumulated at stress Si and the failure occurs when Damage fraction D_f equals 1, E is the modulus of elasticity, $\frac{\Delta\varepsilon_t}{2}$ is the total strain value, σ_f is fatigue strength coefficient, ε_f is fatigue ductility coefficient and b and c are fatigue strength exponent and fatigue ductility exponent respectively and finally, t and T are the fracture time and temperature value in Kelvin [210].

Figure 5.8 presents the results of fatigue analyses for the rotating part of the (SSRT) at the two extreme investigated values of the inlet compressed air temperature; 25 °C and 65 °C. The first examined factor was the life which indicates an important influence of the thermal activities on the overall performance of the rotor, from design life of about 1.15 e5 cycle at 25 °C to 0.767 e5 at 65 °C. In this type of analysis when the amplitude is maintained constant, the fatigue life will be considered if the highest alternating stress defined in the S-N curve is lower than the equivalent alternating stress.

The fatigue damage, as defined in equation 5.15, that might happen to the rotor during its operating period was also determined in this study and it confirmed the same results which showed that the blade- hub connection region is the weakest section in the rotor regardless the temperature value. The maximum damage at 25 °C reached about 56908 (unit less) and similarly for the 65 °C it was around 7.35e+006 which show how the 40 °C difference in the temperature of the working fluid produces higher damage. Regarding the biaxiality factor which can be defined as the ratio between the maximum principle stresses to the minimum principle stress with the principal stress close to zero discounted, it can be noticed that the maximum biaxiality reached 0.95 and 0.99 at the 25 ^{o}C and 65 ^{o}C respectively. Furthermore, it can also be seen from the relevant contour that the maximum biaxiality was concentrated where the two perpendicular axes X axis & Z axis for the both investigated temperature values; 25 ^{o}C and 65 ^{o}C. This can be explained by the flow of the compressed air enters the (SSRT) radially X axis and leaves axially Z axis (referring to the relevant figure).

The fourth figure presents equivalent alternating stress which is another important factor in the fatigue analysis. The main advantage of this factor is that it generally covers all the related fatigue calculations regardless of any property of the fatigue material (not like the tensile strength which results from static material properties which some other mean stress theories depends). Specifically, the ultimate values of this factor have reached about 54.7 MPa and 57.9 MPa at the two examined values of compressed air temperature; 25 ^{o}C and 65 ^{o}C respectively.

Finally, the fatigue safety factor, which is differs from the one calculated at static load because of the fact that it is produced by alternating the load on an element over time. This factor is a fatigue failure at a certain designed life. It can be seen that the minimum value at 25 ^{o}C was around 3.9 and became less than 0.1 when the compressed air entered the stage at 65 ^{o}C. Having said that, the maximum factor of safety were about double where most of the other regions in the rotor have relatively accepted values of the safety factor, which was ranged from 55 at 65 ^{o}C to 3 at 25 ^{o}C.

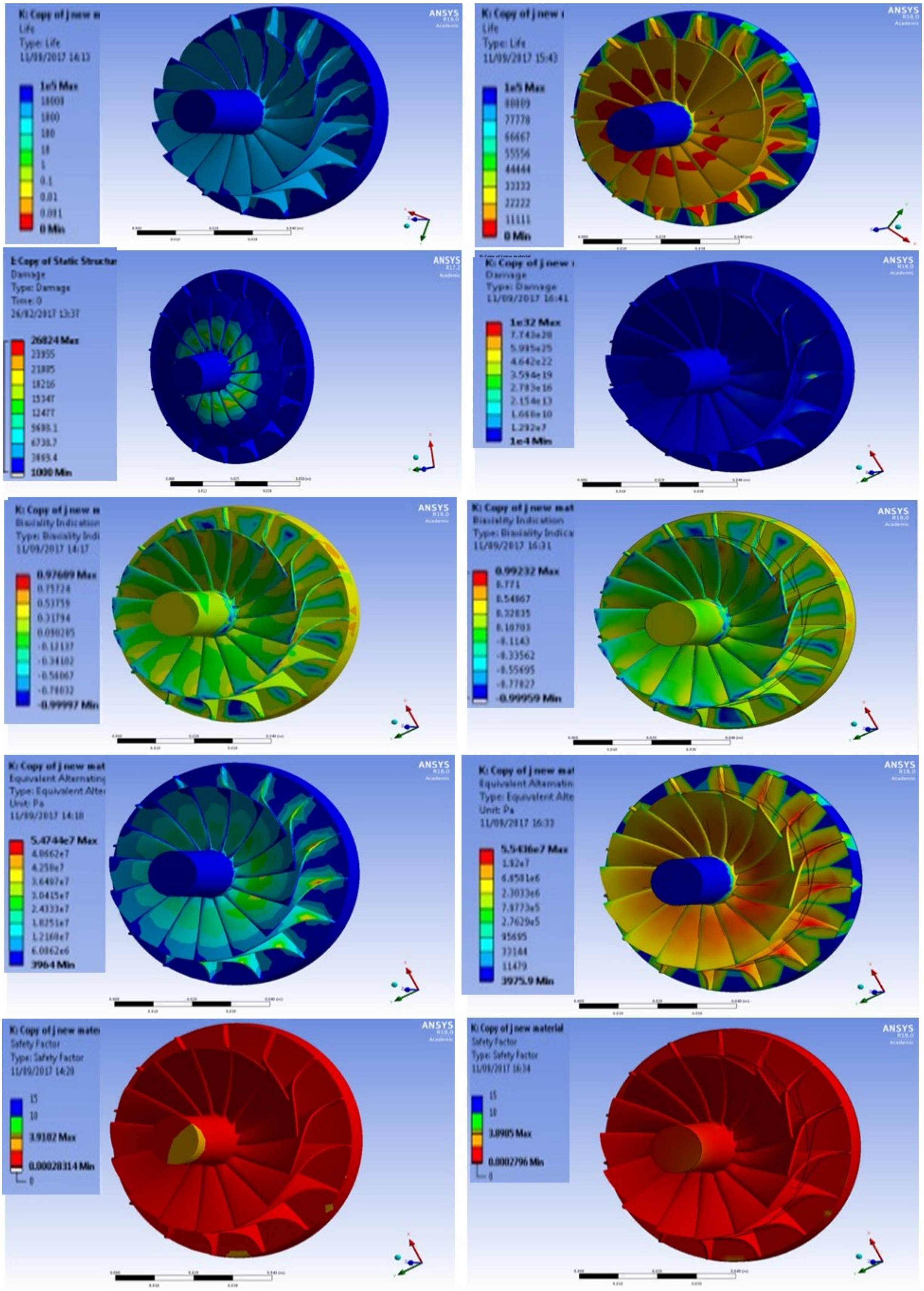

Figure 5.8: An example of fatigue tool (Life, Damage, Biaxiality Indication, Equivalent Alternating Stress and Safety Factor), up to down respectively, in the rotor at two different values of inlet air temperature; 25 °C (LHS) and (RHS): 65 °C.

5.5.3 The Speed Effect:

The effect of the rotor rotational speed on the stress, the deformation and the fatigue life is analysed and presented in the next figures. Figure 5.9 shows the variation of Von Misses stress with the rotor rotational speed at different compressed air inlet temperature. It is clear that the Von Misses stress increases as the rotational speed increases. For example, increasing the rotational speed from 60 krpm to 80 krpm increases the Von Misses stress by 12.5%, 14% and 17% at 25, 45 and 65 ^{o}C respectively. However, at constant rotational speed, increasing the temperature results in increasing Von Misses stresses significantly where at 80 krpm, increasing the temperature from 25 to 65 ^{o}C increases the Von Misses stress by 37%.

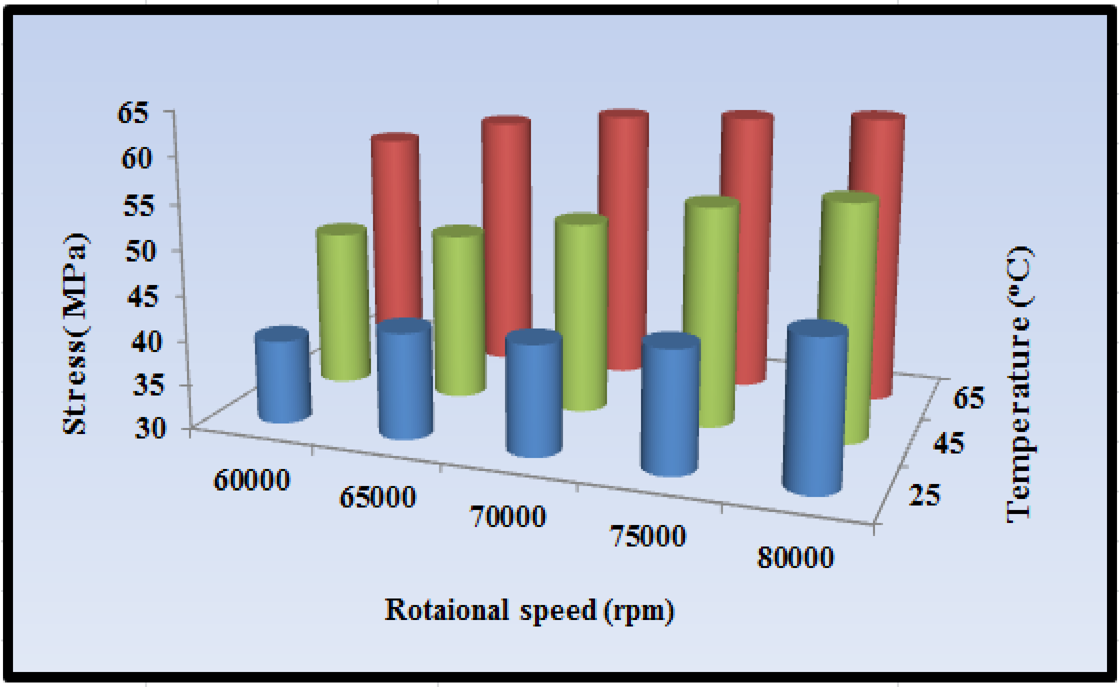

Figure 5.9: The effect of both; inlet air temperature and the rotor rotational speed on the Von Misses stress.

Figure 5.10 shows the effect of the rotor rotational speed on the maximum deformation which occurred at the tip of the blades. The maximum deformations values reached at 60 krpm were about 0.401, 0.592 and 0.874 mm when the fluid temperature values were 25, 45 and 65 ^{o}C respectively. At 80 krpm, these values became around 0.52, 0.63 and 0.87 mm respectively.

The relatively small values of deformation are because of the overall small scale of the investigated turbine. Regarding the deformation variation with fluid temperature, it can be seen that little effect on the rotor's deformation was observed. This might be because of the material's properties which is able to withstand this range of fluid temperature.

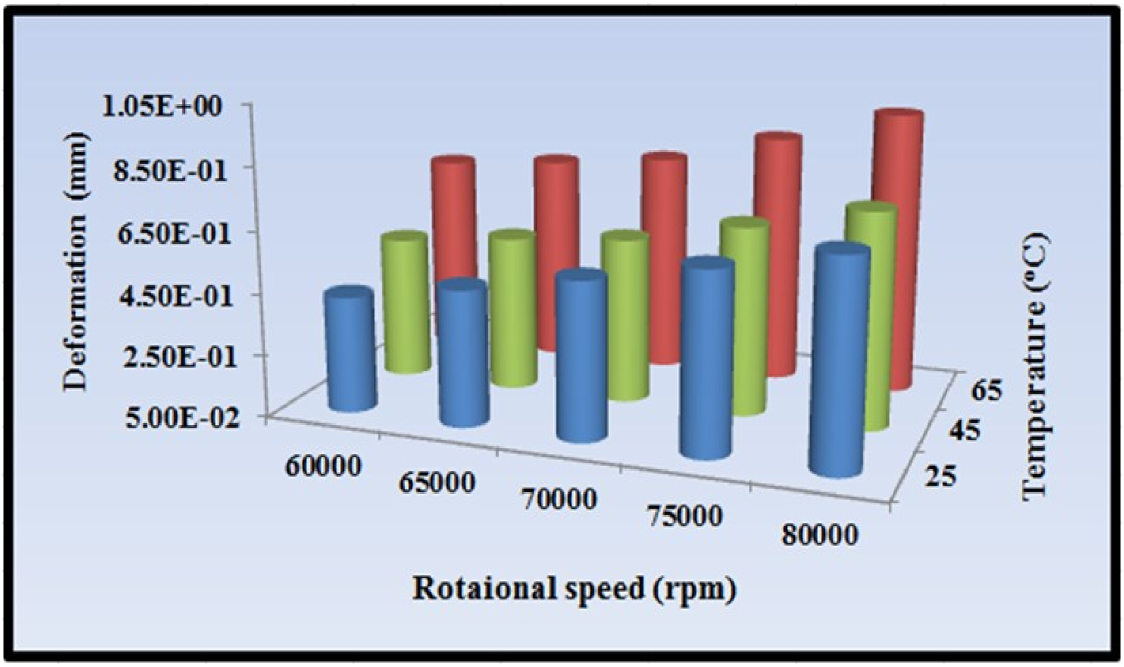

Figure 5.10: The effect of both; inlet air temperature and the rotor rotational speed on the maximum deformation.

Figure 5.11 shows the effect of the rotor rotational speed at the three inlet air temperature on the fatigue life of the rotor. It can be seen from this figure that both factors; the rotational speed and the temperature, have a direct effect on the number of cycles which the rotor is supposed to work without failure because of the fatigue. For example, the numbers of cycles within the endurance limit at rotor rotational speed of 60 krpm were about 0.14 e5, 0.88 e4 and 0.78 e4 when the compressed air temperature was 25, 45 and 65 ^{o}C respectively. While the relevant values at 80 krpm were only about 0.58 e4, 0.53 e4 and 0.5 e4 cycles at 25, 45 and 65 ^{o}C respectively. The related values of fatigue life at 70 krpm were approximately in the middle between the other two temperature values. These values are around 0.109 e5, 0.71 e4 and 0.59 e4 for the inlet compressed temperature values of 25, 45 and 65 °C respectively. Also, it is clear from this analysis that the current achieved results are not satisfactory for this application and the current design needs to be enhanced.

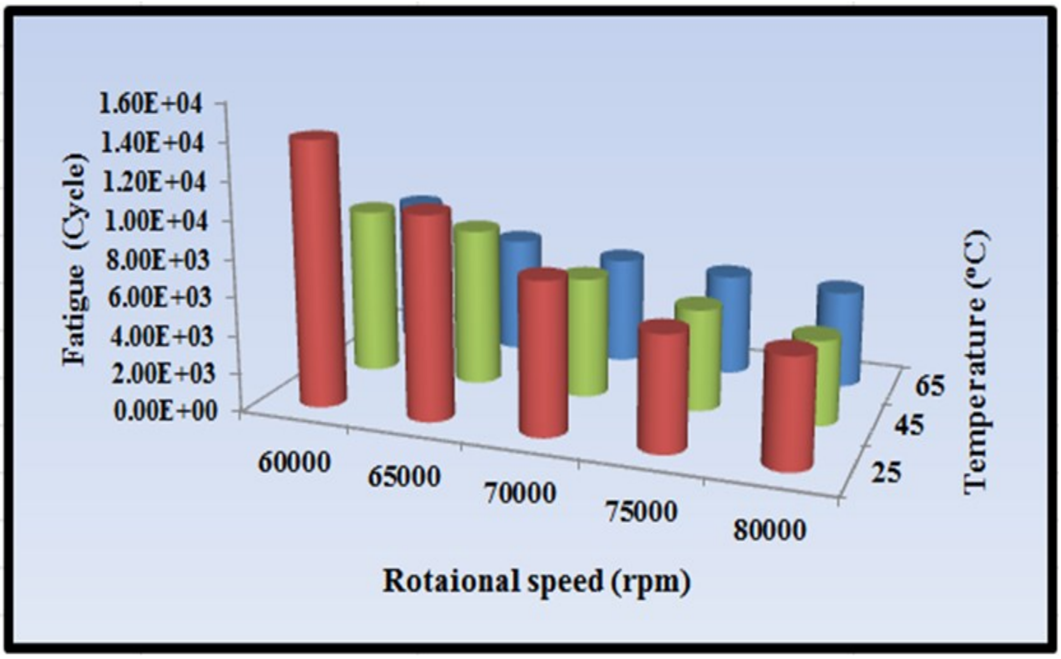

Figure 5.11: The effect of both; inlet air temperature and the rotor rotational speed on the maximum deformation.

5.6 Multidisciplinary Optimization of (SSRT):

The aerodynamic optimization for the (SSRT) was successfully carried out in the previous chapter leading for highly efficient small scale radial turbine. However, in order to ensure mechanically reliable turbine, the (SSRT) needs to be evaluated from the structural view point simultaneously using the (FEA) technique. For this reason, the optimized rotor shape was transferred to the structural analysis, as described previously, and then a number of critical factors were parametrized in order to enhance its structural shape and as a result decrease the relevant stresses and deflection. This approach of optimization combines the (CFD) modelling with (FEA) technique to achieve high turbine efficiency and power output requirements and at the same time maintain stress and deflection within the allowable values. The selected input parameters are the blade angle and thickness along the blade, the solid mass and hub offset while the output parameters are the turbine output power and efficiency (from the aerodynamic analysis), equivalent maximum stress and deflections and the turbine life time (from the structural analysis). The final turbine shape was then successfully obtained by using the multi-objective multidisciplinary optimization [211] and [212] based on compromise between the selected parameters. Figure 5.12 displays a schematic feature of the multi-objective multidisciplinary optimization of (SSRT).

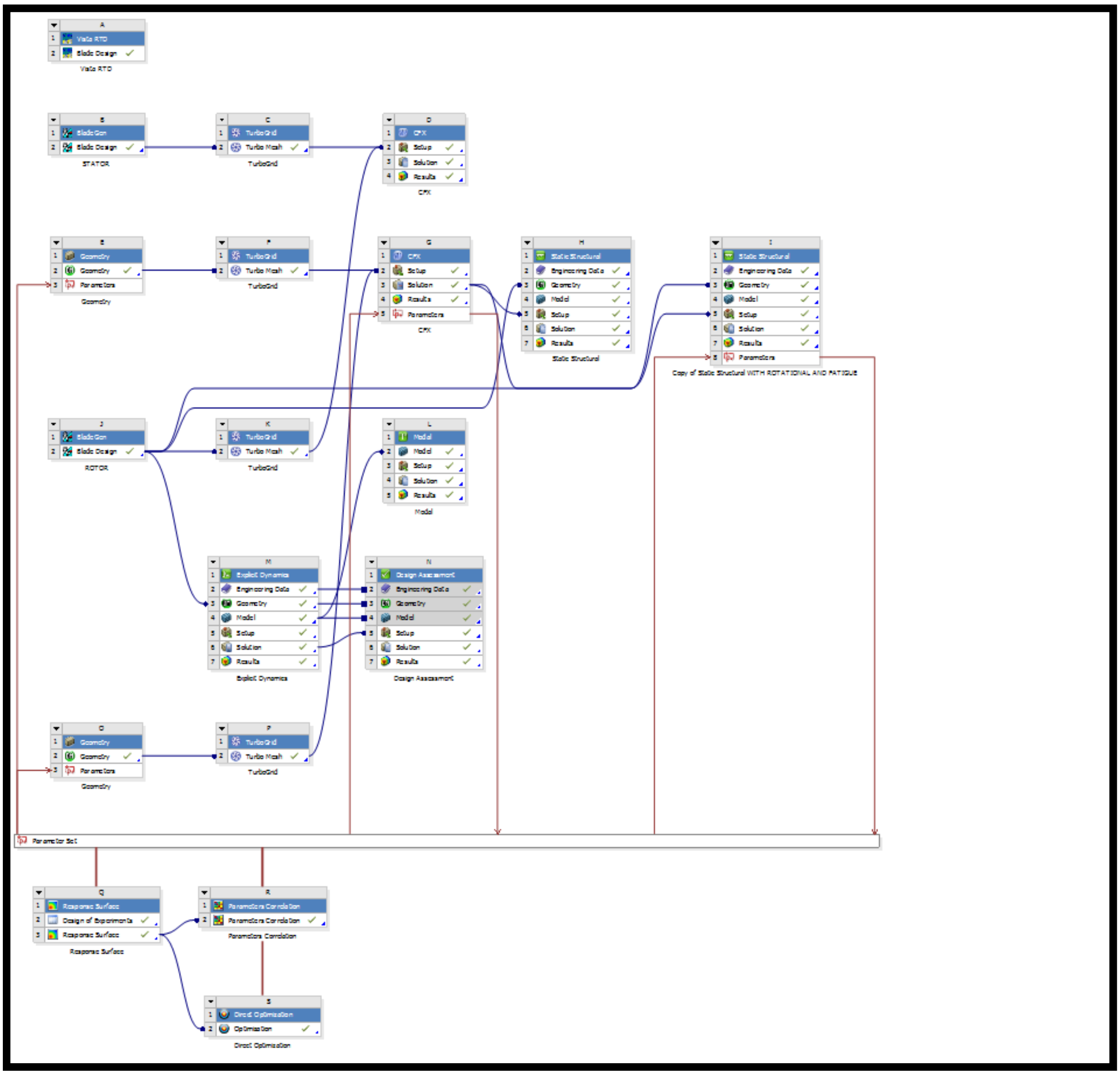

Figure 5.12: Schematic of the 3D optimization multidisciplinary process of the (SSRT) in ANSYS Workbench.

Figure 5.13 shows the parameters parallel chart for the (SSRT) using the selected parameters for the (SSRT) Multidisciplinary optimization. In order to determine the critical parameters, Figure 5.14 shows the sensitivity of the output parameters for each of the input selected parameters. From this figure it can be seen that the most critical parameters were: (1) the rotor rotational speed which directly affects the maximum equivalent stress and the fatigue of the turbine rotor, (2) the rotor blade angle which shows a high effect on each the turbine efficiency and at the amount of stress exerted on the rotor; and (3) the blade thickness which shows more significant effect on the stress value than the other output parameters in regard the aerodynamic performance.

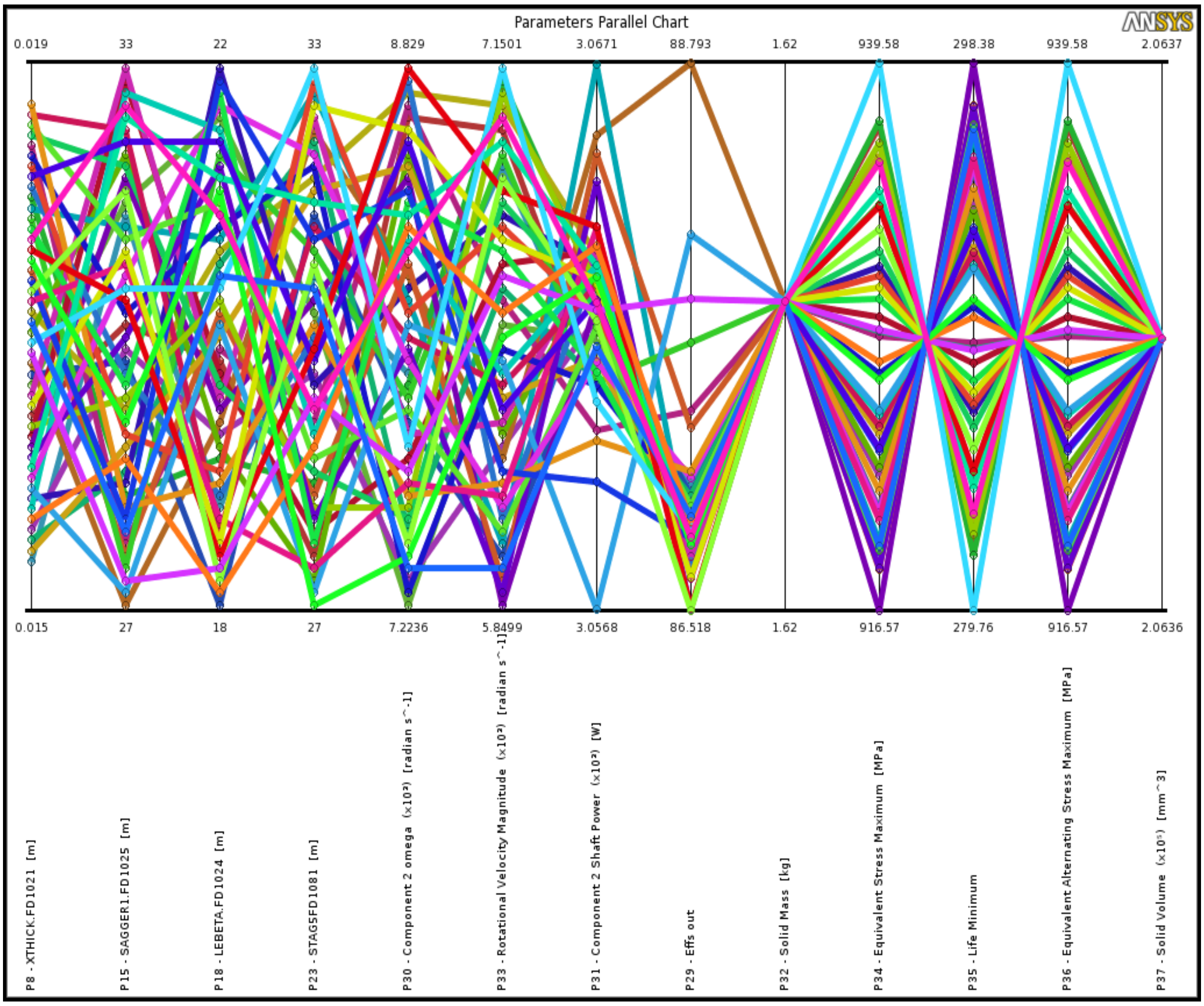

Figure 5.13: Parameters parallel chart for the (SSRT) using the Multidisciplinary optimization.

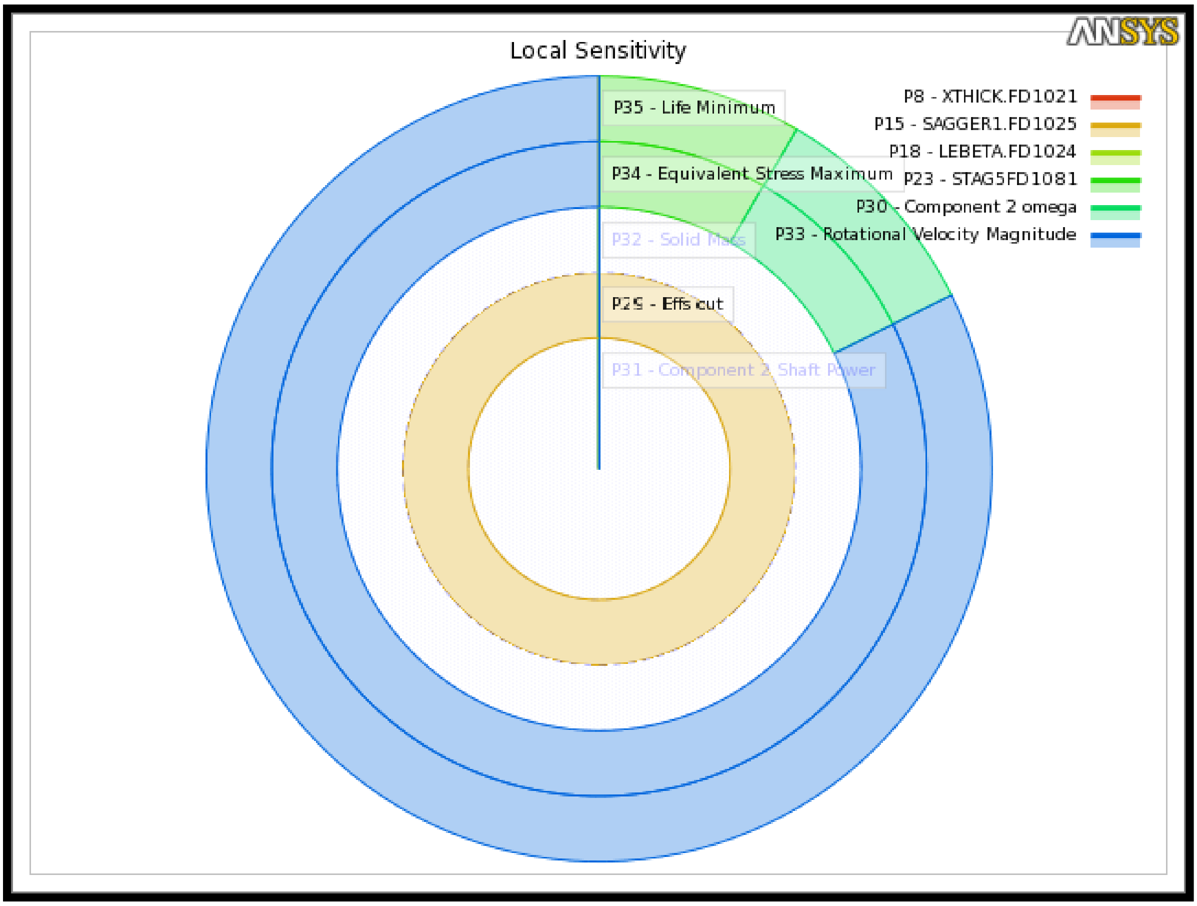

Figure 5.14: The local sensitivity of the output parameters with respect to the input parameters.

The precision and quality of the chosen model has been assessed based on what is known as the goodness of fit for the optimized rotor is exposed in Figure 5.15. It is clear from this figure that the nominated method showed an accurate result when the coefficient of determination equals to unity and maximum relative residual close to zero.

Figure 5.16 presents the response surface diagram for the effect of both the rotor rotational speed and the blade thickness on the rotor fatigue life where increasing the 1st mentioned parameter and decrease the 2nd one lead to lower value of the rotor fatigue life.

Figure 5.17 shows that the rotor efficiency decreased with increasing the blade thickness and decreasing the outlet flow angle.

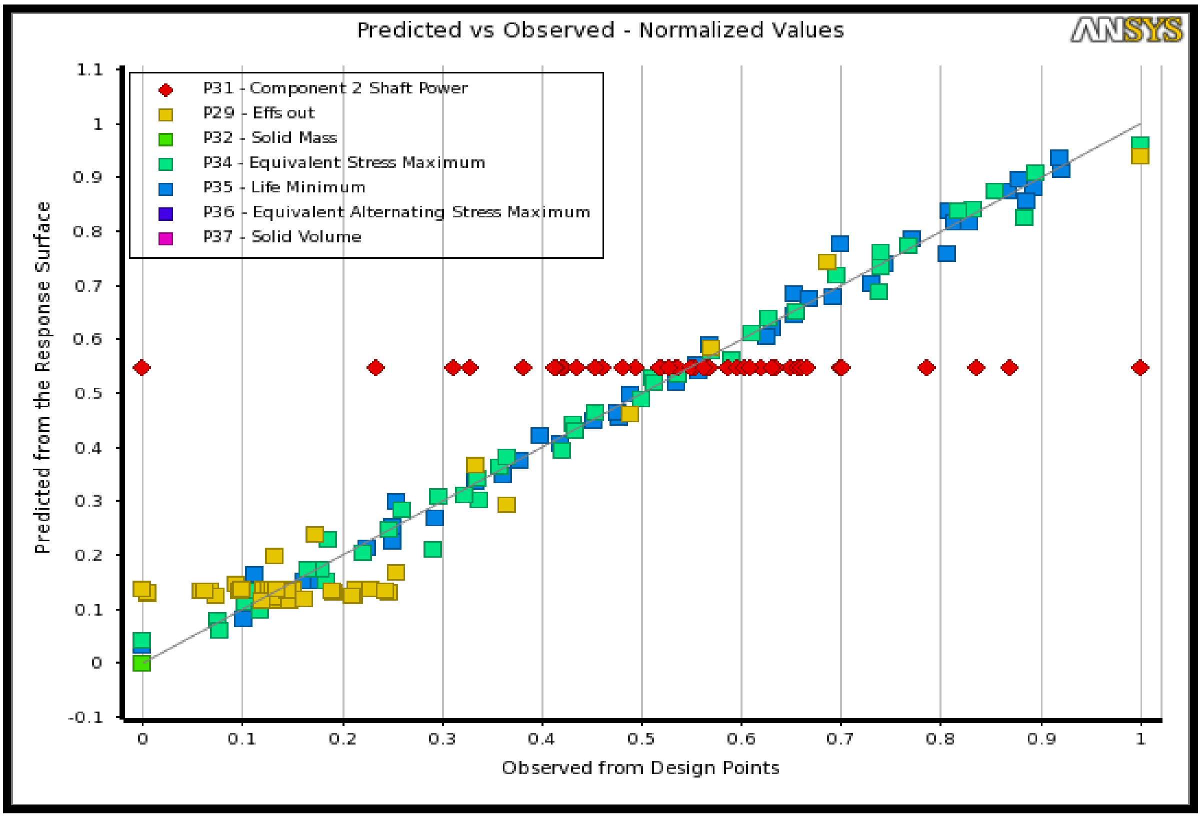

Figure 5.15: The predicted and observed efficiency and power output for the (SSRT) in terms of goodness of fitness shape.

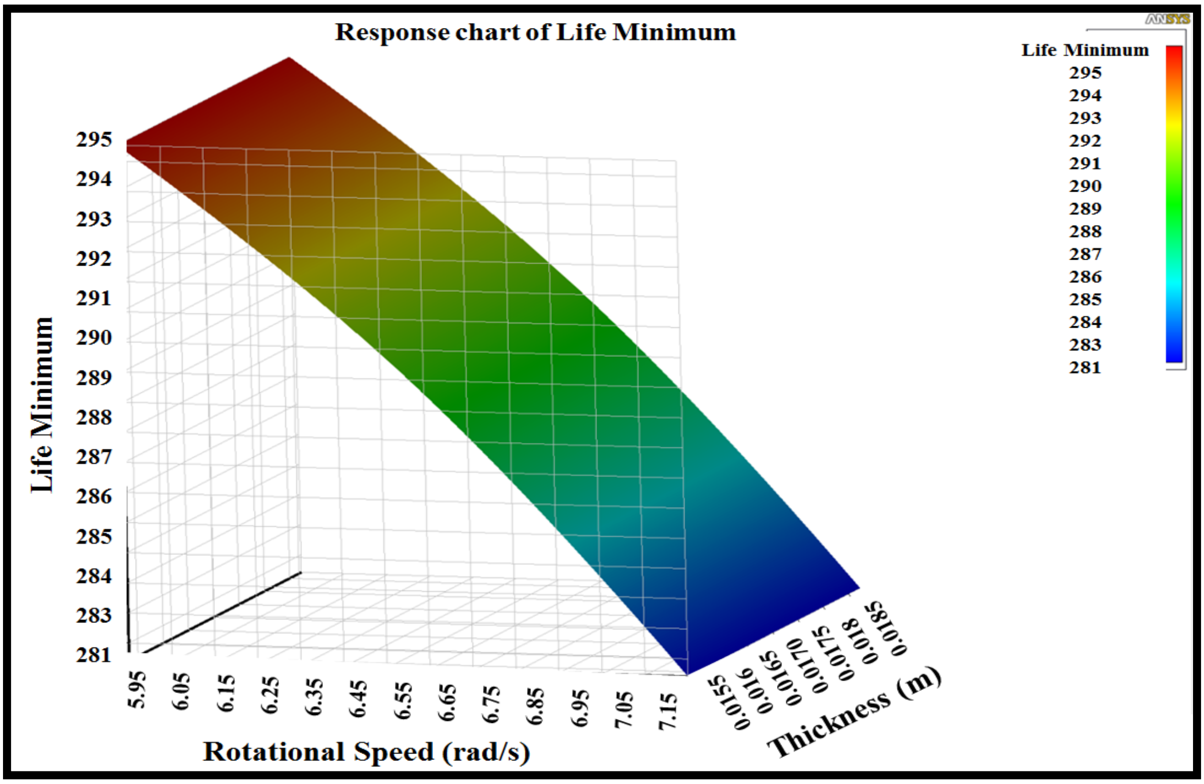

Figure 5.16: The effect of the most influence input parameters on the fatigue life.

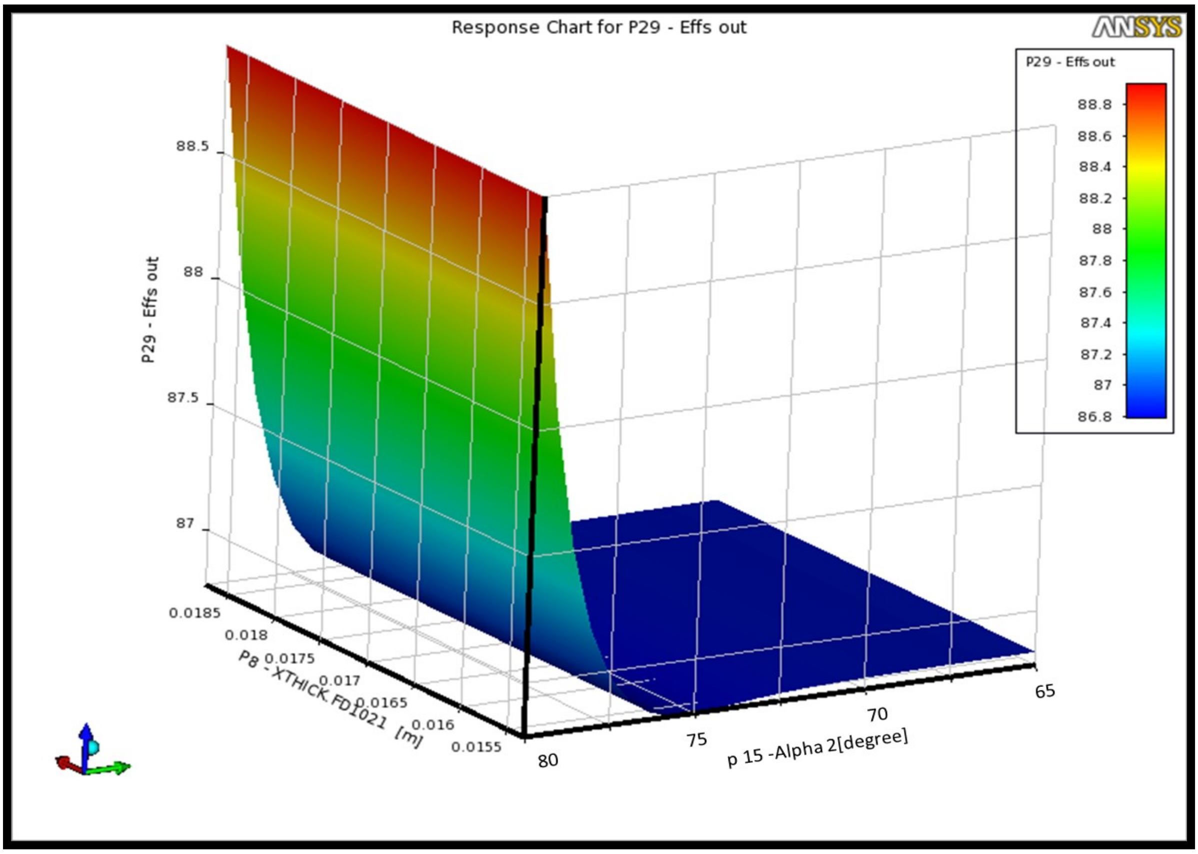

Figure 5.17: The effect of the blade thickness and the outlet flow angle on the rotor efficiency.

From the previous two figures it is noticed that the rotor showed a noticed enhancement in terms of the most important two factors from structural analysis point view, the maximum equivalent stress and the fatigue life where the first output parameter decreased leading to higher number of cycles. Having said that, a decrease of around 2%, in the overall turbine efficiency was the penalty.

Finally, Figure 5.19, Figure 5.20 and Figure 5.21 show the values and the distribution of equivalent stress, the fatigue life and the displacement respectively for the optimized turbine. Figure 5.18 shows the trade-off between the rotor tip width, efficiency and output power produced by ANSYS Academic software. It can be seen that while there are many design points, which be a design solution, there are only few points that are feasible points that can satisfy the required objectives and constraints at simultaneously.

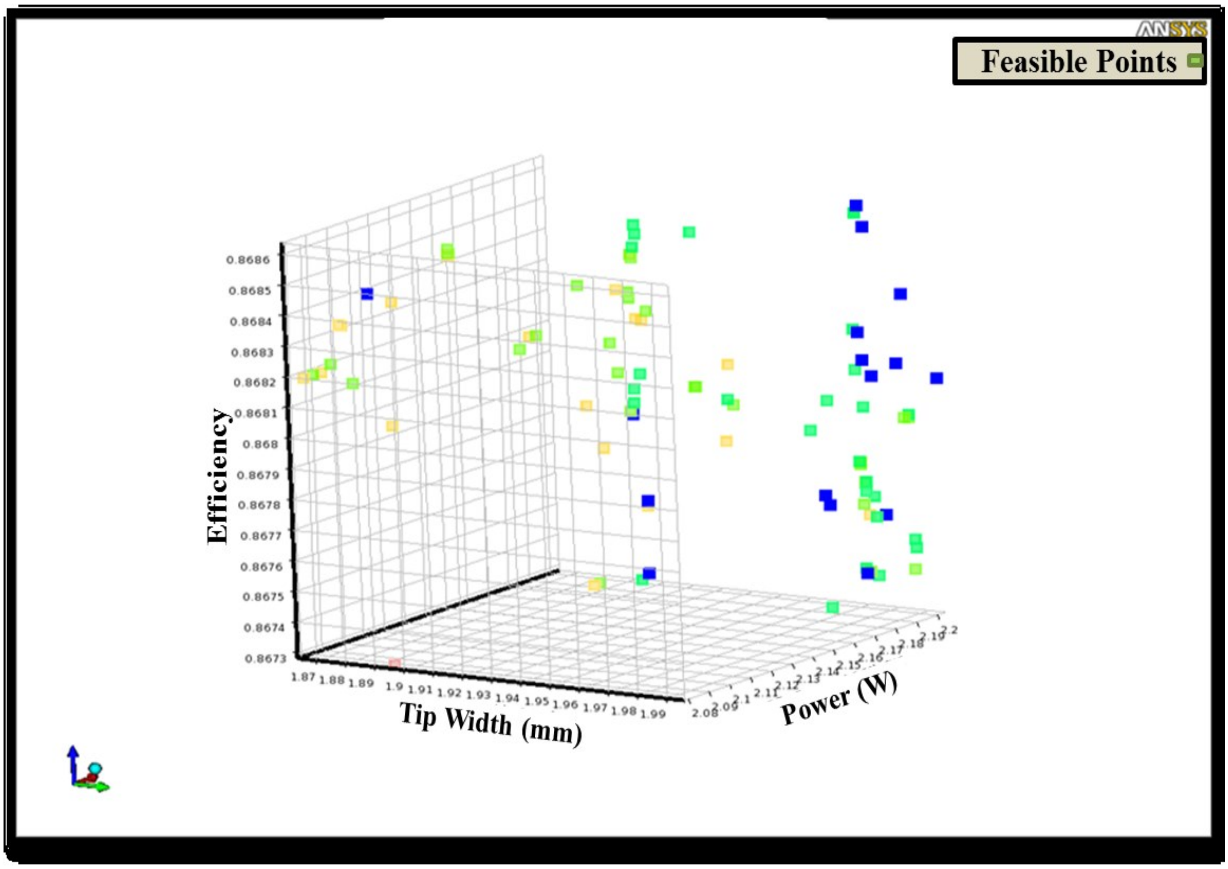

Figure 5.18: Samples of the tradeoff chart between the rotor tip width, output power and efficiency.

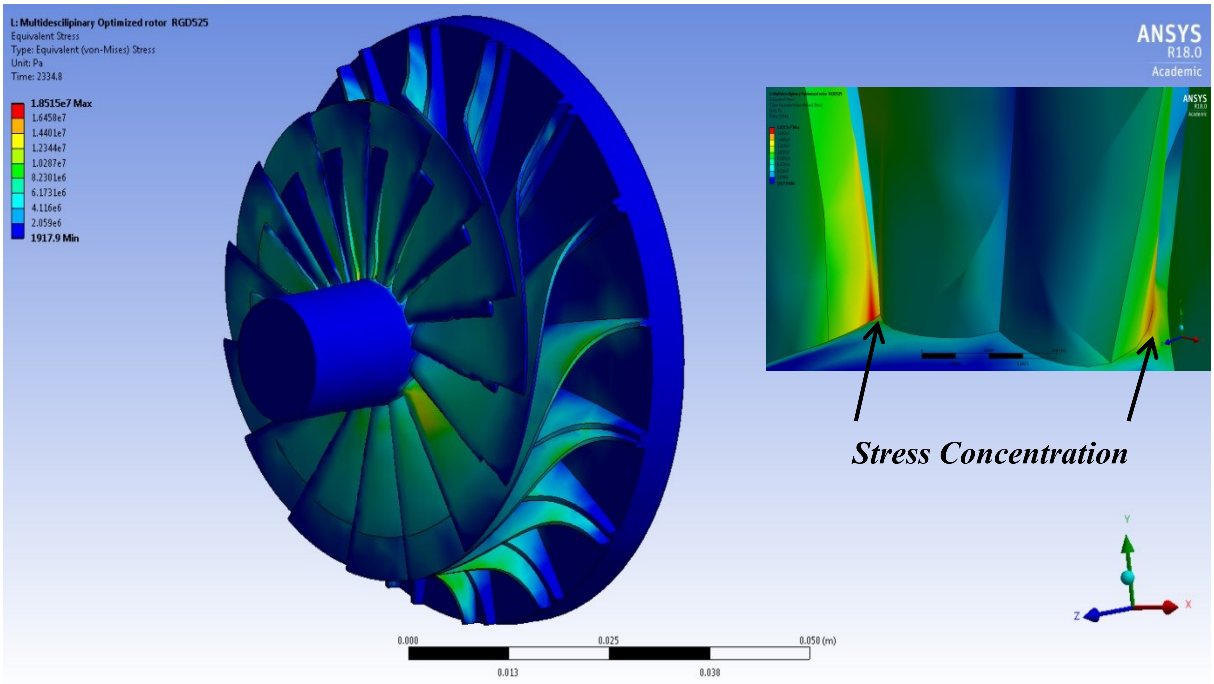

Figure 5.19: The maximum equivalent stress value for the optimized rotor of the (SSRT).

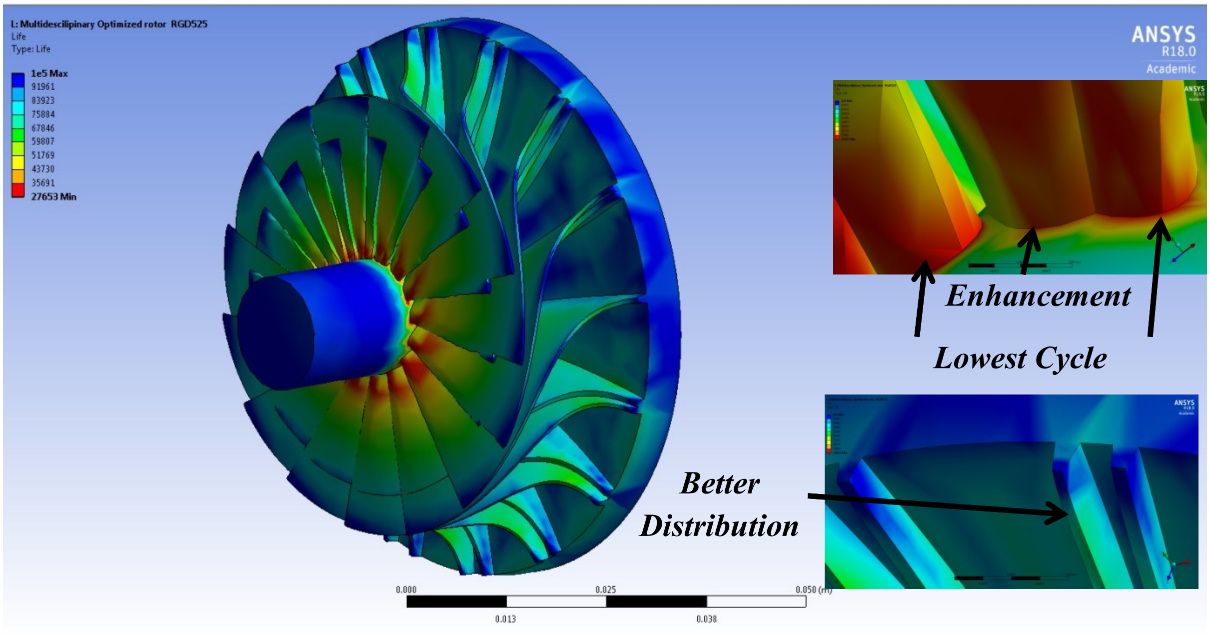

Figure 5.20: The fatigue life for the optimized rotor of the (SSRT).

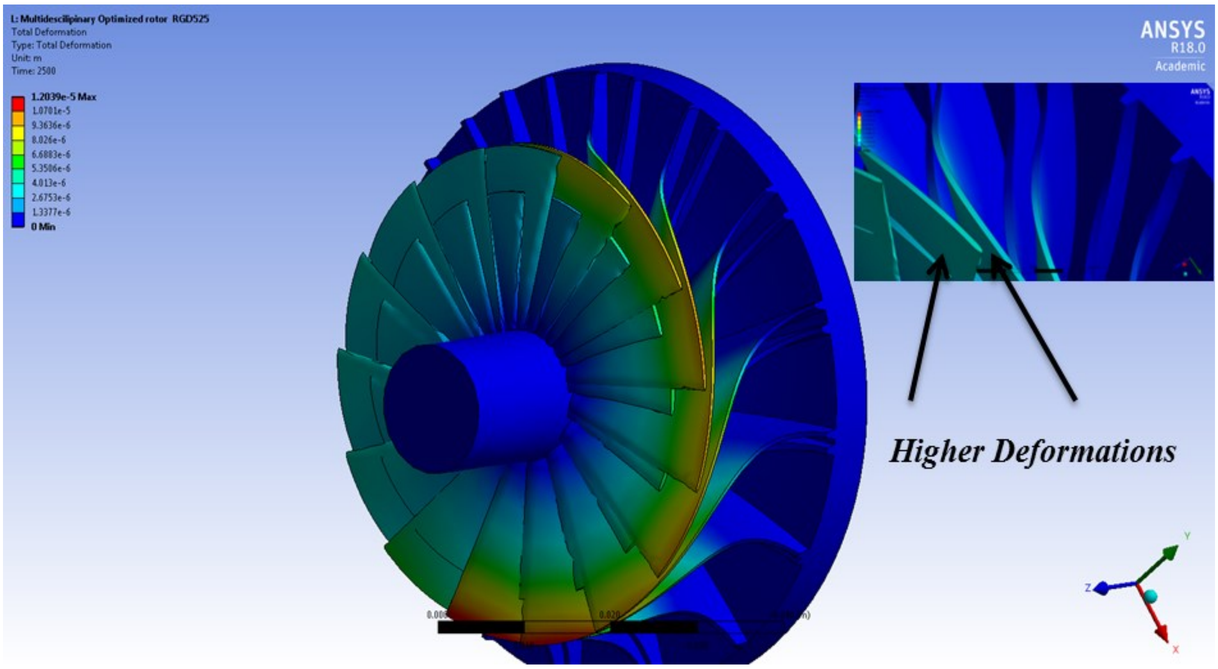

Figure 5.21: The total deformation for the multidisciplinary optimized rotor of the (SSRT).

Table 5.5 presents the data of the trade-off between the maximum equivalent stress, the fatigue life, efficiency and output power for the (SSRT) respectively. From the this table, it can be seen that the a decrease in the overall turbine efficiency with about 1.3 % compared to the aerodynamic optimization occurs while the maximum stress and deformation decreased from around 28 MPa to 23.5 MPa and from 0.85 mm to 0.77 mm respectively.

Table 5.5: The trade-off between the chosen parameters.

Parameter (Unit)	1D Optimization	Aerodynamic Optimization	Multidisciplinary Optimization
Rotor Blade number (-)	17	15	16
Rotor Inlet Flow Angle (deg.)	-55.8	-74.03	-71.6
Rotor Outlet Flow Angle (deg.)	77.3	83.36	79.8
Shroud Ratio (-)	0.81	0.69	0.83
Hub Ratio (-)	0.23	0.21	0.21
Tip Width of Rotor (mm)	1.25	2.1	2.1
Rotor Tip Clearance (mm)	0.45	0.33	0.33
Rotor LE Beta Angle (deg.)	-	-46.31	-41.7
Maximum Equivalent Stress (MPa)	-	28.36	23.515
Maximum Deformation (mm)	-	0.85	0.77
Minimum Fatigue Life (Cycle)	-	19284	24153
Power Output (kW)	1.3	1.15	1.05
Efficiency (-)	89.7	86.75	85.55

5.7 Summary and Conclusions:

The effect of various important operating conditions namely, the inlet temperature of the compressed air and rotor rotational speed on the performance of (SSRT), for (SSSPBC) application has been intensively investigated in the current chapter using (3D CFD) analysis. Moreover, a multidisciplinary optimization technique, which connects the (CFD-FE) analyses, was employed to find the best rotor shape. The main conclusions from this work can be summarised as follows:

- The rotational speed of the rotor has a significant effect on the amount of stress and displacement, where maximum increase of 65% in the stress and 57% in the deformation were noticed when reaching the maximum studied rotational speed of 80 krpm and at compressed air inlet temperature of 65 ^{o}C.

- For the temperature of the working fluid, it is shown that decreasing the compressed air temperature to 25 ^{o}C results in decreasing the maximum stress and deformation of the rotor. Where the increase in their values (compared to the aerodynamic optimized rotor), the corresponding increments mentioned above were only around 23% and 3% respectively.

- The stress concentration was mainly at the area which connects the hub with the blades, so this area needs to be enhanced in order to withstand the high stress concentration.

- The tip shroud location experienced a high deflection values in the rotor, 16.5% of the blade tip width. As a result, the gap between the blade tip and the shroud and between the blades should be equal or higher than the deflection i.e. increment value.

- As, for the fatigue analysis, increasing the compressed air inlet temperature from 25 ^{o}C to 65 ^{o}C resulted in decreasing the rotor fatigue life by about 97%, especially at higher rotational speed. The lowest fatigue life was located in the area where the blades are connected with the rotor’s hub. This place had the highest damage among all other rotor’s body.

- Consequently, the multidisciplinary optimization which includes both the aerodynamic and the structural parameters led to decrease the total equivalent stress and deflection with 17% and 9% and increase the fatigue life with 25%. However, around 8% and 1.5% reduction in the rotor output power and efficiency were also produced.

CHAPTER 6: EXPERIMENTAL RESULTS AND VALIDATION

6.1 Introduction:

This chapter presents a comprehensive experimental study of the solar heater (using electrical light source and thermal cavity receiver) and the Small Scale Radial Turbine (SSRT) at various operating conditions. Three main sections have been included in this chapter to cover the three experimental studies carried out. These are the optical and the thermal experimental testing solar heater, and the aerodynamic and structural analysis of the radial turbine.

6.2 Test Facility:

The system consisted of the following parts:

- The cavity thermal receiver, which was chosen to be the cylindrical shape for the sake of simplicity, had been firstly manufactured.
- The 8 mm diameter cooper tube was formed to have the helical shape and was put inside the cavity receiver to cover its internal surface.
- The Halogen bulb light 800 W was chosen to act as a source at various distances from the aperture of the receiver. This light is chosen as it has similar wavelengths to those come from the sun, especially the infrared rays which give the required heat.
- Seven surface sensors were distributed circumferentially and longitudinally inside the cavity receiver in order to measure the surface temperature of the helical tube.
- Three flux sensors were put on the aperture and also at different places of the helical tube surface in order to measure the incoming flux on the copper tube.
- Data logger which was connected the measuring instruments and PC to display each; the temperature and the irradiance readings.

As for the turbomachinery part, the heated compressed air, when it enters the (SSRT). Similarly, the manufactured parts of the (SSRT) model and the instruments used in this test have been listed as below:

- The (SSRT), which consists of the volute, the stator, the rotor and the bearing housing, was manufactured, using the 3D printing facility.
- One flow meter to measure and control the compressed air mass flow rate, two thermocouples, two pressure transducers were inserted in the system in order to measure the inlet and outlet conditions of the compressed air during its way in the system and torque meter to gauge the power output and turbine rotational speed.
- Electrical heater was put in the system in order to have a full control and at the same time adjust heat supplied to the compressed air before enters the (SSRT).
- Another type of data logger which was connected the measuring instruments and PC to display the temperature and the pressure of the compressed air at different stages.

6.3 Experimental Validation of the Receiver/ Optical Performance:

The experimental optical analysis was carried out in the solar lab using the electrical light source and the cylindrical cavity receiver, models and the instruments mentioned in Appendix C in order to determine the flux distribution as well as the surface temperature on the copper helical tube fitted over the internal surface of the cylindrical cavity receiver. Figure 6.1 shows a halogen light source with its reflectors, the manufactured cylindrical cavity receiver including its helical tube coil (put by structural frame), flux and temperature sensors (connected to data logger) and computer screen.

6.3.1 Optical Test procedure:

The optical experimental work started on May 2017 at atmospheric pressure (1.013 Bar) and temperature (21 ^{o}C). The procedure followed during the optical testing is summarised below:

- Set up the halogen light and direct it on the aperture of the cylindrical cavity receiver in order to supply the required amount of flux on the internal surface of the cavity receiver [99].
- Measure the received flux at various positions on the surface of the copper helical tube inside the cavity of the thermal receiver.
- Similarly, measure the surface temperature on the external surface of the helical tube at different positions in order to determine its values and distribution.
- Vary the distance between the halogen light, and the aperture of the cylindrical receiver in order to achieve various levels of irradiance values of 500, 600, 700, 800, 900 and 1000 W/m^2.
- Repeat the received flux and temperature measurements again at each of the irradiance value and finally;
- Compare the experimental results with the simulation results obtained using the OptisWorks software.

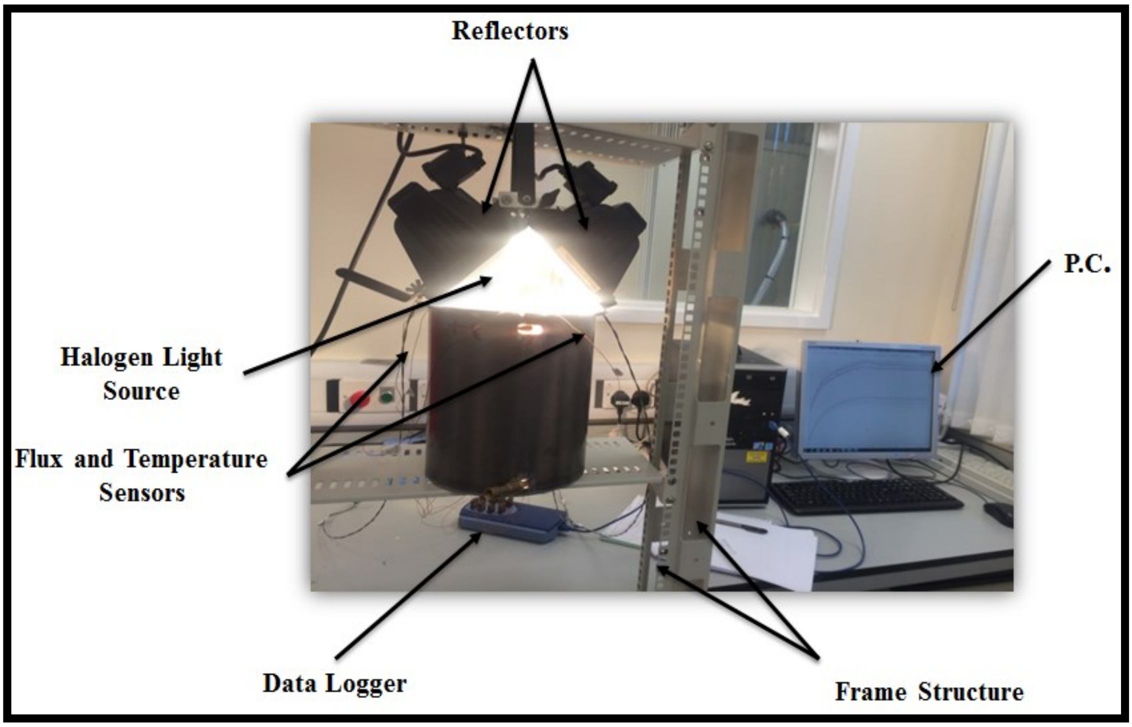

Figure 6.1: The thermal receiver with the electrical lighting source.

6.3.2 Results and Discussion of the Optical Analysis:

6.3.2.1 Receiver Aperture

Figure 6.2 shows the experimental set up used to evaluate the received irradiance at the aperture of the thermal receiver. In this set up, the aperture area was divided into 64 equal size small squares and a flux sensor was used to measure the received irradiance.

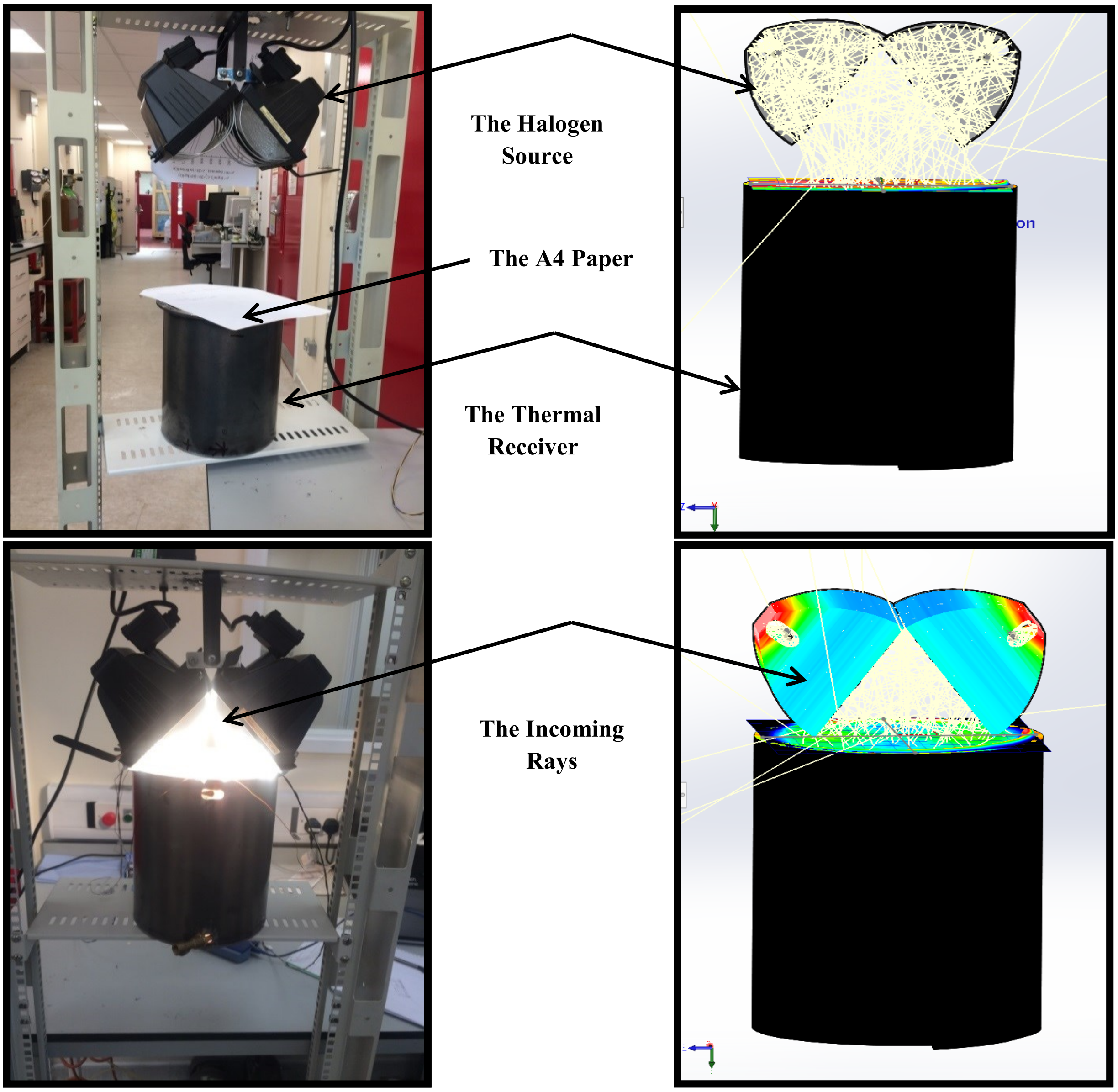

Figure 6.2: The experimental and simulation optical analysis carried.

Figure 6.3 a, b, c, d and e show the flux distribution over the mentioned squares on the receiver aperture at various distances of 0, 1 cm, 3 cm, 5 cm and 7 cm respectively between the receiver aperture surface and the lower edges of the light source. It can be seen that at 0 cm distance, the received irradiance varied from 7500 W/m^2 at the central areas of the receiver to 3500 W/m^2 at the edges respectively. The average received value is 5350 W/m^2. It can be seen that increasing the distance between the light and the receiver from 0 to 1 cm resulted in increasing the average of the irradiance received but further increase in the distance resulted in reducing the received irradiance. Figure 6.3 f compares the measured average received irradiance compared to those predicted by the simulation at irradiance value of 500 W/m^2 as an average value. Also, Figure 6.3 f shows that there is a good agreement between the experimental and the simulation results with a maximum deviation of 11% at 7 cm distance. In this testing, varying the distance between the light source and the thermal receiver was used to control the received flux at the aperture of the cylindrical receiver. This received flux was then related to the radiation received by the parabolic collector, using the simulation described in chapter 3 section 3.3.1. Figure 6.4 shows the received radiation at the receiver aperture at various input irradiance at the aperture of the parabolic collector.

Table 6.1compares the measured received average radiation by varying the distance between the light source and the thermal receiver to the received average radiation predicted by simulation at various input radiation at the aperture of the parabolic collector. Therefore a relationship between the input radiation and distance between the light source and the receiver can be determined and used to alter the input radiation

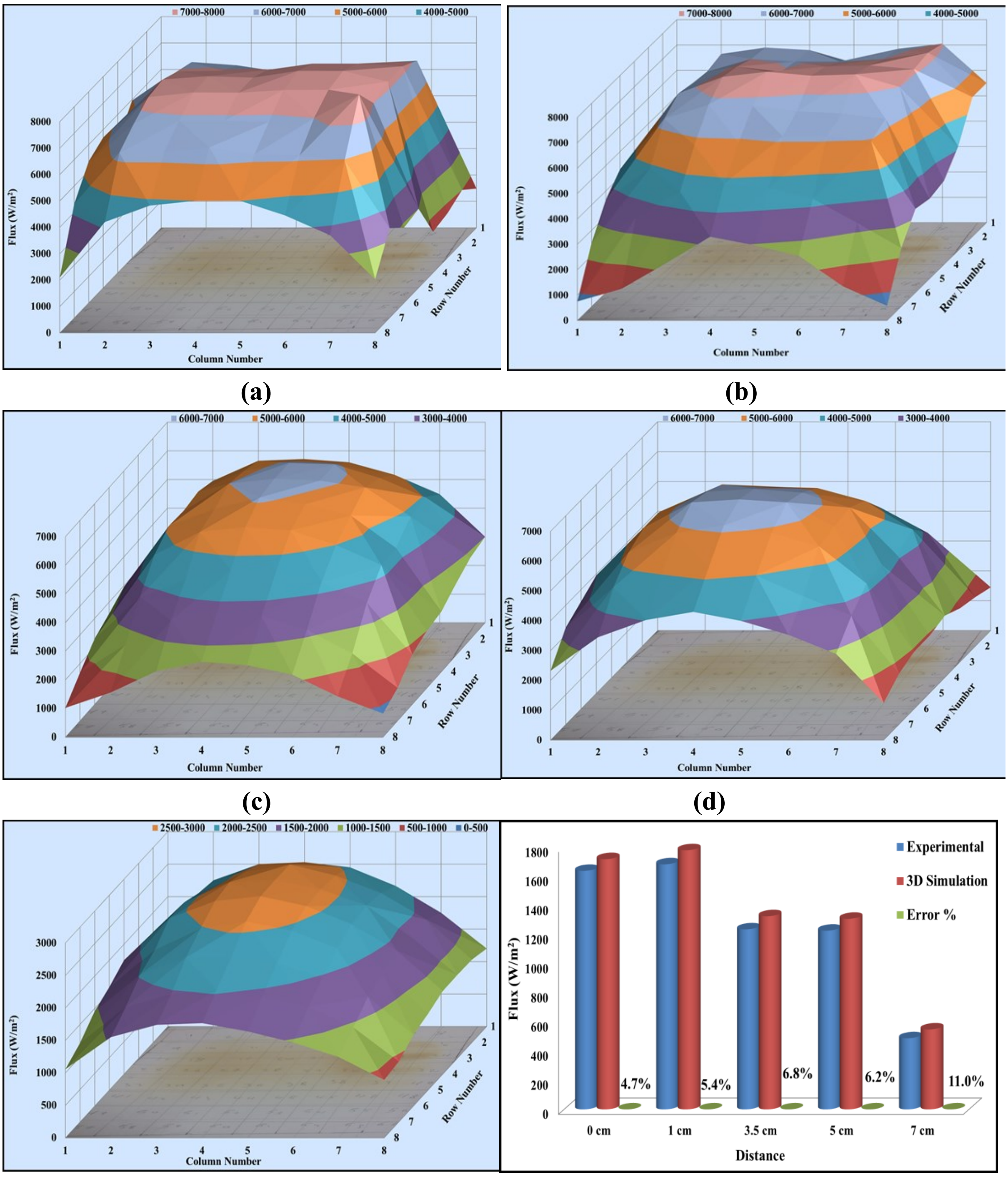

(a) (b)

(c) (d)

(e) (f)

Figure 6.3: The received radiation distribution at: zero distance (a), (b) 1 cm distance, (c) 3.5 cm distance, (d) at 5 cm distance and (e) 7 cm distance, (f) is the comparison between the average theoretical and experimental flux values on the aperture at 500 W/m^2 input radiation.

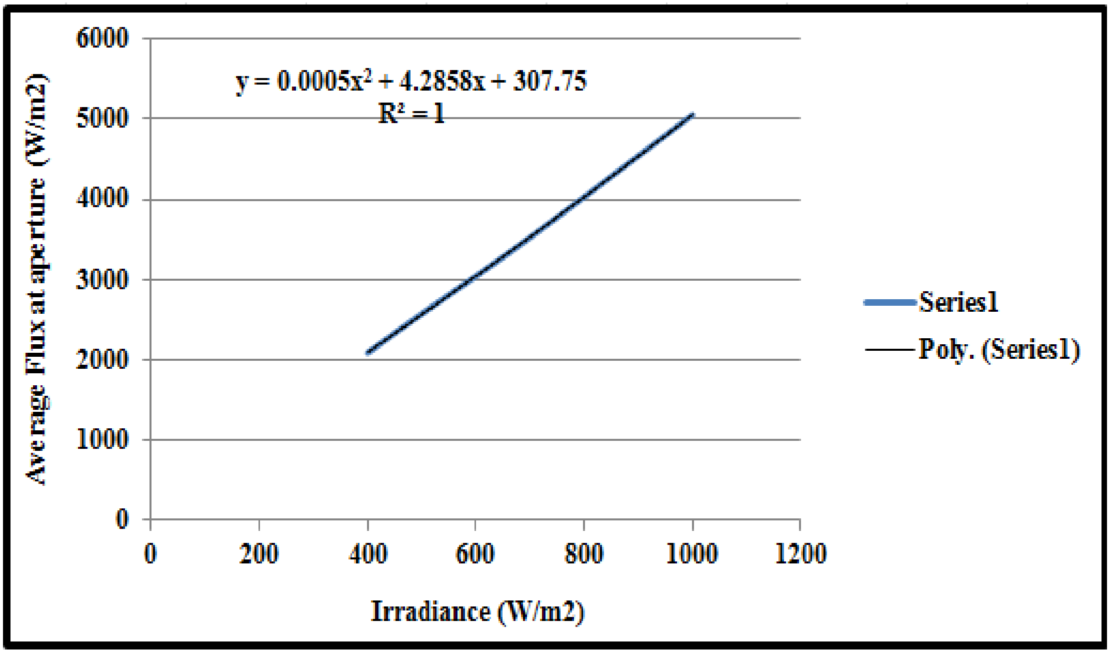

Figure 6.4: The relation between the incoming irradiance and the average flux on the receiver aperture area.

Table 6.1: The chosen distances and their relevant experimental and analytical values of flux.

Irradiance (W/m^2)	From simulation (W/m^2)	From experimental (W/m^2)	The distance (m)
400	2102	1935	0.07
600	3059	3165	0.05
800	4056	3967	0.035
1000	5093	5235	0.01
1050	5359	5599	0

Figure 6.5 shows the uniformity on the aperture area at three different distance values; of zero, 7 cm and 18 cm, described using two different uniformity correlations namely Filipa [159] and Ivan [160] which are introduced in chapter three (equations 3.7 and 3.8) . It is clear from this figure that the distance of 7 cm produces the highest level of uniformity of around 100% while reducing the distance to zero or increasing it to 18 cm produced significantly lower uniformity of around 50% and 60% respectively. Figure 6.5 also shows a difference between

the uniformity values predicting by each correlation where Ivan's correlator shows higher values than those obtained by Filipa correlation as highlighted in chapter 3.

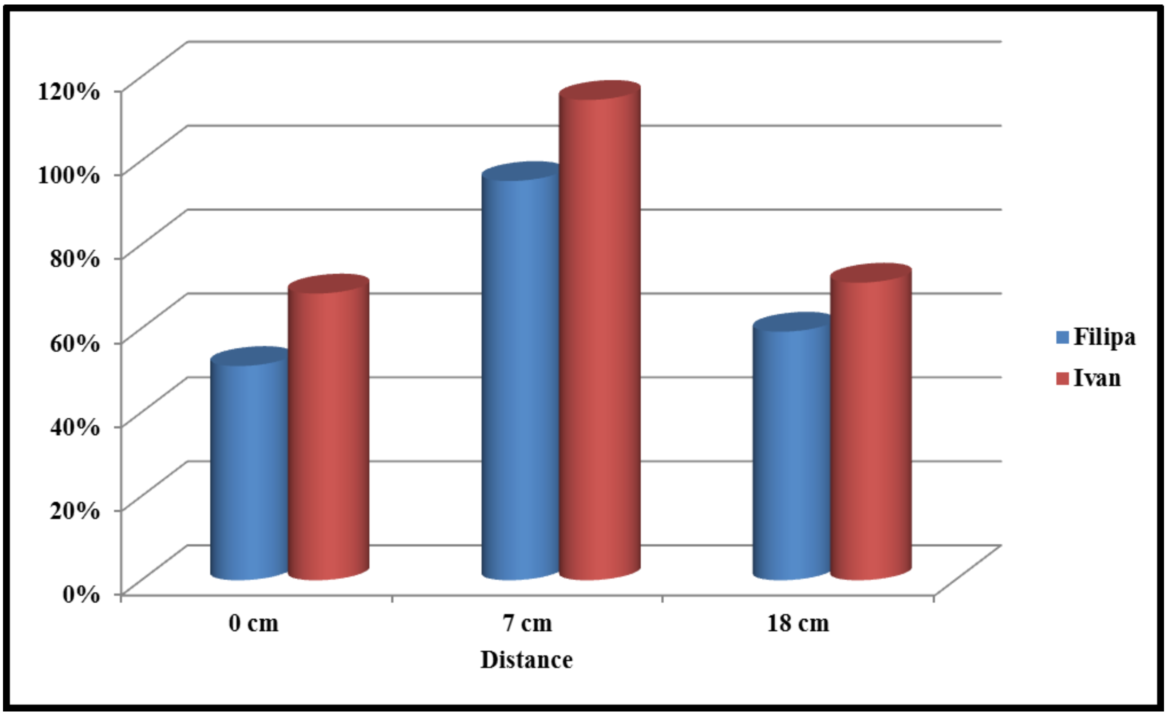

Figure 6.5: The uniformity on the aperture area at three different height values based on three different uniformity correlations.

6.3.2.2 Receiver Body:

Figure 6.6 shows a schematic diagram of the experimental set up to evaluate the received irradiance at the surface of the helical coil fitted inside the thermal receiver [147]. Both the radiation flux and temperature were measured using flux sensors and type T thermocouples. For the radiation sensor, Figure 6.7 shows the radiation sensors fitted on a bar that was moved circumferentially along the perimeter of the cavity receiver. On the bar, three sensors were fitted at 0, 11.5 and 21.0 cm from the aperture of the receiver. Seven thermocouples were fitted directly, with 3 cm distance between each, at the tube helical surface.

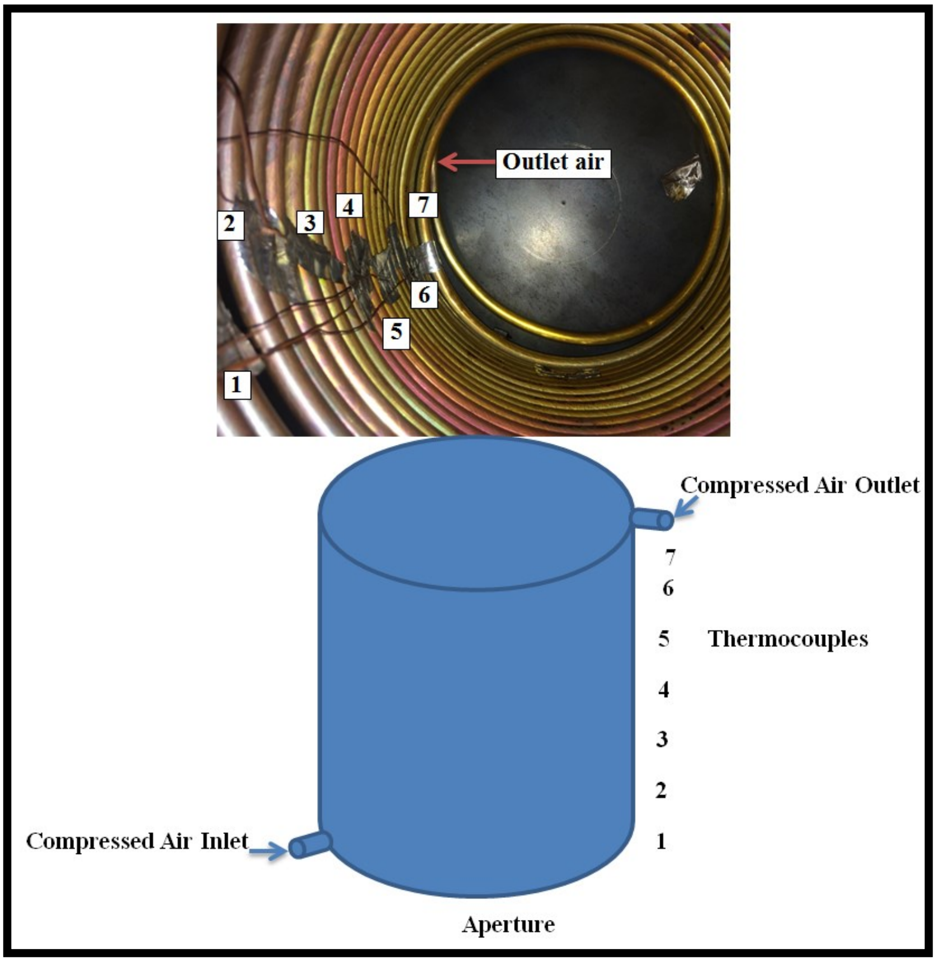

Figure 6.6: The schematic diagram of the optical setting.

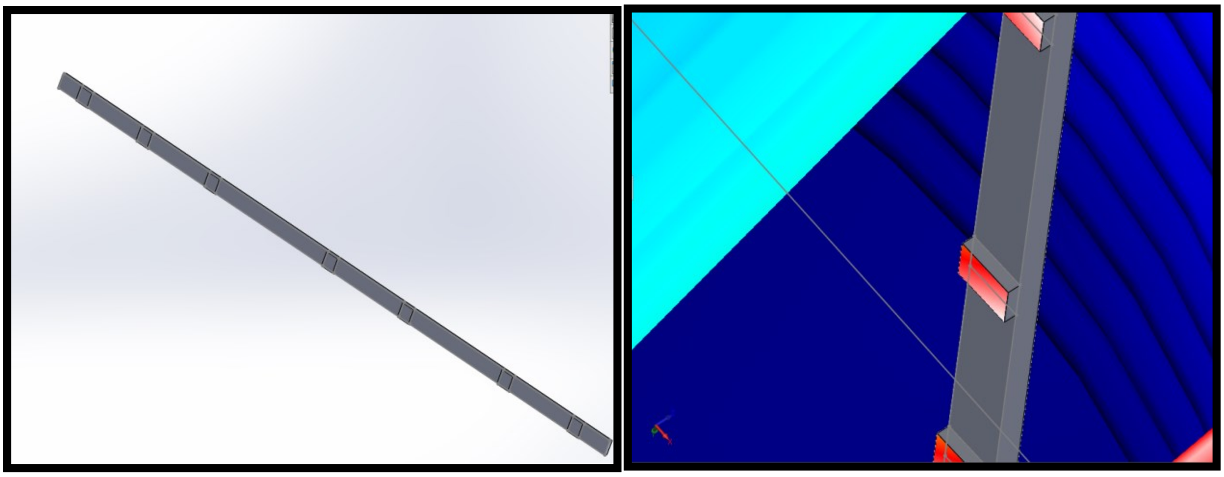

Figure 6.7: The sensors inserted inside the cavity receiver, the helical tube surface.

Figure 6.8 shows the measured flux at various positions on the helical tube coil surface and various distances between the light source and aperture of the cavity receiver respectively, where the position 1 refers to the deepest point inside the receiver. It can be seen from Figure 6.8 that the received irradiance increases with the decrease of the distance between the light source and the thermal receiver. Also, it can be seen that the received flux increases with the coil positions where the tubes close to the aperture have the highest flux.

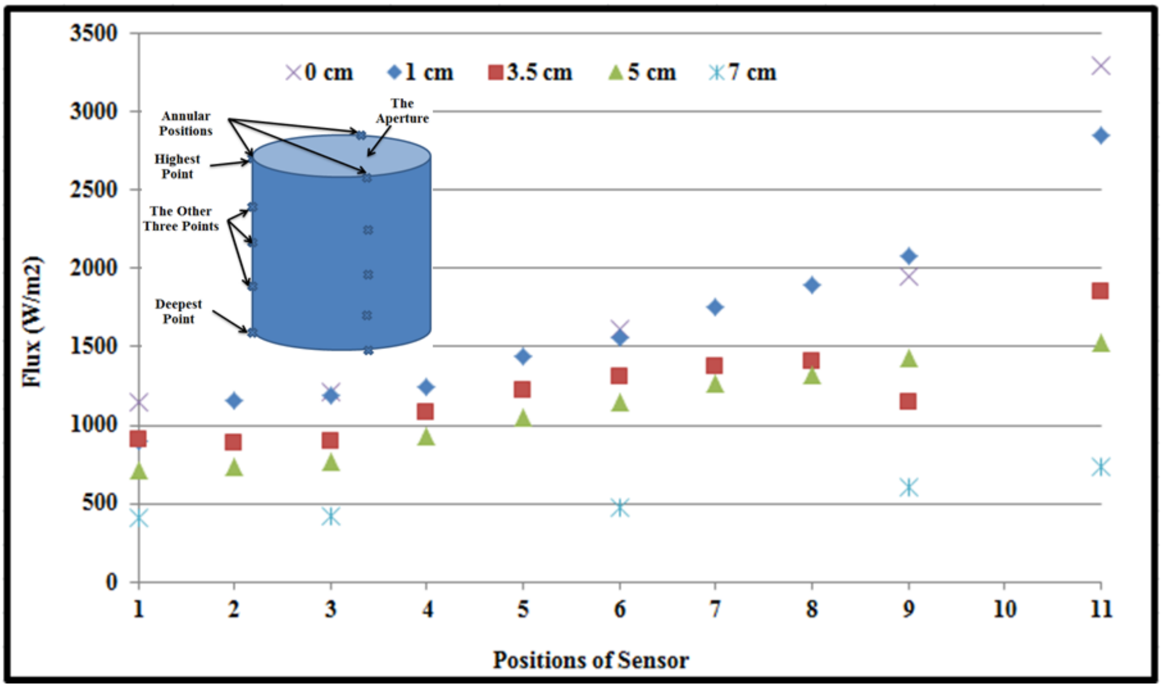

Figure 6.8: The average flux values along the cylinder at different distance values between the source and receiver.

Figure 6.9 compared the measured radiation flux to those predicted by the ray tracing simulation presented in chapter 3 at various positions of the helical tube coil and various distances between the light and the receiver aperture of 1 cm, 3.5 cm and 5 cm. The percentage deviation between the experimental results and simulation results showed a maximum deviation of 13% at 5 cm distance between the light source and the receiver aperture.

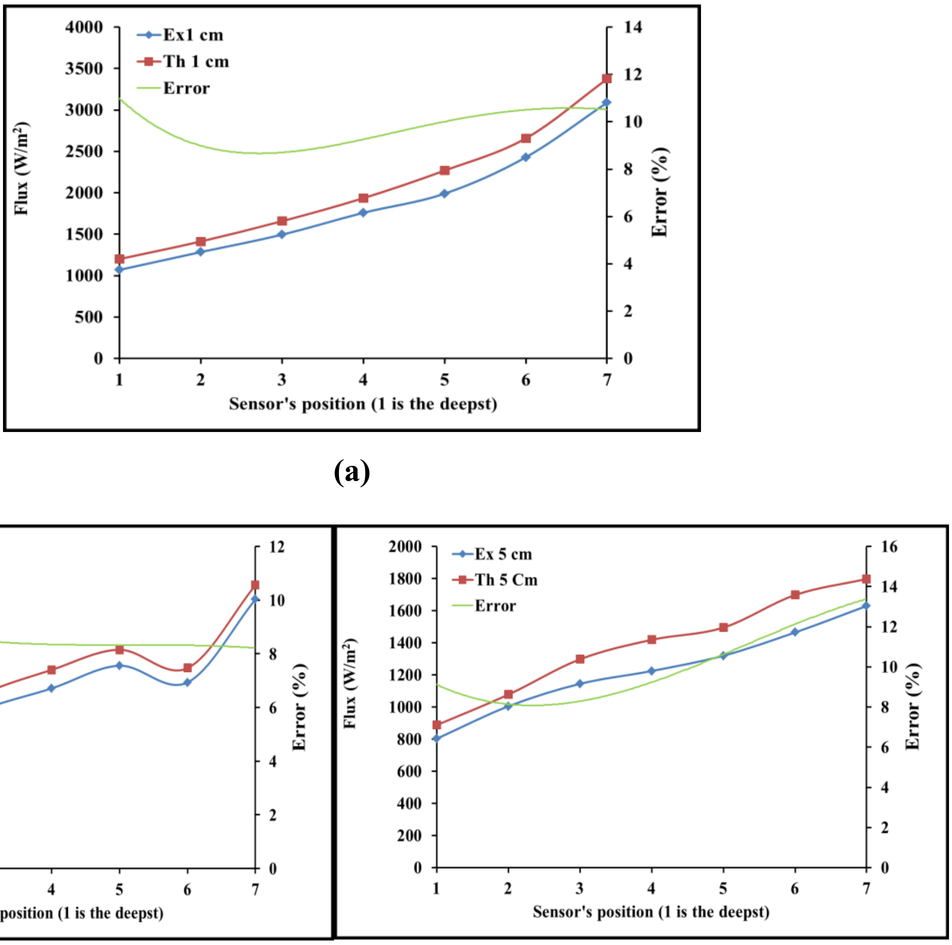

(a)

(b) (c)

Figure 6.9: The comparison between the experimental and the analytical flux values at various distances between the source and the cylindrical receiver; (a): 1 cm, (b): 3.5 cm and (c): 5 cm.

6.4 Experimental Validation of the Receiver Thermal Performance:

Figure 6.10 shows the experimental test facility constructed to evaluate the thermal performance of the thermal receiver. It consists of the light source, thermal receiver and compressed air supply system connected to the helical tube coil fitted inside the thermal receiver. Various measuring devices were used to assess the thermal performance including thermocouples installed, at inlet and outlet from the helical coil and flow rate measuring device. Detailed description of the above is included in Appendix C.

Here, the light source is positioned underneath the thermal receiver to simulate the case when solar radiation is received by parabolic concentrator which in turn directs the radiation to the thermal receiver as presented in chapter 3.

6.4.1 Thermal Performance Testing Procedure:

The experimental work was carried out based on the following procedure:

1- The halogen light source was switched on in order to warm the internal receiver surface area and the helical tube.

2- Monitor the readings of seven surface temperature sensors which were distributed longitudinally at two opposite sides of the helical tube surface and the reading of a thermocouple installed at the receiver exit for measuring the temperature of the compressed air leaving the helical tube.

3- When the steady state, in terms of the temperatures values, was reached, compressed air was passed through the system, at various flow rates, in order to evaluate its exit temperature values.

4- The surface temperature values and the exit air temperature were recorded since the light source switched on until the end of the experiment, at four values of compressed air flow rates of 0.02, 0.015, 0.012 and 0.009 kg/s.

5- Finally, in order to imitate different irradiance values on the receiver aperture area, three different distances, 1 cm, 3.5 cm and 7 cm, between the light source and the receiver were examined.

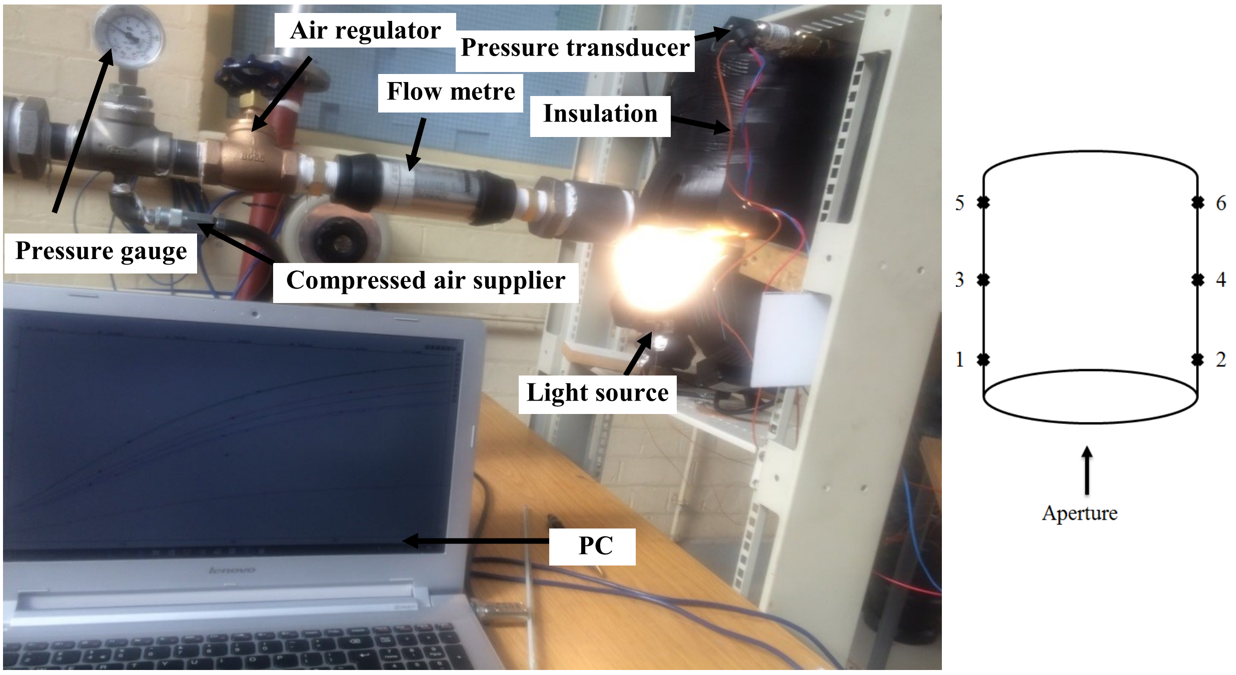

(a) (b)

Figure 6.10: The thermal cavity receiver test facility, a, and b: Schematic shape for the receiver showing the sensors' positions.

6.4.2 Results and Discussion of the Receiver/ Thermal Performance:

Figure 6.11 shows the temperature variations with time for the helical tube surface temperature at six positions and the exit temperature. Figure 6.11 a shows the temperature with the distance between the light source and the receiver is 1 cm where in the time period between 0 and 4820 seconds there was no air flow in the coil. At time of 4820 seconds air flow rate 0.02 kg/s was passed through the coil and then at time of 6000 seconds the flow rate was reduced to 0.015 kg/s and at time of 6700 seconds the flow rate was reduced again to 0.012 kg/s. Figure 6.11 b and c are for the light positioned at distances of 3.5 cm and 7 cm respectively. With no air flow, Figure 6.11 a shows that the helical coil surface temperature decreases with the increased distance from the aperture of the receiver. Thermocouples at positions 1 and 2, 3 and 4, 5 and 6 produced similar values as they are symmetrical. The coil surface temperature at positions 1, 2 increased with time to reach around 270 ^{o}C at time of 4820 seconds. The coil surface temperature at position 3, 4 increased with time to reach an average of 230 °C at the same time of 4820 seconds while the temperature at 5,6 reached 210 °C. Figure 6.11 b shows that the maximum temperatures reached for the case with no flow are 195 °C, 173 °C and 158 °C at positions 1 and 2, 3 and 4 and 5, 6 respectively at longer time of 6175 seconds. Figure 6.11 c shows that the maximum temperatures reached for the case with no flow are 170 °C, 147 °C and 133 °C at positions 1 and 2, 3 and 4 and 5, 6 respectively at longer time of 7754 seconds. When the air is passing through the coil at flow rate of 0.02 kg/s, the coil surface temperature decreased significantly to reach very close values of 52 °C, 41 °C and 31 °C for light positions of 1 cm, 3.5 cm and 7 cm respectively. Decreasing the flow ate resulted in increasing the temperature values where at flow rate of 0.012 kg/s the temperature of the helical coil surface reached 66 °C, 54 °C and around 51 °C at height positions of 1 cm, 3.5 cm and 7 cm respectively.

It was observed that the coil surface temperature was highest at positions 5 and 6 and lowest at positions 1and 2 (opposite to the case of no flow). The main reason for that is when the air is passing; the sensors which are nearest to light source will record the maximum difference between the air temperature values. That difference decreases during its way, through the helical coil, to the sensors 5 and 6 which then will record the highest temperature.

Figure 6.12 shows the variety of compressed air exit temperature with the flow rate for various distances between the light source and the thermal receiver.

It can be seen from Figure 6.12 a, the compressed air exit temperature increases with the decrease in flow rate to reach 72 °C at flow rate of 0.009 kg/s. Increasing the distance between the light source and the aperture of the receiver resulted in decreasing the compressed air exit temperature. For example, at 0.009 kg/s, the compressed air exit temperature decreased from 72 °C to 61.8 °C and 55 °C when the light source and the distance between the light source at the receiver aperture was decreased from 1 cm to 3.5 cm and 7 cm respectively.

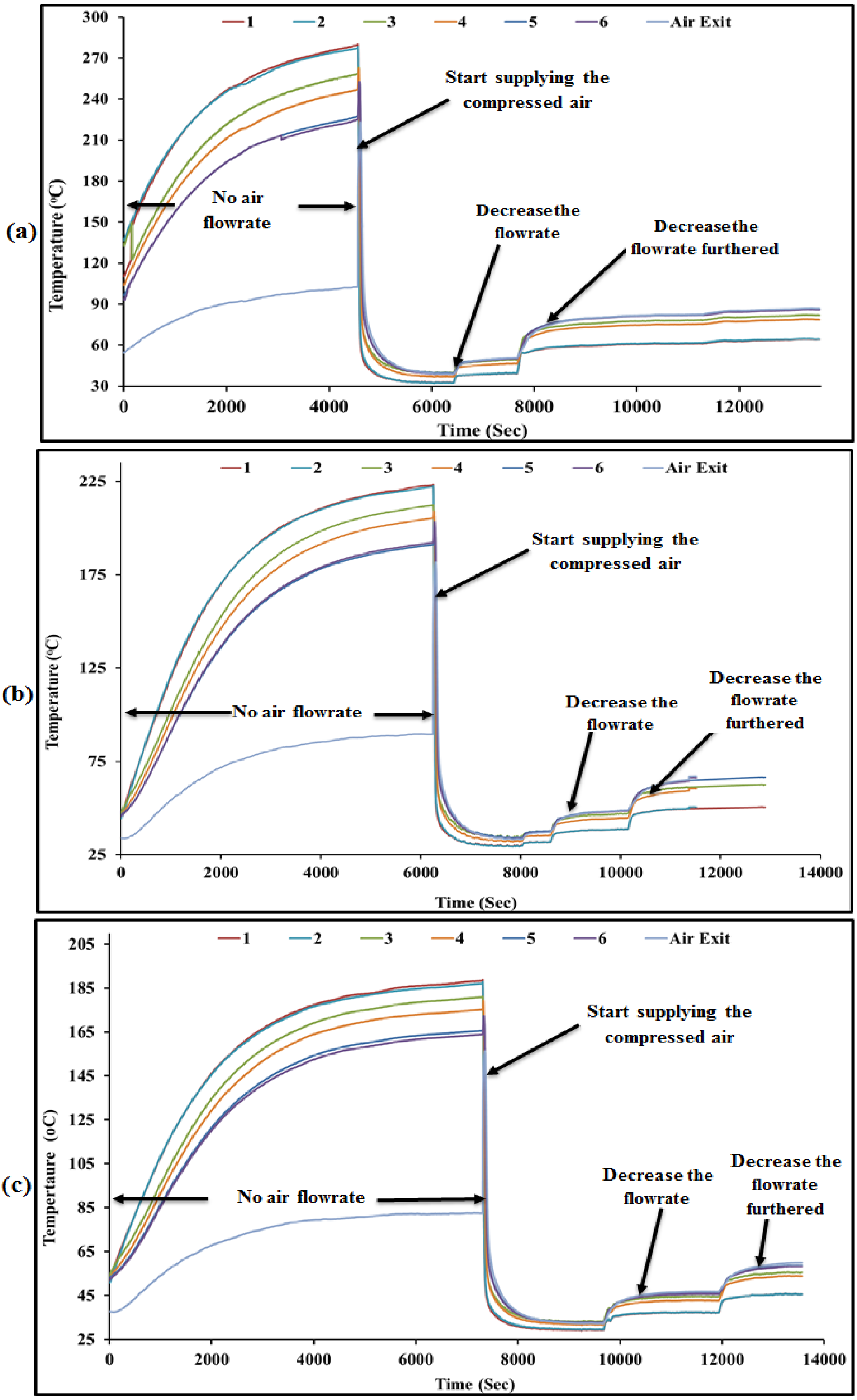

Figure 6.11: The surface temperatures (1 to 6 which refer to figure 6.10 b) and exit air temperature without and with various values of mass flow rate at various distances between the source and the cylindrical receiver; (a): 1 cm, (b): 3.5 cm and (c): 7 cm.

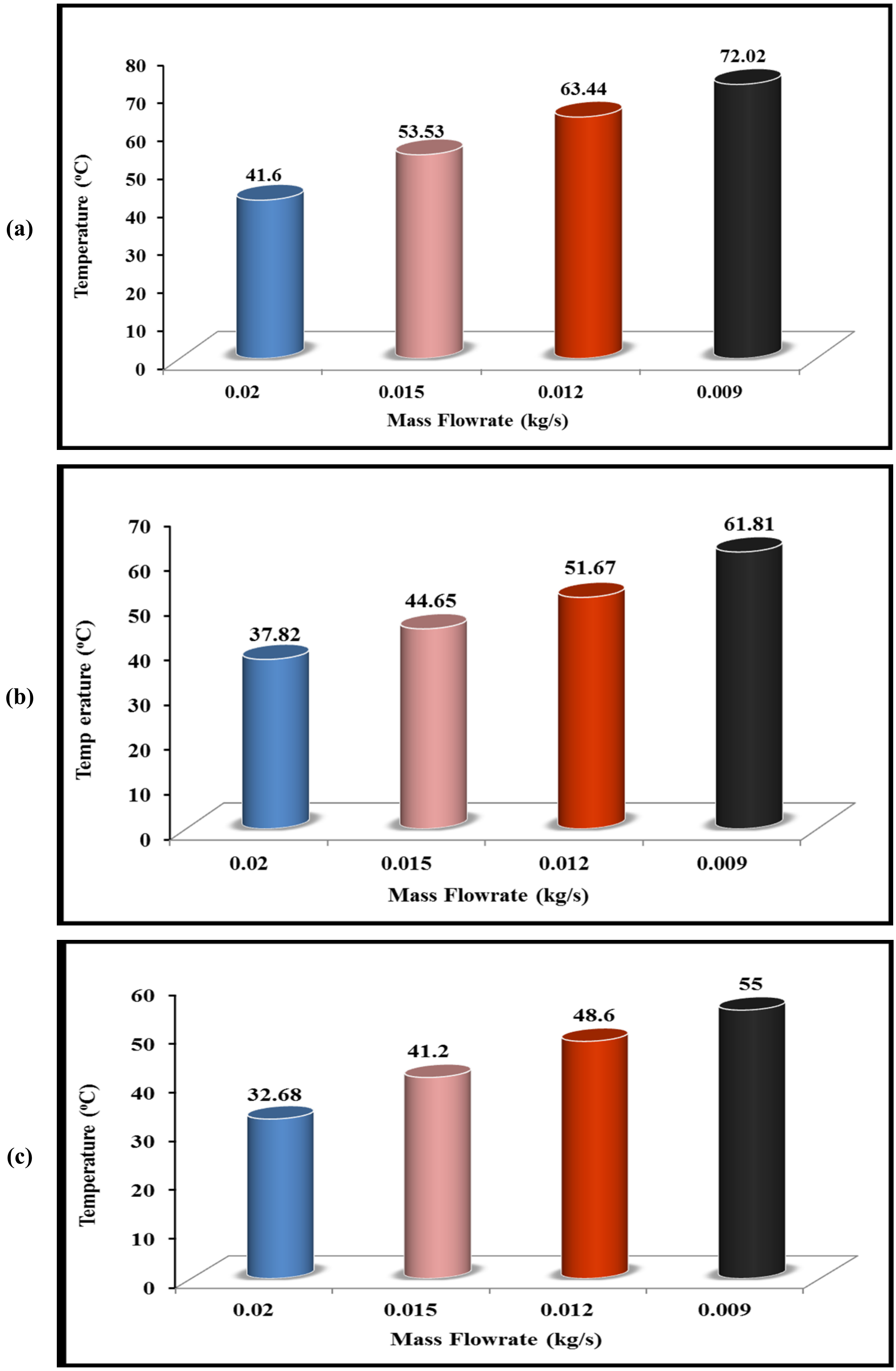

Figure 6.12: The exit air temperature at various mass flow rate and various distances between the light source and the cylindrical receiver; (a): 1 cm, (b): 3.5 and (c): 7 cm.

6.4.3 Experimental Validation of the Thermal Simulation:

The same 3D model of the cylindrical receiver was drawn and then transferred to the ANSYS Academic (CFD) fluent as shown in Figure 6.13, to model the thermal performance of the receiver and predict the compressed air exit temperature. The same irradiance levels and mass flow rate values were used in the simulation and the results were compared with those achieved using the experimental work. The setup of the (CFD) simulation is as described in section 3.4.2.

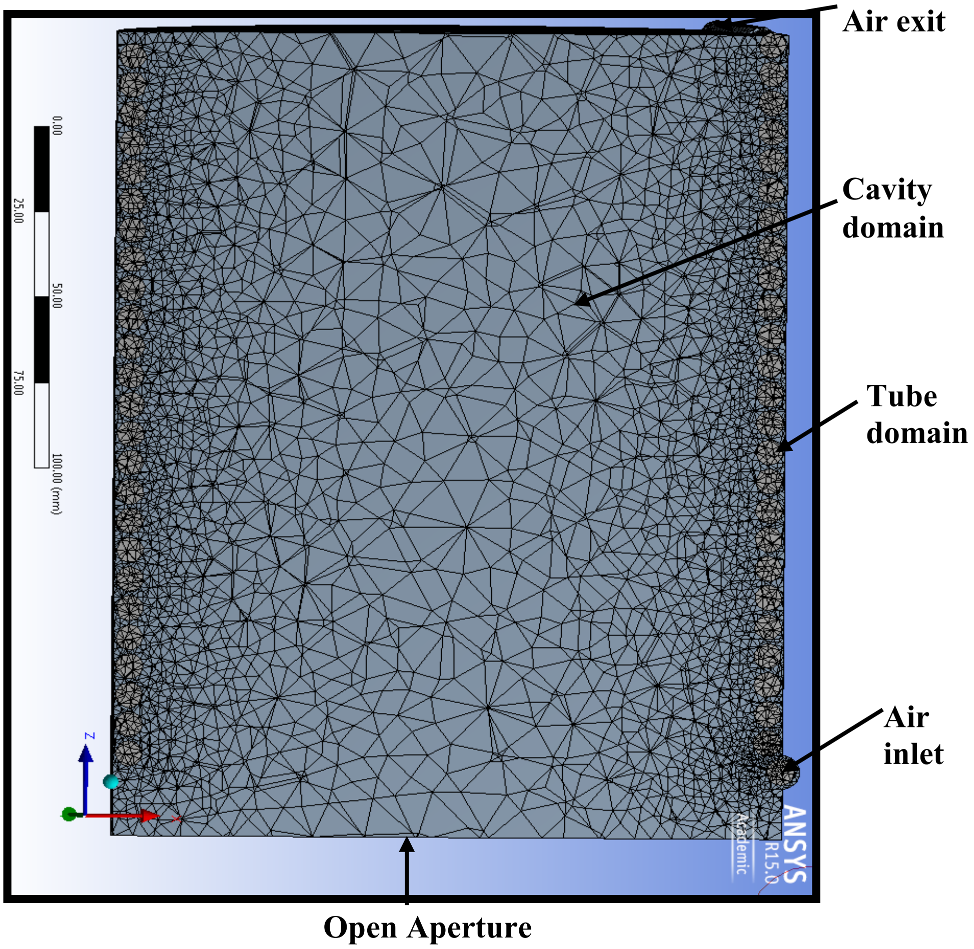

Figure 6.13: The meshed shape of the air domains for both the cavity receiver and its helical tube modelled in ANSYS® 15 [147].

Figure 6.14 shows the temperature distribution for the helical tube walls of the cylindrical receiver model at 1 cm gap and mass flow rate of (a) 0.01 kg/s and (b) 0.02 kg/s. The compressed air enters the tube coil at a relatively low temperature of 24 °C; then the temperature is increased with each turn of the helical tube due to the received radiation until it reaches its final temperature at the end of the tube length.

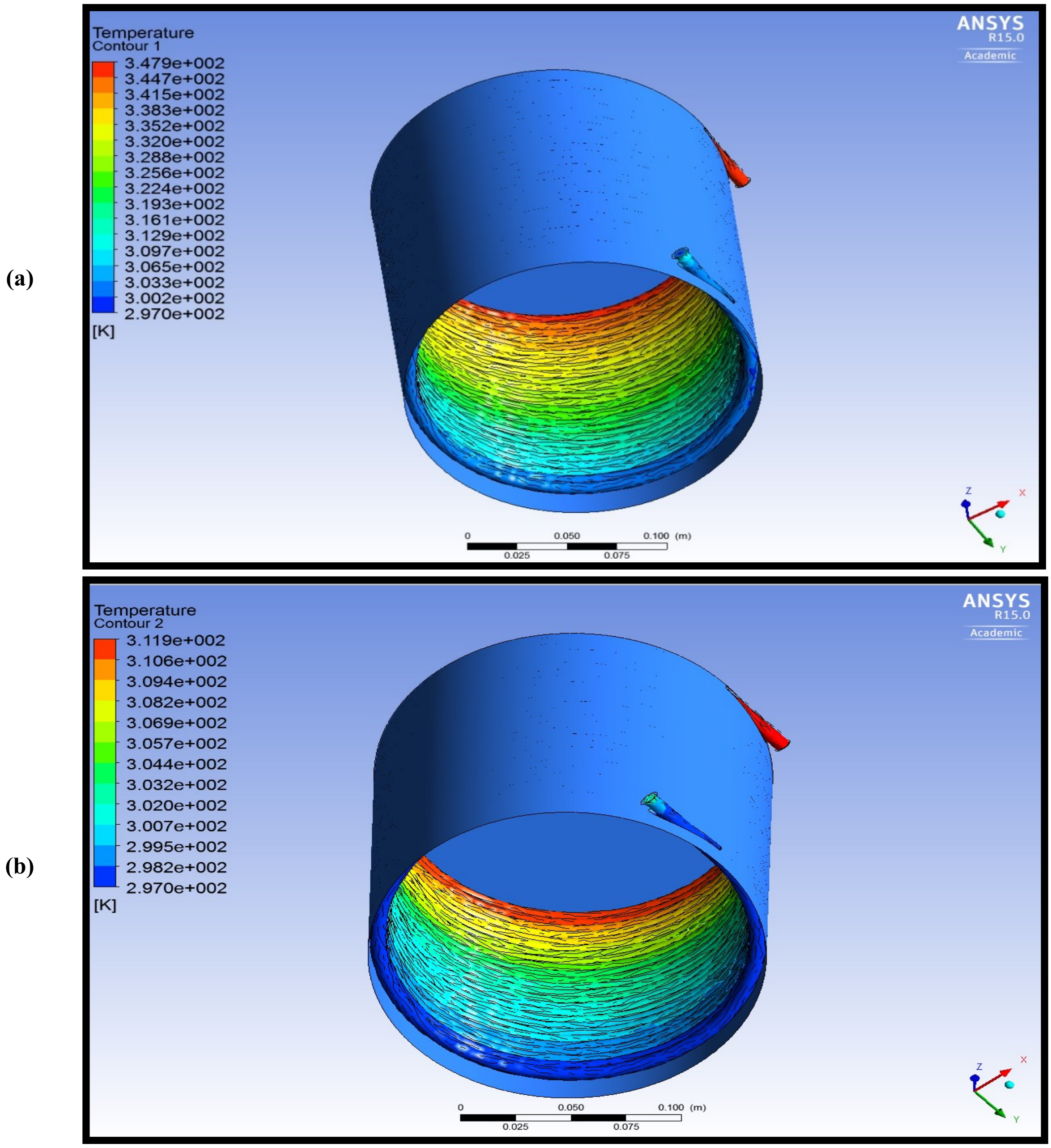

Figure 6.14: The temperature distribution for the cylindrical cavity receiver at; (a): 0.01 kg/s and (b) 0.02 kg/s and minimum gap, modelled in ANSYS® 15.

Figure 6.15 a, b and c compares the measured compressed air exit temperature to those predicted by simulation for the all investigated conditions. Here, it should be highlighted that the following figures were extracted when the system reached steady state at around 220 minutes from the start time and the percentage error (difference) was calculated using the following equation:

$$Error\ \% = \frac{Numerical\ Values - Experimental\ Values}{Numerical\ Values} * 100 \tag{6.1}$$

It is clear from Figure 6.15 a that the temperature value increased from 40 °C to 75 °C when the compressed air mass flow rate was reduced from 0.02 kg/s to 0.01 kg/s at the distance between the light source and the cylindrical receiver of 1 cm.

Similarly, the results for the exit air temperatures at different mass flow rates and 3.5 cm and 7 cm distance between the light source and the receiver aperture are displayed in Figure 6.15 b and Figure 6.15 c respectively. The maximum achieved exit air temperature was noticed to be at the lowest fluid mass flow rate and the lowest distance between the light source and receiver which produced the highest amount of the received radiation flux on the tube surface.

Figure 6.15 a, b and c show that the difference between the measured compressed air exit temperatures and those predicted by simulation ranges from 0.5 °C to 4.8 °C (highlighting the good agreement between the experimental and simulation results where the maximum deviation is 6.48%.

One of the reasons for this difference could be the fluctuation of the compressed air flow rate for the storage tank to the receiver.

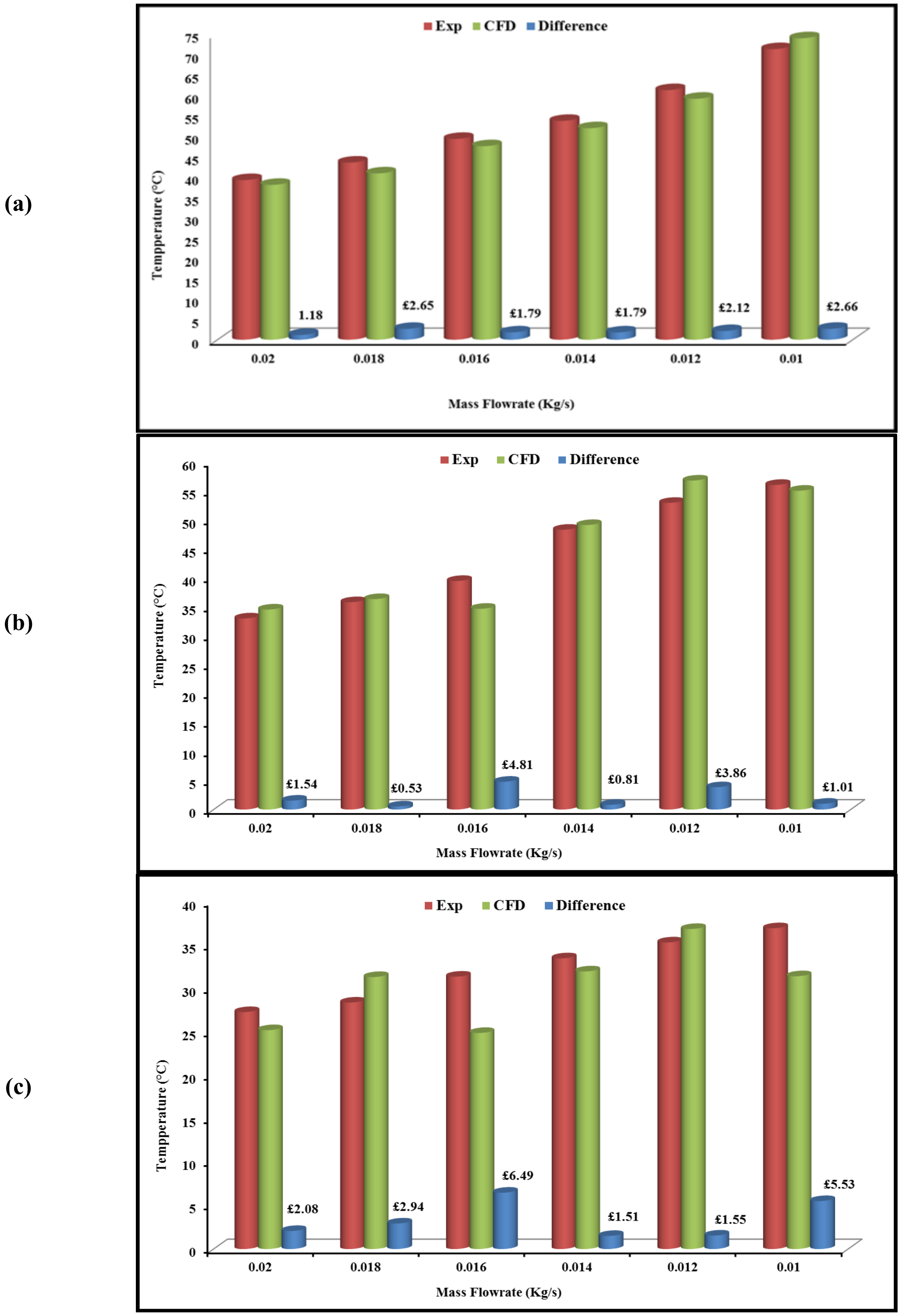

Figure 6.15: The comparison between the experimental and the analytical temperature values at various mass flow rate of compressed air exit temperature and three different distances between the light source and the cylindrical receiver; (a): 1 cm, (b): 3 cm, and (c): 7 cm.

6.5 Experimental Test and Validation of the (SSRT):

This section includes the experimental work carried out for selecting the material to be used in manufacturing the (SSRT).

6.5.1 3D Printing Material and Test Procedure:

In this research, it is proposed to use 3D printing facility to manufacture the (SSRT). Three types of printing materials were investigated namely; VeroBlue, Fullcure 720 and RGD 525 as shown in Figure 6.16. For RGD 525, the manufacturer [213], recorded a thermal procedure to enhance the material properties in terms of its maximum resistance temperature. Table 6.2 shows that RGD 525 has higher mechanical and thermal properties compared to the other two materials.

Figure 6.16: The three investigated types of material.

Table 6.2: The Mechanical properties of the three investigated plastic materials.

Name / Property	FullCure 720	VeroBlue	RGD 525
Tensile strength (MPa)	50-65	50- 65	70- 80
Elongation at break (%)	15-25	15-25	10-15
Density (g/cm^3)	1.18-1.19	1.17-1.18	0.97-0.98
Maximum Temperature (°C)	45- 50	45- 50	63- 67
Maximum Temperature (After Thermal Treatment (°C)	-	-	75- 80
Rockwell Hardness (-)	73-76	73-76	78-83

To confirm these properties, tensile tests at two various temperature values were carried out using samples from the 3D printing materials, air heater to supply heat to the samples and IR thermometer for measuring the samples surface temperature, as shown in Figure 6.17. Figure 6.18 shows that the RGD 525 is the best among the three investigated materials at atmospheric temperature when it showed a maximum stress of 50 MPa compared to 35 MPa and 40 MPa for the VeroBlue, Fullcure 720 respectively.

Figure 6.17: Tensile test carried out for three examined materials; at 40 ^{o}C.

Tensile test samples of RGD 525 were prepared and thermally treated in an oven available in the department of Mechanical Engineering/ University of Birmingham. This material has high tensile strength, thermal resistance and high hardness which make it brittle. The heat treatment is applicable for this material and it enhance its thermal and mechanical properties for example it increases the material isotropic properties [214]. The thermal treatment involved placing the samples on a flat surface inside the oven at room temperature and setting the ramp-up rate to 1°C/ minute.

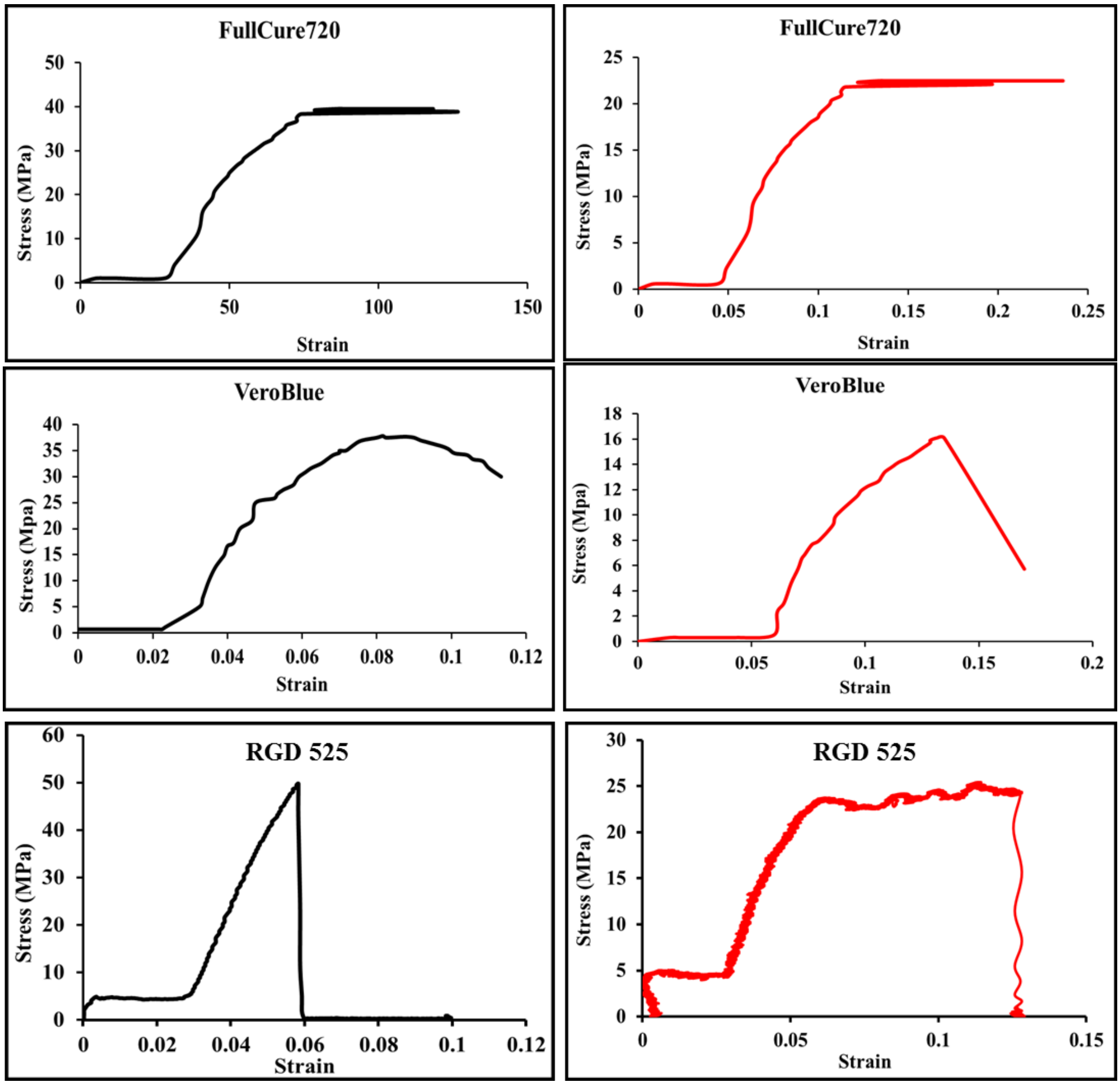

Figure 6.18: Results of the tensile test for three investigated materials before the thermal treatment; at atmospheric temperature (LHS) and at 40 °C (RHS).

Figure 6.19a, shows the thermal treatment facility and the test samples used for the tensile and fatigue tests of the thermally treated RGD 525. Figure 6.19b, shows the temperature variation with time during the thermal treatment where the oven's temperature was increased from 20 °C to 50 °C over 30 minutes and maintained at this temperature for 2 hours. Then the temperature was increased to 60 °C and maintained at this temperature for 2 hours. The oven temperature was increased again to 70 °C and maintained for 1 hour.

(a)

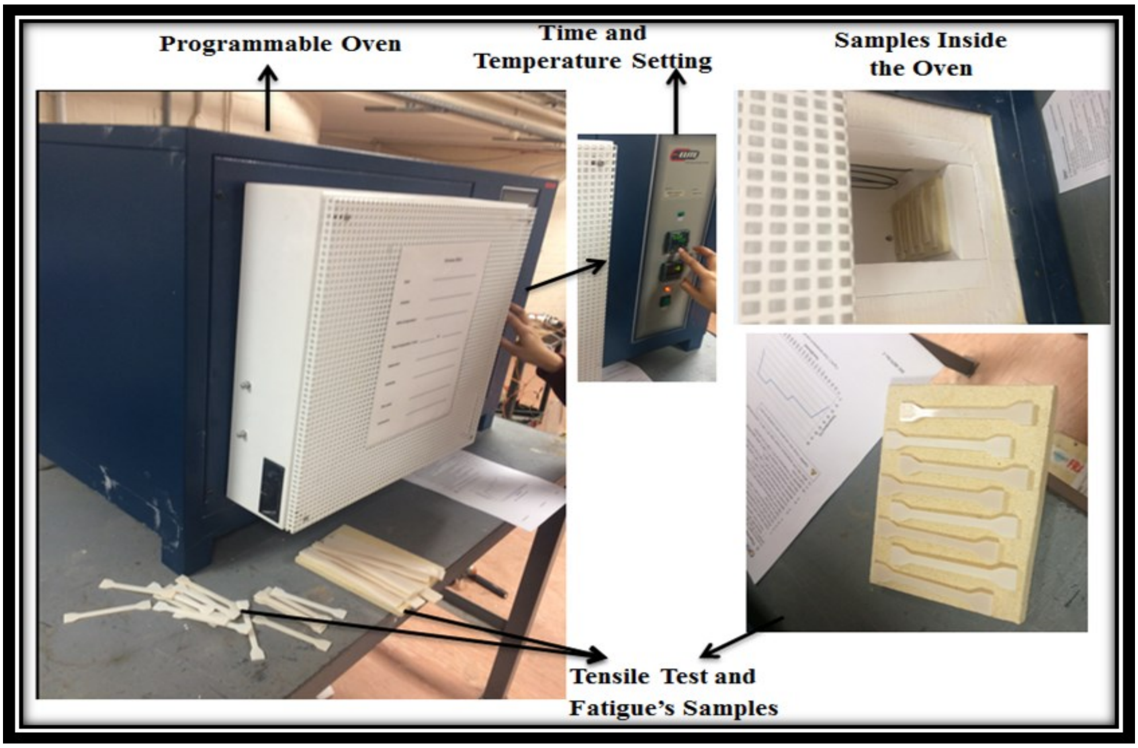

(b)

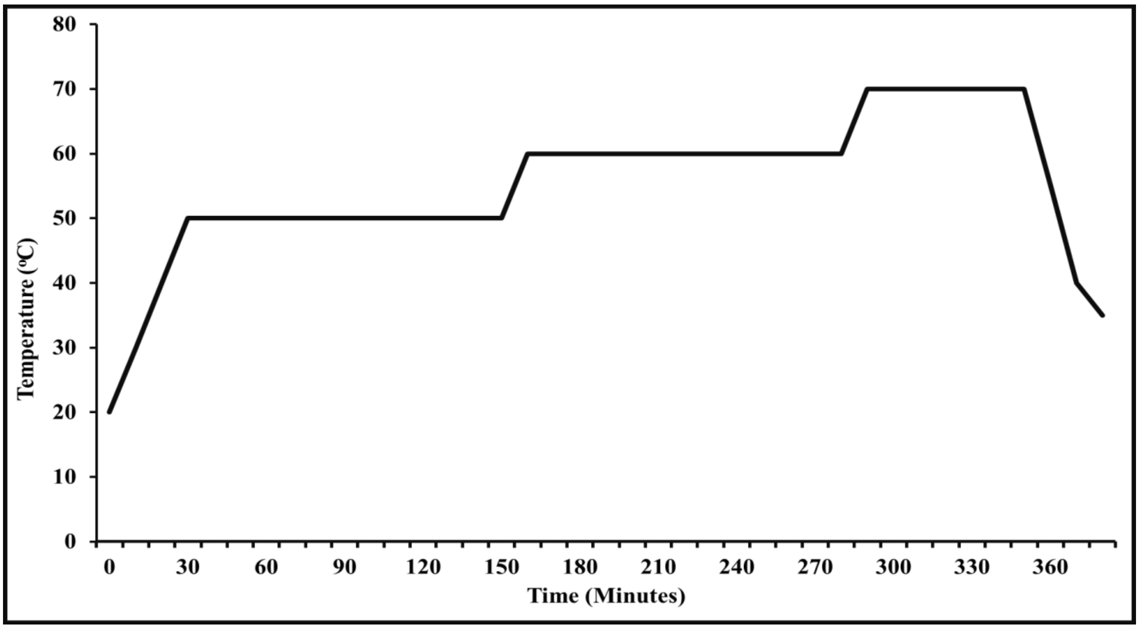

Figure 6.19: Oven used in the heat treatment (a) and (b): Oven temperature over time [213].

Figure 6.20 shows the results of the tensile test of the thermally treated RGD 525 compared to the results for the untreated material. It can be seen from the first figure that while there were a clear enhancement in the tensile test results of around 37.5 % at 35 ^{o}C and around 5% at 45 ^{o}C (which indicates low enhancement in its strength property) there was no real enhancement at the 25 °C. Moreover, it is clear that by increasing the temperature (applied on the samples), the material strength was decreased to the third as a result of the change in molecular structure caused by heating where the material softens.

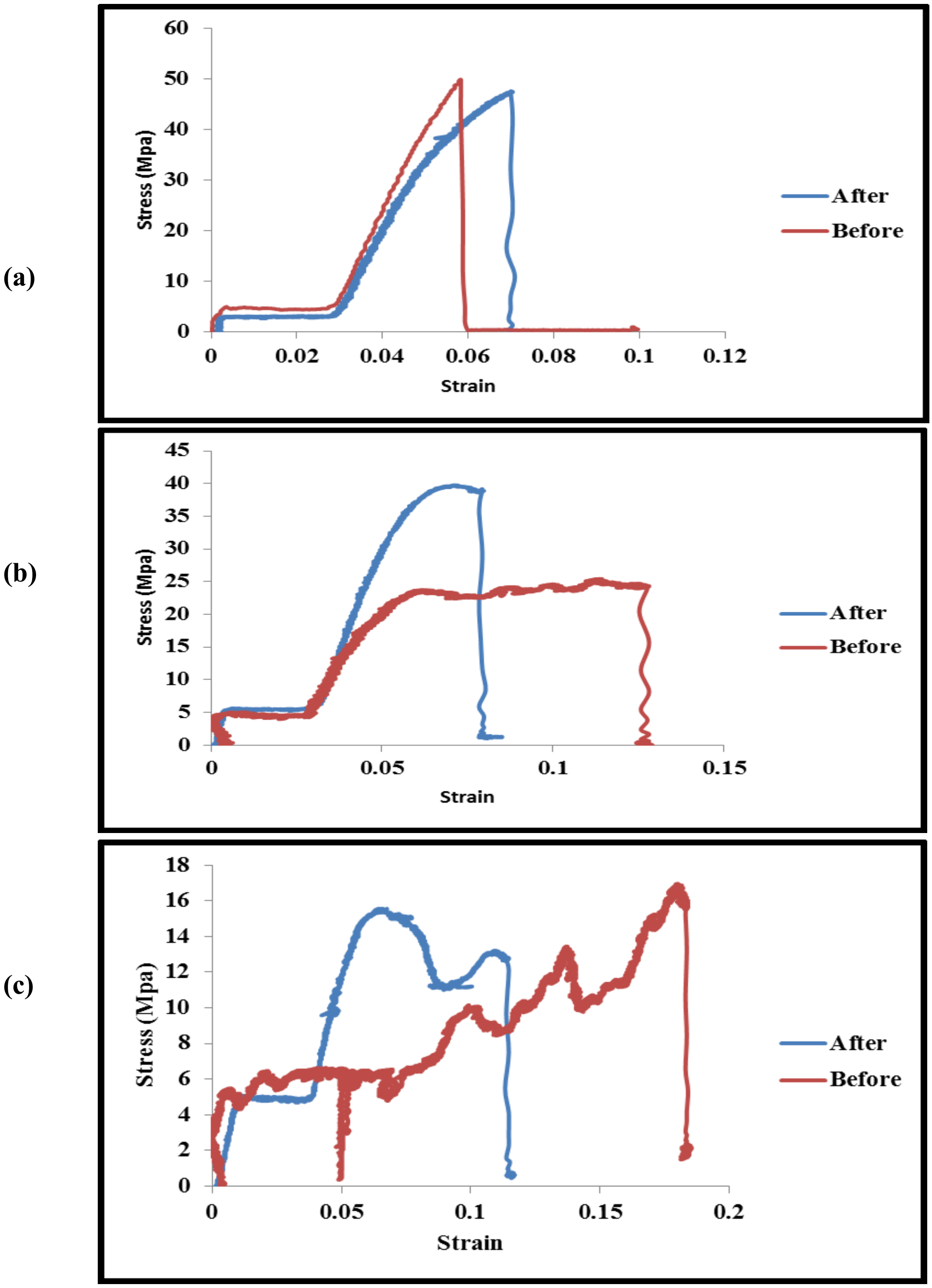

Figure 6.20: Tensile test results of the thermally treateated RGD 525 material; (a): 25 °C, (b): 35 °C and (c): 45 °C.

6.5.2 Fatigue Test:

In order to characterize the thermally treated RGD 525 material properties in terms of fatigue endurance, a fatigue test was carried out using servo hydraulic fatigue testing machine (INSTRON 8801) equipped with self-aligning hydraulic grips, as shown in Figure 6.21. The form of the applied load was a cyclic sine wave with loading ratio of 0.1 at 3 Hz and maximum load varying from 0.473 kN to 1.733 kN to for each sample.

Nine thermally treated fatigue samples of the RGD 525 material were used during this test. Each sample will be under one specific value of load and its endurance limit will be checked, then the number of cycle at that specific load can be determined.

Figure 6.22 shows the relationship between the applied load and the maximum number of cycles that each fatigue specimen reached before failing while Figure 6.23 shows the fractured specimens.

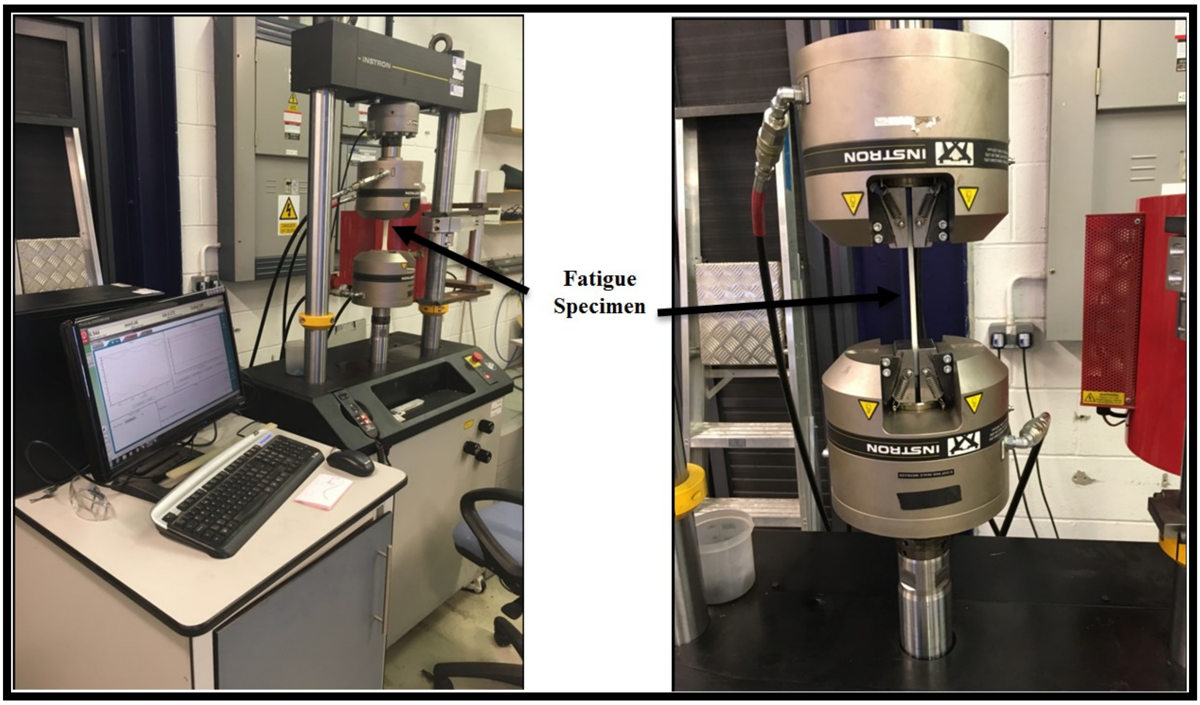

Figure 6.21: Fatigue test carried out using ISTRON 8801 machine.

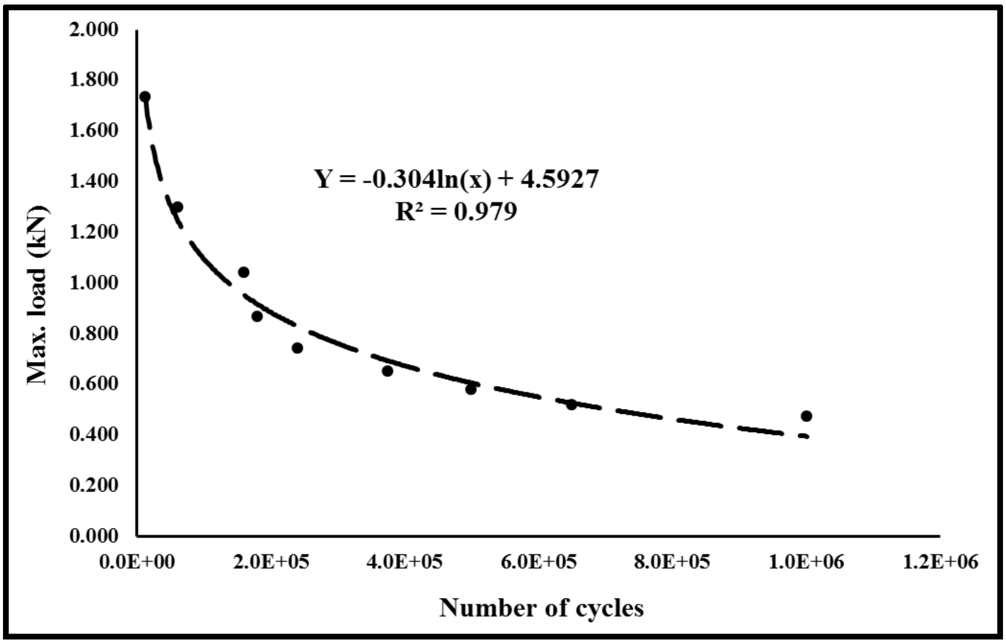

Figure 6.22: The extracted relationship between the applied load values and the maximum number of cycles for thermally treated RGD 525.

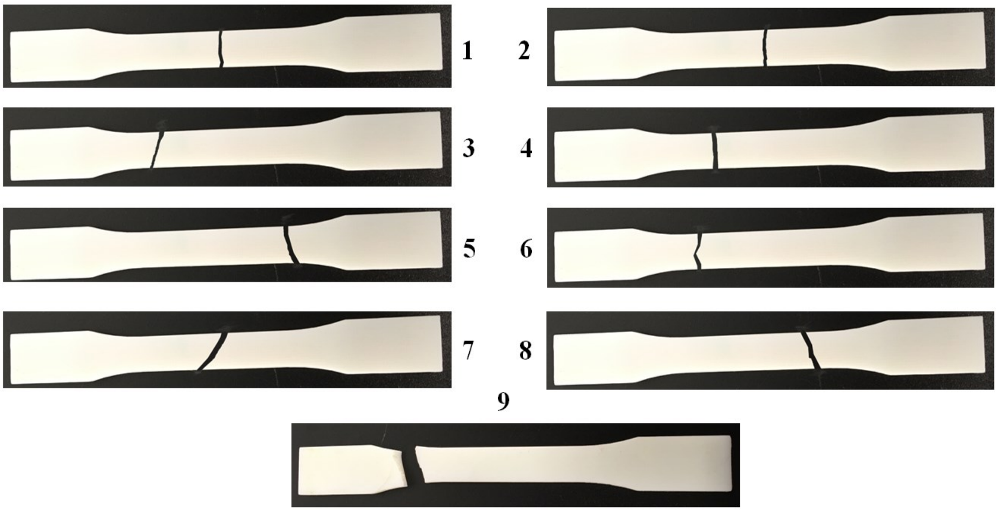

Figure 6.23: The nine fractured specimens of the thermally treated RGD 525 after the fatigue test.

6.5.3 Experimental Validation of the (SSRT):

Figure 6.24 shows the 3D printed components of Small Scale Radial Turbine (SSRT) using RGD 525 material including the inlet and outlet flanges, volute, shroud, stator and the rotor.

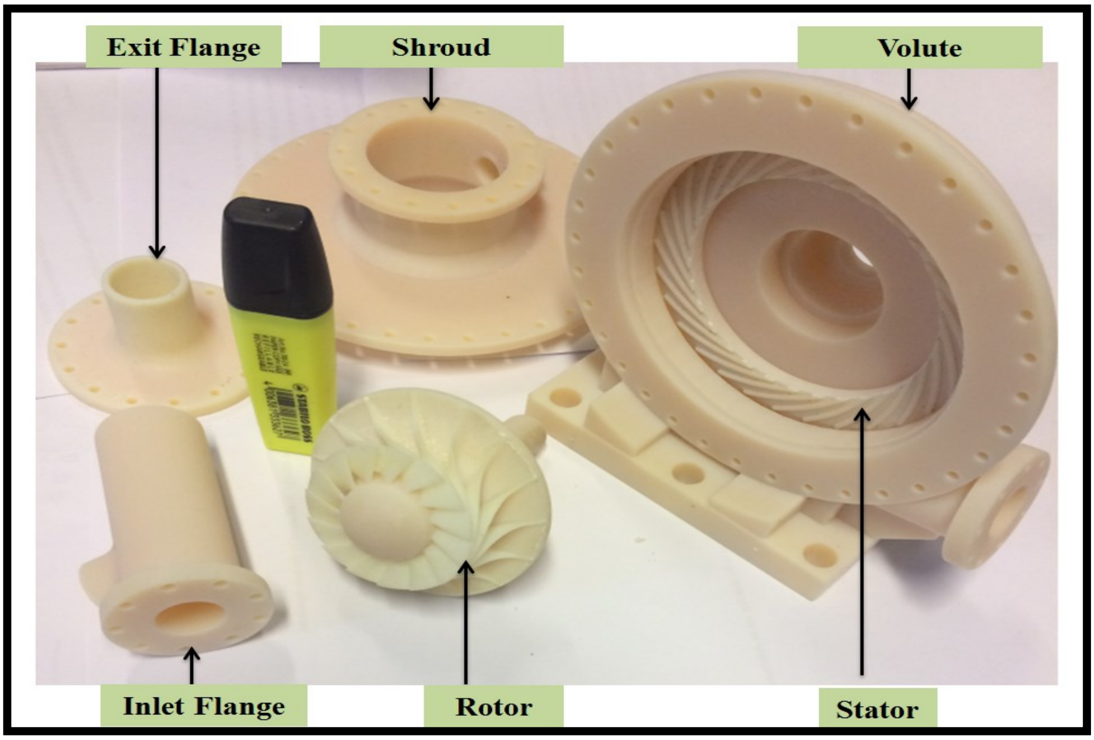

Figure 6.24: The (SSRT) parts manufactured using 3D printing technology.

6.5.3.1 SSRT Test Procedure:

Figure 6.25 shows the assembled (SSRT) installed in the test facility with 3805B2ZTVH Metal Shielded Double Row Angular Contact Ball Bearing 25x37x10mm bearing type. Here it is worth mentioning that the inlet pressure and flow rate were limited by those supplied by the compressed air storage system at the department of mechanical engineering, University of Birmingham. As a result of these limitations, it was not possible to include the light source and thermal receiver as a heat source in the test facility. Instead, the compressed air was supplied to an electrical heater to increase its temperature and then passed to the (SSRT) to produce mechanical power and then released to the atmosphere. The (SSRT) was fitted with temperature and pressure sensors at the inlet and outlet and coupled to a torque meter to evaluate its performance at various operating conditions. The test procedure followed can be summarised as:

1- Allow the compressed air flow through the turbine and monitor the pressure and temperature values of the supplied air using the PicoLog and Pico TC-08 respectively.

2- Adjust the electrical heater input voltage and the air flow rate in order to reach the required pressure and temperature values.

3- Once the required inlet pressure and temperature values reached, both the torque meter and the tachometer were switched on and plugged to the laptop in order to measure the torque and rotor's rotational speed.

4- Record the air flow rate, the air inlet and exit pressure, the air inlet and exit temperatures, the (SSRT) rotational speed, the torque and the extracted power to be analysed and compared with the simulation results of their corresponding operating conditions.

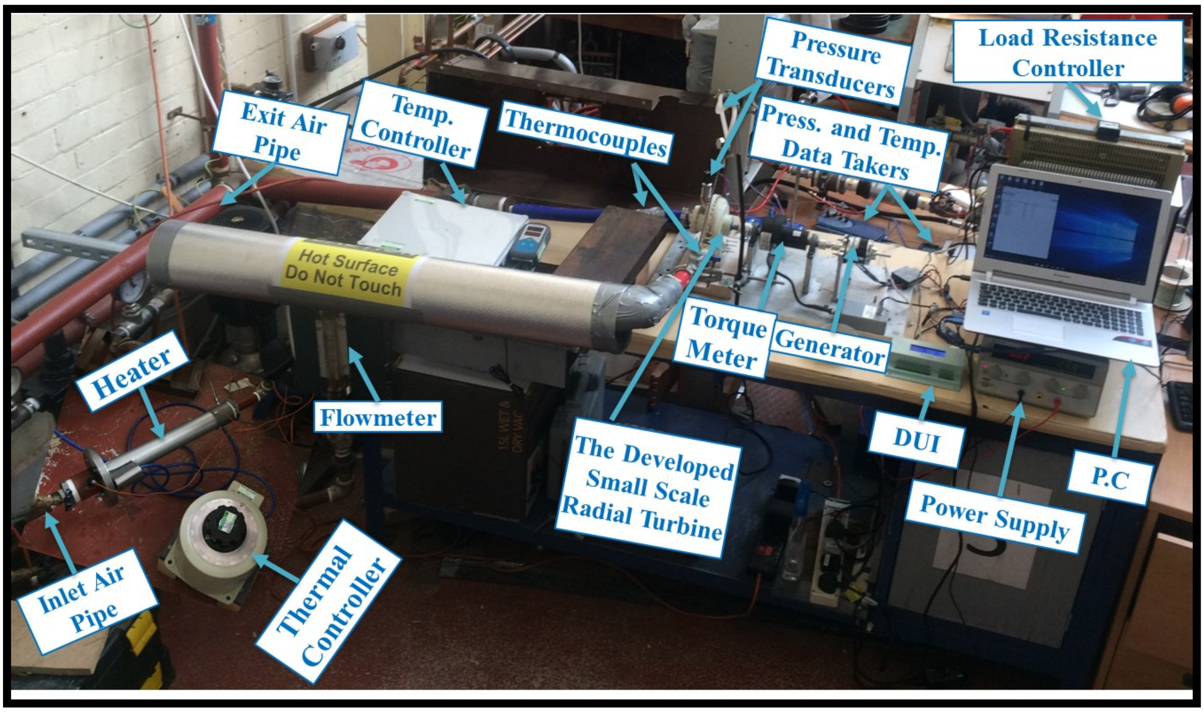

Figure 6.25: Radial air turbine test facility.

6.5.3.2 Results and Discussion of the (SSRT):

Experimental testing of the (SSRT) was carried out at inlet temperature varying from 20 ^{o}C to 40 ^{o}C and inlet pressure values varying from 1.5 to 2.5 Bar. Here it is worth mentioning that the inlet pressure values were limited by those supplied by the compressed air storage system at the department of mechanical engineering. Also, the inlet temperature values used are determined based on those predicted by the optical/ thermal simulation carried out in chapter 3.

Figure 6.26 shows total to static efficiency and the power output of the (SSRT) at compressed air inlet temperature of 20 ^{o}C and maximum rotor rotational speed of 20 krpm. Similarly, the theoretical and the experimental total to static efficiency and power output values of the (SSRT) at inlet temperature values of 30 ^{o}C and 40 ^{o}C were drawn against various values of pressure ratio and maximum rotor rotational speed of 20 krpm, as shown in Figure 6.27 and Figure 6.28 respectively. From the mentioned figures it can be noticed that there is an increase in the efficiency value when the pressure ratio and compressed air inlet temperature increase due to the increase in enthalpy drop value through the turbine. Furthermore, the above figures show good agreement between the experimental and numerical results with maximum deviation of 16% for the efficiency and 15% for the power output. Figure 6.26 to Figure 6.28 show that the highest efficiency and output power were achieved at inlet pressure of 2 Bar, inlet turbine temperature of 40 ^{o}C to be about 47% and 1.09 kW respectively.

The deviation of the experimental results from those predicted by the simulation can be attributed to the following:

- The numerical analysis was conducted under steady state compressed air flow entering the turbine and assumes no heat loss through the turbine body to the atmosphere, while in the experimental testing the compressed air flow rate is fluctuating and heat losses to the surroundings exist.
- In the experimental work, the surface roughness of the manufactured (SSRT) model affected the results while in the numerical analysis using ANSYS CFX the surface roughness was neglected.

- Finally, the mechanical losses in the rotor part, was not included in the CFX analysis as the established model, included only the stator and the rotor without taking these losses into consideration.

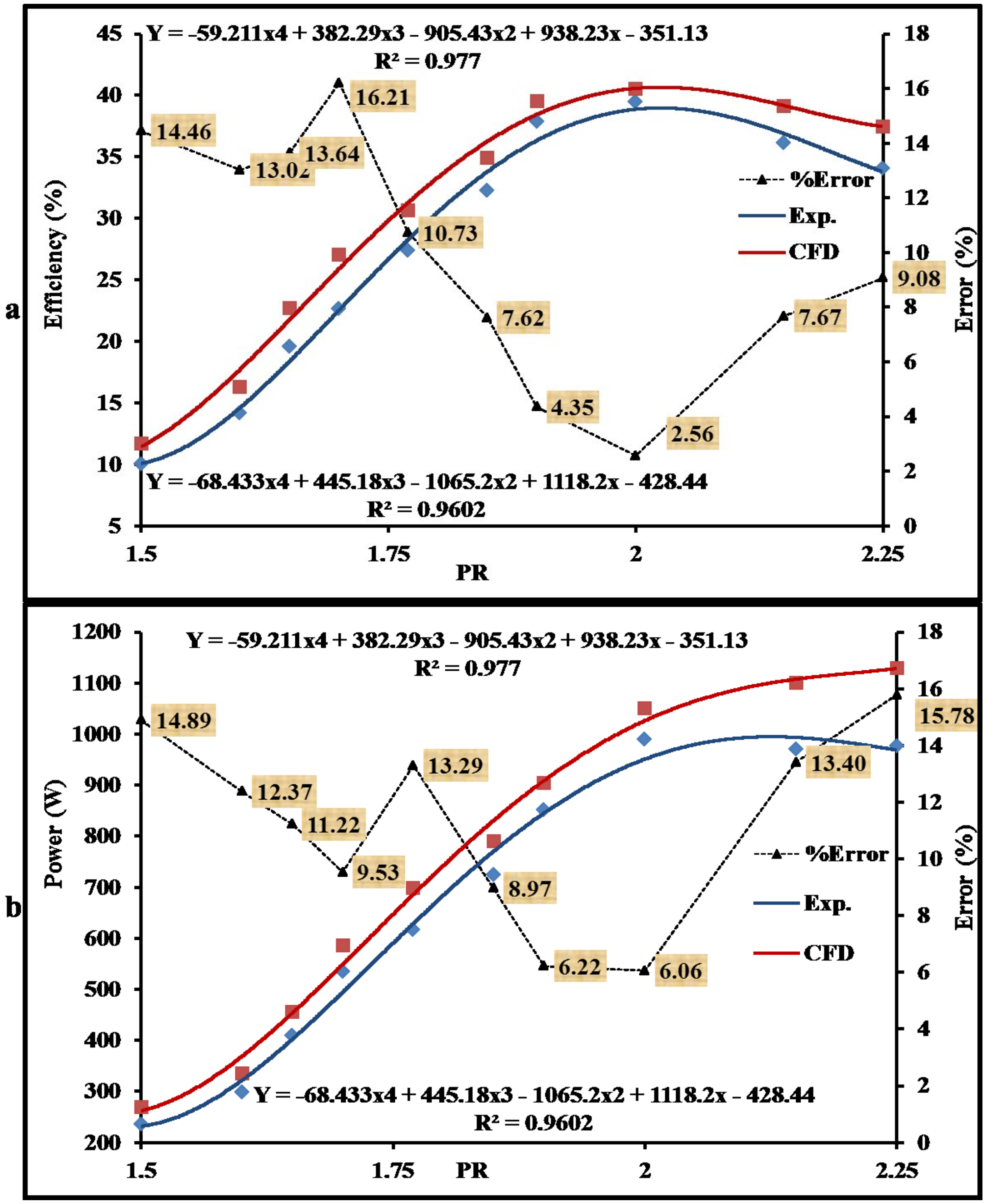

Figure 6.26: Comparing of (CFD) modelling and experimental results for (SSRT) (a) Efficiency and (b) Power at 20 °C.

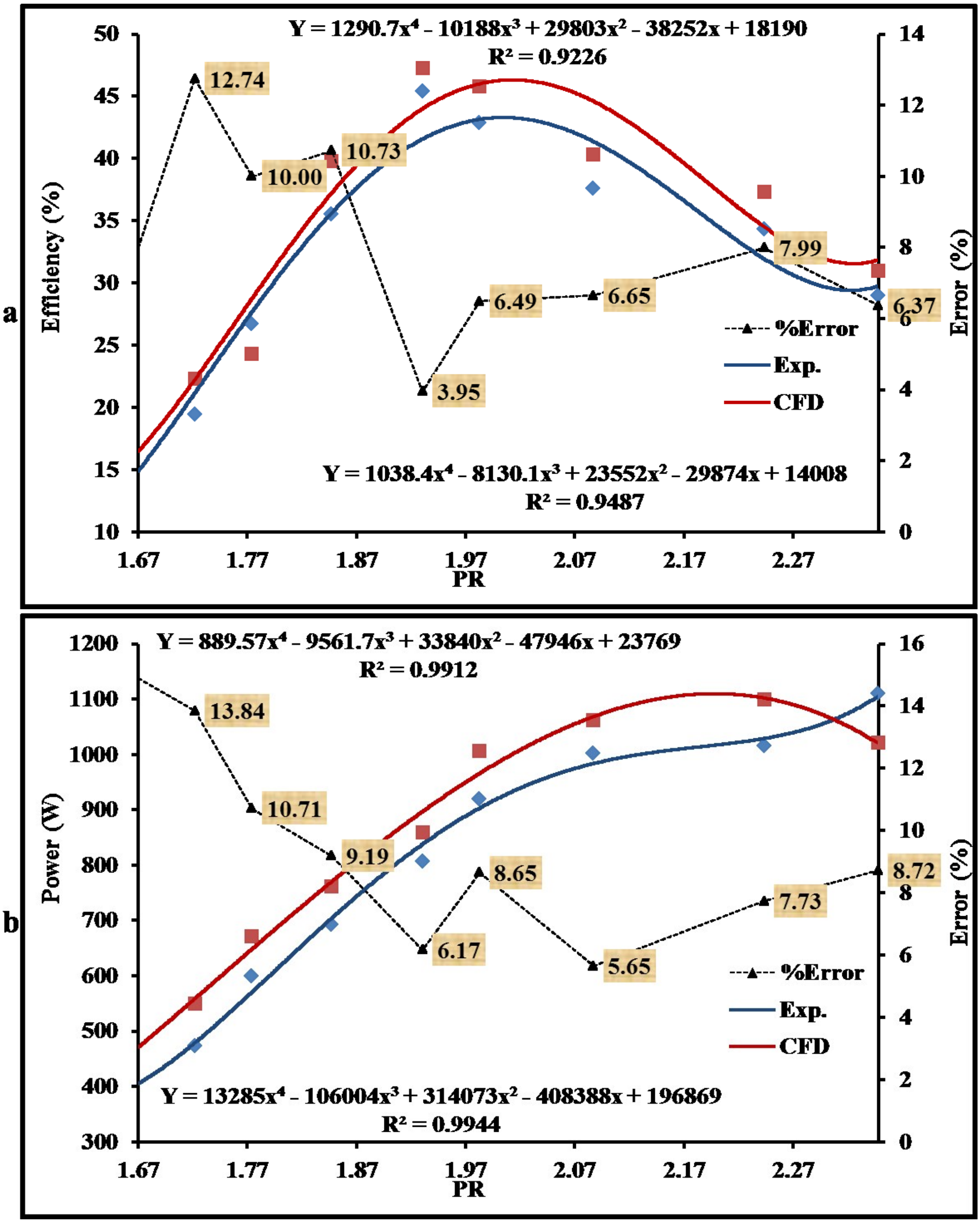

Figure 6.27: Comparing of (CFD) modelling and experimental results for (SSRT) (a) Efficiency and (b) Power at 30 ^{o}C.

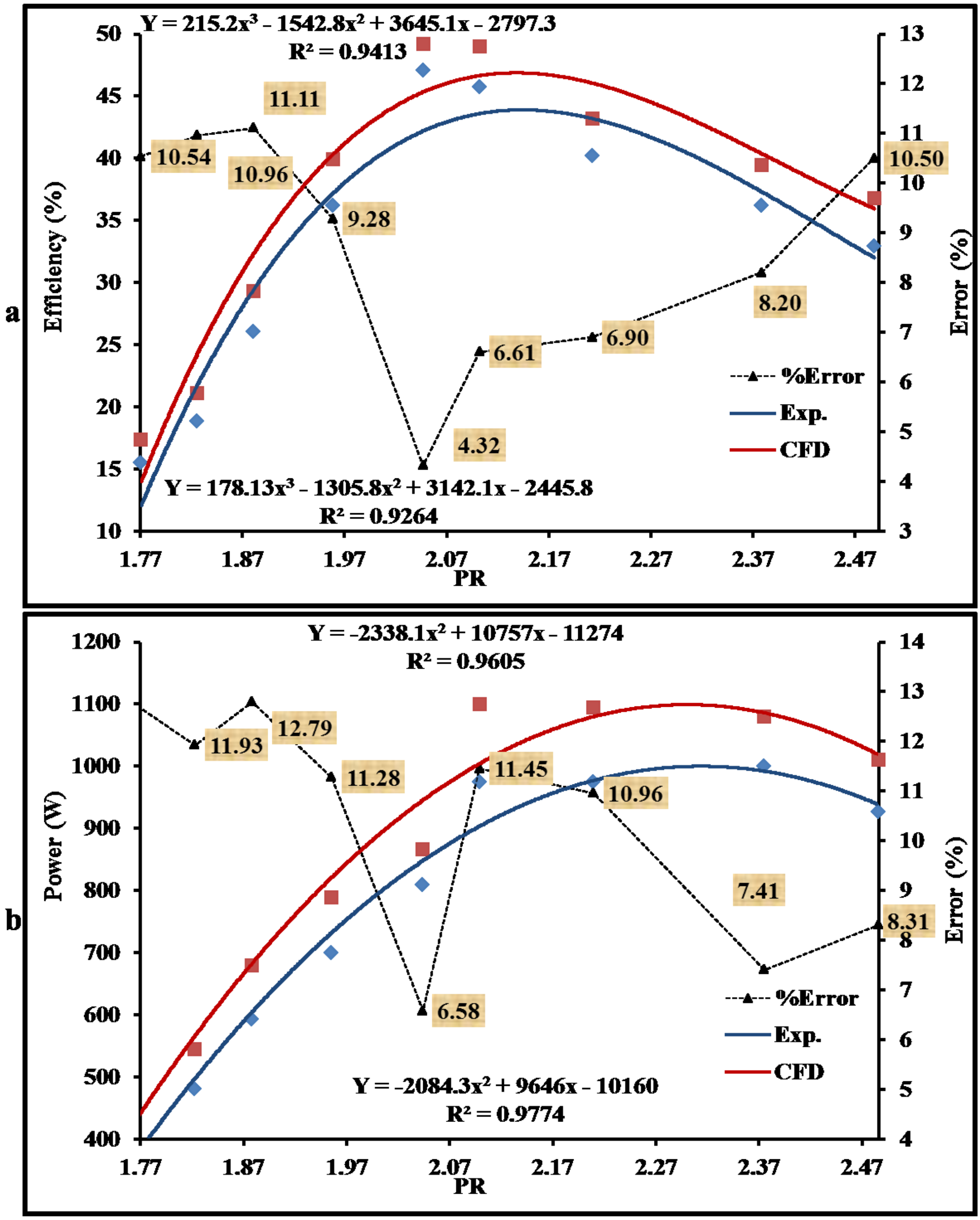

Figure 6.28: Comparing of (CFD) modelling and experimental results for (SSRT) (a) Efficiency and (b) Power at 40 °C.

6.6 Summary and conclusions:

An experimental work for a small scale cylindrical cavity receiver as well as small scale radial turbine for small scale solar powered Brayton cycle was conducted in this chapter. This work included optical and thermal analyses and the achieved results were compared to those predicted by the developed relevant models using OptisWorks ray tracing and ANSYS Academic (CFD) software. Also, it includes the performance testing of the manufactured (SSRT).

For the thermal system of the Brayton cycle, the main conclusions regarding the optical and thermal analysis following conclusions can be made:

- A cylindrical steel cavity fitted with copper helical tube of 8 mm diameter was built and tested in a solar lab with the aim of evaluating its behaviour in terms of flux and temperature distributions and the compressed air exit temperature.
- The results showed, with very good agreement between the experimental results and the numerical, that a relatively good distribution for both flux and temperature was achieved on the surface of the helical tube.
- Depending on the supplied mass flow rate, compressed air outlet temperature of more than 70 ^{o}C can be achieved using small scale parabolic dish as a concentrator for (CSP) in a domestic application.

Similarly, regarding the development of (SSRT) using 3D printing, the following can be concluded:

- A new plastic material, RGD 525, was chosen to manufacture the 3D model of the (SSRT) using 3D printing technology. This material has shown a maximum enhancement in its mechanical properties, 37.5%, when it was thermally treated but only at a specific temperature value. This improvement increases the possibility of using this material not only as a prototype but in real applications when the temperature in interest is less than 60 °C.

- Nine specimens of the RGD 525 material were printed for fatigue testing using the INSTRON 8801, hydraulic fatigue testing machine, with the aim of finding the S-N curve and numerically charactering the (SSRT) model, carried out in the previous chapter.
- The maximum achieved values for the efficiency and output power were attained at inlet turbine pressure and temperature of 2 Bar and 40 °C to be 47% and 1.09 kW respectively. However, at the design conditions of pressure ratio of 3 and inlet temperature of 65 °C, the turbine can produce 1.33 kW and have around 87% efficiency.
- Once the complete model experimentally tested, it is noticed a good agreement between the experimental and numerical results of the (SSRT) efficiency and extracted power, which reflect the accuracy of the methods used during both the simulation and the experimental testing.
- The numerical results of the efficiency and the output power for the developed (SSRT) were over predicted to reach maximum values of 16% and less than 14% respectively, when it is compared to the experimental results.

CHAPTER 7: CONCLUSIONS AND RECOMMENDATIONS

7.1 Introduction:

Small Scale Solar Powered Brayton Cycle have potential in developing new solar power generation systems as it is available, renewable and environmental friendly, thereby became in the interest of researchers and business companies. However, some challenges in terms of developing each of its components are still needed to be carefully considered. Therefore, more research is required for improving the overall cycle efficiency through optimizing the design of the various components including the solar heater and turbine. This study focused on developing the thermal cavity receiver and turbines as they are important parts in the cycle.

7.2 Conclusions:

The SSSPBC can be largely improved not only if each of its components was separately improved but also when they are integrated with each other. As this study deals with both on and off design conditions, it attempts to develop the overall cycle efficiency through enhancing its components for use in small scale domestic applications. The main conclusions are highlighted in the following sections:

7.2.1 Thermal Cavity Receiver

For the cavity receiver, the main conclusions can be summarised in the following points:

- The cavity shape of the thermal receiver has a significant effect on the distribution of the received flux which in turns plays a significant role in terms of the amount of heat losses. Moreover, the receiver shape affects directly the focal point position and the absorption ratio. As a result, the optimum focal point position varies based on the cavity receiver shape and its absorptivity.

- The conical cavity receiver showed the highest illumination uniformity and thereby is capable to receiver more incoming energy compared to the other two cavity shapes. Moreover, the lowest amount of heat losses and therefore the maximum thermal efficiency of around 77.05% is achieved by the conical receiver, compared to 69% for the cylindrical and 63% for the spherical; which indicate its suitability for the SSSPBC application.
- Modelling the real geometries, flux and other boundary conditions are possible through utilising the precise and appropriate solver and applying a suitable setting; though setting up such model is computing- intensive and time consuming. Moreover, there is no more than 6.5 % difference in the exit air temperature when the real flux was applied, instead of being uniformly distributed, which indicates the validity of assuming a uniform flux on the helical tube.
- Using a thermal glass to cover the receiver aperture leads to a significant improvement in the thermal efficiency, reaching 7.4 %.

7.2.2 Small Scale Turbines

Regarding the development of small scale turbines, the main conclusions are summarised as following:

- The (SSRT) is superior if the main interest is to offer higher power output at a relatively low pressure ratio and mass flow rate. At high pressure ratio, its output power value reaches 1.7 higher than that achieved by the (SSAT).
- At low rotor rotational speed and off design conditions, the small scale axial turbine is able to show better performance compared to the radial which can lead to relatively stable cycle efficiency. However, the small scale radial turbine is better when at high rotational speed.

- The maximum efficiency was achieved when the rotor blades were 13 and 10 while the stator trailing edge angles of 60° and at 67° for the (SSRT) and (SSAT) respectively.
- The (SSRT) experiences lower trailing edge thickness losses than tip clearance and together they cause about 4 %. The trailing edge loss can be reduced in the (DSAT) if the rotor trailing edge thickness of the 1st stage and the stator leading edge of 2nd stage were matched carefully.
- For the cycle analysis, it is shown that at 95% compressor efficiency, an improvement in the efficiency of the cycle from 3% to 7% (based on other boundary circumstances) is achievable by increasing the turbine efficiency to 90%.

7.2.3 3D Optimizations

3D optimization using two different optimization methods, for the whole stage of the (SSRT) have been used and the following conclusions can be made:

- An excellent enhancement in the (SSRT) isentropic efficiency, from 82.3% to 87.5% is achieved by (using the (MOGA) techniques). The blade shape and the stator and rotor blade's number were optimised using the direct method of optimization which allows for more than 20 input parameters to be used together.
- In order to confirm the accuracy of the used method, which achieved this high level of turbine efficiency, other approach of (MOGA) 3D optimization which is the response surface optimization was used and the results showed relatively lower efficiency 86.7%. However, it is still high value for this scale of turbines, a power output of about 1 kW with isentropic efficiency of around 87.5%.
- Integrating the meanline approach, (3D CFD) analysis and the (MOGA) 3D optimization in the cycle thermodynamic analysis showed about 5% enhancement in the overall cycle performance with the optimised turbine.

7.2.4 Structural Analysis of the (SSRT):

The main conclusions drawn from the rotor stress analysis are:

- The tip shroud location experienced a higher deflection values in the rotor, 16.5% of the blade tip width. As a result, the gap between the blade tip and the shroud and between the blades should be equal or higher than the deflection, increment, value.
- As, for the fatigue analysis, the highest inlet temperature of the compressed air, has contributed to decreasing the rotor fatigue life of about 97%, especially at higher rotational speed. The lowest fatigue life was located in the area where the blades are connected with the rotor's hub which also has the highest damage.
- The multidisciplinary optimization led to 17%, 9% and 25% enhancement in the maximum equivalent stress, maximum deflection and minimum number of cycles, while the output power and efficiency were decreased by around 8% and 1.5% respectively.

7.2.5 Experimental work

Experimental work was carried out for the optical, thermal and the aerodynamic performance of the developed cavity receiver and (SSRT) to validate the utilised methodologies. The most important conclusions can be summarised as below:

- The results showed, with very good agreement <13% between the experimental and the numerical results, that a relatively good distribution for both flux and temperature was achieved on the circumference of the helical tube.
- Based on the supplied flow rate, up to 70 ^{o}C, depending on the, outlet temperature of the compressed air is reachable which implies the possibility of using small scale parabolic dish as a concentrator for (CSP) for domestic applications.
- The maximum achieved efficiency and output power were attained at inlet turbine pressure and temperature of 2 Bar and 40 ^{o}C to be 47% and 1.09 kW respectively.

- The numerical results of the efficiency and the output power for the developed (SSRT) over predicted the experimental results with maximum values of less than 16% and 14% respectively.

7.2.6 Overall conclusions and contribution to knowledge:

In this research an integrated method for developing (SSTs) for (SSSPB)C including (i) meanline approach for initial design, (ii) detailed (CFD) simulation; (iii) multi-objective genetic algorithm optimization; (iv) structural analysis of stress and fatigue; (iv) multidisciplinary optimization and (v) thermodynamic cycle performance modelling to achieve the best power output and cycle efficiency. These techniques were validated experimentally. This integrated method was not presented before and therefore a new contribution to knowledge in this field.

Optical and thermal simulation of thermal cavity receiver shapes were developed to achieve the optimum configuration of the thermal receiver showing the conically shape receiver produces the highest output.

With the validated methodology, it is predicted that a small scale solar powered Brayton cycle system consisting of (i) 3 m diameter parabolic collector; (ii) conical shape cavity receiver with 0.2 m aperture; (iii) (SSRT) operating at pressure ratio of 3 and inlet temperature of 500 K and compressor with 95%, the (SSSPBC) can achieve cycle efficiency of 15% and power output of 1 kW.

It is explained that this SSSPBC to be cost effective method compared to solar (PV) systems.

7.3 Recommendations:

The main recommendations are basically organized in two groups as two main fields have been discussed. As for the turbomachinery, the following can be recommended for next studies:

- Compressor is one of the main cycle components and its performance affect the cycle operation highly, so, its design performance and enhancement needs to be considered in next studies.
- Including the vibration in the multidisciplinary optimization of the small scale radial turbines which work at high level of rotational speed.

Also, for better solar powered system performance, the following can be recommended:

- Develop a storage system that can store the extra solar energy during the peak times and then recover it at night where there is no sun available.
- Optimize the cavity receiver optically and thermally simultaneously in order to achieve better cycle performance.
- Optimize the overall cycle using different working fluids with the aim of knowing the most relevant working fluid at each specific boundary conditions.

References:

[1] V. R. Putti, M. Tsan, S. Mehta, and S. Kammila, "The state of the global clean and improved cooking sector", 2015.

[2] C. Edge, "Clean Energy Trends 2006", ed, 2006.

[3] L. Scheinman, *The international atomic energy agency and world nuclear order*: Routledge, 2016.

[4] J. Conti, P. Holtberg, J. Diefenderfer, A. LaRose, J. T. Turnure, and L. Westfall, "International Energy Outlook 2016 With Projections to 2040", USDOE Energy Information Administration (EIA), Washington, DC (United States). Office of Energy Analysis2016.

[5] I. PVPS, "International Energy Agency-Photovoltaic Power Systems Programme, 2016", *Snapshot of Global PV Markets,* 2016.

[6] H.-W. Schiffer, "World Energy Resources, World Energy Council", 2016.

[7] W. G. Le Roux, T. Bello-Ochende, and J. P. Meyer, "Operating conditions of an open and direct solar thermal Brayton cycle with optimised cavity receiver and recuperator", *Energy,* vol. 36, pp. 6027-6036, 2011.

[8] H. Riazi and N. Ahmed, "Effect of the ratio of specific heats on a small scale solar Brayton cycle", *Procedia engineering,* vol. 49, pp. 263-270, 2012.

[9] A. Gallo, J. Spelling, M. Romero, and J. González-Aguilar, "Preliminary design and performance analysis of a multi-megawatt scale dense particle suspension receiver", *Energy Procedia,* vol. 69, pp. 388-397, 2015.

[10] J. Sanz-Bermejo, V. Gallardo-Natividad, J. Gonzalez-Aguilar, and M. Romero, "Comparative system performance analysis of direct steam generation central receiver solar thermal power plants in megawatt range", *Journal of Solar Energy Engineering,* vol. 136, p. 010908, 2014.

[11] M. T. White and A. I. Sayma, "A preliminary comparison of different turbine architectures for a 100 kW supercritical CO2 Rankine cycle turbine".

[12] P. J. Mago, L. M. Chamra, K. Srinivasan, and C. Somayaji, "An examination of regenerative organic Rankine cycles using dry fluids", *Applied thermal engineering,* vol. 28, pp. 998-1007, 2008.

[13] K. Braimakis and S. Karellas, "Exergetic optimization of double stage Organic Rankine Cycle (ORC)", *Energy,* vol. 149, pp. 296-313, 2018.

[14] Z. Bai, G. Zhang, Y. Li, G. Xu, and Y. Yang, "A supercritical CO2 Brayton cycle with a bleeding anabranch used in coal-fired power plants", *Energy,* vol. 142, pp. 731-738, 2018.

[15] A. de la Calle, A. Bayon, and Y. C. S. Too, "Impact of ambient temperature on supercritical CO 2 recompression Brayton cycle in arid locations: Finding the optimal design conditions", *Energy,* 2018.

[16] J. Galindo, C. Guardiola, V. Dolz, and P. Kleut, "Further analysis of a compression-expansion machine for a Brayton Waste Heat Recovery cycle on an IC engine", *Applied Thermal Engineering,* vol. 128, pp. 345-356, 2018.

[17] W. G. Le Roux, T. Bello-Ochende, and J. P. Meyer, "The efficiency of an open-cavity tubular solar receiver for a small-scale solar thermal Brayton cycle", *Energy Conversion and Management,* vol. 84, pp. 457-470, 2014.

[18] W. G. Le Roux, T. Bello-Ochende, and J. P. Meyer, "Optimum performance of the small-scale open and direct solar thermal Brayton cycle at various environmental conditions and constraints", *Energy,* vol. 46, pp. 42-50, 2012.

References

[19] R. Wüstenhagen, M. Wolsink, and M. J. Bürer, "Social acceptance of renewable energy innovation: An introduction to the concept", *Energy policy,* vol. 35, pp. 2683-2691, 2007.

[20] H. Ibrahim, A. Ilinca, and J. Perron, "Energy storage systems—characteristics and comparisons", *Renewable and sustainable energy reviews,* vol. 12, pp. 1221-1250, 2008.

[21] E. PROTECTION, "ENVIRONMENTAL PROTECTION AGENCY (EPA)", 2003.

[22] L. García-Rodríguez and J. Blanco-Gálvez, "Solar-heated Rankine cycles for water and electricity production: POWERSOL project", *Desalination,* vol. 212, pp. 311-318, 2007.

[23] M. Villarini, E. Bocci, M. Moneti, A. Di Carlo, and A. Micangeli, "State of art of small scale solar powered ORC systems: a review of the different typologies and technology perspectives", *Energy Procedia,* vol. 45, pp. 257-267, 2014.

[24] U. EUROPEA, "Horizon 2020 Work Programme 2014–2015 16", *Science with and for Society. Recuperado desde http://ec. europa. eu/research/participants/data/ref/h2020/wp/2014_2015/main/h2020-wp1415-swfs_en. pdf,* 2014.

[25] B. a. A. P. Roy, "Turbomachinery Aerodynamics", 2012.

[26] G. Pei, J. Li, Y. Li, D. Wang, and J. Ji, "Construction and dynamic test of a small-scale organic rankine cycle", *Energy,* vol. 36, pp. 3215-3223, 2011.

[27] T. Ackermann, G. Andersson, and L. Söder, "Distributed generation: a definition1", *Electric power systems research,* vol. 57, pp. 195-204, 2001.

[28] A. M. Daabo, A. Al Jubori, S. Mahmoud, and R. K. Al-Dadah, "Parametric study of efficient small-scale axial and radial turbines for solar powered Brayton cycle application", *Energy Conversion and Management,* vol. 128, pp. 343-360, 2016.

[29] S. Dixon, *Fluid Mechanics-Thermodynamics of Turbomachinery (in SI/Metric Units)*, 1978.

[30] R. H. Aungier, *Centrifugal compressors: a strategy for aerodynamic design and analysis*: American Society of Mechanical Engineers, 2000.

[31] D. W. G. a. R. H. Perry, *Perry's Chemical Engineers' Handbook, Eighth Edition*. Sydney, Toronto: McGraw-Hill, 2008.

[32] R. Shah, "Compact Heat Exchangers-Recuperators and Regenerators", *Handbook of Energy Efficiency and Renewable Energy. Kreith F., Yogi Goswami D,* 2007.

[33] C. Dey, "Heat transfer aspects of an elevated linear absorber", *Solar Energy,* vol. 76, pp. 243-249, 2004.

[34] N. El Gharbi, H. Derbal, S. Bouaichaoui, and N. Said, "A comparative study between parabolic trough collector and linear Fresnel reflector technologies", *Energy Procedia,* vol. 6, pp. 565-572, 2011.

[35] A. Barbón, N. Barbón, L. Bayón, and J. Sánchez-Rodríguez, "Parametric study of the small scale linear Fresnel reflector", *Renewable Energy,* vol. 116, pp. 64-74, 2018.

[36] J. M. Pedraza, "The Current Situation and Perspectives on the Use of Renewable Energy Sources for Electricity Generation", in *Electrical Energy Generation in Europe*, ed: Springer, 2015, pp. 55-92.

[37] M. Orosz, P. Mathaha, A. Tsiu, B. Taele, L. Mabea, M. Ntee*, et al.*, "Low-cost small scale parabolic trough collector design for manufacturing and deployment in Africa", in *AIP Conference Proceedings*, 2016, p. 020016.

[38] G. K. Abdulsada and A. E. Sa'ad-Aldeen, "Experimental Small Scale Solar Power Tower in Iraq".

[39] J. Harrison, "Investigation of reflective materials for the solar cooker", *Solar Energy Web Site,* vol. 24, 2001.

References

[40] W. B. Stine, "International survey of parabolic dish/Stirling engine electrical power generation technology", *ASME, NEW YORK, NY(USA).* pp. 421-427, 1993.

[41] W. B. Stine, "Cavity receiver convection heat loss", in *Proc. of the International Solar Energy Society. Solar World Congress*, 1989.

[42] W. LE ROUX, T. Bello-Ochende, and J. Meyer, "Solar tracking for a parabolic dish used in a solar thermal Brayton cycle", in *Proceedings of the Postgraduate Symposium*, 2012.

[43] S. Pavlovic, A. M. Daabo, E. Bellos, V. Stefanovic, S. Mahmoud, and R. K. Al-Dadah, "Experimental and numerical investigation on the optical and thermal performance of solar parabolic dish and corrugated spiral cavity receiver", *Journal of Cleaner Production,* vol. 150, pp. 75-92, 2017.

[44] B. Hoffschmidt, "Receivers for Solar Tower Systems", 2014.

[45] M. Lin, K. Sumathy, Y. Dai, and X. Zhao, "Performance investigation on a linear Fresnel lens solar collector using cavity receiver", *Solar Energy,* vol. 107, pp. 50-62, 2014.

[46] Y. Tian and C.-Y. Zhao, "A review of solar collectors and thermal energy storage in solar thermal applications", *Applied energy,* vol. 104, pp. 538-553, 2013.

[47] R. Lahlou, P. Armstrong, B. Grange, S. Almheiri, N. Calvet, A. Slocum*, et al.*, "Thermal modeling of a secondary concentrator integrated with an open direct-absorption molten-salt volumetric receiver in a beam-down tower system", in *AIP Conference Proceedings*, 2016, p. 020012.

[48] A. Mishra, A. Shukla, and A. Sharma, "Latent heat storage through phase change materials", *Resonance,* vol. 20, pp. 532-541, 2015.

[49] K. Lovegrove, A. Luzzi, I. Soldiani, and H. Kreetz, "Developing ammonia based thermochemical energy storage for dish power plants", *Solar Energy,* vol. 76, pp. 331-337, 2004.

[50] F. S. Union, N. Africa, S.-S. Africa, S. Asia, C. planned Asia, and O. Pacific, "Yearly solar fluxes & human consumption".

[51] G. J. Kolb, C. K. Ho, T. R. Mancini, and J. A. Gary, "Power tower technology roadmap and cost reduction plan", *Sandia National Laboratories, Albuquerque, NM, Report No. SAND2011-2419,* 2011.

[52] D. Biello, "How to use solar energy at night", *Scientific American,* vol. 18, 2009.

[53] R. Ehrlich, *Renewable energy: a first course*: CRC Press, 2013.

[54] S.-Y. Wu, L. Xiao, Y. Cao, and Y.-R. Li, "Convection heat loss from cavity receiver in parabolic dish solar thermal power system: A review", *Solar Energy,* vol. 84, pp. 1342-1355, 2010.

[55] W. G. Le Roux, T. Bello-Ochende, and J. P. Meyer, "A review on the thermodynamic optimisation and modelling of the solar thermal Brayton cycle", *Renewable and sustainable energy reviews,* vol. 28, pp. 677-690, 2013.

[56] J. A. Harris and T. G. Lenz, "Thermal performance of solar concentrator/cavity receiver systems", *Solar energy,* vol. 34, pp. 135-142, 1985.

[57] M. I. Roldán, L. Valenzuela, and E. Zarza, "Thermal analysis of solar receiver pipes with superheated steam", *Applied energy,* vol. 103, pp. 73-84, 2013.

[58] T. Melchior, C. Perkins, A. W. Weimer, and A. Steinfeld, "A cavity-receiver containing a tubular absorber for high-temperature thermochemical processing using concentrated solar energy", *International Journal of Thermal Sciences,* vol. 47, pp. 1496-1503, 2008.

[59] A. Steinfeld and M. Schubnell, "Optimum aperture size and operating temperature of a solar cavity-receiver", *Solar Energy,* vol. 50, pp. 19-25, 1993.

References

[60] K. Qiu, L. Yan, M. Ni, C. Wang, G. Xiao, Z. Luo*, et al.*, "Simulation and experimental study of an air tube-cavity solar receiver", *Energy Conversion and Management,* vol. 103, pp. 847-858, 2015.

[61] F. Wang, R. Lin, B. Liu, H. Tan, and Y. Shuai, "Optical efficiency analysis of cylindrical cavity receiver with bottom surface convex", *Solar Energy,* vol. 90, pp. 195-204, 2013.

[62] H. Von Storch, M. Roeb, H. Stadler, C. Sattler, and B. Hoffschmidt, "Available online Efficiency potential of indirectly heated solar reforming with different types of solar air receivers", *Applied Thermal Engineering,* vol. 92, pp. 202-209, 2016.

[63] M. Patil, R. Jahagirdar, and E. Deore, "Experimental investigation of heat loss from hemispherical solar concentrator receiver", *Frontiers in Heat and Mass Transfer (FHMT),* vol. 3, 2012.

[64] V. Sakhare and V. Kapatkar, "Experimental analysis of parabolic solar dish with copper helical coil receiver", *Int J Innov Res Adv Eng (IJIRAE),* vol. 1, pp. 199-204, 2014.

[65] M. Eswaramoorthy, S. Shanmugam, and A. Veerappan, "Experimental study on solar parabolic dish thermoelectric generator", *International Journal of Energy Engineering,* vol. 3, p. 62, 2013.

[66] A. Fleming, C. Folsom, H. Ban, and Z. Ma, "A general method to analyze the thermal performance of multi-cavity concentrating solar power receivers", *Solar Energy,* vol. 150, pp. 608-618, 2017.

[67] L. Ngo, T. Bello-Ochende, and J. P. Meyer, "Numerical modelling and optimisation of natural convection heat loss suppression in a solar cavity receiver with plate fins", *Renewable Energy,* vol. 74, pp. 95-105, 2015.

[68] J. Samanes, J. Garcia-Barberena, and F. Zaversky, "Modeling solar cavity receivers: a review and comparison of natural convection heat loss correlations", *Energy Procedia,* vol. 69, pp. 543-552, 2015.

[69] L. Aichmayer, J. Spelling, and B. Laumert, "Preliminary design and analysis of a novel solar receiver for a micro gas-turbine based solar dish system", *Solar energy,* vol. 114, pp. 378-396, 2015.

[70] T. Taumoefolau and K. Lovegrove, "An experimental study of natural convection heat loss from a solar concentrator cavity receiver at varying orientation", in *Proceedings of solar*, 2002.

[71] S. Paitoonsurikarn and K. Lovegrove, "On the study of convection loss from open cavity receivers in solar paraboloidal dish applications", in *Proceedings of solar*, 2003.

[72] M. Prakash, "Numerical study of natural convection heat loss from cylindrical solar cavity receivers", *ISRN Renewable Energy,* vol. 2014, 2014.

[73] R. Uhlig, R. Flesch, B. Gobereit, S. Giuliano, and P. Liedke, "Strategies enhancing efficiency of cavity receivers", *Energy Procedia,* vol. 49, pp. 538-550, 2014.

[74] E. Abbasi-Shavazi, G. Hughes, and J. Pye, "Investigation of heat loss from a solar cavity receiver", *Energy Procedia,* vol. 69, pp. 269-278, 2015.

[75] M. Lin, K. Sumathy, Y. Dai, R. Wang, and Y. Chen, "Experimental and theoretical analysis on a linear Fresnel reflector solar collector prototype with V-shaped cavity receiver", *Applied Thermal Engineering,* vol. 51, pp. 963-972, 2013.

[76] N. Tu, J. Wei, and J. Fang, "Experimental and numerical study on the thermal performance of a water/steam cavity receiver", *Energies,* vol. 6, pp. 1198-1216, 2013.

[77] N. S. Kumar and K. Reddy, "Numerical investigation of natural convection heat loss in modified cavity receiver for fuzzy focal solar dish concentrator", *Solar Energy,* vol. 81, pp. 846-855, 2007.

References

[78] S.-Y. Wu, Z.-G. Shen, L. Xiao, and D.-L. Li, "Experimental study on combined convective heat loss of a fully open cylindrical cavity under wind conditions", *International Journal of Heat and Mass Transfer,* vol. 83, pp. 509-521, 2015.

[79] K. Reddy and N. S. Kumar, "Combined laminar natural convection and surface radiation heat transfer in a modified cavity receiver of solar parabolic dish", *International Journal of Thermal Sciences,* vol. 47, pp. 1647-1657, 2008.

[80] W. Wu, L. Amsbeck, R. Buck, N. Waibel, P. Langner, and R. Pitz-Paal, "On the influence of rotation on thermal convection in a rotating cavity for solar receiver applications", *Applied Thermal Engineering,* vol. 70, pp. 694-704, 2014.

[81] A. P. Ortiz, J. F. H. Palafox, and C. A. E. Gasca, "Numerical study of heat transfer losses by mixed convection and surface thermal radiation in an open cavity receiver for a solar tower system", *Energy Procedia,* vol. 57, pp. 467-476, 2014.

[82] S. Paitoonsurikarn, K. Lovegrove, G. Hughes, and J. Pye, "Numerical investigation of natural convection loss from cavity receivers in solar dish applications", *Journal of Solar Energy Engineering,* vol. 133, p. 021004, 2011.

[83] J. Fang, N. Tu, and J. Wei, "Effects of absorber emissivity on thermal performance of a solar cavity receiver", *Advances in Condensed Matter Physics,* vol. 2014, 2014.

[84] S.-Y. Wu, D.-L. Li, L. Xiao, and Z.-G. Shen, "Experimental study on the effect of wind on heat losses from a fully open cylindrical cavity with only bottom wall heated", *International journal of green energy,* vol. 12, pp. 1244-1254, 2015.

[85] S. Yong, W. Fu-Qiang, X. Xin-Lin, T. He-Ping, and L. Ying-Chun, "Radiative properties of a solar cavity receiver/reactor with quartz window", *International journal of hydrogen energy,* vol. 36, pp. 12148-12158, 2011.

[86] M. Wang and K. Siddiqui, "The impact of geometrical parameters on the thermal performance of a solar receiver of dish-type concentrated solar energy system", *Renewable Energy,* vol. 35, pp. 2501-2513, 2010.

[87] D. Lei, Z. Wang, and Z. Wang, "Effects of geometry and material properties on the residual Stress of glass-to-metal seals in solar receiver tubes", *Energy Procedia,* vol. 49, pp. 418-427, 2014.

[88] G. Xiao, L. Yan, M. Ni, C. Wang, Z. Luo, and K. Cen, "Experimental study of an air tube-cavity solar receiver", *Energy Procedia,* vol. 61, pp. 496-499, 2014.

[89] A.-H. OM, R. Alomosh, and D. Aldebie, "Reliability Simulation of Solar Concentrator Receiver".

[90] O. M. Al-Habahbeh, R. A. Alomosh, and D. K. Aldebie, "Reliability simulation of solar concentrator receiver", *International Journal of Sustainable Energy,* vol. 35, pp. 793-801, 2016.

[91] L. Jianfeng, D. Jing, and Y. Jianping, "Heat transfer performance and exergetic optimization for solar receiver pipe", *Renewable energy,* vol. 35, pp. 1477-1483, 2010.

[92] J. Fang, N. Tu, and J. Wei, "Numerical investigation of start-up performance of a solar cavity receiver", *Renewable energy,* vol. 53, pp. 35-42, 2013.

[93] J. Capeillere, A. Toutant, G. Olalde, and A. Boubault, "Thermomechanical behavior of a plate ceramic solar receiver irradiated by concentrated sunlight", *Solar Energy,* vol. 110, pp. 174-187, 2014.

[94] Z. Liao, X. Li, C. Xu, C. Chang, and Z. Wang, "Allowable flux density on a solar central receiver", *Renewable Energy,* vol. 62, pp. 747-753, 2014.

[95] T. Fend, P. Schwarzbözl, O. Smirnova, D. Schöllgen, and C. Jakob, "Numerical investigation of flow and heat transfer in a volumetric solar receiver", *Renewable energy,* vol. 60, pp. 655-661, 2013.

References

[96] M. Roldán, E. Zarza, and J. Casas, "Modelling and testing of a solar-receiver system applied to high-temperature processes", *Renewable Energy,* vol. 76, pp. 608-618, 2015.

[97] F. Bai, "One dimensional thermal analysis of silicon carbide ceramic foam used for solar air receiver", *International Journal of Thermal Sciences,* vol. 49, pp. 2400-2404, 2010.

[98] Z. Wu and Z. Wang, "Fully coupled transient modeling of ceramic foam volumetric solar air receiver", *Solar Energy,* vol. 89, pp. 122-133, 2013.

[99] A. M. Daabo, S. Mahmoud, and R. K. Al-Dadah, "The optical efficiency of three different geometries of a small scale cavity receiver for concentrated solar applications", *Applied energy,* vol. 179, pp. 1081-1096, 2016.

[100] Z. Wu, C. Caliot, G. Flamant, and Z. Wang, "Coupled radiation and flow modeling in ceramic foam volumetric solar air receivers", *Solar Energy,* vol. 85, pp. 2374-2385, 2011.

[101] L. Xiao, S.-Y. Wu, and Y.-R. Li, "Numerical study on combined free-forced convection heat loss of solar cavity receiver under wind environments", *International Journal of Thermal Sciences,* vol. 60, pp. 182-194, 2012.

[102] J.-B. Fang, J.-J. Wei, X.-W. Dong, and Y. Wang, "Thermal performance simulation of a solar cavity receiver under windy conditions", *Solar Energy,* vol. 85, pp. 126-138, 2011.

[103] N. S. Kumar and K. Reddy, "Comparison of receivers for solar dish collector system", *Energy Conversion and Management,* vol. 49, pp. 812-819, 2008.

[104] K. Reddy and N. S. Kumar, "Convection and surface radiation heat losses from modified cavity receiver of solar parabolic dish collector with two-stage concentration", *Heat and Mass Transfer,* vol. 45, pp. 363-373, 2009.

[105] S. Paitoonsurikarn and K. Lovegrove, "Numerical investigation of natural convection loss in cavity-type solar receivers", in *Proceedings of Solar*, 2002, pp. 1-6.

[106] A. Daabo, S. Mahmoud, and A.-D. Raya, "Effect of open cavity configuration on solar receiver thermal performance", in *Extended Abstracts*, 2016, p. 47.

[107] L. Xiao, S.-Y. Wu, and Y.-R. Li, "Natural convection heat loss estimation of solar cavity receiver by incorporating a modified aperture ratio", *IET Renewable Power Generation,* vol. 6, pp. 122-128, 2012.

[108] R. Jilte, S. Kedare, and J. Nayak, "Investigation on convective heat losses from solar cavities under wind conditions", *Energy Procedia,* vol. 57, pp. 437-446, 2014.

[109] I. L. Mohammed, "Design and development of a parabolic dish solar water heater", *Int. J. Eng,* vol. 2, pp. 822-830, 2012.

[110] V. Sakhare and V. Kapatkar, "Experimental Analysis of Parabolic Solar Dish with Copper Helical coil Receiver", 2014.

[111] M. Prakash, S. Kedare, and J. Nayak, "Investigations on heat losses from a solar cavity receiver", *Solar Energy,* vol. 83, pp. 157-170, 2009.

[112] A. M. Daabo, S. Mahmoud, R. K. Al-Dadah, and A. Ahmad, "Numerical investigation of pitch value on thermal performance of solar receiver for solar powered Brayton cycle application", *Energy,* vol. 119, pp. 523-539, 2017.

[113] S. Yahya, *Turbines compressors and fans*: Tata McGraw-Hill Education, 2010.

[114] A. Bahr Ennil, "Optimization of small-scale axial turbine for distributed compressed air energy storage system", University of Birmingham, 2017.

[115] S. L. Dixon and C. Hall, *Fluid mechanics and thermodynamics of turbomachinery*: Butterworth-Heinemann, 2013.

References

[116] P. Klonowicz, A. Borsukiewicz-Gozdur, P. Hanausek, W. Kryłłowicz, and D. Brüggemann, "Design and performance measurements of an organic vapour turbine", *Applied Thermal Engineering,* vol. 63, pp. 297-303, 2014.

[117] L. Fu, Z.-p. Feng, G.-j. Li, Q.-h. Deng, Y. Shi, and T.-y. Gao, "Experimental validation of an integrated optimization design of a radial turbine for micro gas turbines", *Journal of Zhejiang University-SCIENCE A,* vol. 16, pp. 241-249, 2015.

[118] F. Basrawi, T. Yamada, K. Nakanishi, and S. Naing, "Effect of ambient temperature on the performance of micro gas turbine with cogeneration system in cold region", *Applied thermal engineering,* vol. 31, pp. 1058-1067, 2011.

[119] A. B. Ennil, R. Al-Dadah, S. Mahmoud, A. Al-Jubori, and K. Rahbar, "Prediction of Losses in Small Scale Axial Air Turbine Based on CFD Modelling", *Energy Procedia,* vol. 75, pp. 3271-3276, 2015.

[120] J. Kammeyer, C. Natkaniec, and J. Seume, "Influence of tip-qap losses on the stage efficiency of downsizing turbochanger turbines", in *Proceedings of 9th International Conference on Turbochangers and Turbocharging (IMechE)*, 2010, pp. 293-306.

[121] P. Klonowicz, F. Heberle, M. Preißinger, and D. Brüggemann, "Significance of loss correlations in performance prediction of small scale, highly loaded turbine stages working in Organic Rankine Cycles", *Energy,* vol. 72, pp. 322-330, 2014.

[122] K. Rahbar, S. Mahmoud, and R. K. Al-Dadah, "Mean-line modeling and CFD analysis of a miniature radial turbine for distributed power generation systems", *International Journal of Low-Carbon Technologies,* vol. 11, pp. 157-168, 2016.

[123] A. C. Jones, "Design and test of a small, high pressure ratio radial turbine", in *ASME 1994 International Gas Turbine and Aeroengine Congress and Exposition*, 1994, pp. V001T01A045-V001T01A045.

[124] C. S. Mistry and S. Channiwala, "Design of Nozzle-Less Radial Inflow Gas Turbine for Small Capacity (20 kW) Gas Turbine Engine", in *ASME 2004 International Mechanical Engineering Congress and Exposition*, 2004, pp. 545-552.

[125] C. S. Mistry and S. Channiwala, "Preliminary Design Concepts for High Solidity Nozzle-Less Radial Inflow Gas Turbine for Small Capacity Gas Turbine Engine", in *ASME Turbo Expo 2006: Power for Land, Sea, and Air*, 2006, pp. 1113-1120.

[126] R. A. M. Carrillo and M. A. Nascimento, "Numerical Meanline Analysis and Overall Performance Prediction of Radial-Inflow Turbine for a 600 kW Cycle Gas Engine", in *ASME 2011 Turbo Expo: Turbine Technical Conference and Exposition*, 2011, pp. 891-898.

[127] B. H. Dennis, I. N. Egorov, Z.-X. Han, G. S. Dulikravich, and C. Poloni, "Multi-objective optimization of turbomachinery cascades for minimum loss, maximum loading, and maximum gap-to-chord ratio", *International Journal of Turbo and Jet Engines,* vol. 18, pp. 201-210, 2001.

[128] O. BALJE and R. BINSLEY, "Axial turbine performance evaluation. I- Loss-geometry relationships(Generalized loss correlations for axial turbine performance evaluation, discussing effects of Reynolds number, blade angles, height, tip clearance, etc)", 1968.

[129] O. BALJE and R. BINSLEY, "Axial turbine performance evaluation. II(Optimization and geometry of axial flow turbines calculated using generalized loss correlations, considering role of wide range specific speeds)", 1968.

[130] S. Rao and R. Gupta, "Optimum Design of Axial Flow Gas Turbine Stage—Part I: Formulation and Analysis of Optimization Problem", *Journal of Engineering for Power,* vol. 102, pp. 782-789, 1980.

References

[131] D. Sasaki, S. Obayashi, and H.-J. Kim, "Evolutionary algorithm vs. adjoint method applied to sst shape optimization", in *The Annual Conference of CFD Society of Canada, Waterloo*, 2001.

[132] T. De Jaeger, "Development of a CFD simulation methodology for", 2014.

[133] A. M.-S. Moreau, "Analysis of the Flow Structure in a Radial Turbine".

[134] I. Tsalicoglou and B. Phillipsen, "Design of radial turbine meridional profiles using particle swarm optimization", in *2nd International Conference on Engineering Optimization*, 2010.

[135] L. Fu, Y. Shi, Q. Deng, H. Li, and Z. Feng, "Integrated optimization design for a radial turbine wheel of a 100 kW-class microturbine", *Journal of Engineering for Gas Turbines and Power,* vol. 134, p. 012301, 2012.

[136] L. Mueller, Z. Alsalihi, and T. Verstraete, "Multidisciplinary optimization of a turbocharger radial turbine", *Journal of turbomachinery,* vol. 135, p. 021022, 2013.

[137] Q. Zhang and C. Ma, "Multiple-objective aerodynamic optimization design of a radial air turbine impeller", in *Remote Sensing, Environment and Transportation Engineering (RSETE), 2011 International Conference on*, 2011, pp. 1362-1365.

[138] R. Van den Braembussche, "Optimization of radial impeller geometry", VON KARMAN INST FOR FLUID DYNAMICS RHODE-SAINT-GENESE (BELGIUM)2006.

[139] M. M. Shanechi, M. Odabaee, and K. Hooman, "Optimisation of a High Pressure Ratio Radial-Inflow Turbine: Coupled CFD-FE Analysis", in *ASME Turbo Expo 2015: Turbine Technical Conference and Exposition*, 2015, pp. V02CT45A003-V02CT45A003.

[140] E. Poursaeidi and H. Bazvandi, "Effects of emergency and fired shut down on transient thermal fatigue life of a gas turbine casing", *Applied Thermal Engineering,* vol. 100, pp. 453-461, 2016.

[141] D. Barsi, A. Perrone, L. Ratto, D. Simoni, and P. Zunino, "Radial inflow turbine design through multi-disciplinary optimisation technique", in *ASME turbo expo 2015: turbine technical conference and exposition*, 2015, pp. V008T23A009-V008T23A009.

[142] H.-l. Wang and G. Xi, "Effect of thermal and mechanical loads on the centrifugal impeller deformation and its structure optimization", in *ASME Turbo Expo 2009: Power for Land, Sea, and Air*, 2009, pp. 75-84.

[143] Z. Feng, Q. Deng, and J. Li, "Aerothermodynamic design and numerical simulation of radial inflow turbine impeller for a 100kW microturbine", in *ASME Turbo Expo 2005: Power for Land, Sea, and Air*, 2005, pp. 873-880.

[144] S. Guo, "Investigations on the blade vibration of a radial inflow micro gas turbine wheel", *International Journal of Rotating Machinery,* vol. 2007, 2007.

[145] G. Qiu, H. Liu, and S. Riffat, "Expanders for micro-CHP systems with organic Rankine cycle", *Applied Thermal Engineering,* vol. 31, pp. 3301-3307, 2011.

[146] M. Benner, S. Sjolander, and S. Moustapha, "An Empirical Prediction Method for Secondary Losses in Turbines—Part II: A New Secondary Loss Correlation", *Journal of turbomachinery,* vol. 128, pp. 281-291, 2006.

[147] A. M. Daabo, A. Ahmad, S. Mahmoud, and R. K. Al-Dadah, "Parametric analysis of small scale cavity receiver with optimum shape for solar powered closed Brayton cycle applications", *Applied Thermal Engineering,* vol. 122, pp. 626-641, 2017.

[148] A. M. Daabo, S. Mahmoud, and R. K. Al-Dadah, "The effect of receiver geometry on the optical performance of a small-scale solar cavity receiver for parabolic dish applications", *Energy,* vol. 114, pp. 513-525, 2016.

[149] M. Geyer and W. B. Stine, "Power from the Sun (Powerfromthesun. net)", *JT Lyle Center,* 2001.

References

[150] B. Abdullahi, R. Al-Dadah, S. Mahmoud, and R. Hood, "Optical and thermal performance of double receiver compound parabolic concentrator", *Applied energy,* vol. 159, pp. 1-10, 2015.

[151] G. E. Arnaoutakis, J. Marques-Hueso, A. Ivaturi, S. Fischer, J. C. Goldschmidt, K. W. Krämer*, et al.*, "Enhanced energy conversion of up-conversion solar cells by the integration of compound parabolic concentrating optics", *Solar energy materials and solar cells,* vol. 140, pp. 217-223, 2015.

[152] I. M. S. Ali, T. S. O'Donovan, K. Reddy, and T. K. Mallick, "An optical analysis of a static 3-D solar concentrator", *Solar Energy,* vol. 88, pp. 57-70, 2013.

[153] N. Sellami and T. K. Mallick, "Optical characterisation and optimisation of a static Window Integrated Concentrating Photovoltaic system", *Solar Energy,* vol. 91, pp. 273-282, 2013.

[154] T. Mancini, P. Heller, B. Butler, B. Osborn, W. Schiel, V. Goldberg*, et al.*, "Dish-Stirling systems: An overview of development and status", *Journal of Solar Energy Engineering,* vol. 125, pp. 135-151, 2003.

[155] A. Kribus, "Thermal integral micro-generation systems for solar and conventional use", *Journal of solar energy engineering,* vol. 124, pp. 189-197, 2002.

[156] D. Feuermann and J. M. Gordon, "High-concentration photovoltaic designs based on miniature parabolic dishes", *Solar Energy,* vol. 70, pp. 423-430, 2001.

[157] M. Alaphilippe, S. Bonnet, and P. Stouffs, "Low power thermodynamic solar energy conversion: coupling of a parabolic trough concentrator and an Ericsson engine", *International Journal of Thermodynamics,* vol. 10, pp. 37-45, 2010.

[158] A. Segal and M. Epstein, "Optimized working temperatures of a solar central receiver", *Solar Energy,* vol. 75, pp. 503-510, 2003.

[159] F. Reis, "Development of photovoltaic systems with concentration", 2013.

[160] I. Moreno, "Illumination uniformity assessment based on human vision", *Optics letters,* vol. 35, pp. 4030-4032, 2010.

[161] T. L. Bergman and F. P. Incropera, *Fundamentals of heat and mass transfer*: John Wiley & Sons, 2011.

[162] A. Bejan, "Heat Transfer John Wiley & Sons", *New York,* 1993.

[163] E. Eckert and R. Drake Jr, "Introduction to the Transfer of Heat and Mass McGraw-Hill", *New York, New York,* p. 273, 1950.

[164] S. W. Churchill and H. H. Chu, "Correlating equations for laminar and turbulent free convection from a vertical plate", *International journal of heat and mass transfer,* vol. 18, pp. 1323-1329, 1975.

[165] W. M. Rohsenow, J. P. Hartnett, and Y. I. Cho, *Handbook of heat transfer* vol. 3: McGraw-Hill New York, 1998.

[166] R. Jilte, S. Kedare, and J. Nayak, "Natural convection and radiation heat loss from open cavities of different shapes and sizes used with dish concentrator", *Mechanical Engineering Research,* vol. 3, p. 25, 2013.

[167] Y. Wu and L. Wen, "Solar receiver performance of point focusing collector system", *American Society of Mechanical Engineers,* 1978.

[168] A. Fluent, "Ansys fluent theory guide", *ANSYS Inc., USA,* vol. 15317, pp. 724-746, 2011.

[169] U. U. Rehman, "Heat transfer optimization of shell-and-tube heat exchanger through CFD studies", 2012.

[170] A. Fluent, "Ansys fluent", *Academic Research. Release,* vol. 14, 2015.

[171] A. M. Daabo, A. Al Jubori, S. Mahmoud, and R. K. Al-Dadah, "Development of three-dimensional optimization of a small-scale radial turbine for solar powered

Brayton cycle application", *Applied Thermal Engineering,* vol. 111, pp. 718-733, 2017.

[172] A. M. Daabo, S. Mahmoud, R. K. Al-Dadah, A. M. Al Jubori, and A. B. Ennil, "Numerical analysis of small scale axial and radial turbines for solar powered Brayton cycle application", *Applied Thermal Engineering,* vol. 120, pp. 672-693, 2017.

[173] A. M. Daabo, S. Mahmoud, and R. K. Al-Dadah, "Development of Small-Scale Axial Turbine for solar powered Brayton Cycle", in *Students on Applied Engineering (ICSAE), International Conference for*, 2016, pp. 170-175.

[174] H. Moustapha, M. F. Zelesky, N. C. Baines, and D. Japikse, *Axial and radial turbines* vol. 2: Concepts NREC White River Junction, VT, 2003.

[175] A. B. Ennil, R. Al-Dadah, S. Mahmoud, K. Rahbar, and A. AlJubori, "Minimization of loss in small scale axial air turbine using CFD modeling and evolutionary algorithm optimization", *Applied Thermal Engineering,* vol. 102, pp. 841-848, 2016.

[176] K. Rahbar, S. Mahmoud, R. K. Al-Dadah, and N. Moazami, "Modelling and optimization of organic Rankine cycle based on a small-scale radial inflow turbine", *Energy conversion and management,* vol. 91, pp. 186-198, 2015.

[177] S. Smith, "A simple correlation of turbine efficiency", *The Aeronautical Journal,* vol. 69, pp. 467-470, 1965.

[178] H. J. Wood, "Current technology of radial-inflow turbines for compressible fluids", in *ASME 1962 Gas Turbine Power Conference and Exhibit*, 1962, pp. V001T01A009-V001T01A009.

[179] O. Balje, *Turbomachines-A guide to design, selection, and theory*: John Wiley & Sons, 1981.

[180] C. Rodgers, "Mainline performance prediction for radial inflow turbine in small high pressure ratio turbine", Tech. rep., Von Karman Institute Lecture Series1987.

[181] A. Whitfield and N. C. Baines, "Design of radial turbomachines", 1990.

[182] H. E. Rohlik, "Analytical determination of radial inflow turbine design geometry for maximum efficiency", 1968.

[183] C. Hirsch, *Numerical computation of internal and external flows: The fundamentals of computational fluid dynamics*: Butterworth-Heinemann, 2007.

[184] A. T. S. U. s. Guide, "ANSYS Turbo System Work-flow", *Topology*.

[185] C. Ansys, "release 13.0 CFX-solver modeling guide", Technical report, Ansys2010.

[186] I. ANSYS, "CFX-Solver Theory Guide", ed: R, 2009.

[187] P. L. Meitner and A. J. Glassman, "Off-Design Performance Loss Model for Radial Turbines with Pivoting, Variable-Area Stators", NATIONAL AERONAUTICS AND SPACE ADMINISTRATION CLEVELAND OH LEWIS RESEARCH CENTER1980.

[188] P. Lampart, "Investigation of endwall flows and losses in axial turbines. Part I. Formation of endwall flows and losses", *Journal of theoretical and applied mechanics,* vol. 47, pp. 321-342, 2009.

[189] J. Horlock, "Losses and efficiencies in axial-flow turbines", *International Journal of Mechanical Sciences,* vol. 2, pp. 48-75, 1960.

[190] C. A. Wasserbauer and A. J. Glassman, "FORTRAN program for predicting off-design performance of radial-inflow turbines", 1975.

[191] N. Andréasson, A. Evgrafov, and M. Patriksson, "An Introduction to Optimization: Foundations and Fundamental Algorithms", ed: Chalmers University of Technology Press, 2005.

[192] F. Rothlauf, *Design of modern heuristics: principles and application*: Springer Science & Business Media, 2011.

References

[193] A. Antoniou and W.-S. Lu, *Practical optimization: algorithms and engineering applications*: Springer Science & Business Media, 2007.

[194] O. Ansys, "Ansys CFX-Solver Theory Guide Ansys CFX Release 10.0. Ansys", ed: Inc, 2005.

[195] A. a. Samad, "Turbomachinery design and optimization : a systematic approach for turbomachinery blade design, flow analysis and performance optimization / Abdus Samad", ed: [S.l.] : LAP LAMBERT Academic Publishing, 2012., 2012.

[196] L. dos Santos Coelho, *Multi-objective swarm intelligent systems: theory & experiences* vol. 261: Springer, 2009.

[197] R. Badhurshah and A. Samad, "Multi-objective optimization of a bidirectional impulse turbine", *Proceedings of the Institution of Mechanical Engineers, Part A: Journal of Power and Energy,* vol. 229, pp. 584-596, 2015.

[198] S. A. Klein, "Engineering equation solver", in *F-chart Software*, ed: Middleton, WI, 2013.

[199] A. B. Janjua, M. S. Khalil, and M. Saeed, "Blade profile optimization of kaplan turbine using cfd analysis", *Mehran University Research Journal of Engineering and Technology,* vol. 32, pp. 559-574, 2013.

[200] A. U. s. Manual, "Ansys", *Inc. Modeling, CFX,* vol. 11, 2000.

[201] F. U. s. Guide, "Release 15.0, 2014, SAS IP", ed: Inc.

[202] D. G. Wilson and T. Korakianitis, *The design of high-efficiency turbomachinery and gas turbines*: MIT press, 2014.

[203] J.-H. Kim, J.-H. Choi, A. Husain, and K.-Y. Kim, "Performance enhancement of axial fan blade through multi-objective optimization techniques", *Journal of Mechanical Science and Technology,* vol. 24, pp. 2059-2066, 2010.

[204] N. Surekha, S. Kolla, D. R. Ch, and K. Sreekanth, "Optimization of principal dimensions of radial flow gas turbine rotor using genetic algorithm", *International Journal of Scientific & Engineering Research,* vol. 3, 2012.

[205] H. P. Bloch and M. Singh, *Steam Turbines: Design, Application, and Re-Rating*: McGraw Hill Professional, 2008.

[206] H. I. H. Saravanamuttoo, G. F. C. Rogers, and H. Cohen, *Gas turbine theory*: Pearson Education, 2001.

[207] R. S. Gorla and A. A. Khan, *Turbomachinery: design and theory*: CRC Press, 2003.

[208] B. Shahriari, M. Jalali, and M. Karamooz Ravari, "Vibration analysis of a rotating variable thickness bladed disk for aircraft gas turbine engine using generalized differential quadrature method", *Proceedings of the Institution of Mechanical Engineers, Part G: Journal of Aerospace Engineering,* vol. 231, pp. 2739-2749, 2017.

[209] E. Poursaeidi and M. Salavatian, "Fatigue crack growth simulation in a generator fan blade", *Engineering Failure Analysis,* vol. 16, pp. 888-898, 2009.

[210] D. Shi, C. Wang, X. Yang, and S. Li, "Failure assessment of the first stage high-pressure turbine blades in an aero-engine turbine", *Fatigue & Fracture of Engineering Materials & Structures,* 2017.

[211] J. Korte, A. Salas, H. Dunn, N. Alexandrov, W. Follett, G. Orient*, et al.*, "Multidisciplinary approach to linear Aerospike nozzle design", *Journal of Propulsion and Power,* vol. 17, pp. 93-98, 2001.

[212] D. Thevenin and G. Janiga, "and Computational Fluid Dynamics", 2008.

[213] R. 525. Thermal Post Cure Procedure Objet RD 525, http://WWW/files/doc-08270_e_raged_thermal-treatment. [Online].

[214] T. Redman, "The design of a robotic hand with multiple actuators for children", University of Southampton, 2016.

References

[215] R. J. Moffat, "Using uncertainty analysis in the planning of an experiment", *ASME, Transactions, Journal of Fluids Engineering(ISSN 0098-2202),* vol. 107, pp. 173-178, 1985.

[216] D. G. Cacuci, M. Ionescu-Bujor, and I. M. Navon, *Sensitivity and uncertainty analysis, volume II: applications to large-scale systems* vol. 2: CRC press, 2005.

[217] X. Du and W. Chen, "Efficient uncertainty analysis methods for multidisciplinary robust design", *AIAA journal,* vol. 40, pp. 545-552, 2002.

[218] M. Lange, "On the uncertainty of wind power predictions-Analysis of the forecast accuracy and statistical distribution of errors", *Transactions of the ASME-N-Journal of Solar Energy Engineering,* vol. 127, pp. 177-184, 2005.

[219] R. Moffat, "Contributions to the theory of single-sample uncertainty analysis", *ASME, Transactions, Journal of Fluids Engineering,* vol. 104, pp. 250-258, 1982.

[220] A. M. Elsayed, "Heat transfer in helically coiled small diameter tubes for miniature cooling systems", University of Birmingham, 2011.

[221] R. Moffat, "Contributions to the theory of single-sample uncertainty analysis", *Journal of Fluids Engineering,* vol. 104, pp. 250-258, 1982.

[222] F. Stern, M. Muste, M.-L. Beninati, and W. E. Eichinger, "Summary of experimental uncertainty assessment methodology with example", IIHR Report1999.

[223] H. W. Coleman and W. G. Steele, *Experimentation, validation, and uncertainty analysis for engineers*: John Wiley & Sons, 2009.

Appendix A: Aerodynamic Simulation of the SSRT

Appendix A

Aerodynamic Simulation of the (SSRT)

In order to ensure a smooth and streamlined flow, which ensures lower losses, a complete aerodynamic steady state simulation for the all turbine’s parts was accomplished using ANSYS CFX.

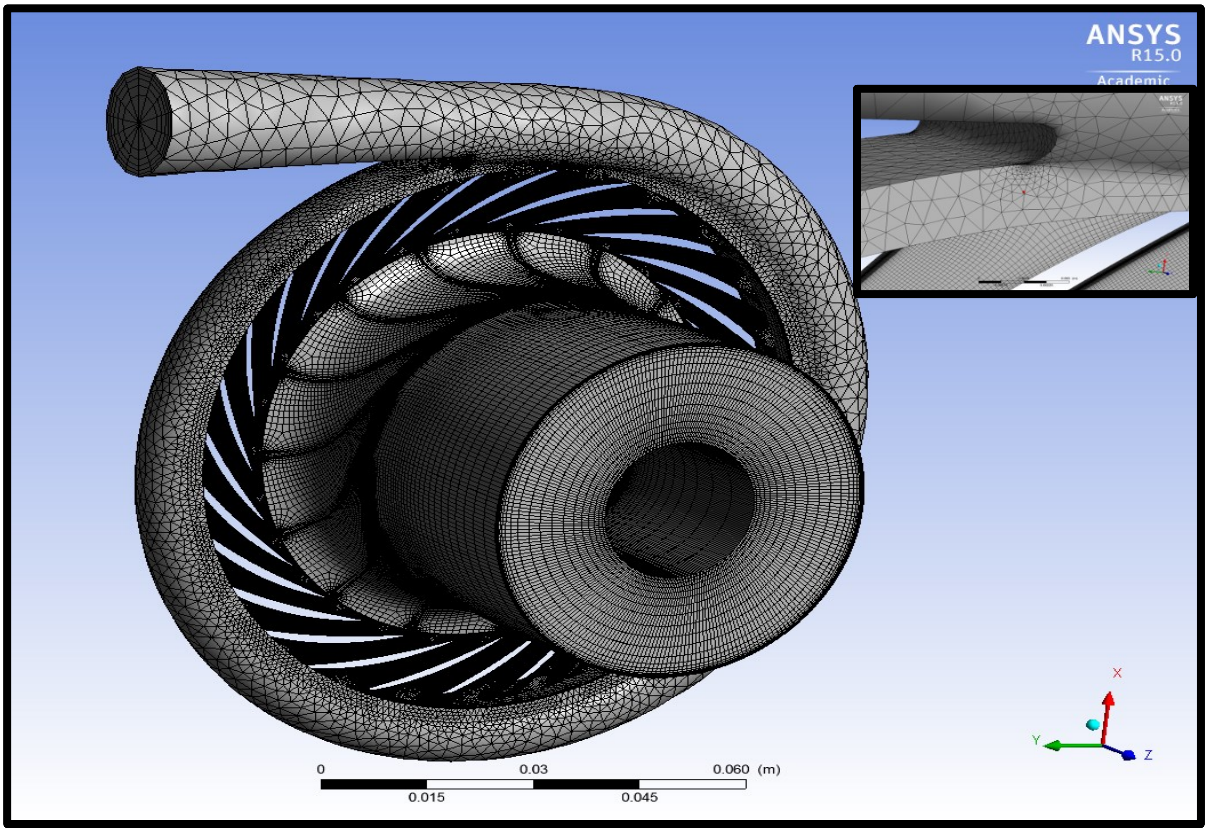

Figure A. 1: The air domain of the complete (SSRT) stage using the Turbogrid/ CFX/ ANSYS.

Appendix A: Aerodynamic Simulation of the SSRT

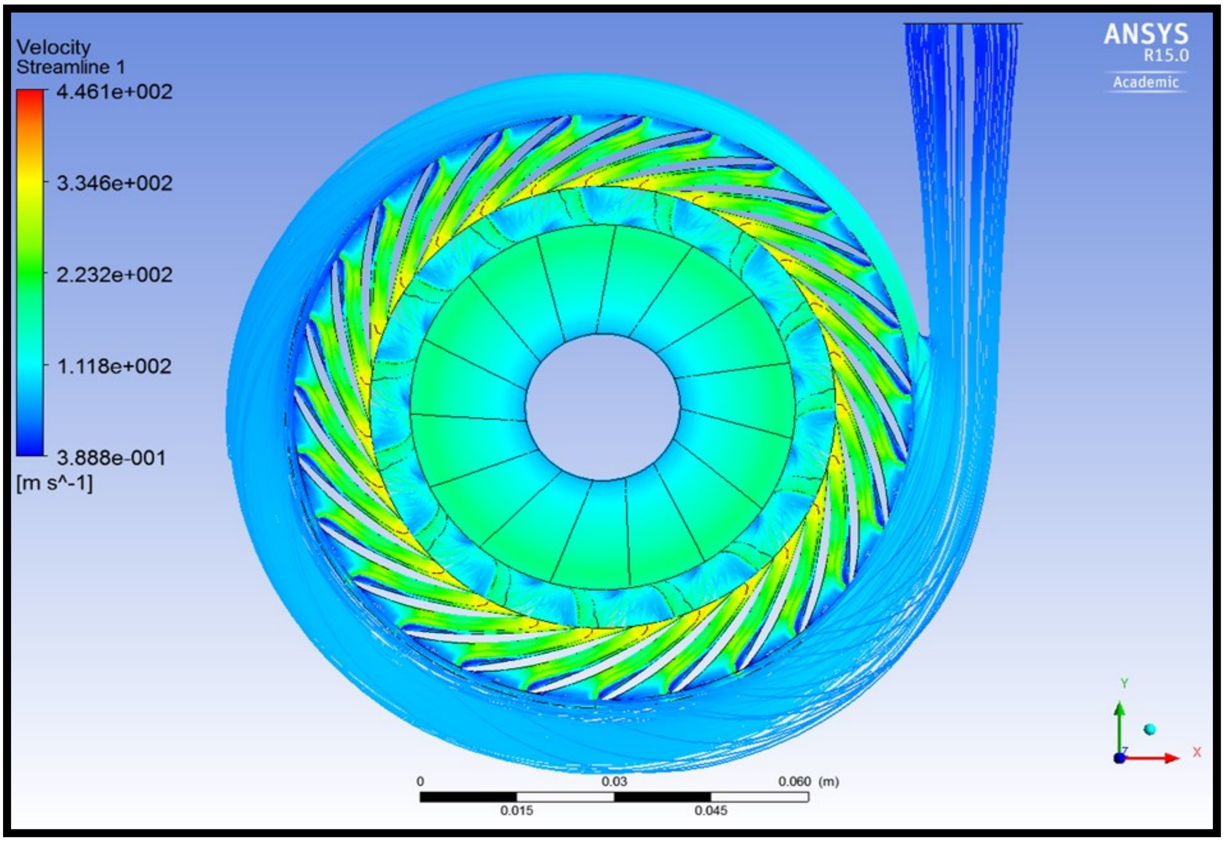

Figure A. 2: The velocity streamline for the complete (SSRT) stage using ANSYS CFX.

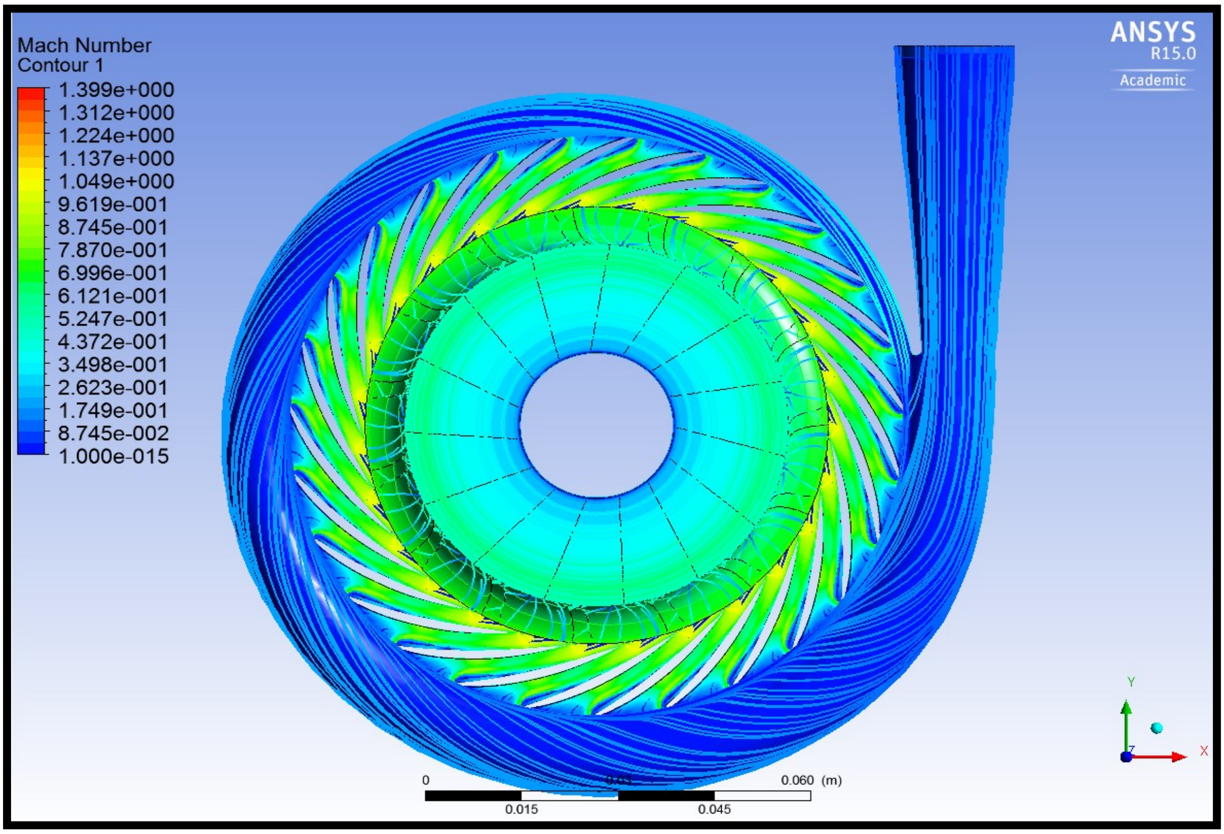

Figure A. 3: The Mach number contour for the complete (SSRT) stage using ANSYS CFX.

Appendix A: Aerodynamic Simulation of the SSRT

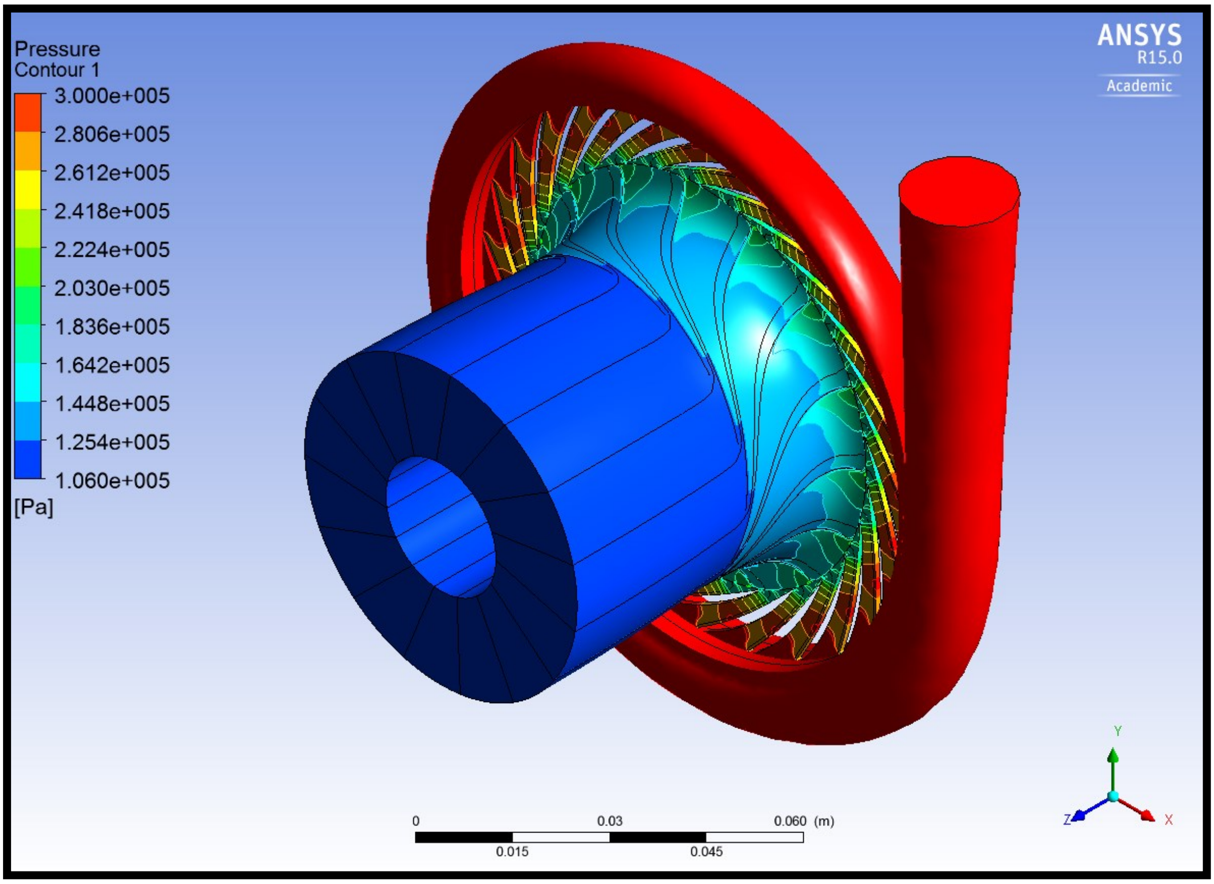

Figure A. 4: The pressure contour for the complete (SSRT) stage using ANSYS CFX.

Appendix B: Manufacturing Drawing of the SSRT Parts

Appendix B

Manufacturing Drawing of the (SSRT) Parts

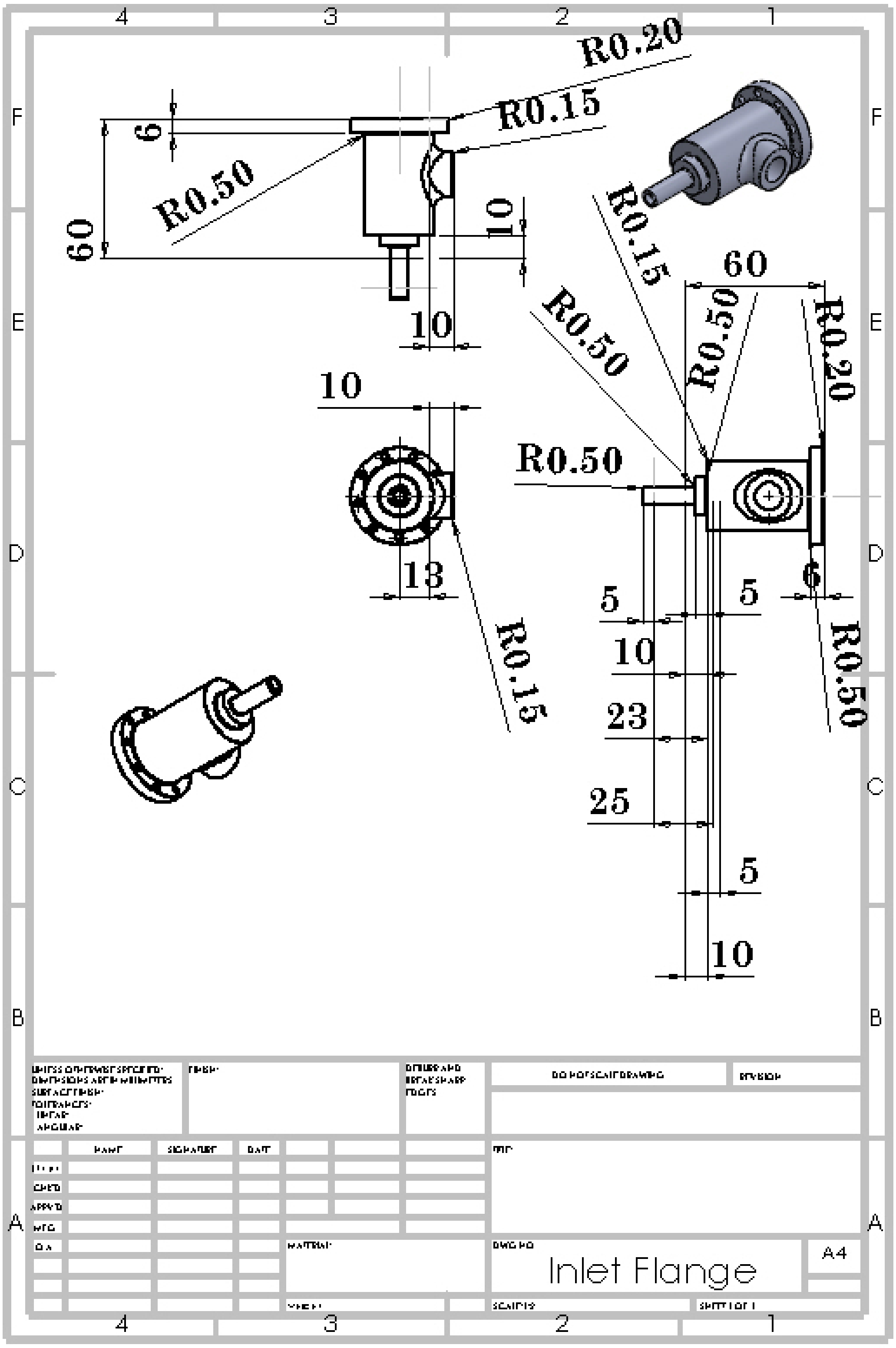

Figure B. 1: The drawing sheet of the inlet flange.

Appendix B: Manufacturing Drawing of the SSRT Parts

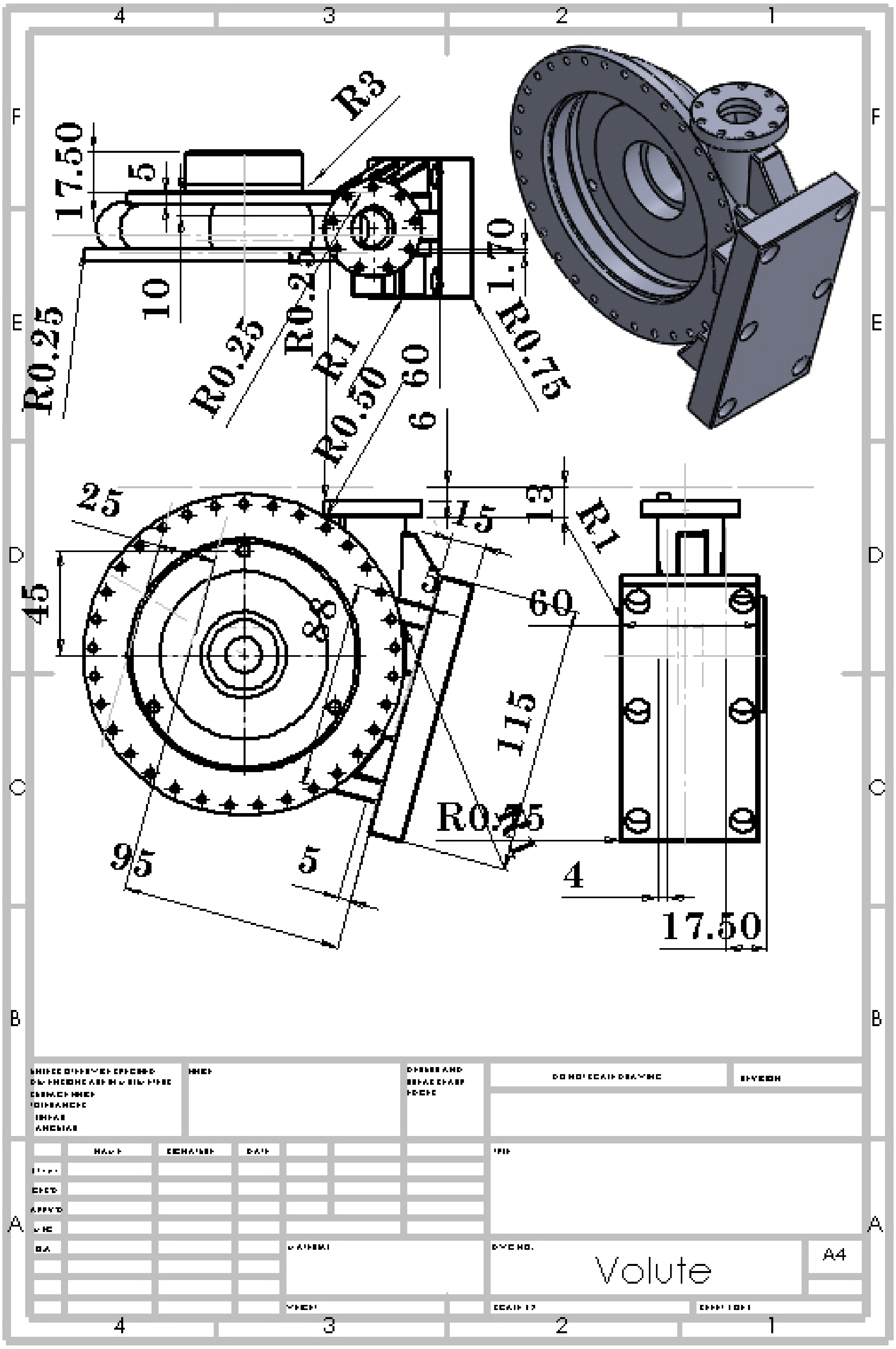

Figure B. 2: The drawing sheet of the volute.

Appendix B: Manufacturing Drawing of the SSRT Parts

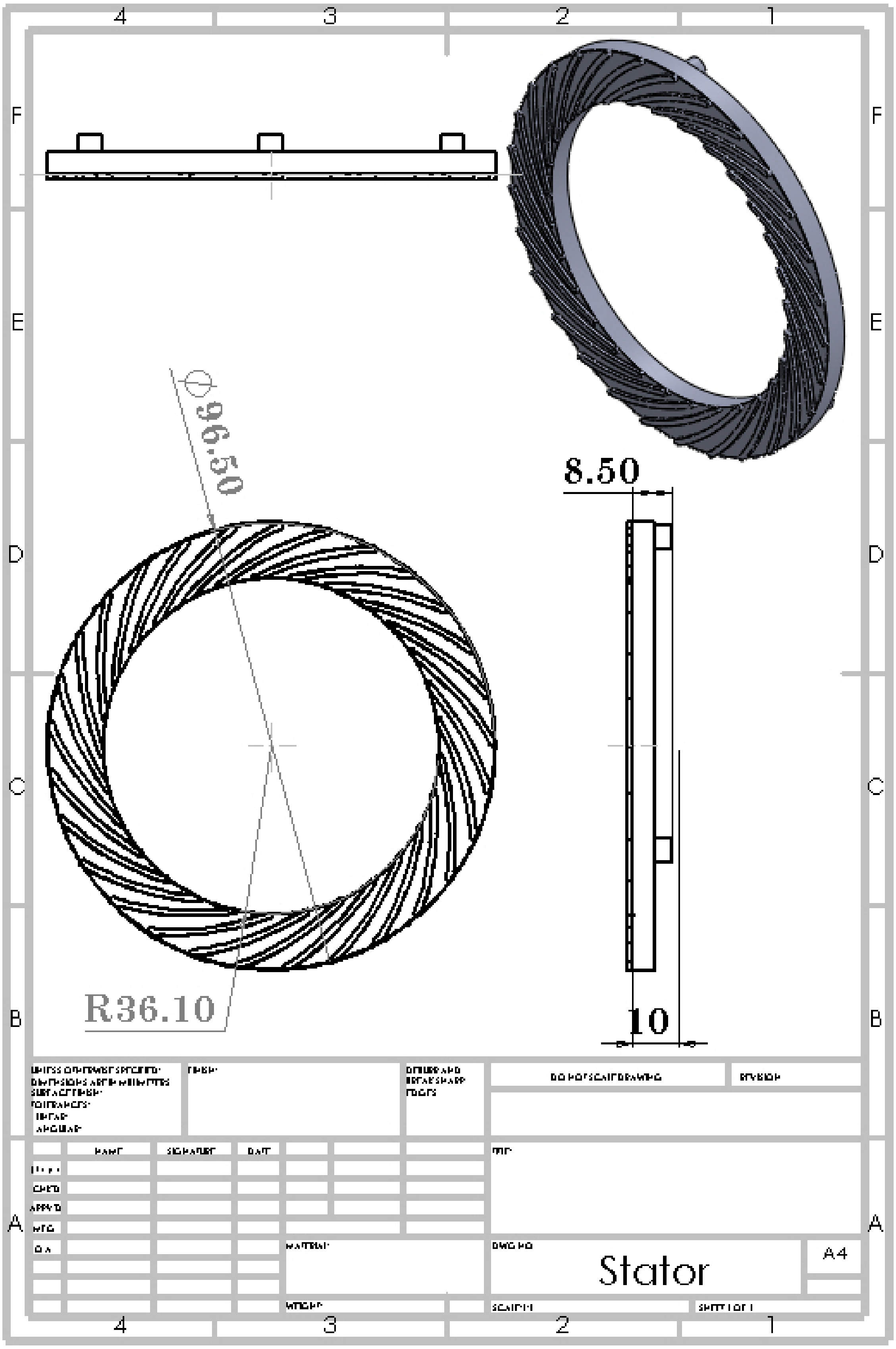

Figure B. 3: The drawing sheet of the stator.

Appendix B: Manufacturing Drawing of the SSRT Parts

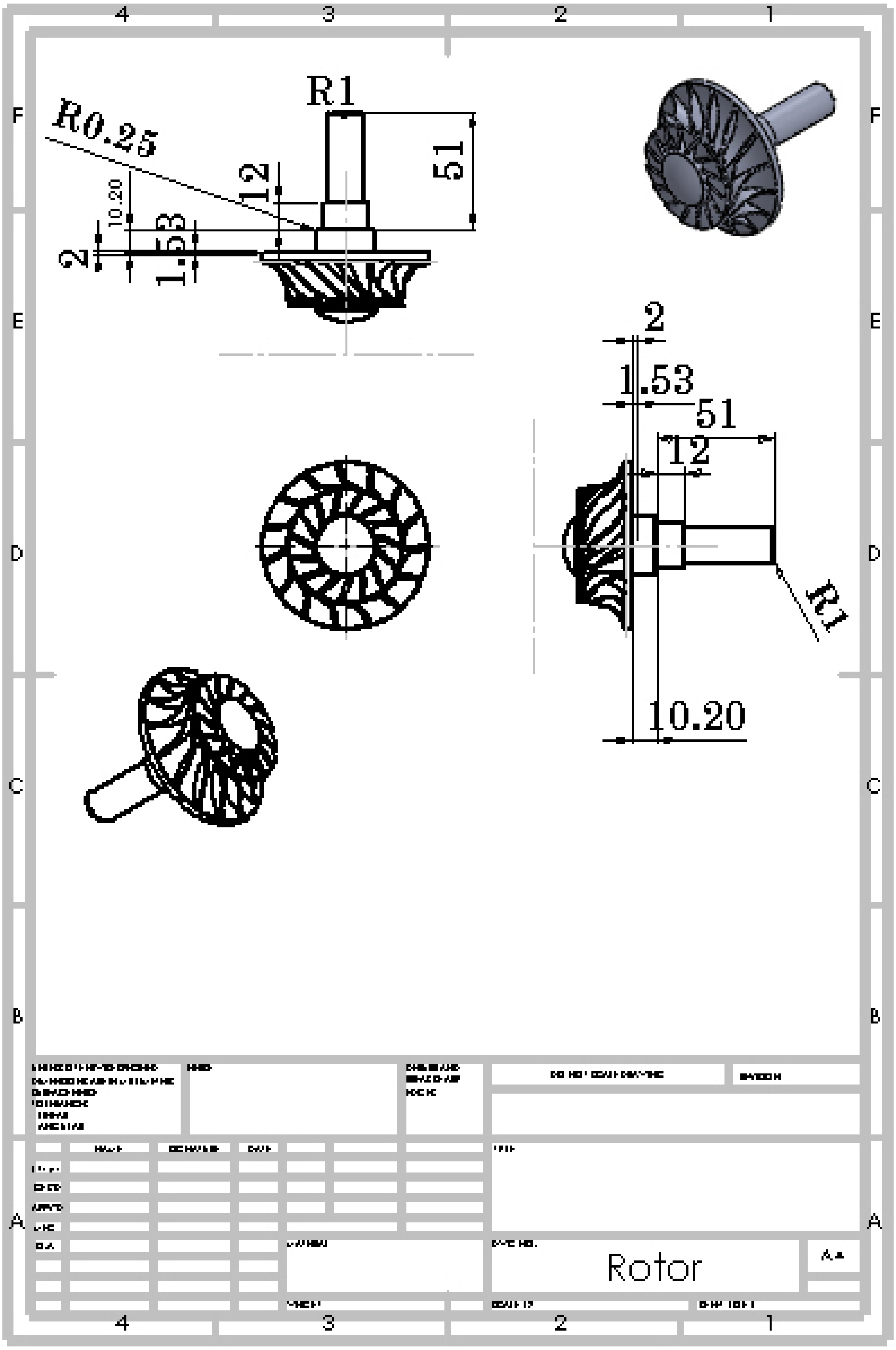

Figure B. 4: The drawing sheet of the rotor.

Appendix B: Manufacturing Drawing of the SSRT Parts

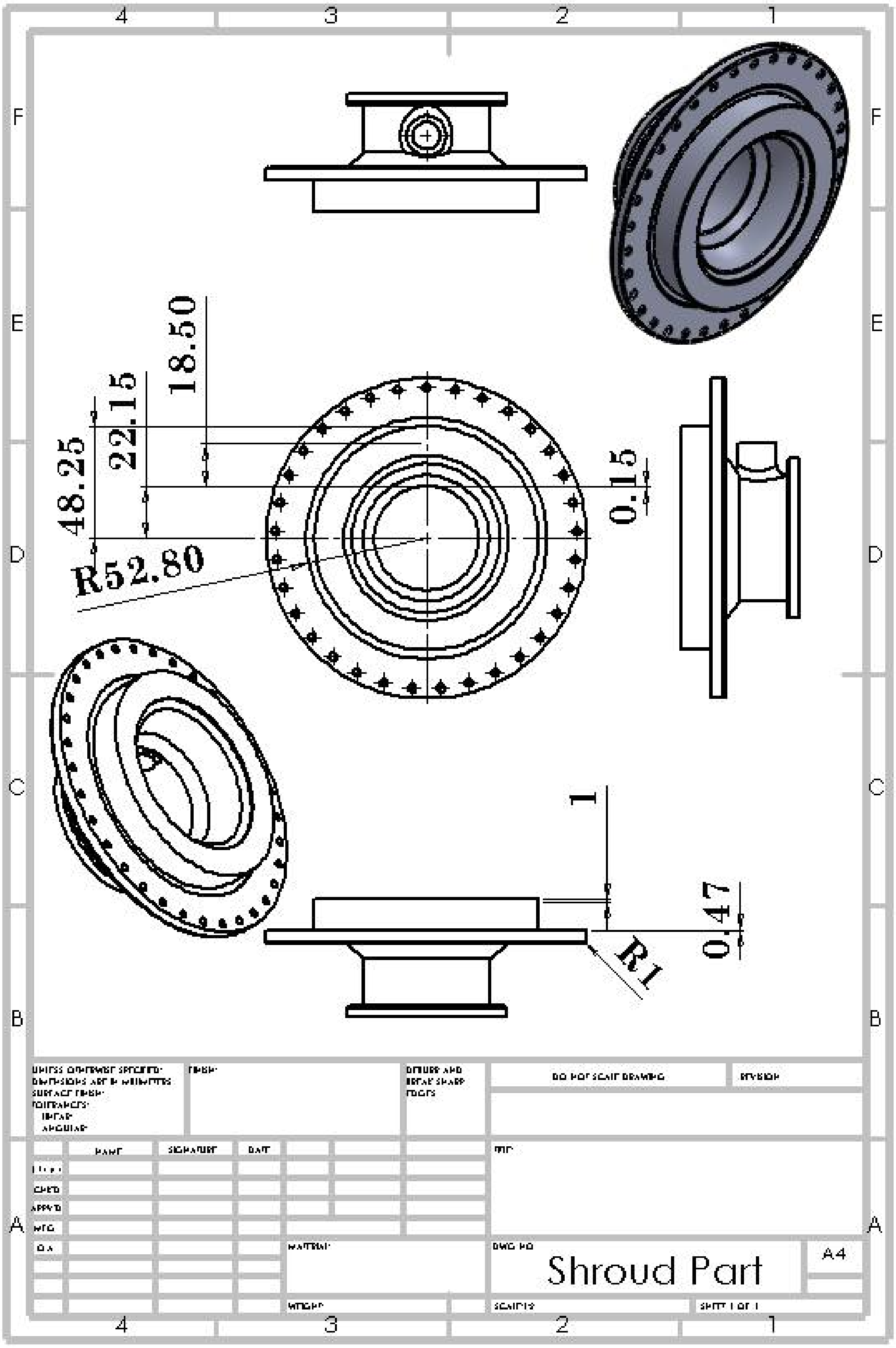

Figure B. 5: The drawing sheet of the shroud part.

Appendix B: Manufacturing Drawing of the SSRT Parts

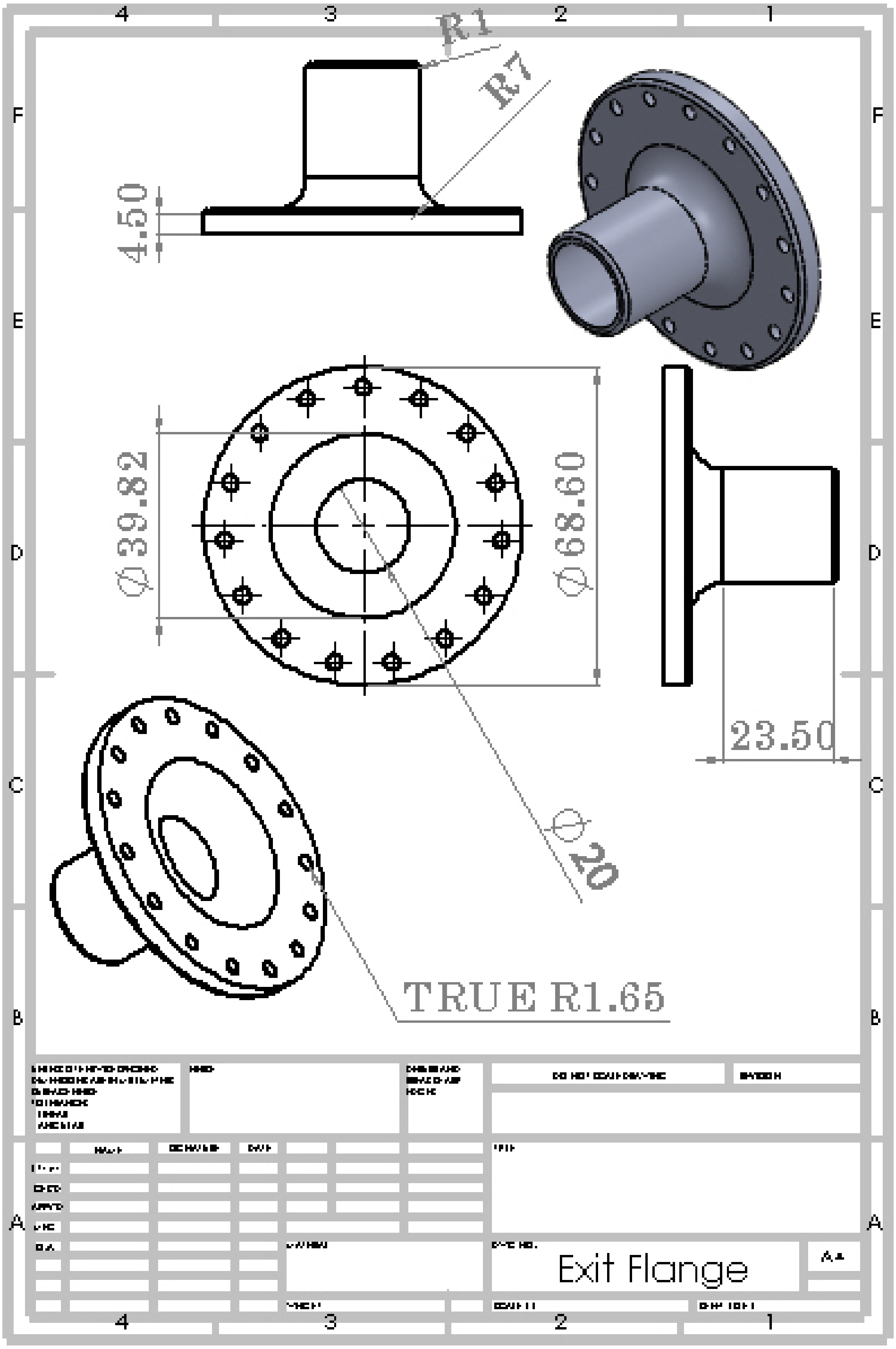

Figure B. 6: The drawing sheet of the exit Flange.

Appendix C

Test Rig Facility

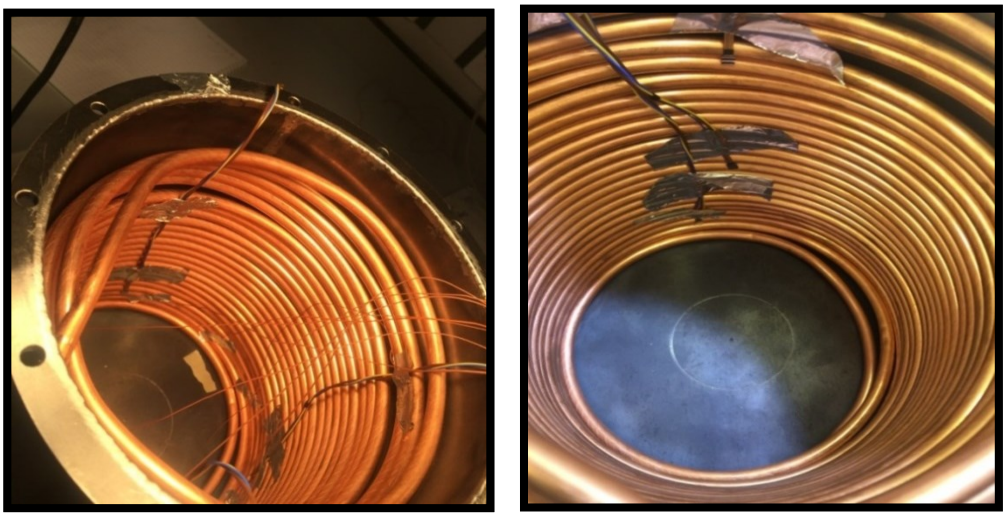

Figure C. 7: The seven surface sensors (LHS) and the three flux sensors (RHS).

C.1 Measuring Devices:

These instruments listed below were used in the developed test facilities will be described in the following sections.

- Flow meter.
- Pressure transducers.
- Thermocouples.
- Radian flux sensor.
- Torque meter.

In order to calibrate the flow meter readings, a digital anemometer was employed in order to measure the fluid velocity at the tube exit, using the fluid density and the tube cross section area. This procedure was repeated for various inlet pressure of the compressed air. The two readings were then compared and the outcomes have been presented in Figure C. 8. As it can be seen, the percentage differences between the two values are smaller than ±1.89%.

Appendix C: Test Rig Facility

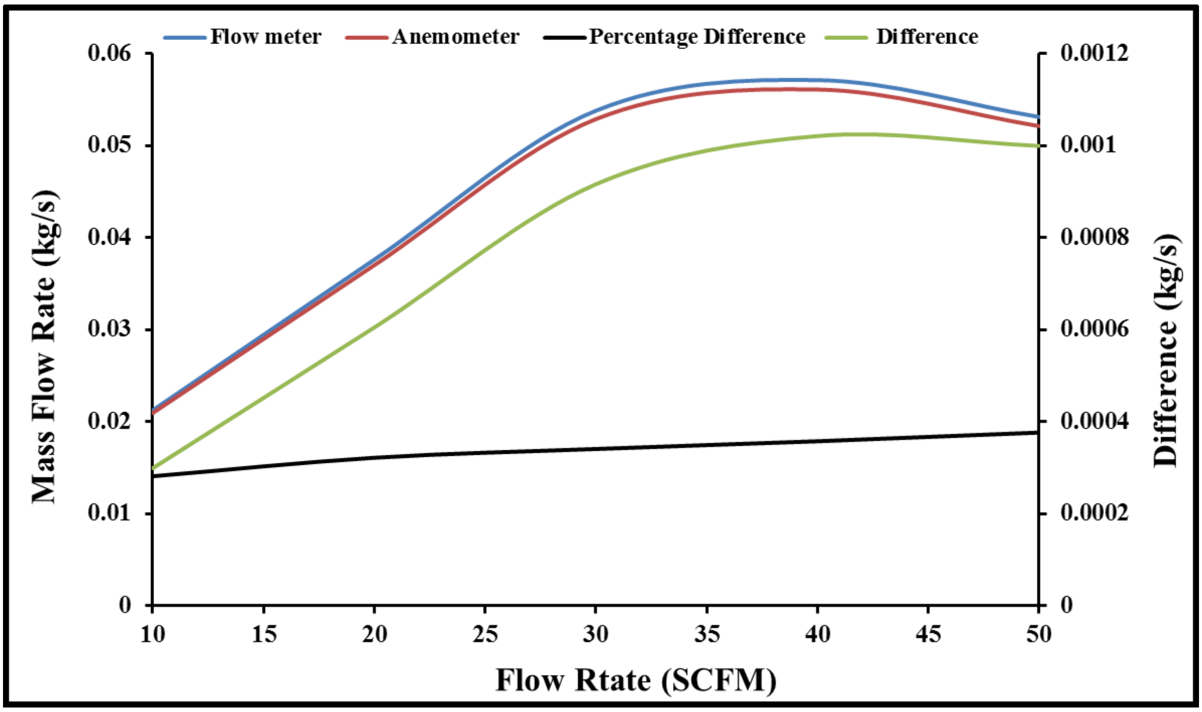

Figure C. 8: Calibration of the compressed air mass flow rate using the integrated flowmeter.

C.1.1 Pressure Transducers:

Three pressure transducers were used in the testing facility for measuring the static inlet, total inlet and static outlet pressure of the (SSRT). The pressure transducers were linked to the data logger and together with a (DC) power supply for data recording as presented in Figure C. 9. As for the calibration, it has been carried out using a standard pressure gauge which has an accuracy value of ± 0.04 Bar. Each of the used pressure transducers was calibrated using the same procedure mentioned below:

1- Connect the pressure transducer to a compressed air source to measure its pressure

2- The value of the received voltage (for the pressure transducer) was recorded and compared with the corresponding reading of the standard gage pressure.

3- In order to have a wide range of pressure readings, the pressure of the air cylinder was altered. This can give a correlation between the standard pressure gauge readings and the pressure transducer output signals as shown in Figure C. 10.

Appendix C: Test Rig Facility

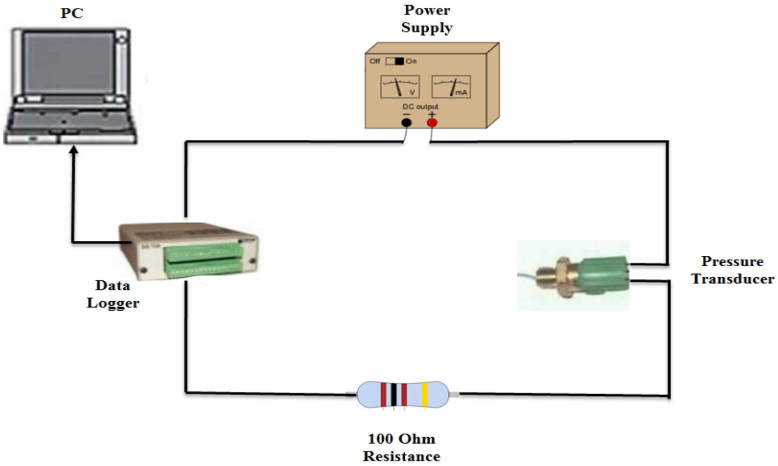

Figure C. 9: Pressure transducer electrical wiring.

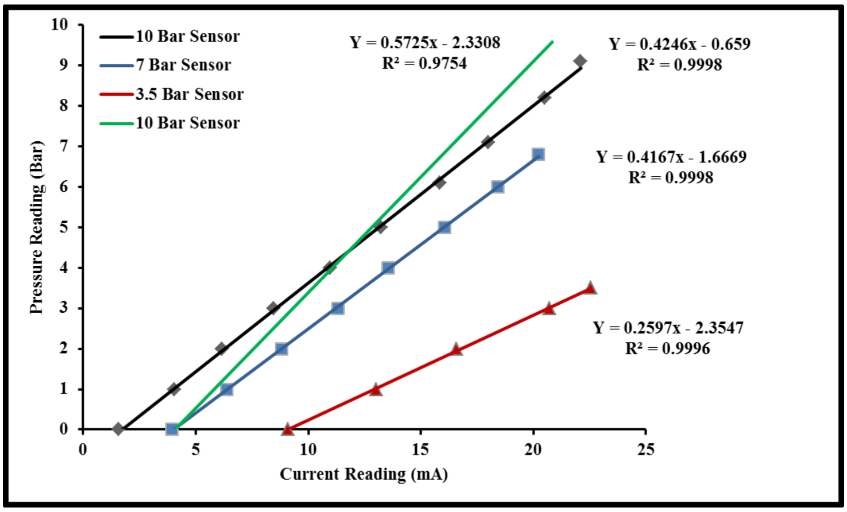

Figure C. 10: The calibration line for the four pressure transducers.

C.1.2 Thermocouples:

Two types of thermocouples were employed in the current rig in order to measure the helical tube surface temperature and the compressed air temperature at inlet and outlet from the helical coil. The first one is K type 1 to 3 mm Diameter with a Miniature Plug which was utilized for measuring the helical surface temperature values. For the compressed air temperature measurements, T type thermocouple probe with 150 mm length, 0.75 mm diameter and accuracy ±0.5 ^{o}C (based on the data sheet) were fitted at three different places in the test rig facility. Figure C. 11 shows the calibration curve for the T type thermocouples used.

Appendix C: Test Rig Facility

The following steps were followed for calibrating the surface temperature:

1- Both, the thermocouples and the (RTD) were immersed at the same level in a water bath that is heated using electrical heater controlled using a thermostat.

2- Once the steady state temperature was reached, the readings of the (RTD) and the thermocouples were recorded and sent to a data logger in order to be reduced in a PC.

3- The results showed that the maximum difference between the two readings was less than 1.5° C for the all 7 thermocouples used in the experiment. Figure C. 12 presents the achieved curve.

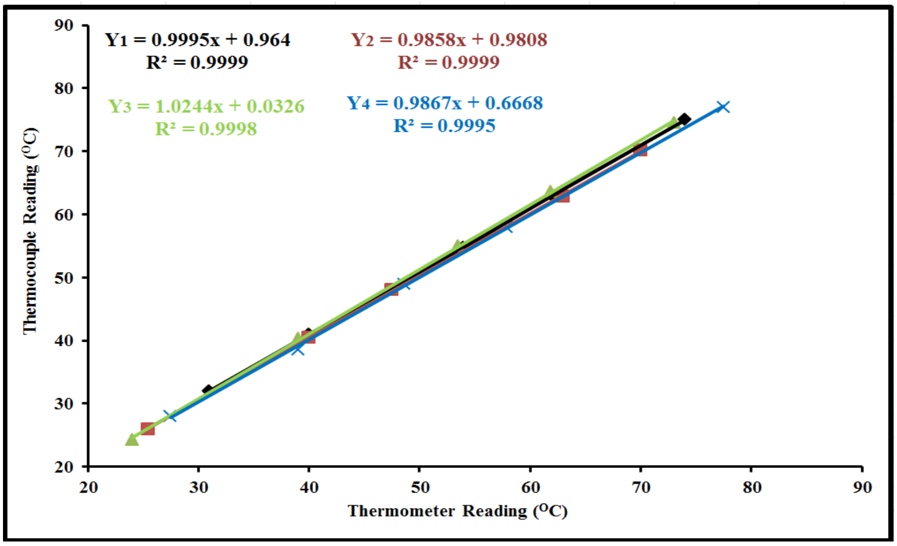

Figure C. 11: The calibration lines of the four thermocouples.

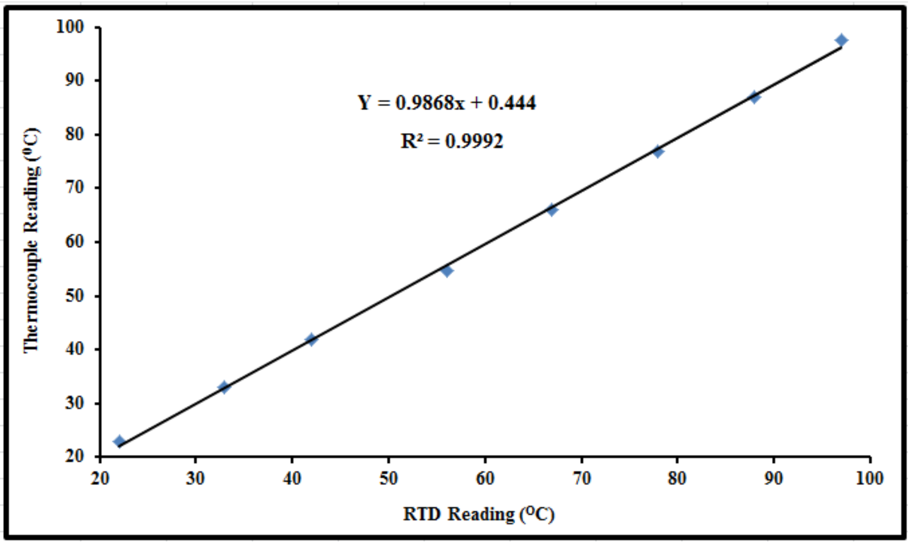

Figure C. 12: The calibration line of one of the seven surface thermocouples.

Appendix C: Test Rig Facility

Figure C. 13 and Figure C. 14 show the calibration conducted for each the Pressure transducers and the thermocouples respectively.

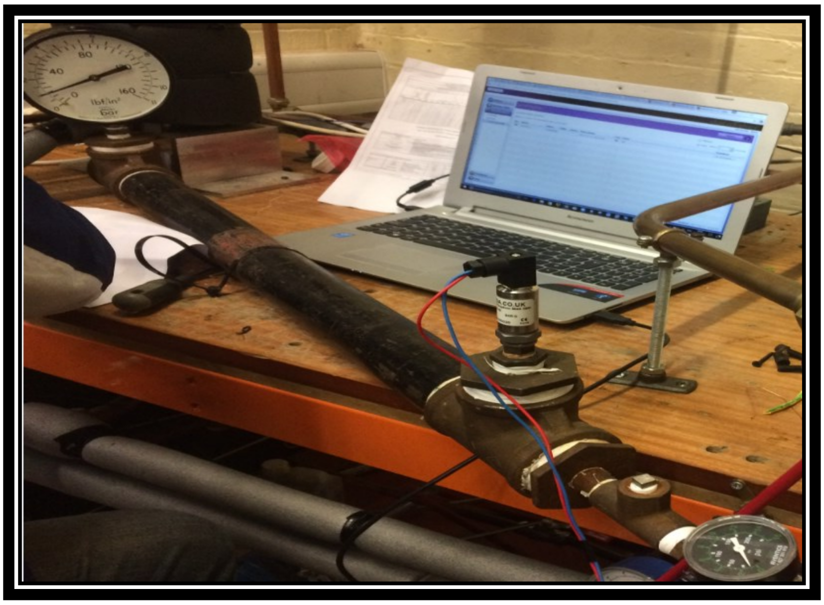

Figure C. 13: Calibration of the utilised pressure transducer.

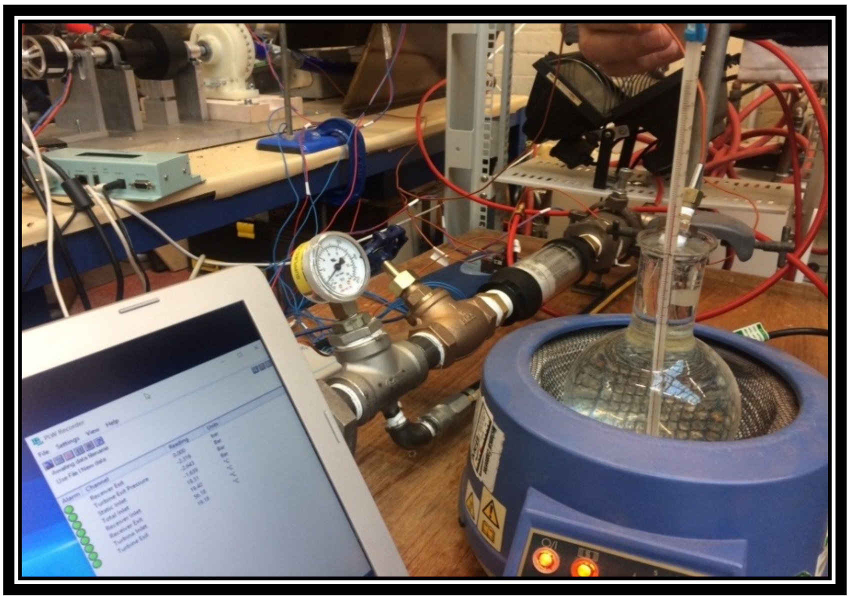

Figure C. 14: Thermocouple calibration process.

Appendix C: Test Rig Facility

C.1.3 Irradiance Flux Sensor:

Three high sensitivity 5x5 mm radiant flux sensors, Figure C. 15, were placed at different positions of the receiver aperture area first, then on the external faces of the helical tube inside the receiver. Using a power supply and the data taker the signal of each sensor was obtained (using their scales shown in Table C 1) and then converted to flux to be ready for appearing on the PC monitor.

Figure C. 15: The photograph of the three 5 X 5 mm flux sensors on the helical tube surface.

Table C 1: Calibration of the flux sensors.

Sensor	Sensitivity, Micro Volt (W/m^2)
1	0.101
2	0.0853
3	0.0952

C.1.4 Torque Meter:

In order to measure the power produced by the (SSRT), a torque meter made by Datum electronics Ltd which can read up to 10 Nm torque and 20 krpm as maximum speed, was connected to the rotor shaft and its Datum Universal Interface where the latter was connected to the PC. As a result, 100 samples per second of the torque, the rotational speed and the power output were recorded and sent to the PC with around 0.1% accuracy, based on the manufacturer data sheet. Figure C. 16 shows the torque meter components.

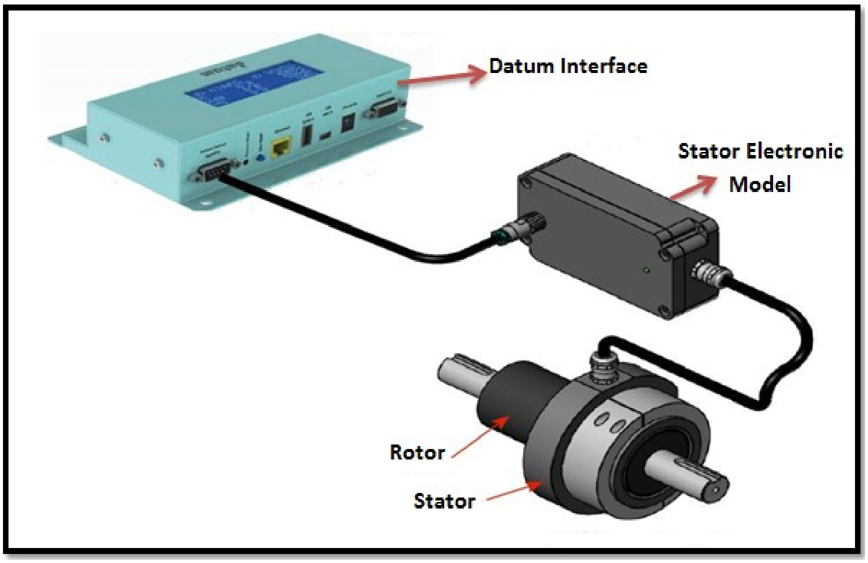

Figure C. 16: Torque meter components [114].

C.2 Data Acquisition System:

A power supply is required when there is a need for converting the DC current and or the voltage to the required digital signal. Two data loggers were used to record the pressure, torque, rotational speed and temperature readings. The first three data were connected to Pico 1012 logger through an electrical board for converting current signal to voltage. Temperature thermocouples were connected to Pico TC-8 data logger. Both the data loggers are connected to PC to monitor the required reading.

C.3 Uncertainty in Measuring Devises:

In the following subsections an evaluation of the uncertainty for the measuring devices utilized in the experimental work is carried out.

Appendix C: Test Rig Facility

C.3.1 Uncertainty Analysis:

The test type and the procedure of data-reduction can have significant effect on the results precision, as the best procedure for some circumstances is not always the optimum choice for other ranges [215]. Many methods for determining the uncertainty analysis have been developed recently in order to accurately govern the various devices and applications, but there is no unified terminology are successfully able to be used for all methods [216]. Some researchers attempts to find the most reliable way for calculating the uncertainty in various complex engineering systems [217, 218].

Two main error types exit in experimental measurements, fixed or bias errors and random or precision errors. Removing or decreasing the first type was conducted in [219]. The first type of errors is associated with measurement accuracy which can be compromised because of bad instrument calibration and/ or poor instrument installation. User faults during taking readings or measurements can also be added to this type of error. The random type, however, can be reduced by following accurate calibration and correct connection of measuring devices.

A common representation of results, R, is provided in equation C.1, as a result of a function of a number of variables which contribute to error accumulation. Some of these variables can be controlled indirectly by the experimenter, others with direct control and some of them can be observed but not controlled and others are not even detected.

$$R=R(X_1, X_2, X_3, X_4, X_5, X_6...X_n) \tag{C.1}$$

The type of measurement process for each individual parameter (X_i) is in fact influenced by the errors developments throughout the actual experiment and this leads to the deviation from the correct expected value. The two mentioned types of errors can be presented in Figure C. 17 [114, 220]. Experimentally, it is not easy to determine the precise value of the required measured variable so; it is essential to approximately use an error value in order to define the precise value interval (±U) depending on uncertainty analysis. In order to calculate the overall uncertainty or deviation in the measured parameters, the Standard Mean Square (SMS) approach is normally used. This approach requires the two mentioned types of errors to be firstly calculated; (U_{random}) and (U_{sys}).

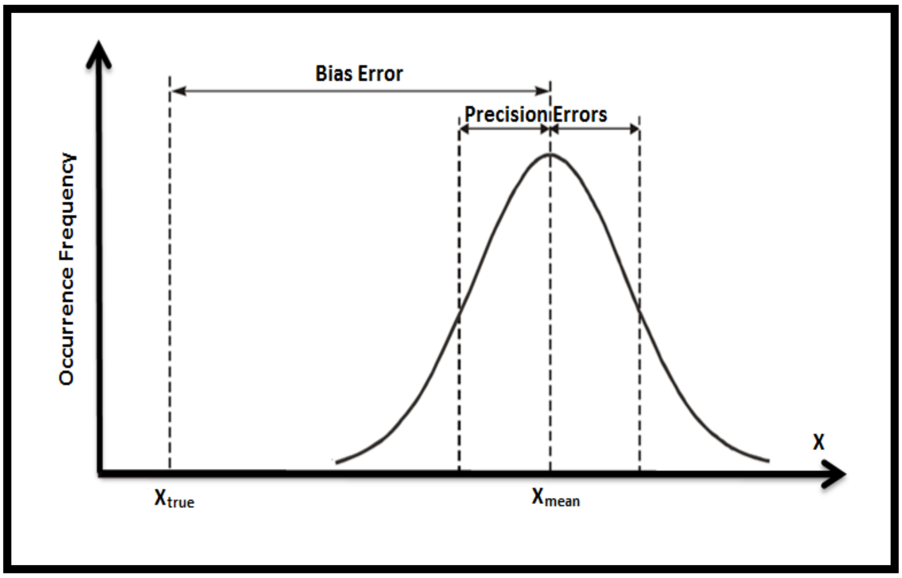

Figure C. 17: Defining precision error and bias errors [221].

The random errors U_{random} can be assessed using standard mean deviation approach as shown in equation C.2;

$$U_{random} = t_{N-1,95\%}\sigma_{\bar{S}} \tag{C.2}$$

Here, N is the sample number, t is the coefficient of student distribution with a degree of freedom equals to N-1.

The $\sigma_{\bar{S}}$; mean deviation; can be calculated as given in equation C.3:

$$\sigma_{\bar{S}} = \frac{1}{\sqrt{N}}\sqrt{\frac{\sum_{i=1}^{N}(X_i-\bar{X})^2}{N-1}} \tag{C.3}$$

Similarly, the systematic error for a number M of fixed type of error sources can be assessed using equation C.4:

$$U_{Sys} = \sqrt{\sum_{i=1}^{M} U_{i,Sys}^2} \tag{C.4}$$

By calculating the two mentioned sources of the uncertainty, the, overall, uncertainty can be determined using equation C.5:

$$U_{Overall} = \pm\sqrt{U_{Sys}^2 + U_{random}^2} \qquad \text{(C.5)}$$

C.3.2 Uncertainty Propagation:

As previously shown in equation C.1, where each individual measured parameter was presented as X_i, each; the random errors and the systematic errors propagate in the overall experimental result R and impact of that propagation on the computed result R can be characterized as shown in Figure C. 18. This figure shows how the small error in any measured devises can propagate leading to a large deviation in the required results. The value of this error can be determined by multiplying the error product (in the measured variable, in X_i value) by the result derivative with respect to that specific variable i.e. data reduction equation slope, sensitivity factor $(\frac{dR}{dX_i})$.

$$U_{R,X_i} = \left[\frac{dR}{dX_i}\right] U_{X_i} \qquad \text{(C.6)}$$

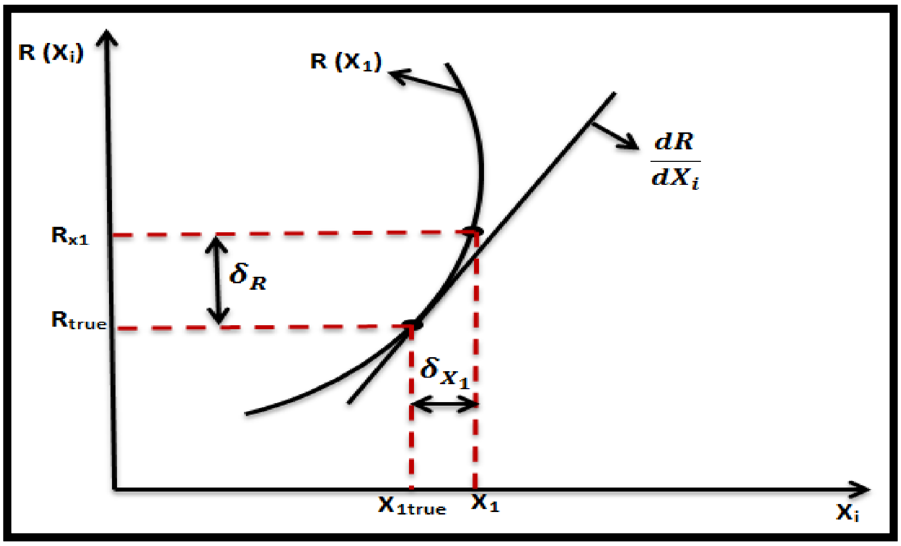

Figure C. 18: Error propagation in R from parameter X1[221, 222].

Finally, the overall accumulated uncertainty value for any experimental result, because of the errors found in all measured variables can be expressed using equation C.7, [222, 223]:

$$U_R = \sqrt{\left(\left[\frac{dR}{dX_1}\right] U_{X_1}\right)^2 + \left(\left[\frac{dR}{dX_2}\right] U_{X_2}\right)^2 + \cdots + \left(\left[\frac{dR}{dX_k}\right] U_{X_k}\right)^2} \qquad \text{(C.7)}$$

C.3.3 Uncertainty in Fluid Temperature Measurement:

Table C 2 shows the uncertainty values of four T types thermocouple installed in the test facility to measure the air temperature at various positions. It can be seen that the uncertainty of temperature measured varies from ± 0.391668809 to ±0.68 °C.

Table C 2: Calibration and uncertainty for the fluid thermocouples.

Thermocouple	**Position**	**Curve Fit Formula**	**Uncertainty (˚C)**
Thermocouple-1	Receiver Inlet	$Y_1 = 0.9995T + 0.964$	± 0.47381431
Thermocouple-2	Receiver Exit	$Y_2 = 0.9858T + 0.9808$	± 0.20125854

C.3.4 Uncertainty in Pressure Measurement:

As written in section C.1.1, two pressure transducers of PXM309 series with pressure ranges from 0 to 7 Bar at the inlet and from 0 to 3.5 Bar at the turbine exit. Also, two other pressure transducers, as shown below, were utilised in the test. The uncertainty of those pressure transducers were summarised below in Table C 3 and their overall average uncertainty is ±0.281586.

Table C 3: Calibration and uncertainty for the pressure transducers.

Transducer	**Position**	**Curve Fit Formula**	**Uncertainty (Bar)**
GE UNIK 5000-1	Pitot Total Pressure Port	$Y = 0.4246I - 0.659$	± 0.051835566
GE UNIK 5000-2	Pitot Static Pressure Port	$Y = 0.5725I - 2.3308$	± 0.191739117
PXM319-3.5GI	Rotor Exit	$Y = 0.2597I - 2.3547$	± 0.276157497

C.3.5 Uncertainty in Power Values:

The uncertainty in the measured power resulted from the uncertainty of the various measuring devices like the torque meter, data logger and the tachometer. The power extracted from the (SSRT) output power was calculated using C.8 (where the turbine torque is τ and ω represents its rotational speed). Equation C.7 was used to calculate the uncertainty in measuring the power.

Table **C 4** presents an example of the uncertainty calculation.

$$Power\ output = \tau\omega \tag{C.8}$$

Table C 4: Uncertainty propagation in power of the (SSRT).

Run	**Inlet temp.**	**Average temp. (˚C)**	**Inlet press. (Bar)**	**Average press. (Bar)**	**Power Uncertainty**
1	20	19.8	1.5	1.48	0.18425
2	30	29.3	1.8	1.85	0.43658
3	40	38.78	2	1.97	0.25123

C.3.6 Uncertainty in Efficiency Values:

The uncertainty in the (SSRT) efficiency was calculated based on equations C.7, which highlight the relevant measuring devices such as the pressure transducers, the thermocouples and the data logger and Equation 4.29. Table C 5 shows a sample of the uncertainty calculation of efficiency.

Table C 5: Uncertainty propagation in efficiency of the (SSRT).

Run	**Inlet temp. (˚C)**	**Average temp. (˚C)**	**Inlet press. (Bar)**	**Average press. (Bar)**	**Efficiency Uncertainty**
1	20	19.8	1.5	1.48	0.635422431
2	30	29.3	1.8	1.85	0.8756988
3	40	3	2	1.97	0.5369822